



Electron molecule collisions : study of reaction mechanisms and applications

Abdillah Abdoulanziz

► To cite this version:

Abdillah Abdoulanziz. Electron molecule collisions : study of reaction mechanisms and applications. Physics [physics]. Normandie Université, 2021. English. NNT : 2021NORMMLH14 . tel-03553064

HAL Id: tel-03553064

<https://theses.hal.science/tel-03553064>

Submitted on 2 Feb 2022

HAL is a multi-disciplinary open access archive for the deposit and dissemination of scientific research documents, whether they are published or not. The documents may come from teaching and research institutions in France or abroad, or from public or private research centers.

L'archive ouverte pluridisciplinaire **HAL**, est destinée au dépôt et à la diffusion de documents scientifiques de niveau recherche, publiés ou non, émanant des établissements d'enseignement et de recherche français ou étrangers, des laboratoires publics ou privés.

THÈSE

Pour obtenir le diplôme de doctorat

Spécialité **PHYSIQUE**

Préparée au sein de l'Université Le Havre Normandie

Collisions électron-molécule : étude des mécanismes réactionnels et applications

**Présentée et soutenue par
Abdillah ABDOULANZIZ**

**Thèse soutenue le 15/07/2021
devant le jury composé de**

M. MEHDI AYOZ	MAÎTRE DE CONFERENCES (HDR), UNIVERSITE PARIS-SACLAY	Membre du jury
M. ARNAUD BULTEL	MAÎTRE DE CONFERENCES (HDR), UNIVERSITE DE ROUEN NORMANDIE	Co-directeur de thèse
M. VINCENZO LAPORTA	CHARGE DE RECHERCHE (HDR), ISTP - CNR - RARI ITALIE	Membre du jury
M. GUILLAUME LOMBARDI	PROFESSEUR DES UNIVERSITES, UNIVERSITE PARIS 13 PARIS-NORD	Rapporteur du jury
Mme FRANCOISE MAUGE	DIRECTEUR DE RECHERCHE, UNIVERSITE CAEN NORMANDIE	Membre du jury
M. IOAN SCHNEIDER	PROFESSEUR DES UNIVERSITES, UNIVERSITE LE HAVRE NORMANDIE	Directeur de thèse
M. THIERRY STOECKLIN	DIRECTEUR DE RECHERCHE, UNIVERSITE BORDEAUX 1 SCIENCES ET TECHNO	Membre du jury
M. LAURENT WIESENFELD	DIRECTEUR DE RECHERCHE, UNIVERSITE PARIS-SACLAY	Rapporteur du jury

Thèse dirigée par IOAN SCHNEIDER et ARNAUD BULTEL, Laboratoire Ondes et Milieux Complexes

Remerciements

Ce travail de thèse a été réalisé au Laboratoire Ondes et Milieux Complexes (LOMC) de l'Université Le Havre Normandie, je tiens à présenter mes remerciements les plus sincères à mon directeur de thèse, le professeur Ioan SCHNEIDER, pour m'avoir donné la chance de réaliser mon stage de master 2 puis ce travail de thèse avec lui. Je le remercie pour sa disponibilité, son accompagnement, son encadrement, sa patience, sa rigueur scientifique, ses conseils et surtout pour sa confiance tout au long de ma thèse.

Ce travail est le fruit d'une collaboration scientifique de plusieurs chercheurs nationaux et internationaux. Je remercie mon codirecteur de thèse, monsieur Arnaud BULTEL et mon encadrant, monsieur Vincenzo LAPORTA pour leur assistance. Je remercie également Zsolt MEZEI pour son encadrement, sa pédagogie et pour les différents fructueux échanges partagés pendant ces années de thèse. Je tiens également à remercier le professeur Jonathan TENNYSON de m'avoir accueilli dans son unité de recherche à Londres pour pouvoir m'initier aux calculs de structures moléculaires avec les méthodes R-matrix ; merci beaucoup pour votre accompagnement et votre disponibilité durant toute la durée de ma thèse. Merci à Tom (Tomas MELTZE) pour ton temps et pour toutes les astuces partagées pendant ma visite à l'University College London (UCL). J'ai eu l'occasion de pouvoir m'initier aux études de molécules polyatomiques avec l'aide de Mehdi AYOZ, merci très sincèrement pour le temps et pour les conseils partagés avec moi au cours de mes dernières années de thèse.

Je tiens à exprimer mes remerciements aux membres du jury plus particulièrement aux professeurs Laurent WIESENFELD et Guillaume LOMBARDI pour avoir accepté de juger mon travail.

Je tiens à remercier tous ceux qui, de près ou de loin, ont contribué à la réalisation de ce travail. Dans toute équipe, outre les projets communs, les relations humaines sont au cœur du travail à réaliser et à ce titre, j'ai une pensée particulière

aux potos ; Bouba, Belaïd, Ziad, Oussama, Emérance, Paul, Abdessamad, Hrishi, Dr Cheick, Ahmad, Nihad, Tess, Ragav ..., merci pour ces années passées ensemble, c'étais pour moi un plaisir de partager ces moments avec vous.

Je ne saurais terminer ce travail de thèse sans le soutien profond de ma famille. Un grand merci à mes parents et mes oncles et plus particulièrement à Soilihi MOHAMED qui a œuvré toute sa vie pour notre réussite. Ce travail est le fruit de vos encouragements et de vos conseils, merci infiniment!!!. Merci à mes frères et sœurs, plus particulièrement à mon grand frère Abderemane et sa famille ainsi qu'à ma défunte sœur, que Dieu t'accueille dans les plus hauts degrés du paradis.

Enfin je voudrais adresser un merci particulier à ma très chère épouse et à ma fille pour tout leur amour sans oublier ma belle famille.

Contents

Introduction	xvi
1 General Introduction	1
2 Molecular states	5
2.1 Born-Oppenheimer approximation	7
2.2 An option for the electronic part: the adiabatic choice	9
2.2.1 The Hartree-Fock method	10
2.2.2 Post-Hartree-Fock methods	13
2.3 Basis set	14
2.4 Beyond the Born-Oppenheimer approximation	16
2.4.1 Adiabatic representation	18
2.4.2 Quasi-Diabatic representations	20
3 Multi-channel Quantum Defect Theory (MQDT): Application on reactive collisions	21
3.1 Subdivision of the configuration space	22
3.1.1 Inner region	22
3.1.2 Outer region	23
3.2 The channel notion	23
3.2.1 One-channel case	24
3.2.2 Lippmann-Schwinger equation	27
3.3 Multi-channel case	28
3.4 Multi-channel Quantum Defect Theory (MQDT) approach of the reactive collisions	32
3.4.1 General ideas	34
3.4.2 Vibrational dynamics Neglecting Rotational effects(VNR)	34

4	Electron scattering on ArH^+	45
4.1	Introduction	45
4.2	Molecular data	46
4.3	Results and discussion	50
4.4	Astrophysical consequences	54
4.5	Quantum defect influence on vibrational excitation	56
4.6	Conclusions	57
5	Electron scattering on HD^+	59
5.1	Introduction	59
5.2	Molecular data	60
5.3	Results	61
5.4	Conclusion	67
6	Electron induced reaction on N_2^+	69
6.1	Introduction	69
6.2	Theoretical approach	70
6.3	Molecular data	72
6.4	Results and discussions	73
6.5	Conclusions	79
7	Carbon dioxide electron impact reactions	81
7.1	Step of calculation	82
7.2	Theoretical approach	83
7.2.1	Basis set choice	83
7.2.2	Potential Energy Curve of CO_2	83
7.2.3	Dissociative electron attachment and dissociative excitation on carbon dioxide	89
7.3	R-matrix results	90
7.3.1	General ideas	90
7.3.2	Calculations	93
7.4	Conclusion	96
8	Electron scattering on formylium molecule (HCO^+)	97
8.1	Introduction	97
8.2	General ideas on theoretical approach	98
8.3	Target properties	99
8.4	Probabilities and cross section	104

8.5	Results	108
8.6	Conclusion	110
9	Conclusion and perspectives	113
10	Appendix A	115

List of Figures

1.1	Ranges of temperature and electron density for several laboratory and cosmic plasmas and their characteristic physical parameters: Debye length λ_D , plasma frequency ω_{pe} , and number of electrons N_D in a Debye sphere. MHD stand for magnetohydrodynamic. . . .	2
2.1	Particle coordinates in a diatomic molecule AB	6
2.2	Avoided crossing	20
3.1	Distribution of configuration space in terms of inter-nuclear (x axis) and electronic (y -axis) coordinates which lead to dissociation and ionization respectively. <i>BO</i> here means regions where the Born-Oppenheimer approximation can be applied while <i>CC</i> is the region where a close coupling representation is appropriate	24
3.2	Dissociative recombination mechanisms: (A) Direct mechanism: A dissociative state of the neutral (blue line) crossing the ion potential energy curve (black line). The electron is captured into this state and then dissociation occurs. (B) Indirect mechanism: The electron is first captured on a vibrational level of the neutral state belonging to a Rydberg series which converges to the ground state of the ion, coupled to the resonant state leading to dissociation.	34

- 3.3 Overlap between the relevant wave functions in electron/molecular cation collision, for several cases of vibrationally excited target, collided by a very slow (energy almost zero) electron. The solid curves are the target bound vibrational wave functions and the dashed ones are the dissociative ones. The colored horizontal lines correspond to the vibrational levels of the ion. The target potential energy curves of the ion (black line) and of the dissociative state of the neutral (dashed violet) are given. This example is valid for the H_2^+/H_2^{**} system. 36
- 4.1 R-matrix results for the resonant states of $^2\Pi$ symmetry. The dashed lines are the potential energy curves of the target ground electronic and excited states (blue curves) of ArH^+ . The dotted green curves are those of the Rydberg states converging to the ground electronic state and the red curves converging to the excited electronic states. 47
- 4.2 Potential energy curves used in the present calculations. The ArH^+ potential curves - ground state, $X^1\Sigma^+$, and the lowest excited electronic states - are displayed as black lines. The molecular data sets for the different symmetries of the neutral system are displayed with different colors: $^2\Sigma$ in red, $^2\Pi$ in blue and $^2\Delta$ in green. 48
- 4.3 Electronic couplings used in the present calculations. The molecular data sets for the different symmetries of the neutral system are displayed with different colors: $^2\Sigma$ in red, $^2\Pi$ in blue and $^2\Delta$ in green. 48
- 4.4 Quantum defects used in the present calculations. The molecular data sets for the different symmetries of the neutral system are displayed with different colors: $^2\Sigma$ in red, $^2\Pi$ in blue and $^2\Delta$ in green. 49
- 4.5 Dissociative recombination of vibrationally relaxed ArH^+ . Broken colored lines: The contributions coming from all the dissociative states having the same asymptotic atomic limit. Solid black line (partially hidden by the red curve): Total cross section coming from the sum over all the available dissociative states. 51
- 4.6 Dissociative recombination of ArH^+ on its lowest vibrational levels: (a) global cross sections, coming from the sum over all the available dissociative states; (b) the corresponding Maxwellian-averaged rate coefficients. 52

4.7	Dissociative recombination of vibrationally relaxed ArH^+ . Comparison between the rate coefficient measured in the CRYRING storage ring and the anisotropic rate coefficient obtained by the convolution of our MQDT-computed cross section using the temperatures characterizing the relative velocities of the electrons with respect to the ions in the experiment.	53
4.8	Vibrational excitation (VE) of ArH^+ on its lowest vibrational levels: Cross sections for $\Delta v^+ = 1$ (solid lines). The dissociative recombination (DR) cross section are also shown for comparison (broken line).	53
4.9	Dissociative recombination rate of vibrationally relaxed ArH^+ and ArD^+ as a function of electron temperature: The isotopic effects. . .	54
4.10	Relative abundance of ArH^+ as a function of the rate coefficients for the case of (a) diffuse ISM (temperature $T = 100$ K) and (b) Crab nebula (temperature $T = 1000$ K).	54
4.11	Variable quantum defect	56
4.12	Constant quantum defect	56
5.1	Cross section for Dissociative Recombination(DR), Elastic Collisions (EC), Dissociative Excitation (DE) and Vibrational Excitation (VE) of HD^+ on its vibrational levels (left pannel) global cross sections, coming from the sum over all the available dissociative states; right pannel the corresponding Maxwellian-averaged rate coefficients. (a) and (b) are results for $v_i^+ = 0$ and (c) and (d) for $v_i^+ = 1$	62
5.2	Same as figure (5.1) for $v_i^+ = 2$ ((a) and (b)) and $v_i^+ = 3$ ((c) and (d))	63
5.3	Same as figure (5.1) for $v_i^+ = 5$ ((a) and (b)) and $v_i^+ = 10$ ((c) and (d))	64
5.4	Same as figure (5.1) for $v_i^+ = 15$ ((a) and (b)) and $v_i^+ = 20$ ((c) and (d))	65
5.5	Maxwellian-averaged rate coefficients for Dissociative Recombination(DR) over the 11 levels for $T = 100, 1000, 5000$ and $10000K$	66

- 6.1 Potential energy curves (PEC) relevant for DR of N_2^+ , compiled from Figures. 2 and 3 of Little *et al.*. The color code of the curves is the following: Target cation: ground electronic state ($X^2\Sigma_g^+$): black; 1st excited state ($A^2\Pi_u$): red; 2nd excited state $B^2\Sigma_u^+$: green. Dissociative states of N_2 -left panel: $^1\Pi_u$: blue; $^1\Delta_g$: magenta; $a''^1\Sigma_g^+$: cyan; and $^1\Phi_u$: orange. Dissociative states of N_2 -right panel: $^3\Pi_u$: blue; $H^3\Delta_g$: magenta; and $^3\Phi_u$: orange. The lowest five vibrational levels of each electronic state of the ion and the dissociative asymptotic limits for all states are shown. The green dashed line gives the upper limit of the collision energy. 71
- 6.2 Molecular data sets relevant for the DR of N_2^+ limited to internuclear distances around the equilibrium geometry of the ion. 1st row: PECs of the ionic and neutral states for all relevant symmetries. 2nd row: all Rydberg-valence electronic couplings. 3rd row: the relevant Rydberg-Rydberg couplings. 4th row: quantum defects. 73
- 6.3 Global DR, VE and VdE cross sections of the N_2^+ $v_i^+ = 0$ (A), $v_i^+ = 1$ (B) and $v_i^+ = 5$ (C) as a function of the collision energy. For vibrational transitions (VE and VdE) we label the processes as transitions from the initial to the final vibrational levels of the target. The vertical dashed dark-green line gives the precision limit of the calculations. 75
- 6.4 Isotropic Maxwell rate coefficients of N_2^+ for $v_i^+ = 0 - 5$ initial vibrational levels for all relevant electron induced processes: Dissociative recombination (black line), elastic collision (indigo dashed line), vibrational excitation (thin coloured lines) and vibrational de-excitation (symbols and thick coloured lines). For the vibrational excitations all transitions are shown up to $\Delta v^+ = v_f^+ - v_i^+ = 8$ with the lowest transition being labeled on each figure. excitation and de-excitation to final vibrational quantum numbers are given. The green dashed line gives the precision limits of our calculation given in temperatures. 77
- 6.5 Relative difference between the calculated and fitted isotropic Maxwell rate coefficients. The fitting parameters of the (3), and (4) Arrhenius type formulas are listed in tables (6.2) and (6.3). The target vibrational quantum number is $v_i^+ = 1$ 78

7.1	Potential energy curves of the ground electronic state of CO_2 as function of the distance between the two oxygen atoms, the CO distance being frozen to its equilibrium value. The black solid curve is the singlet ground electronic state and the dashed one is the singlet excited state. The blue curve is the degenerate excited triplet state.	85
7.2	Potential energy curves of the ground electronic state of CO_2 as on figure (7.1) and different vibrational wave functions on colors. . . .	89
7.3	Partition of configuration space in fixed-nuclei R-matrix theory for CO_2 molecule. Space is divided into an inner and an outer regions .	91
7.4	Eigenphase sum for electron- CO_2 scattering	93
7.5	Potential energy curves of the ground electronic state of CO_2 as function of distance between the two oxygen atoms, the CO distance being frozen to its equilibrium value. The black solid curve is the singlet ground electronic state and the blue one is the triplet excited state. The red curves are Close Coupling (CC) results and the cyan curve the static exchange plus polarization (SEP) results. The circle marked curve are the results from Moradmand <i>et al</i>	95
7.6	Width for CO_2^- as function of the inter-nuclear distance. The dashed curve is the SEP result according to Figure 7.5 and the solid curve, the CC result	95
8.1	Representation of the normal modes of HCO^+ molecule: Symmetric stretching (a), bending (b) and asymmetric stretching (c). The carbon atom is represented by the black ball, the oxygen by the red ball and the hydrogen by the gray one	100
8.2	Potential energy curves of the ground electronic state of HCO^+ as function of the dimensionless geometry (Q) for bending (left panel), symmetric stretching (middle) and asymmetric stretching (right panel) modes. Red curves are results from Quantemol-N and black curves from Molpro.	102
8.3	Eigenphases as a function of the dimensionless geometry (Q) for electron-scattering energy $E_{el} = 0.1$ eV for the symmetric stretching (left bottom panel), bending (upper panel), and asymmetric stretching (right bottom panel) modes. The curves of different colors correspond to different symmetries	103

8.4	Eigenphase sums as a function of the incident electron energy for $q = 0.001$ (dimensionless) for the bending mode in C_s group symmetry (upper panel), symmetric stretching (left bottom panel) and asymmetric stretching (right bottom panel) modes in C_{2v} point group. The curves of different colors correspond to different symmetries of the electron HCO^+ scattering. For bending mode, black curve is for A' symmetry and the red one for A'' . For symmetric and asymmetric stretching, the black curve is for A_1 , red and green curves are for doublet degenerate symmetries B_1 and B_2 and the blue curve is for A_2 symmetry	109
8.5	DR cross section as on figure (6) of dos Santo <i>et al.</i> . The violet solid and dashed curves are respectively the calculated cross section and its convolution compared to previous works. Black curves are cross section calculation obtained with probabilities from dos Santo <i>et al.</i>	110
8.6	Excitation probabilities	111

Abstract

Electron-molecule collisions are present in various astrophysical media such as interstellar molecular clouds, in planetary atmospheres, and in cold natural or man-made plasmas. Theoretical investigations are presented in this thesis for diatomic molecular cation and polyatomic molecules. Using an approach based on the multichannel quantum defect theory, the dissociative recombination and competitive processes are calculated for diatomic molecules. Different approaches of this theory are used to compute the cross-section and the corresponding rate coefficients for ArH^+ molecular cation in a first case where a good agreement with merged beams measurement at low energy is shown. An extension of the theory is used to fully account the dissociative excitation and then computing all the processes cross-section of the HD^+ molecular cation. In a second extension of the same theory, with more target states, results are presented for the N_2^+ molecular cation. The potential energy curves of the carbon dioxide negative ion is calculated and results are in good agreement with the previous calculation. Finally, the electron induces dissociation of HCO^+ molecule is modeled in this thesis using an approach that combines the normal modes approximation for the vibrational states of the target molecule, the UK R-matrix code to obtain electron-molecule S-matrix for fixed geometries of the target and the vibrational frame transformation. The importance of the rate-coefficients in the collisional-radiative models of cold ionized media is outlined for all these species.

Keywords: Dissociative recombination, dissociative excitation, vibrational excitation, dissociative electron attachment, cross sections, rate coefficients

Résumé

Les collisions électron-molécule sont présentes dans divers milieux astrophysiques tels que les nuages moléculaires interstellaires, les atmosphères planétaires et les

plasmas froids naturels ou artificiels. Des études théoriques sont présentées dans cette thèse pour les cations moléculaires diatomiques et pour les molécules polyatomiques. En utilisant une approche basée sur la théorie des défauts quantiques multivoies, la recombinaison dissociative et les processus compétitifs sont calculés pour les molécules diatomiques. Différentes approches de cette théorie sont utilisées pour calculer la section efficace et les taux de réactions correspondants pour le cation moléculaire ArH^+ dans un premier cas où un bon accord avec l'expérience à basse énergie est montré. Une extension de la théorie est utilisée pour prendre entièrement en compte l'excitation dissociative et ensuite calculer la section efficace de tous les processus pour cation moléculaire HD^+ . Dans une deuxième extension de la même théorie, avec plus d'états cibles, des résultats sont présentés pour le cation moléculaire N_2^+ . Les courbes d'énergie potentielle de l'ion négatif du dioxyde de carbone sont calculées et les résultats sont en bon accord avec les calculs précédents. Enfin, la recombinaison dissociative de la molécule HCO^+ est aussi calculée dans cette thèse en utilisant une approche qui combine l'approximation des modes normaux pour les états vibrationnels de la molécule cible, le code UK R-matrix pour obtenir la matrice S, pour des géométries fixes et une "vibrational frame transformation". L'importance des coefficients de vitesse dans les modèles collisionnels-radiatifs des milieux ionisés froids est soulignée pour toutes ces espèces.

Mots clés : Recombinaison dissociative recombination, excitation dissociative, excitation vibrationnelle, attachment dissociative, sections efficaces, taux de réactions

Chapter 1

General Introduction

Electron-molecule collisions are major processes that occur in cold ionized media containing molecules: planetary atmospheres, interstellar molecular clouds, and cold natural or man-made plasmas. Plasmas can be observed in a lot of media in the universe but it also can be produced in laboratory and its temperature can vary from a few hundred to billions of Kelvin as it is shown in Figure (1.1) taken from [1]. The man-made plasma is widely used in laboratory and one of the most famous is the International Thermonuclear Experimental Reactor ([ITER](#)) which is an international project aiming to demonstrate the scientific and technical feasibility of nuclear fusion as a new source of clean energy for humanity. The world's annual energy consumption is increasing daily and to satisfy this energy demand, the main production of energy is based on the use of widely exploited and limited resources, the environmental consequences being catastrophic. The use of plasma-based thermonuclear fusion reactions, where the hydrogen isotopes, deuterium, and tritium react together to give the helium, is the probably the best candidate for future energy clean productions.

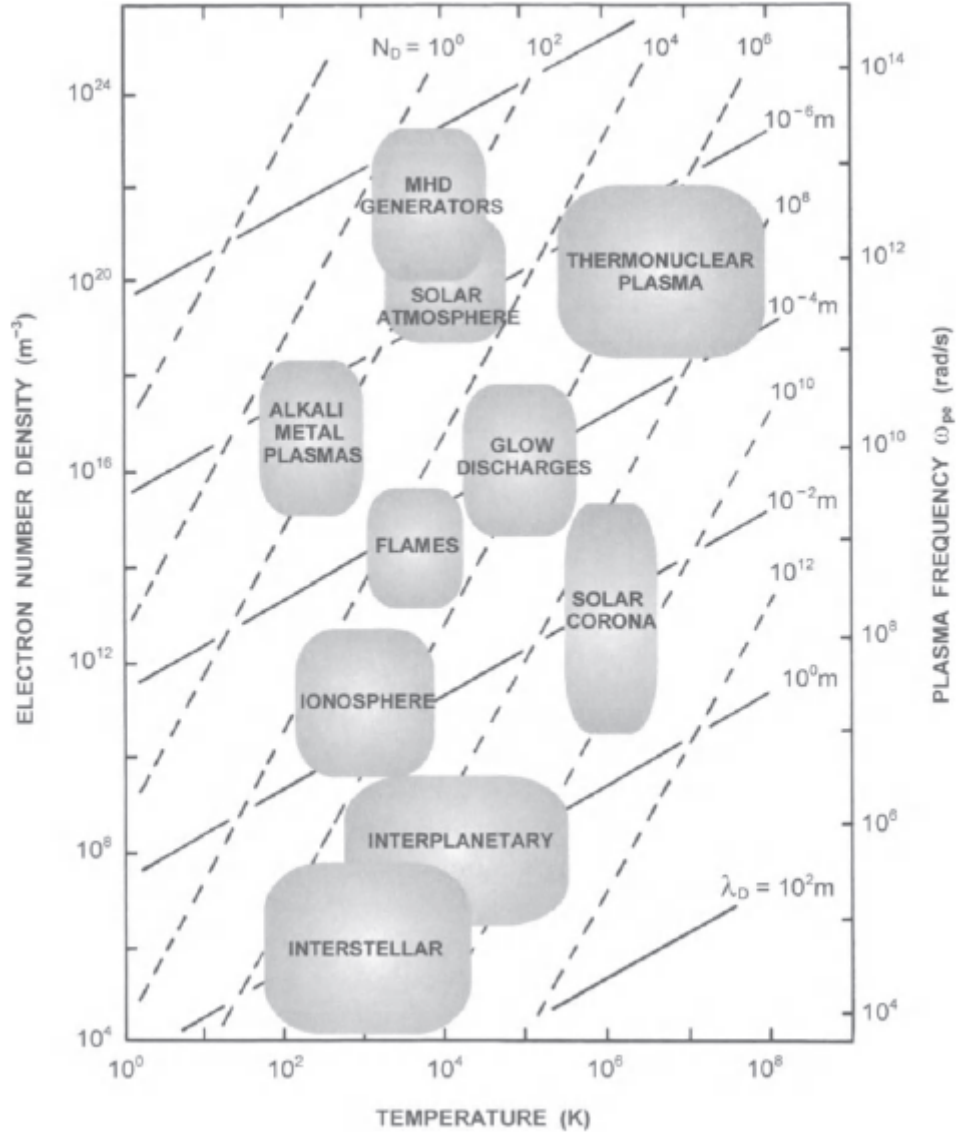
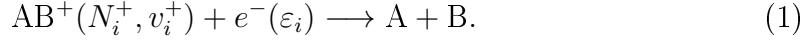


Figure 1.1: Ranges of temperature and electron density for several laboratory and cosmic plasmas and their characteristic physical parameters: Debye length λ_D , plasma frequency ω_{pe} , and number of electrons N_D in a Debye sphere. MHD stand for magnetohydrodynamic.

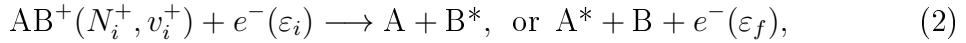
The biological effect of the low-energy electrons is shown by Budaiiffa *et. al.* [2] where the DNA damage is pointed out in their results. They show that abundant free secondary electrons are produced during ionization radiation with energy ranging from 1 and 20 eV. These electrons can induce the breaking of the DNA.

The study of electron-molecule collisions is more than crucial to model and understand the behavior of ionized media. Cross-sections and rate coefficients for these reactions are important for modelizers. In the case of molecular cations, the major reaction is the dissociative recombination (DR). It consists in the capture of

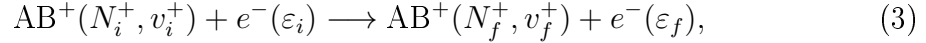
the incident electron by the target followed by the break-up of the neutral complex into two neutral fragments



This process is in competition with the dissociative excitation (DE) at high energy, above the dissociation energy of the molecule, where one of the two fragments is excited:



and the vibrational excitation (VE) and deexcitation (VdE) where the initial vibrational target state is lower and higher respectively:

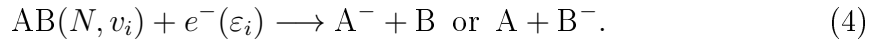


Here $N_i^+, N_f^+, v_i^+, v_f^+, \varepsilon_i$ and ε_f are respectively the initial and final rotational quantum number, the initial and final vibrational quantum number and the initial and final incident electron energy.

For poly-atomic molecules the processes remain the same with a multitude dissociation pathways and complexity because of the additional degrees of freedom that are introduced in the target such as vibration and rotation of the nuclei.

In addition to these processes, we mention the elastic collision (EC) where $\varepsilon_i = \varepsilon_f$ and $N_i^+ = N_f^+, v_i^+ = v_f^+$ in reaction (3).

For the case of neutral molecules, the processes are similar to those of reactions (2), (3) and reaction (1) is replaced by dissociative electron attachment (DEA) which is a process whereby the incoming electron attaches to a molecule causing it to a neutral and anion fragments as:



The need of data for all of these reactions is important for scientists performing measurements of cross-section and rate coefficients. But these experiments can be very expensive and theoretical calculations can be the best way to overcome the lack of experimental measurements. The calculation is relatively cheap compared to experiments and we can get information about all possible transitions of the molecule for a wide range of energy. The aim of this thesis is to provide theoretical studies for reactions listed above for collision between electron and molecules at electron

impact energy below the dissociation energy of the target for some molecules and above this dissociation for others with different theoretical approaches.

The organization of this thesis is as follows. The next chapter denoted "molecular states" will describe the relevant theory appropriate for the the different target states used in this thesis. It is a general overview of the quantum chemistry methods used followed by the the presentation of the Multi-channel Quantum Defect Theory (MQDT) in chapter (3) which is used for the case of molecular cation target. Its application is the subject of the next three chapters. The first application is the electron scattering on the ArH^+ molecular cation in chapter (4) where cross-sections are presented for dissociative recombination and electron-impact vibrational excitation at electron energies appropriate for the interstellar environment. The cross sections and the corresponding Maxwellian rate coefficients are computed using the simplest approach of the MQDT. It consists in taking into account the target ground electronic state and incident electron energy below the ion's dissociation limit in the calculation. The second application is the electron scattering on HD^+ molecular cation in chapter (5). The cross-section and rate coefficients of reactions (1), (2) and (3) for DR, DE, EC, VE and VdE are computed respectively. The MQDT approach used in this chapter includes the first excited state of the target and the calculation goes above the dissociation limit. The last application considers as target the N_2^+ molecular cation in chapter (6) where cross-sections and thermal rate coefficients are computed for electron-impact DR, VE and VdE of the N_2^+ molecular ion in its lowest six vibrational levels, for collision energies up to 2.3 eV. The two last chapter are devoted to poly-atomic molecules. In chapter (7) we compute the potential energy curves of the CO_2 molecule as target, as well as those of the different resonant state of CO_2^- using quantum chemistry and R-matrix [3, 4] methods. In chapter (8) we compute the DR cross-section for electron scattering with formylium molecule (HCO^+). Finally the thesis is concluded with a summary of the obtained results and perspectives.

Chapter 2

Molecular states

The description of the molecular dynamics in our formalism starts by a good knowledge of the target states. Once they are correctly described, we can build the states of the whole molecular system - intermediate or resonant states - formed during the collision with an electron. An accurate calculation of both these types of states is crucial for the prediction of the reaction products.

Our purpose in this chapter is to identify the major molecular states involved in the collisional processes addressed in our study and to describe the different ways to compute them.

We start this description by writing the non-relativistic time-independent Schrödinger equation

$$H\Psi = E\Psi, \quad (1)$$

where the Hamiltonian H is splitted in an electronic and nuclear part:

$$H = T_N + H^{(e)}, \quad (2)$$

$H^{(e)}$ being called electronic Hamiltonian, since it describes the movement of the electrons for a given geometry of the internuclear arrangement, and T_N being the kinetic-energy operator associated to the motion of the nuclei.

In order to explicitate the Hamiltonian in equation (2), let us consider a diatomic molecule AB with M_A and M_B the masses of the nuclei A and B respectively.

In figure(2.1) the molecular coordinates are shown. q_{iA} , q_{iB} , q_{ij} and $R = R_{AB}$ are respectively the distance between the electron i and the nucleus A, the distance between the electron i and the nucleus B, the distance between the electrons i and j , and the inter-nuclear distance, *i.e.* the distance between the nuclei A and B. According to these coordinates, the two parts (2) of the general Hamiltonian in the

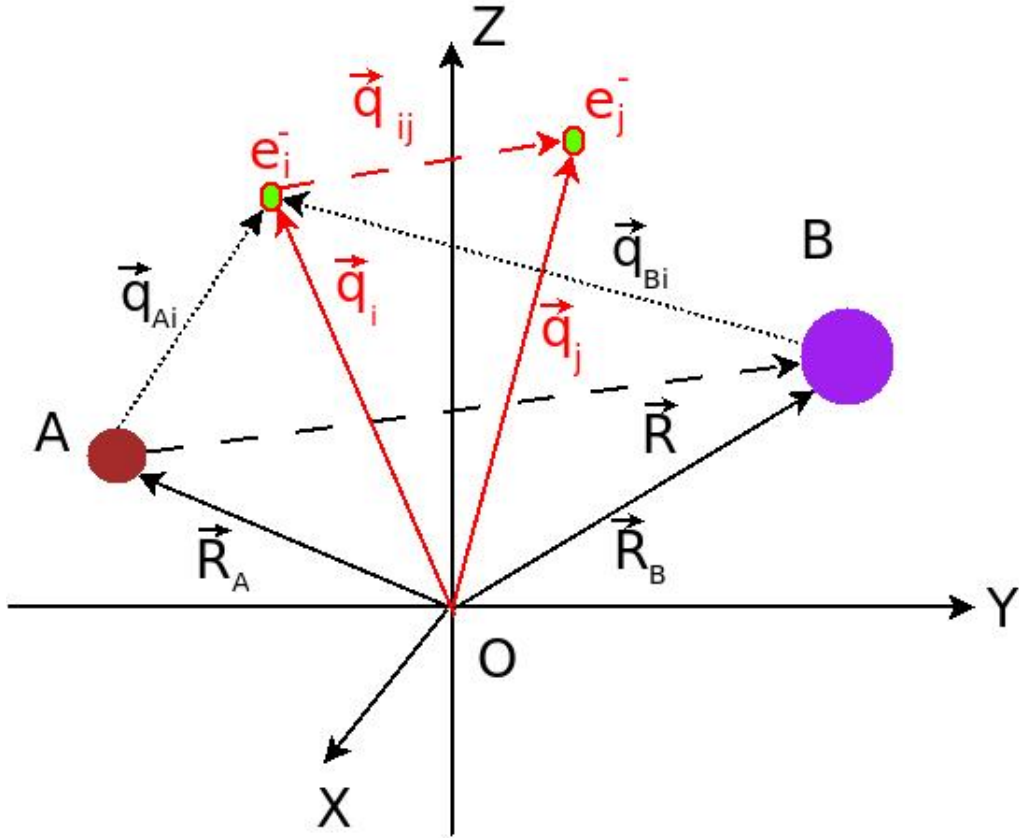


Figure 2.1: Particle coordinates in a diatomic molecule AB

Schrödinger equation (1) can be explicitly be written as:

$$T_N = -\frac{\hbar^2}{2M_A}\Delta R_A - \frac{\hbar^2}{2M_B}\Delta R_B, \quad (3)$$

and

$$H^{(e)} = T_e + V_{NN} + V_{eN} + V_{ee}, \quad (4)$$

where

$$T_e = -\frac{\hbar^2}{2m_e} \sum_{i=0}^n \Delta q_i \quad (5)$$

is the electron's kinetic energy,

$$V_{NN} = \frac{Z_A Z_B e^2}{4\pi\epsilon_0 |R|} \quad (6)$$

the nucleus-nucleus repulsion,

$$V_{eN} = - \sum_{i=0}^n \frac{Z_A e^2}{4\pi\epsilon_0 |q_{Ai}|} - \sum_{i=0}^n \frac{Z_B e^2}{4\pi\epsilon_0 |q_{Bi}|} \quad (7)$$

the electron-nucleus attraction and

$$V_{ee} = \sum_{i < j} \frac{e^2}{4\pi\epsilon_0 |q_{ij}|}, \quad (8)$$

the electron-electron repulsion. If we work in the center of mass frame, the relevant nuclei kinetic energy (3) will be:

$$T_N = -\frac{\hbar^2}{2\mu} \Delta R, \quad (9)$$

and the all the other parts of the Hamiltonian are the same.

The resolution of equation (1) is *a priori* very complex, due to the number of degrees of freedom to be taken into account. Hopefully, approximations exist to make it simpler, if the physics is well modeled. An intuitive choice is to separate as much as possible the variables, and this can be achieved in the Born-Oppenheimer context, illustrated below.

2.1 Born-Oppenheimer approximation

[5] The proton and the electron masses are known to be respectively $m_p = 1.676231 \times 10^{-27}$ kg and $m_e = 9.1093897 \times 10^{-31}$ kg. Otherwise, $m_p \approx 1836m_e$. This huge mass ratio plays a fundamental role in the simplification of the study of the energy and of the dynamics of molecules. For low total energy of the molecular system, the electron average velocity is much larger compared to that of the nuclei. We can thus, in a first step, study the movement of the electrons by considering the nuclei as fixed, determine their energy within this assumption, and study eventually the vibration movement of the nuclei in an average potential relying on the previously determined electronic energy. This is called the Born-Oppenheimer approximation [6]. Within this approximation, the total wave function Ψ in equation (1) is divided in two parts and it can be written as a product between a nuclear

and an electronic part, involving all the nuclei and electronic coordinates:

$$\Psi = \psi(\vec{q}_i, R)\chi(\vec{R}), \quad (10)$$

where $\psi(\vec{q}_i, R)$ and $\chi(\vec{R})$ are respectively electronic and nuclear wave functions.

Applying the Schrödinger equation(1) together with equation (2) we obtain:

$$H^{(e)}\psi(\vec{q}_i, R)\chi(\vec{R}) + T_N(\psi(\vec{q}_i, R)\chi(\vec{R})) = E\psi(\vec{q}_i, R)\chi(\vec{R}) \quad (11)$$

$H^{(e)}$ acts only on $\psi(\vec{q}_i, R)$ while T_N acts both on $\chi(\vec{R})$ and $\psi(\vec{q}_i, R)$

$$T_N(\psi(\vec{q}_i, R)\chi(\vec{R})) = \frac{-\hbar^2}{2\mu} \left[\psi(\vec{q}_i, R)\Delta\chi(\vec{R}) + 2\vec{\nabla}\psi(\vec{q}_i, R) \cdot \vec{\nabla}\chi(\vec{R}) + \chi(\vec{R})\Delta\psi(\vec{q}_i, R) \right] \quad (12)$$

Using the normalization of the electronic part wave function ($\langle \psi(\vec{q}_i, R) | \psi(\vec{q}_i, R) \rangle = 1$) when making the scalar product of the electronic wave function $\psi(\vec{q}_i, R)$ at the left of equation (11) we can write:

$$\begin{aligned} & \left[\langle \psi(\vec{q}_i, R) | H^{(e)} | \psi(\vec{q}_i, R) \rangle + T_N + \langle \psi(\vec{q}_i, R) | T_N | \psi(\vec{q}_i, R) \rangle \right] \chi(\vec{R}) + \\ & \left[-\frac{\hbar^2}{\mu} \langle \psi(\vec{q}_i, R) | \vec{\nabla} \psi(\vec{q}_i, R) \rangle \cdot \vec{\nabla} \right] \chi(\vec{R}) = E\chi(\vec{R}) \end{aligned} \quad (13)$$

By defining the \hat{B} operator as:

$$\hat{B} = \langle \psi(\vec{q}_i, R) | T_N | \psi(\vec{q}_i, R) \rangle - \langle \psi(\vec{q}_i, R) | \hat{C} \psi(\vec{q}_i, R) \rangle \quad \hat{C} \quad (14)$$

where $\hat{C} = \frac{\hbar}{\sqrt{\mu}} \vec{\nabla}$ and the energy term $U(R)$

$$U(R) = \langle \psi(\vec{q}_i, R) | H^{(e)} | \psi(\vec{q}_i, R) \rangle \quad (15)$$

1

$$\begin{aligned} \Delta(\chi\psi) &= \vec{\nabla}(\psi\vec{\nabla}\chi + \chi\vec{\nabla}\psi) \\ &= \vec{\nabla}(\psi\vec{\nabla}\chi) + \vec{\nabla}(\chi\vec{\nabla}\psi) \\ &= \psi\Delta\chi + 2\vec{\nabla}\chi \cdot \vec{\nabla}\psi + \chi\Delta\psi \end{aligned}$$

the equation (13) becomes

$$\left[U(R) + T_N + \hat{B} - E \right] \chi(\vec{R}) = 0 \quad (16)$$

The Born-Oppenheimer approximation consist in the neglect the term $\hat{B}\chi(\vec{R})$:

$$\hat{B}\chi(\vec{R}) \approx 0 \quad (17)$$

which is partially justified by the fact that the mass ratio between nuclei and electron is huge. Then we can rewrite equation (10) as :

$$\Psi_{BO} = \psi_{BO}(\vec{q}_i, R) \chi_{BO}(\vec{R}), \quad (18)$$

where $\chi_{BO}(\vec{R})$ is the solution of the eigenvalues equation:

$$[U(R) + T_N - E] \chi(\vec{R}) = 0 \quad (19)$$

Within this approximation we can focus ourselves to reach the physical meaning of this $\psi_{BO}(\vec{q}_i, R)$ and $U(R)$ and this is the aim of the next sections.

2.2 An option for the electronic part: the adiabatic choice

Concerning the physical significance of $\psi_{BO}(\vec{q}_i, R)$, a natural choice is to take this wave function as the eigen-function corresponding to the eigen-energy of the *electronic* Schrödinger equation:

$$H^{(e)} \psi^{(ad)} = U^{(ad)} \psi^{(ad)} \quad (20)$$

where $H^{(e)}$ is the *electronic* Hamiltonian, defined by equation (2). Consequently, by taking $\psi_{BO}(\vec{q}_i, R) = \psi^{(ad)}$ naturally we can see that $U(R) = U^{(ad)}(R)$ can be considered as the electronic energy of our molecular system for a given inter-nuclear distance R . This is the so-called *adiabatic* choice, and it is the basis of the traditional quantum chemistry. Over the years, different methods have been elaborated in order to solve the equation (20), and we will focus ourselves to some of the *ab initio* methods based on Hartree and post-Hartree Fock methods in the

following sections.

2.2.1 The Hartree-Fock method

In the coming paragraphs, I am describing the major quantum chemistry details related to my molecular structure calculation, as exposed by Attila Szabo and Neil S. Ostlund in "MODERN QUANTUM CHEMISTRY" [7]

The Schrödinger equation is known to be a many-body problem which can not be solved analytically. Within the framework of the polyelectronic wave function representation by a Slater determinant, the Hartree-Fock method makes possible to solve the Schrödinger equation by substituting the Hamiltonian's eigenvalues and eigenfunctions search by those of a monoelectronic \hat{F} *pseudo* operator

$$H^h = \sum_{i=1}^Z \hat{F}(i) \quad (21)$$

representing the interaction of an electron with the nuclei on one hand and a local repulsive field taking into account the presence of the other electrons on the other hand as :

$$\hat{F}(i)\psi(q_i) = \epsilon_i\psi_i(q_i) \quad (22)$$

where $\psi_i(q_i)$ are orbital functions representing the position vector q_i and ϵ_i are the monoelectronic energies. The total electronic energy in this approximation is the sum of these monoelectronic energies.

$$E_e^h = \sum_{i=1}^Z \epsilon_i \quad (23)$$

In equation(20) the Ψ wave function is an anti-symmetric sum of products of spin-orbit ϕ_i eigenfunctions of the $\hat{F}(i)$ operator. It can be written as a Slater determinant :

$$\Psi_{elec} = \frac{1}{\sqrt{n!}} \begin{pmatrix} \phi_1(1) & \dots & \phi_1(n) \\ \dots & \dots & \dots \\ \phi_n(1) & \dots & \phi_n(n) \end{pmatrix} \quad (24)$$

where $\phi_i(j) = \psi_i(q_i) \times \psi^{spin}(s_j)$ and $\psi^{spin}(s_j) = \alpha$ or β . Here α and β are two orthonormal functions describing the spin up and down of the electron, respectively.

In this approximation, the *independent-electron assumption* [8] is stated, which means that, the electron-electron interaction is completely neglected.

The further step is to take into account the general effect of other electrons on a given electron i . The Fock operator (22) can be written as :

$$\hat{F}(i) = -\frac{\hbar^2}{2m_e} \vec{\nabla}^2 - \frac{Ze^2}{4\pi\epsilon_0 q_i} + \sum_{i \neq j} V_j \quad (25)$$

Here $-\frac{\hbar^2}{2m_e} \vec{\nabla}^2 - \frac{Ze^2}{4\pi\epsilon_0 q_i} = \hat{h}(i)$ is the mono-electronic hydrogenoid Hamiltonian. The interaction of the j electron with the i electron are not included in this operator. The Hartree Fock method does not take into account the *electronic correlation*. To find out V_j let us apply ϕ_i on (25)

$$\langle \phi_i | \hat{F}(i) | \phi_i \rangle = \langle \phi_i | \hat{h}(i) | \phi_i \rangle + \sum_{i \neq j} Rep_{ij} \quad (26)$$

Rep_{ij} is the average value of the electronic repulsion operator $\frac{e^2}{4\pi\epsilon_0 q_{ij}}$ between i and j electrons with ϕ_i and ϕ_j spin-orbitals. The wave function of the two-electron-system bellow, is a Slater determinant $\phi_i \phi_j$

$$Rep_{ij} = J_{ij} - K_{ij} = \left(\langle \phi_i \phi_j | \frac{e^2}{4\pi\epsilon_0 q_{ij}} | \phi_i \phi_j \rangle \right) \quad (27)$$

where the Coulomb operator

$$J_{ij} = \frac{e^2}{4\pi\epsilon_0} \iint \phi_i(1)^* \phi_i(1) \frac{1}{q_{ij}} \phi_j(2)^* \phi_j(2) d\vec{q}_1 d\vec{s}_1 d\vec{q}_2 d\vec{s}_2 \quad (28)$$

and the exchange operator

$$K_{ij} = \frac{e^2}{4\pi\epsilon_0} \iint \phi_i(1)^* \phi_j(1) \frac{1}{q_{ij}} \phi_j(2)^* \phi_i(2) d\vec{q}_1 d\vec{s}_1 d\vec{q}_2 d\vec{s}_2 \quad (29)$$

We can see that $\hat{F}(i)$ can be written as :

$$\hat{F} = \hat{h} + \sum_{j=1}^Z \hat{J}_j - \hat{K}_j \quad (30)$$

with

$$\hat{J}_j \phi_i(1) = \phi_i(1) \int \frac{e^2 \phi_j(2)^* \phi_j(2)}{4\pi\epsilon_0 q_{ij}} d\vec{q}_2 d\vec{s}_2 \quad (31)$$

and

$$\hat{K}_j \phi_i(1) = \phi_j(1) \int \frac{e^2 \phi_j(2)^* \phi_i(2)}{4\pi\epsilon_0 q_{ij}} d\vec{q}_2 d\vec{s}_2 \quad (32)$$

The resolution of eq.(22) is done with the variational method since the Fock operator contains eigenfunctions which are the solutions of this equation. We start by choosing a set of M orbitals χ which constitute the expansion basis of the ψ solution [9].

$$\psi_i = \sum_k^M C_{ik} \chi_k \quad (33)$$

Plugging eq.(33) into eq.(22) yields

$$\begin{aligned} \sum_k^M C_{ik} \hat{F} |\chi_k\rangle &= \epsilon_i \sum_k^M C_{ik} |\chi_k\rangle \\ \sum_k^M C_{ik} \langle \chi_l | \hat{F} | \chi_k \rangle &= \epsilon_i \sum_k^M C_{ik} \langle \chi_l | \chi_k \rangle, \forall l = 1, \dots, M \end{aligned} \quad (34)$$

Here eq.(34) can be written as:

$$[\tilde{F}\tilde{C} - \epsilon\tilde{S}\tilde{C}] = 0 \quad (35)$$

where $\tilde{F} = \langle \chi_l | \hat{F} | \chi_k \rangle$ and $\tilde{S} = \langle \chi_l | \chi_k \rangle$. We have a set of M equations with M unknown ψ_i and ϵ orbital energies. The calculation of \hat{F} supposes to know a set of ψ_i orbitals which can form a Slater determinant eigenfunction of the system and this is precisely what we are looking for. Therefore, the calculation will start with a set of orbitals ψ_j^0 combinations of basic functions χ_k which will form a determinant called the *trial function*. They are used to calculate the matrix elements \tilde{F}^0 and to solve the secular equations giving ψ_j^1 and so on iteratively up to reach convergence defined by $\psi_j^r = \psi_j^{r+1}$. This is called the self-consistent field (SCF) method. Only occupied orbitals in the fundamental determinant are optimized because they are involved in F (J and K), the others are virtual.

The total energy E_e^{SCF} is calculated using the electronic Hamiltonian $H^{(e)}$ with

the approximate optimized wave function $\Psi^{SCF} = |\phi_1^{opt} \dots \phi_Z^{opt}|$:

$$\begin{aligned} E_e^{SCF} &= \langle \Psi^{SCF} | \hat{H}^{(e)} | \Psi^{SCF} \rangle \\ &= \sum_i h_{ii} + \sum_i \sum_{i>j} (J_{ij} - K_{ij}) \\ &= \sum_{i=1}^Z \epsilon_i - \sum_i \sum_{i>j} Rep_{ij} \end{aligned} \quad (36)$$

The Hartree-Fock method is useful to begin a calculation of wave function and eigenvalue of a molecular or atomic system and as mentioned previously the *electron-electron interaction* is not taken into account in this method. This is a major weakness because of the neglect of the electron correlation which can lead to large deviations from experimental results. Several approaches to this weakness, in general, called post-Hartree-Fock methods, have been derived to include electron correlation to the multi-electron wave function.

2.2.2 Post-Hartree-Fock methods

The post-Hartree-Fock methods are splitted into three standard models based on configuration interaction (CI), coupled-cluster (CC) and many-body perturbation theories [10]. In this work, only configuration interaction methods are used to calculate the wave function and the total energy beyond the Hartree-Fock approximation. The configuration interaction uses a linear combination of several electronic configuration wave functions [11, 12] which can be written as:

$$\Psi_{CI}(\vec{q}_i, \vec{R}) = a_0 \Phi_0 + \sum_k^{\infty} a_k \Phi_k(\vec{q}_i, \vec{R}) \quad (37)$$

where Φ_0 is the reference Hartree-Fock wave function [10] and Φ_k is a Slater determinant for singly-, doubly-, ... excited states. In the following part only two configuration interaction based on Multi-Configurational Self-Consistent Field (MCSCF) and Multi-Reference Configuration Interaction (MRCI) are described since the most potential energy curves used on this work are calculated with these two configuration interaction methods.

2.2.2.1 Multi-Configurational Self-Consistent Field (MCSCF)

The MCSCF method uses a set of coefficients where the determinants and the basis functions in the molecular orbitals in equation (37) are varied to obtain the

total electronic wave-function with the lowest possible energy using a variational minimization. It is a generalization of the Hartree-Fock method with the use of a combination between configuration interaction and the Hartree-Fock method. A specific type of the MCSCF method is the complete active space self-consistent field or (CASSCF) in which the number of determinants used in the expansion of CI vector is divided into three subspaces: The first one is *the inactive space*, where all orbitals are doubly occupied. The second one is known as *the active space*, and within electrons and orbitals included in this subspace are those that contribute mostly to the multireference character of the particular system of study. The last one is termed as *the virtual space*, where orbitals are kept unoccupied. The number of determinants is decreased in this method since core electrons and orbitals are inactive and active space electrons are distributed over all possible excitation on equation (37) [12]. Good knowledge of the chemical system under study is needed for the proper choice of the different configurations.

2.2.2.2 Multi-Reference Configuration Interaction (MRCI)

The MRCI is a more accurate CI method where the reference wave function is constructed by generating a CI vector representing the multi-configuration space taken on an MCSCF calculation. This leads to having more configuration since the interactions come from a CI calculation added to the different excitations from the MRCI equations [12]:

$$\Psi_{MRCI}(\vec{q}_i, \vec{R}) = a_0 \Phi_{MCSCF} + \sum_s a_s \Phi_{MCSCF}^s + \sum_d a_d \Phi_{MCSCF}^d + \sum_t a_t \Phi_{MCSCF}^t + \dots \quad (38)$$

where Φ_{MCSCF}^s , Φ_{MCSCF}^d and Φ_{MCSCF}^t are single, double and triple excitation functions respectively come from an MCSCF calculation. A truncation must be done [10] with single and double excitation to provide a highly accurate description of the molecular system because the calculation become heavier and heavier with the inclusion of configurations from MCSCF calculation. Note that it is important to include the dominant configuration in the MCSCF calculation in order to get an accurate MRCI calculation.

2.3 Basis set

The notion of basis set is primordial to any quantum chemistry calculation. The Hartree Fock method described in section (2.2.1) uses molecular orbitals de-

veloped on a given atomic orbital basis according to the Linear Combination of Atomic Orbitals (LCAO) approximation as shown in equation (33). The definition of orbital basis allowing the description of molecular orbitals is necessary to better describe a molecular system. There are two basic types of functions mainly used in an electronic structure calculation: the solutions of the Schrödinger equation of hydrogen-like atoms called Slater Type Orbitals (STO) and Gaussian Type Orbitals (GTO).

The STO's functions can be written as:

$$\chi_{\zeta,n,l,m}(r, \theta, \phi) = NY_{l,m}(\theta, \phi)r^{n-1}e^{-\zeta r} \quad (39)$$

where N is a normalization constant, $Y_{l,m}(\theta, \phi)$ are the spherical harmonic functions depending on angular coordinates and describe the shape of orbitals and n , l , and m are the principal, orbital, and magnetic quantum numbers respectively. The exponential dependence of the distance between the nucleus and the electrons is that of the orbitals of the hydrogen atom. Thus, a linear combination of several STOs allows to reproduce correctly the true orbitals. Even if the dependency in r allows to write correctly the behavior of the orbitals when $r \rightarrow 0$, the computation of integrals with more centers, such as bi-electronic integrals, is not analytically possible. So, for molecules, instead of STOs which decay with e^{-r} it is useful to use GTO which can be written in Cartesian coordinates as:

$$\chi_{\zeta,l_x,l_y,l_z}(x, y, z) = Nx^{l_x}y^{l_y}z^{l_z}e^{(-\alpha r^2)} \quad (40)$$

Here the sum $l_x + l_y + l_z$ allows to determine the orbital type: $l_x + l_y + l_z = 0$ is an orbital of type s , $l_x + l_y + l_z = 1$ is an orbital of type p , $l_x + l_y + l_z = 2$ is an orbital of type d , $l_x + l_y + l_z = 3$ is an orbital of type f , etc.

The multiplication of two GTO results in a new GTO. Therefore, bi-electronic integrals are much easier to evaluate with GTO than with STO functions. However they have the disadvantage of not correctly describing the exact orbital in the vicinity of the nucleus at $r \rightarrow 0$, but also of decreasing too quickly as a function of r at $r \rightarrow \infty$. Hence, the representation of molecular orbitals requires many more GTO numbers than Slater functions. Despite this drawback, the ease of computation of bi-electronic integrals makes Gaussian functions the most widely used orbitals in quantum chemistry.

STO functions can be represented by a linear combination of GTO functions. And the smallest of these latter can be used to well describe molecular orbitals. They are called *minimal basis*, and are typically consisting of the minimum number

of basic functions required to represent all the electrons in each atom. A minimal basis is the one in which, on each atom of the system, only basic function is used for each orbital in a calculation. These basis can be expanded by including double, triple, or quadruple orbitals on the valence functions to have *Double Zeta*, *Triple Zeta*, or *Quadruple Zeta* orbitals. This allows the electron density to be contracted.

The most common addition to a minimal basis is the *polarization functions* which are auxiliary functions with an extra node. Another common addition is the *diffuse functions*. These are very soft Gaussian base functions, which represent more precisely the "tails" of the atomic orbitals, distant from the atomic nucleus.

The Dunning's [13] correlation consistent polarized basis sets are widely used in post-Hartree-Fock calculations. They start with 'cc-p', for correlation consistent polarized followed by 'V' for valence and Z for Zeta. They are *Double*, *Triple*, *Quadruple ... Zeta* (cc-pVDZ, cc-pVTZ, cc-pVQZ ...).

2.4 Beyond the Born-Oppenheimer approximation

The electronic solution described in section (2.2) is calculated with a parametrization of the internuclear distances in the Born-Oppenheimer approximation. Within this approximation, we can get *ab initio* potential energy curves (PEC) of the ground electronic and weakly-excited states of our molecular system. In the case of dynamic calculations, like those for electron-molecule collisions which are the subject of this thesis, we are lead to calculate couplings involving two different Born-Oppenheimer or adiabatic states, since the Born-Oppenheimer approximation may not be available because we involve highly-excited molecular states and the electron's movement is not necessarily more rapid than those of the nuclei. In such cases, we have to find another way to choose the total wave function describing our molecular dynamic. An adequate solution is to take the total wave function not as a Born-Oppenheimer product solution but as a sum of these products [14, 15].

$$\Psi = \sum_{m,v} \psi_m(\vec{q}_i, R) \chi_{mv}(\vec{R}), \quad (41)$$

Here m stands for a Born-Oppenheimer electronic state and v for a vibrational quantum number associated to the electronic state m . For the sake of simplification, we will omit the v symbol in the following equations. The total wave function (41)

becomes:

$$\Psi = \sum_m \psi_m(\vec{q}_i, R) \chi_m(\vec{R}), \quad (42)$$

we can write the Schrödinger equation (1) as :

$$H_e \sum_m \psi_m(\vec{q}_i, R) \chi_m(\vec{R}) + T_N \sum_m \psi_m(\vec{q}_i, R) \chi_m(\vec{R}) = E \sum_m \psi_m(\vec{q}_i, R) \chi_m(\vec{R}) \quad (43)$$

$$\begin{aligned} H_e \sum_m \psi_m(\vec{q}_i, R) \chi_m(\vec{R}) + \sum_m \psi_m(\vec{q}_i, R) T_N \chi_m(\vec{R}) - \sum_m \hat{C} \psi_m(\vec{q}_i, R) \hat{C} \chi_m(\vec{R}) \\ + \sum_m \chi_m(\vec{R}) T_N \psi_m(\vec{q}_i, R) = E \sum_m \psi_m(\vec{q}_i, R) \chi_m(\vec{R}) \end{aligned} \quad (44)$$

Let make the scalar product of a given $\{\psi_n(\vec{q}_i, R)\}$ functions on the left of equation (43), we can write :

$$\begin{aligned} & \langle \psi_n(\vec{q}_i, R) | H_e | \psi_n(\vec{q}_i, R) \chi_n(\vec{R}) \rangle + \langle \psi_n(\vec{q}_i, R) | \psi_n(\vec{q}_i, R) T_N \chi_n(\vec{R}) \rangle - \\ & \langle \psi_n(\vec{q}_i, R) | \hat{C} \psi_n(\vec{q}_i, R) \hat{C} \chi_n(\vec{R}) \rangle + \langle \psi_n(\vec{q}_i, R) | \chi_n(\vec{R}) T_N \psi_n(\vec{q}_i, R) \rangle - \\ & E \langle \psi_n(\vec{q}_i, R) | \psi_n(\vec{q}_i, R) \chi_n(\vec{R}) \rangle \\ = & \sum_{m \neq n} \langle \psi_n(\vec{q}_i, R) | H_e | \psi_m(\vec{q}_i, R) \chi_m(\vec{R}) \rangle - \sum_{m \neq n} \langle \psi_n(\vec{q}_i, R) | \psi_m(\vec{q}_i, R) T_N \chi_m(\vec{R}) \rangle + \\ & \sum_{m \neq n} \langle \psi_n(\vec{q}_i, R) | \hat{C} \psi_m(\vec{q}_i, R) \hat{C} \chi_m(\vec{R}) \rangle - \sum_{m \neq n} \langle \psi_n(\vec{q}_i, R) | \chi_m(\vec{R}) T_N \psi_m(\vec{q}_i, R) \rangle \end{aligned} \quad (45)$$

Knowing that the Kronecker delta act as $\delta_{mn} = 1$ or 0 if $m = n$ or $m \neq n$ respectively, equation (46) becomes:

$$\begin{aligned} [U_n + T_N - E] \chi_n(\vec{R}) &= \sum_{m \neq n} \langle \psi_n(\vec{q}_i, R) | H_e | \psi_m(\vec{q}_i, R) \chi_m(\vec{R}) \rangle \\ &- \sum_{m \neq n} \langle \psi_n(\vec{q}_i, R) | \hat{C} \psi_m(\vec{q}_i, R) \hat{C} \chi_m(\vec{R}) \rangle \\ &- \sum_{m \neq n} \langle \psi_n(\vec{q}_i, R) | T_N \psi_m(\vec{q}_i, R) \rangle \chi_m(\vec{R}) \end{aligned} \quad (46)$$

and by taking into account the \hat{B}_{nm} operator(14),

$$\hat{B}_{nm} = \langle \psi_n(\vec{q}_i, R) | T_N | \psi_m(\vec{q}_i, R) \rangle - \langle \psi_n(\vec{q}_i, R) | \hat{C} \psi_m(\vec{q}_i, R) \rangle \hat{C} \quad (47)$$

we can express this equation (46) as:

$$[U_n + T_N - E] \chi_n(\vec{R}) = \sum_{m \neq n} V_{nm} \chi_m(\vec{R}) - \sum_{m \neq n} \hat{B}_{nm} \chi_m(\vec{R}) \quad (48)$$

where

$$V_{nm} = \langle \psi_n(\vec{q}_i, R) | H_e | \psi_m(\vec{q}_i, R) \rangle \quad (49)$$

The choice (41) leads also to thinking about the appropriate choice of the electronic wave function basis. Three choices are shown and discussed in the following subsection.

2.4.1 Adiabatic representation

The adiabatic representation consist in choosing for $\psi_m(\vec{q}_i, R)$ in equation (41) the adiabatic wave function given by:

$$\Psi = \sum_m \psi_m^{(ad)}(\vec{q}_i, R) \chi_m(\vec{R}), \quad (50)$$

Where $\psi_m^{(ad)}(\vec{q}_i, R)$ are the solutions of the electronic eigenvalue problem:

$$H^{(e)} \psi_m^{(ad)}(\vec{q}_i, R) = U_m^{(ad)}(R) \psi_m^{(ad)}(\vec{q}_i, R) \quad (51)$$

and $U_m^{(ad)}(R)$ is the potential energy of the studied system in the adiabatic state m . The consequences of this assumption in equation (48) are :

$$[U_n^{(ad)} + T_N - E] \chi_n(\vec{R}) = - \sum_{m \neq n} \hat{B}_{nm} \chi_m(\vec{R}) \quad (52)$$

because of the vanishing of coupling terms in equation (49)

$$V_{nm} = \langle \psi_n(\vec{q}_i, R) | H_e | \psi_m(\vec{q}_i, R) \rangle = U_n^{(ad)} \langle \psi_n(\vec{q}_i, R) | \psi_m(\vec{q}_i, R) \rangle = 0 \quad (53)$$

Hence the Schrödinger equation to be solved in this case will be expressed as:

$$[U_n^{(ad)} + T_N - E] \chi_n(\vec{R}) + \sum_{m \neq n} \hat{B}_{nm} \chi_m(\vec{R}) = 0 \quad (54)$$

and in the resolution of this equation, we will face radial couplings of the form:

$$F_{nm}^{\vec{R}} = \langle \psi_n^{(ad)}(\vec{q}, R) | \vec{\nabla}_{\vec{R}} | \psi_m^{(ad)}(\vec{q}, R) \rangle \quad (55)$$

and

$$G_{nm}^{\vec{R}} = \langle \psi_n^{(ad)}(\vec{q}, R) | \Delta_{\vec{R}} | \psi_m^{(ad)}(\vec{q}, R) \rangle \quad (56)$$

According to Hellmann-Feynman theorem, we can write:

$$\begin{aligned} F_{mn}^{\vec{R}} &= \langle \psi_n^{(ad)}(\vec{q}, R) | \vec{\nabla}_{\vec{R}} | \psi_m^{(ad)}(\vec{q}, R) \rangle \\ &= \frac{\langle \psi_n^{(ad)}(\vec{q}, R) | \vec{\nabla}_{\vec{R}} H^{(e)} | \psi_m^{(ad)}(\vec{q}, R) \rangle}{U_n(R) - U_m(R)} \end{aligned} \quad (57)$$

Very often $F_{mn}^{\vec{R}}$ and $G_{mn}^{\vec{R}}$ are small, which allows us to make a perturbative resolution of the Schrodinger equation (54). However in the vicinity of the avoided crossings -see Figure (2.2)- where the $|U_m'(R_2) - U_n'(R_2)|$ difference is small, $F_{mn}^{\vec{R}}$ and $G_{mn}^{\vec{R}}$ diverge according to the Hellmann-Feynman relation (57) and a perturbative approach can not be used in this case. Indeed, in an adiabatic basis, two states of the same spatial and spin symmetry interact and cannot have the same value of potential energy [16]. These potential energy curves, instead of crossing each other, are avoided.

In the adiabatic approximation, the electronic movement is parametrical on the position of the nuclei of two PECs of adiabatic states of the same symmetry. The adiabatic PEC and wave function is calculated by solving the Schrodinger equation (1) in the Born-Oppenheimer approximation for each value of the inter-nuclear distance. The adiabatic approximation suggests to not take into account the non-adiabatic couplings terms ($F_{mn}^{\vec{R}}$ and $G_{mn}^{\vec{R}}$) on equations(55,56) for the remaining terms, due to the mass ratio of the nucleus and the electrons. However, in some important processes, this adiabatic treatment fails and the so-called non-adiabatic effect becomes very important. This is the case of reactive collisions where very highly excited (or double excited) states, close to the ground state of the ion, are involved. In the case of electron-molecular cation scattering, the energy increases along with a Rydberg series, the Rydberg electrons motion becomes progressively slower and closer to that of the vibrations and rotations of the nucleus. The energy exchange between the Rydberg electron and the nucleus becomes very efficient resulting in the fragmentation of the molecule or the ejection of the electron. The adiabatic representation is therefore no longer valid in this situation and another

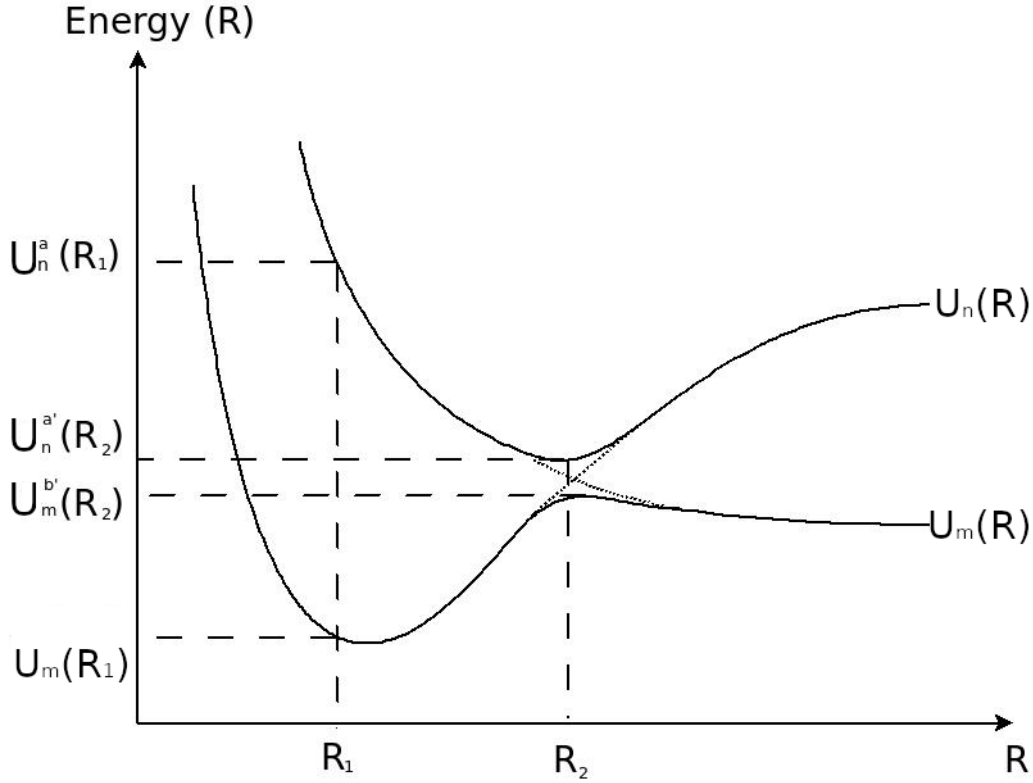


Figure 2.2: Avoided crossing

representation must be employed

2.4.2 Quasi-Diabatic representations

In order to describe well the molecular dynamic it's necessary to take into account non-adiabatic couplings. Using the quasi-diabatic representation can allow us to incorporate derivative couplings into the description of molecular states[17, 18, 19]. In this representation, the electronic Hamiltonian is partially diagonalized and the non-adiabatic couplings are few and small. Indeed this latter vanishes between two configurations when they differ by one orbital[14]. At each nuclear configuration, diagonalization of the molecular Hamiltonian is performed in an adiabatic basis by isolating the interacting electronic states. Far from the region of avoided crossing, quasi-diabatic states are the same as adiabatic states.

Chapter 3

Multi-channel Quantum Defect Theory (MQDT): Application on reactive collisions

After the collision of an electron with a molecular cation, a neutral intermediate state is formed and two general issues can be presented:

- The first one is the *autoionization* which consists to the re-emission of the incoming electron. the neutral molecule reemits the electron back to the ionization continuum and falls back into a vibrational state of the ion. The molecular cation target can keep its initial configuration with the possibility to be excited. This phenomenon takes place under energy and total orbital angular momentum conservation.
- The second one is the *predissociation* which occurs in the same timescale as the *autoionization* and it consists of the dissociation of the molecular cation. The electron capture can be done directly in a doubly excited state called *dissociative state* which brings the molecule to dissociate or in a *bound nonexcited Rydberg state* of the molecular cation. In this latter, the energy of the incident electron can be transferred into another electron or into the vibrational-rotational motion of the target and in this case, an internal energy conversion of the Rydberg electron may cause the electron to change from this bound state of the molecule to a dissociative state in the vicinity of the crossing between the corresponding potential energy curves

In the case of crossing between the dissociative state and the ion ground-state, autoionization is no longer possible since the dissociative state becomes energetically

stable towards autoionization[20]. The probability for electron capture into an autoionization is related to the autoionization width, which is inversely proportional to the lifetime of the dissociative state.

The $U(R)$ of a neutral molecule in a given molecular state can be related to the energy of the ion in its ground state $U^+(R)$ by the formula:

$$U(R) = U^+(R) - \frac{Ryd}{\nu^2} \quad (1)$$

where $Ryd = 13.605698$ eV is the Rydberg constant, and $\nu = n - \mu$ is the effective quantum number in relation with the principal quantum number and the quantum defect μ . At positive energies this latter multiplied by π is the *phase shift* of the scattered electron wave function relative to the hydrogen-like atom wave function at large distances. The quantum defect theory was developed initially to describe the electron-atomic-cation scattering by Seaton[21] and then extended to the molecular case[22, 23, 24, 25] in order to describe the electron scattering by molecular cations.

3.1 Subdivision of the configuration space

The *quantum defect theory* is based in the subdivision of the configuration space (q, R) into a finite inner region and an outer region based on the distinction between short and long-range interactions according to the electronic and inter-nuclear coordinates.

3.1.1 Inner region

The inner region or *reaction zone*[26, 27] is characterized by an incident electron that experiences strong short-range interactions with the target ion. It is delimited by a couple of (q_0, R_0) coordinates in Figure (3.1). The Born Oppenheimer approximation remains valid inside this region in which other methods than the quantum defect theory are used (either quantum chemistry [28] or the R-matrix method [3]. All the characteristics of this zone are stored in the large distance phase-shift of the wave function with respect to reference situation (either electron in the field of the ion, or two neutrals resulting from dissociation) and its derivative boundary continuity conditions, the net effect of this delimited zone being transmitted to the outer region.

3.1.2 Outer region

The external region is the remaining configuration space outside (q_0, R_0) coordinates. It is divided into a region where the Born-Oppenheimer approximation is considered since the incident electron is faster than the nuclear motion due to strong Coulomb attraction between the positively charged core and the scattered electron, and another region, beyond q_{BO} , called the asymptotic region, where the incident electron can not exchange with core for $R < R_0$) [29, 23]. In this latter region, the interactions between the incident electron and the ionic core are weak and dominated by long-range Coulomb interactions. The electron can not exchange with the core and the Born-Oppenheimer approximation is not valid. Then a *frame transformation* must be applied in order to use a close coupling basis to express the wave function with core effect saved in the form of a quantum defect and take into account closed or open channels.

3.2 The channel notion

In the quantum defect theory the description of an incoming electron colliding with an ion uses the partition of configuration space in an inner and outer region as is shown in section (3.1). During this collision, the scattered electron is captured into a bound state belonging to one of the molecular complex Rydberg series or into a dissociative state of the neutral molecule. This capture is the starting point of a lot of reactions ending-up either in the dissociation of the molecule or in the vibrational transitions of the ion with the re-emission of an electron. In both cases we can talk about *channels* which are sets or a families of states, having in common the same quantum numbers and the same fragmentation threshold but having different energies [28, 12]. An ionization channel is then described by the internal target ion state and the orbital quantum number of the incoming or captured electron. A channel can be open if the total energy of the molecular system is higher than the fragmentation threshold energy of the considered channel or closed in the opposite case. The distinction between open or closed channels is done on the asymptotic limit of the configuration-space.

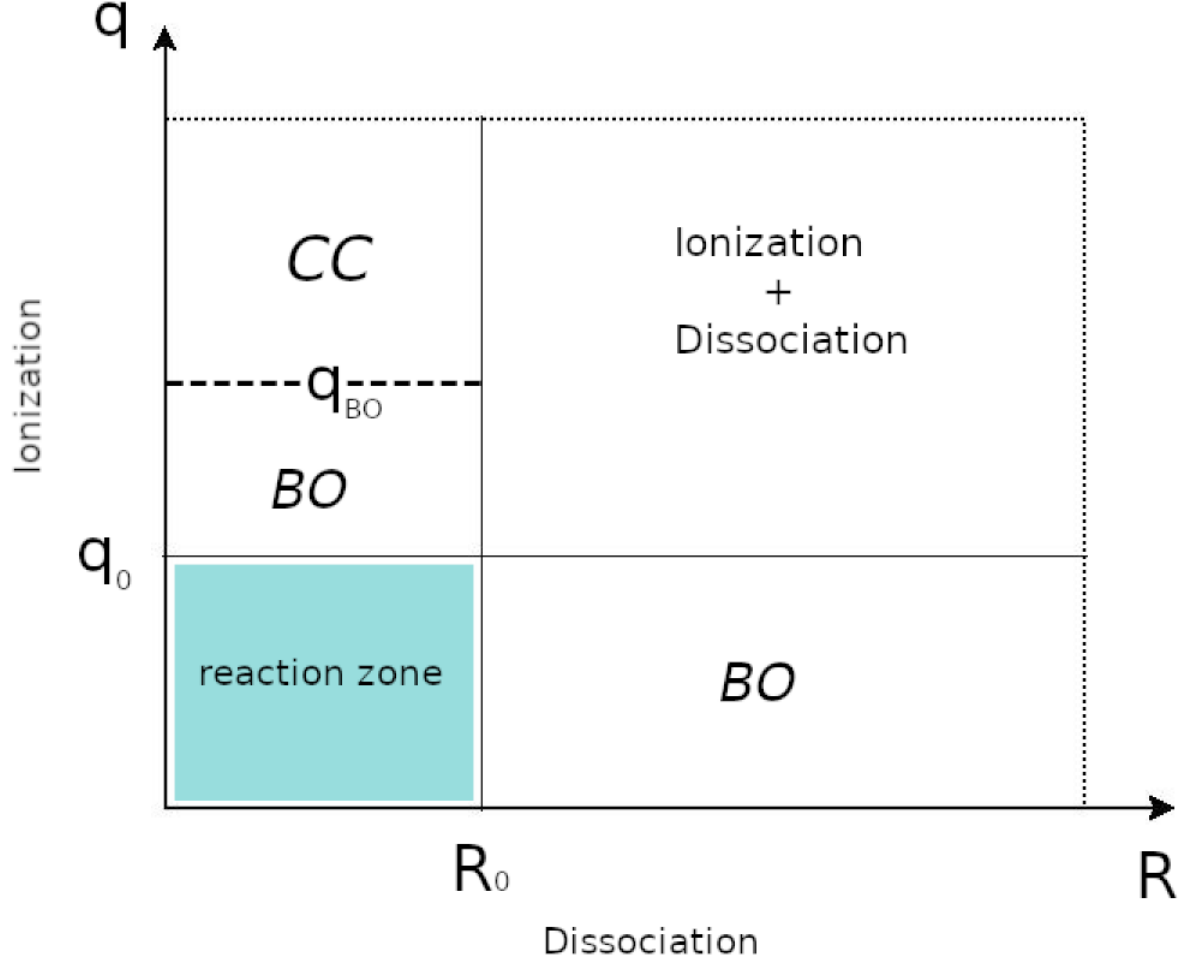


Figure 3.1: Distribution of configuration space in terms of inter-nuclear (x axis) and electronic (y -axis) coordinates which lead to dissociation and ionization respectively. BO here means regions where the Born-Oppenheimer approximation can be applied while CC is the region where a close coupling representation is appropriate

3.2.1 One-channel case

Let-us consider the radial Hamiltonian H_0 for one particle in 1D-space having a continuous spectrum and $V(r)$ an additional limited strong range potential:

$$V(r) = 0 \quad \text{where} \quad r > r_0; \quad (2)$$

$f_E(r)$ and $g_E(r)$ are two independent eigenfunctions of H_0 and having the same energy E where:

$$H_0 f_E(r) = E f_E(r) \quad \text{and} \quad \lim_{r \rightarrow 0} f_E(r) = 0 \quad (3)$$

and

$$H_0 g_E(r) = E g_E(r) \quad \text{and} \quad \lim_{r \rightarrow 0} g_E(r) = \infty \quad (4)$$

For a given energy E , the Shrödinger equation's solution for another particle where the Hamiltonian can be written as:

$$H(r) = H_0 + V(r) \quad (5)$$

is expressed as a linear combination of $f_E(r)$ and $g_E(r)$:

$$\varphi_E(r) \underset{r > r_0}{=} f_E(r) \cos(\eta(E)) - g_E(r) \sin(\eta(E)) \quad (6)$$

where $\varphi_E(r)$ is the total wave function and $\eta(E)$ is the phase-shift which reflects the $V(r)$ potential effect on the wave function. We can define a $\tan \eta(E)$ ratio between the wave function (6) coefficients which is an element of the reaction matrix \mathcal{K} for a given collision energy E :

$$\tan \eta(E) = -\pi K(E) \quad (7)$$

and allows the connection between the quantum defect theory and the configuration interaction[12, 28]. In the case of a given $E > E_{lim}$ energy, where E_{lim} is a limit energy between discrete and continuous spectrum and can be a fragmentation threshold energy for atomic system or dissociation limit for a molecular system, the f and g functions behave as:

$$f_E(r) \underset{r \rightarrow \infty (E > E_{lim})}{\approx} A(E) \sin(kr + \delta(E)) \quad (8)$$

and

$$g_E(r) \underset{r \rightarrow \infty (E > E_{lim})}{\approx} A(E) \sin(kr + \delta(E) - \frac{\pi}{2}) = -A(E) \cos(kr + \delta(E)) \quad (9)$$

Here k is the wavenumber corresponding to $E - E_{lim} = \frac{\hbar^2 k^2}{2\mu}$ and $A(E)$ a normalization coefficient chosen such a way that the f and g functions are energy independent at $r \rightarrow 0$. We can see that g function is phase lagged by $\frac{\pi}{2}$ with respect to f function. According to equation (6) the total wave function behavior

is then:

$$\begin{aligned}\varphi_E(r) &\underset{r \rightarrow \infty (E > E_{lim})}{\approx} A(E) \sin(kr + \delta(E)) \cos(\eta(E)) + A(E) \cos(kr + \delta(E)) \sin(\eta(E)) \\ &= A(E) [\sin(kr + \delta(E)) \cos(\eta(E)) + \cos(kr + \delta(E)) \sin(\eta(E))] \\ &= A(E) [\sin(kr + \delta(E)) + \eta(E)]\end{aligned}\quad (10)$$

In an interaction formalism configuration the wave function(10) can be written in the form[30]:

$$\varphi_E(r) = \int dE' a(E', E) f_{E'}(r) \quad (11)$$

where E is the total energy, E' a given energy of the system described by H_0 and the coefficient $a(E', E)$ can nevertheless be expressed by a mathematical Dirac notation [31]

$$a(E'', E) = \mathcal{P} \int \frac{1}{E - E'} K(E', E) + \delta(E - E') \quad (12)$$

here $\delta(E - E')$ is the Dirac delta function, and the symbol \mathcal{P} specifies the principal part integration which should be taken over the singularity of $\frac{1}{E - E'}$ on the summation.

We can then explicitate the wave function by putting the $a(E', E)$ expression into equation (12):

$$\begin{aligned}\varphi_E(r) &= \int dE' \left[\mathcal{P} \int \frac{1}{E - E'} K(E', E) + \delta(E - E') \right] f_{E'}(r) \\ &= \int dE' f_E'(r) \delta(E - E') + \mathcal{P} \int dE' \frac{1}{E - E'} K(E', E) f_{E'}(r) \\ &= f_E(r) + \mathcal{P} \int dE' \frac{1}{E - E'} K(E', E) f_{E'}(r)\end{aligned}\quad (13)$$

This formula for the wave function is the same as that established in references [28, 14]. For $r > r_0$ it was shown that the configuration interaction wave function (13) coincide with the quantum defect wave function (6), since Green *et al* [32] and Fano [30]demonstrated that, for a short-range interaction $V(r)$:

$$\mathcal{P} \int dE' \frac{1}{E - E'} K(E', E) f_{E'}(r) = \pi K(E) g_E(r) \quad (14)$$

providing that

$$K(E) = -\frac{1}{\pi} \tan(\eta(E)) = K(E, E) \quad (15)$$

consequently, we can write :

$$\varphi_E(r) = f_E(r) + \pi K(E)g_E(r) \quad (16)$$

3.2.2 Lippmann-Schwinger equation

The Lippmann-Schwinger equation is a fundamental step in the quantum defect theory. It allows to make the connection between short and long-range interactions. We show in this section the different step to establish it.

One starts by putting the wave function (13) on the Schrödinger equation:

$$(H_0 + V(r) - E) \left[f_E(r) + \mathcal{P} \int dE'' \frac{1}{E - E''} K(E'', E) f_{E''}(r) \right] = 0 \quad (17)$$

we can make the scalar product of $f_{E'}(r)$ on the left of this equation (17) and integrate on the radial coordinate:

$$\begin{aligned} & \langle f_{E'}(r) | (H_0 + V(r) - E) \left[f_E(r) + \mathcal{P} \int dE'' \frac{1}{E - E''} K(E'', E) f_{E''}(r) \right] \rangle = 0 \\ &= \langle f_{E'}(r) | H_0 | f_E(r) \rangle + \mathcal{P} \int dE'' \frac{1}{E - E''} K(E'', E) \langle f_{E'}(r) | H_0 | f_{E''}(r) \rangle \\ &+ \langle f_{E'}(r) | V(r) | f_E(r) \rangle + \mathcal{P} \int dE'' \frac{1}{E - E''} K(E'', E) \langle f_{E'}(r) | V(r) | f_{E''}(r) \rangle \\ &- \langle f_{E'}(r) | E | f_E(r) \rangle - E \mathcal{P} \int dE'' \frac{1}{E - E''} K(E'', E) \langle f_{E'}(r) | f_{E''}(r) \rangle = 0 \quad (18) \end{aligned}$$

We expand this equation and we get:

$$\begin{aligned} & E \delta(E' - E) + \mathcal{P} \int dE'' \frac{1}{E - E''} K(E'', E) E'' \delta(E' - E'') \\ &+ \langle f_{E'}(r) | V(r) | f_E(r) \rangle + \mathcal{P} \int dE'' \frac{\langle f_{E'}(r) | V(r) | f_{E''}(r) \rangle}{E - E''} K(E'', E) \\ &- E \delta(E' - E) - E \mathcal{P} \int dE'' \frac{1}{E - E''} K(E'', E) \delta(E' - E'') = 0 \quad (19) \end{aligned}$$

we can factorize this equation as:

$$\begin{aligned} & -\mathcal{P} \int dE'' \frac{1}{(E - E'')(E - E'')} K(E'', E) \delta(E' - E'') \\ &+ \langle f_{E'}(r) | V(r) | f_E(r) \rangle + \mathcal{P} \int dE'' \frac{\langle f_{E'}(r) | V(r) | f_{E''}(r) \rangle}{E - E''} K(E'', E) = 0 \quad (20) \end{aligned}$$

and consequently

$$\begin{aligned} \mathcal{P} \int dE'' K(E'', E) \delta(E' - E'') = & \langle f_{E'}(r) | V(r) | f_E(r) \rangle + \\ & \mathcal{P} \int dE'' \frac{\langle f_{E'}(r) | V(r) | f_{E''}(r) \rangle}{E - E''} K(E'', E) \end{aligned} \quad (21)$$

and we have the Lippmann-Schwinger equation:

$$K(E', E) = \langle f_{E'}(r) | V(r) | f_E(r) \rangle + \mathcal{P} \int dE'' \frac{\langle f_{E'}(r) | V(r) | f_{E''}(r) \rangle}{E - E''} K(E'', E) \quad (22)$$

3.3 Multi-channel case

For the multi-channel case, we need to search the wave functions by including all the different fragmentation channels. Let $Q = (r_p, \Omega_p; p = 1, \dots, N)$ be the set of N coordinates of the molecular system, where r_p is a radial coordinate and Ω_p the angular and spin coordinates for each particle. For a system experiencing fragmentation, and for each i channel, we limit ourselves to a fragmentation coordinate r_I . According to the eigenvalue equations (3) and (4), the non perturbed Hamiltonian H_0 solutions, in the multichannel case, can be written as:

$$H_0 f_{iE}(Q) = E f_{iE}(Q) \quad \text{and} \quad \lim_{r_I \rightarrow 0} f_{iE}(Q) = 0 \quad (23)$$

and

$$H_0 g_{iE}(Q) = E g_{iE}(Q) \quad \text{and} \quad \lim_{r_I \rightarrow 0} g_{iE}(Q) = \infty \quad (24)$$

where

$$f_{iE}(Q_I) \underset{r_I \rightarrow \infty (E > E_{th}^{(i)})}{\approx} A_{iE} \phi_{iE}(Q_I) \sin(k_I r_I + \delta_i(E)) \quad (25)$$

and

$$g_{iE}(Q_I) \underset{r_I \rightarrow \infty (E > E_{th}^{(i)})}{\approx} -A_{iE} \phi_{iE}(Q_I) \cos(k_I r_I + \delta_i(E)) \quad (26)$$

Here r_I are the fragmentation coordinates, k_I the momentum associated wavenumber to the fragmented system and $E_{th}^{(i)}$ the fragmentation threshold energy for the corresponding channel i . For a given channel, we will talk about an open channel when the energy is higher than the fragmentation threshold $E_{th}^{(i)}$ and a closed one in the opposite case.

The total wave function for a channel i is expressed as:

$$\Psi_{iE}(Q) = f_{iE}(Q) + \sum_j \mathcal{P} \int dE' \frac{1}{E-E'} K_{ji}(E', E) f_{iE'}(Q) \quad (27)$$

as it is established in the one channel case in equation (13). Here $K_{ji}(E', E)$ are the \mathcal{K} matrix elements which satisfy the integro-differential equation:

$$K_{ji}(E', E) = \langle f_{jE'} | V | f_{iE} \rangle + \sum_j \mathcal{P} \int dE'' \frac{\langle f_{jE'} | V(r) | f_{kE''}(r) \rangle}{E - E''} K_{ki}(E'', E) \quad (28)$$

The proof of this can be performed as we did in order to obtain for the one channel case in equation (22).

In the case of a limited potential:

$$V(Q)_{r_I > r_{I,0}} = 0 \quad \text{where} \quad r_I = 1, \dots, N_f; \quad (29)$$

and N_f the number of different coordinates involved in the fragmentation, as in the one channel case we can based ourselves to equation (14) to write:

$$\mathcal{P} \int dE' \frac{1}{E - E'} K_{ji}(E', E) f_{jE'}(Q) = \pi K_{ji}(E, E) g_{jE}(Q), \quad r_I > r_{I,0}; \quad (30)$$

consequently the multichannel wave function (27) can be written as :

$$\Psi_{iE}(Q) = f_{iE}(Q) + \pi \sum_j K_{ji}(E, E) g_{jE}(Q) \quad r_I > r_{I,0}; \quad (31)$$

The asymptotic behavior of the wave function allows us to know the net effect the inner region strong-interactions. So by using the relation (31), we express the total wave function as large distances as a linear combination of the regular function $f_{iE}(Q_I)$ (25) and irregular function $g_{iE}(Q_I)$ (26):

$$\Psi_{iE} \underset{r_I \rightarrow \infty (E > E_{th}^{(i)})}{=} A_{iE} \phi_{iE}(Q_I) \sin [k_i r_i + \delta_i(E)] - \pi \sum_j K_{ji}(E) A_{jE} \phi_{jE}(Q_I) \cos [k_j r_j + \delta_j(E)] \quad (32)$$

Within this asymptotic wave function relation (32), we can not highlight the short-range interaction in terms of a phaseshift as it was the case in the one channel

case. One performs a basic change in order to get a physically meaningful wave function behavior. Let us consider a basis wave function $\{\Psi_\alpha\}_{\alpha=1,\dots,N_f}$ describing the molecular system as:

$$\Psi_{\alpha_E} = \sum_i C_{i\alpha_E} \Psi_{i_E} \quad (33)$$

where $C_{i\alpha_E}$ coefficients have to be determined. By putting relation (32) on equation (33), we can express the wave function in the new basis as:

$$\begin{aligned} \Psi_{\alpha_E} = & \sum_i C_{i\alpha_E} A_{i_E} \Phi_{i_E}(Q_I) \sin[k_i r_i + \delta_i(E)] - \\ & \sum_i C_{i\alpha_E} \sum_j \pi K_{ji}(E) A_{j_E} \Phi_{j_E}(Q_I) \cos[k_j r_j + \delta_j(E)] \end{aligned} \quad (34)$$

In the other hand, we request that Ψ_{α_E} given by equation (33) behaves asymptotically as :

$$\Psi_{\alpha_E} = \sum_i \mathcal{U}_{i\alpha_E} A_{i_E} \Phi_{i_E}(Q_I) \sin[k_i r_i + \delta_i(E) + \eta_\alpha(E)] \quad (35)$$

We can expand the \sin in equation (35) in order to write it in the form of equation (32)

$$\Psi_{\alpha_E} = \sum_i \mathcal{U}_{i\alpha_E} A_{i_E} \Phi_{i_E}(Q_I) \left[\sin(k_i r_i + \delta_i(E)) \cos(\eta_\alpha(E)) + \cos(k_i r_i + \delta_i(E)) \sin(\eta_\alpha(E)) \right] \quad (36)$$

then

$$\begin{aligned} \Psi_{\alpha_E} = & \cos(\eta_\alpha(E)) \sum_i \mathcal{U}_{i\alpha_E} A_{i_E} \Phi_{i_E}(Q_I) \sin(k_i r_i + \delta_i(E)) + \\ & \sin(\eta_\alpha(E)) \sum_i \mathcal{U}_{i\alpha_E} A_{i_E} \Phi_{i_E}(Q_I) \cos(k_i r_i + \delta_i(E)) \end{aligned} \quad (37)$$

So the $C_{i\alpha_E}$ coefficients can be found by comparing equation (37) with equation (34) and by identifying the similar terms. Consequently:

$$\begin{cases} C_{i\alpha_E} = \mathcal{U}_{i\alpha_E} \cos(\eta_\alpha(E)) \\ \text{and} \\ -C_{i\alpha_E} \sum_j \pi K_{ji}(E) = \mathcal{U}_{j\alpha_E} \sin(\eta_\alpha(E)) \end{cases} \quad (38)$$

or

$$\begin{cases} C_{i\alpha_E} = \mathcal{U}_{i\alpha_E} \cos(\eta_\alpha(E)) \\ \text{and} \\ \mathcal{U}_{i\alpha_E} \sin(\eta_\alpha(E)) = - \sum_j \pi K_{ij}(E) C_{i\alpha_E} \end{cases} \quad (39)$$

We can put the $C_{i\alpha_E}$ coefficients on the second relation of (39) to get:

$$\mathcal{U}_{i\alpha_E} \sin(\eta_\alpha(E)) = -\cos(\eta_\alpha(E)) \sum_j \pi K_{ij}(E) \mathcal{U}_{i\alpha_E} \quad (40)$$

Hence

$$\sum_i K_{ij}(E) \mathcal{U}_{i\alpha_E} = -\frac{\tan(\eta_\alpha(E))}{\pi} \mathcal{U}_{j\alpha_E} \quad (41)$$

Here $\mathcal{U}_{i\alpha_E}$ can be expressed in terms of a column vector and K_{ij} as a matrix :

$$\hat{K} \vec{\mathcal{U}}_{\alpha_E} = -\frac{\tan(\eta_\alpha(E))}{\pi} \vec{\mathcal{U}}_{\alpha_E} \quad (42)$$

where

$$\vec{\mathcal{U}}_{j\alpha_E} = \begin{pmatrix} \mathcal{U}_{1\alpha_E} \\ \mathcal{U}_{2\alpha_E} \\ \vdots \\ \mathcal{U}_{N_{ch}\alpha_E} \end{pmatrix} \quad (43)$$

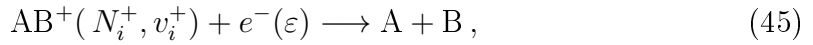
The equation (42) is an eigenvalue equation and $\mathcal{U}_{i\alpha_E}$ and $-\frac{\tan(\eta_\alpha(E))}{\pi}$ are respectively the components of the eigenvectors and the eigenvalues of the K matrix. As for $\eta_\alpha(E)$, it is the phaseshift due to the limited potential $V(Q)$ for an eigenchannel α . Let us take an example for a channel number $N_{ch} = 2$ in order to well understand the relation (42). A set of two independent solutions must be taken into account. They can be written in the form:

$$\begin{cases} \begin{pmatrix} K_{11} & K_{12} \\ K_{21} & K_{22} \end{pmatrix} \begin{pmatrix} U_{11} \\ U_{12} \end{pmatrix} = -\frac{\tan(\eta_1(E))}{\pi} \begin{pmatrix} U_{11} \\ U_{12} \end{pmatrix} \\ \begin{pmatrix} K_{11} & K_{12} \\ K_{21} & K_{22} \end{pmatrix} \begin{pmatrix} U_{21} \\ U_{22} \end{pmatrix} = -\frac{\tan(\eta_2(E))}{\pi} \begin{pmatrix} U_{21} \\ U_{22} \end{pmatrix} \end{cases} \quad (44)$$

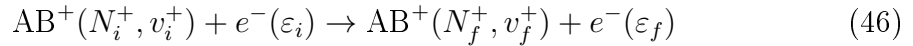
So the vector $\vec{\mathcal{U}} = (\vec{\mathcal{U}}_1, \vec{\mathcal{U}}_2)$ is build with two column vectors $\vec{\mathcal{U}}_1 = \begin{pmatrix} U_{11} \\ U_{12} \end{pmatrix}$ and $\vec{\mathcal{U}}_2 = \begin{pmatrix} U_{21} \\ U_{22} \end{pmatrix}$ is the eigenvector of the equation (42) in the case of $N_{ch} = 2$

3.4 Multi-channel Quantum Defect Theory (MQDT) approach of the reactive collisions

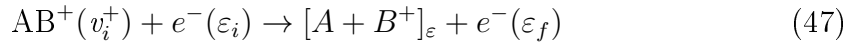
As we have shown in the introduction (1), reactive collisions between an electron and a molecular cation are of fundamental scientific interest, but also of interest for applications, notably by their importance in the kinetics of astrophysical media and technological and energetic processes. These are the reasons why their description is crucial in atomic and molecular physics. The Dissociative Recombination (DR) of a molecular cation colliding with an electron with a kinetic energy ε :



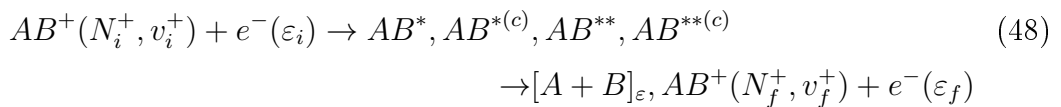
in competition with related processes such as elastic (EC), inelastic (IC) and super-elastic (SEC) collision where $\varepsilon_i = \varepsilon_f$, $\varepsilon_i < \varepsilon_f$ or $\varepsilon_i > \varepsilon_f$ respectively:



and dissociative excitation:



are the main reactions which occur during molecular electron-cation collision in cold energy media [33]. Here $N_i^+, N_f^+, v_i^+, v_f^+, \varepsilon_i$ and ε_f are respectively the initial and final rotational quantum number, the initial and final vibrational quantum number and the initial and final incident electron energy. The processes (45), (46) and also (47), one can lead to the formation of temporary excited states of the neutral system AB. We can therefore rewrite the reactions (45-47) by taken into account these states :



where $AB^{*(c)}$ belong to the monoelectronic ionization continuum but are bound states from the vibrational point of view, AB^{**} belong to the vibrational continuum but is bound from the electronic point of view, and AB^* are electronically and vibrationally bound states.

The "Rydberg resonances" AB^* in equation (48) play a fundamental role in all these processes [34, 35, 36, 37, 38, 28]. The occurrence of these different states lead to the consideration of two mechanisms of DR. The first one called the *direct mechanism* consists of the capture of the incident electron into a resonant state of type AB^{**} before dissociating as it is shown in Figure (3.2 - (A)) taken from [39]. In this mechanism, the incident electron is captured into a doubly excited state of the neutral molecule which evolves either towards dissociation into neutral or ionized fragments -i.e. DR (45) or DE (47) - or towards the reemission of the incident electron VE or VdE or EC (46)[40] -i.e. autoionization. The second mechanism is the *indirect* one Figure (3.2 - (B)) and it consists in the capture of the incident electron into a Rydberg state AB^* , subsequently predissociated by the resonant state. The two mechanisms "interfere" together to give the *total process*. It is important to take into account this unified treatment in order to have a good modeling of the process and a relevant comparison between theoretical and experimental results.

The processes in equation (48) are treated using a quasidiabatic representation [38, 28, 41] and they result from the coupling between ionization and dissociation channels.

We can now describe more precisely these channels, previously defined. A ionization channel, in the case of the reactive collisions (48) is a family of states built on a vibrational state v^+ of the ion corresponding to an electronic state (ground or excited) and is completed by all the possible monoelectronic states of a given orbital quantum number l , describing an "optical" electron. These monoelectronic states describe, with respect to the v^+ threshold, either a "free" electron—in which case the total state $AB^{*(c)}$ corresponds to (auto)ionization—or a bound electron—in which case the total state AB^* corresponds to a temporary capture into a Rydberg state. On the other hand, a dissociation channel consists in an electronically bound state of type AB^{**} whose potential energy in the asymptotic limit is situated below the total energy of the system. Accordingly, the ionization channels gather together AB^* and $AB^{*(c)}$ states, and the dissociation channels correspond to AB^{**} states. Given the total energy of the molecular system, a channel is open if this energy is higher than the energy of its fragmentation threshold and is closed in the opposite case.

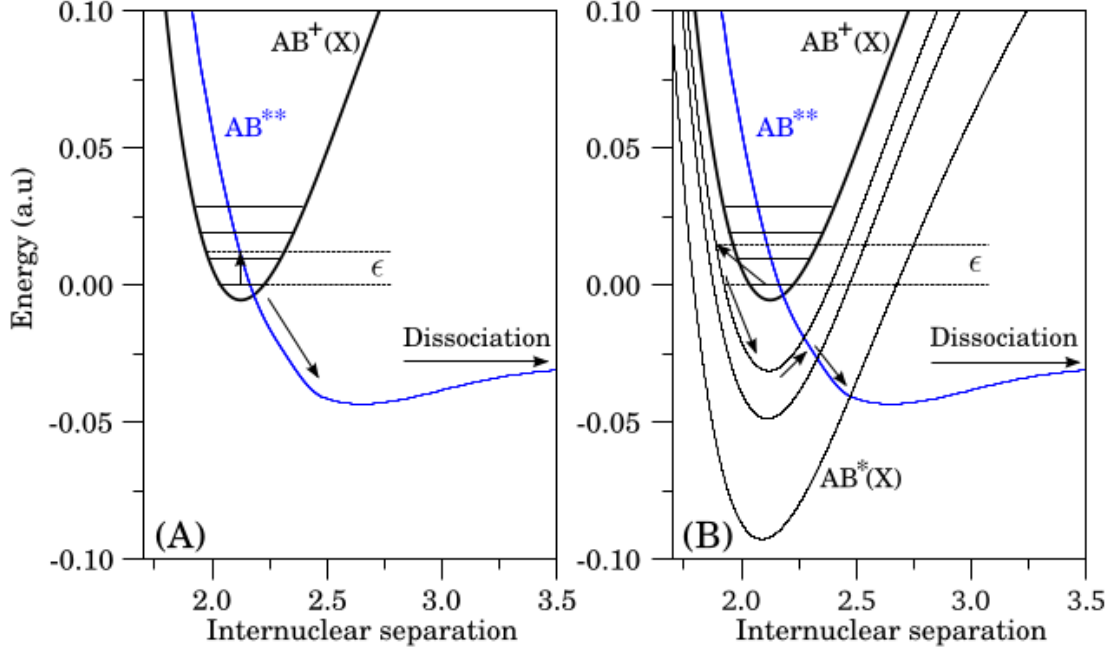


Figure 3.2: Dissociative recombination mechanisms: **(A)** Direct mechanism: A dissociative state of the neutral (blue line) crossing the ion potential energy curve (black line). The electron is captured into this state and then dissociation occurs. **(B)** Indirect mechanism: The electron is first captured on a vibrational level of the neutral state belonging to a Rydberg series which converges to the ground state of the ion, coupled to the resonant state leading to dissociation.

3.4.1 General ideas

3.4.2 Vibrational dynamics Neglecting Rotational effects(VNR)

In this subsection we will restrict ourselves to the cases where rotational excitation and couplings during the collision are neglected.

The MQDT approach starts with the building of the interaction matrix \mathbf{V} , performed in the so-called ‘A-region’ of the configuration space [23], where the Born-Oppenheimer approximation is appropriate for the description of the collision system. One has to perform separate calculations for each relevant ensemble ω of quantum numbers and symmetry parameters (QNSP), i.e.:

- i) the projection of the total angular momentum of electrons on the internuclear axis - quantum number Λ ,
- ii) the total electronic spin momentum - quantum number S ,
- iii) parity for the inversion of the nuclei with respect to the center of mass, g/u in

the case of homonuclear molecules,

and, in the case of Σ states,

iv) parity for the reflexion of the electrons with respect to any surface containing the internuclear axis, $+/-$.

3.4.2.1 Ionization channels built on the ground electronic state of the ion: the "single-core" case (VNR-SC)

We will start by considering that the target ion is initially in its ground electronic state AB (X), that it can not be electronically excited during the collision and, moreover, that all the ionization channels gather electronic states having as core the ground electronic state of the ion, i.e. states of the type $(\varepsilon l \lambda_{g/u})$, ε being positive for open channels and negative for the closed ones.

In the A-region, the states belonging to an ionization channel may be characterized with respect to hydrogenic states in terms of the quantum defect μ_l^ω , which is dependent on the internuclear distance R but, within our approach, is assumed to be independent of energy. An ionization channel associated to the vibrational state of quantum number v^+ is coupled to a dissociation one, labeled d_j , *electronically* first, through an R -dependent scaled 'Rydberg-valence' interaction term, $V_{d_j,l}^{(el)\omega}$, which is assumed to be, as the quantum defect μ_l^ω , independent of the energy of the electronic state:

$$V_{d_j,l}^{(el)\omega} = \langle \Phi_{d_j}^{(el)\omega} | H_e | \Phi_l^{(el)\omega} \rangle, \quad (49)$$

where H_e denotes the electronic Hamiltonian, $\Phi_{d_j}^{(el)\omega}$ is the electronic wave function of the dissociative state, and $\Phi_l^{(el)\omega}$ is the wave function describing the neutral molecular system "electron + ion".

This Rydberg-valence term corresponds to the coupling (49) described before in section (2.4). It is expressed as:

$$V_{d_j,l}^{(el)\omega}(R) = \sqrt{\frac{\Gamma(R)_{d_j,l}}{2\pi}}. \quad (50)$$

where $\Gamma(R)$ is the autoionization width of the dissociative state

Eventually, for a given value of the total energy E of the system, the convolution of the electronic coupling $V_{d_j,l}^{(el)\omega}$ with the local Franck-Condon factor provides the elements of the interaction matrix \mathcal{V} :

$$\mathcal{V}_{d_j,lv^+}^\omega(E) = \langle F_{d_j}^\omega(E) | V_{d_j,l}^{(el)\omega} | \chi_{v^+} \rangle, \quad (51)$$

where $F_{d_j}^\omega(E)$ and χ_{v^+} are the internuclear wave-functions corresponding to the

dissociative state d_j and to the ionization channel associated to v^+ , respectively. This procedure applies in each ω -subspace, and results in a block-diagonal global interaction matrix.

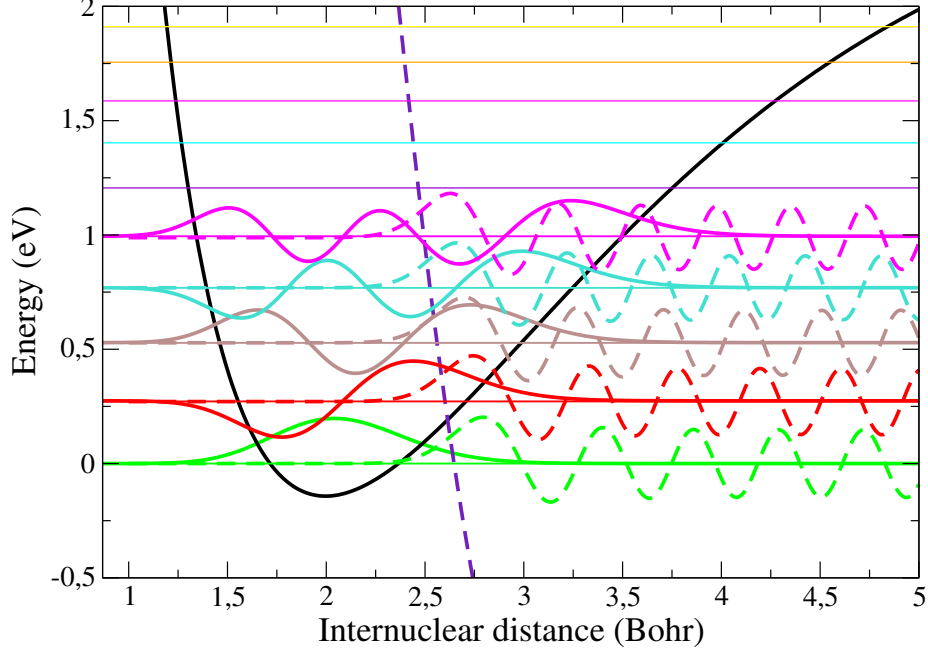


Figure 3.3: Overlap between the relevant wave functions in electron/molecular cation collision, for several cases of vibrationally excited target, collided by a very slow (energy almost zero) electron. The solid curves are the target bound vibrational wave functions and the dashed ones are the dissociative ones. The colored horizontal lines correspond to the vibrational levels of the ion. The target potential energy curves of the ion (black line) and of the dissociative state of the neutral (dashed violet) are given. This example is valid for the H_2^+/H_2^{**} system.

In the case of a weakly-variable Rydberg-valence interaction $V_{d_j,l}^{(el)\omega}$,

$$\mathcal{V}_{d_j,lv^+}^\omega(E) \approx V_{d_j,l}^{(el)\omega} \langle F_{d_j}^\omega(E) | \chi_{v^+} \rangle, \quad (52)$$

for a given total energy of the system and a given vibrational level, the overlap between the two wave functions $F_{d_j}^\omega(E)$ and χ_{v^+} depends on the inter-nuclear distance. The dissociative wave function has its main peak not far from the crossing point between the dissociative curve and the total energy level E , at the right of this point as we can see it on Figure (3.3). For the energy range explored in a collision study, by focusing on the two wave functions, it can be seen from the Figure (3.3) that, as the energy rises, there can be more or less overlaps. Since, as it will be shown below, the dissociative recombination cross section strongly depends on the R-INTEGRATED overlap, we can conclude that its variation with energy

can be predicted by examining diagrams like Figure (3.3). The internuclear wavefunctions χ_{v+} are calculated by the resolution of the nuclear Schrödinger equation corresponding to the electronic potential energie curves using the Numerov method. Starting from the interaction matrix \mathbf{V} and from the zero-order Hamiltonian \mathbf{H}_0 , we build the reaction \mathbf{K} -matrix with total energy E , which satisfies the Lippmann-Schwinger equation [42]:

$$\mathbf{K} = \mathbf{V} + \mathbf{V} \frac{1}{E - \mathbf{H}_0} \mathbf{K}. \quad (53)$$

In the following we will consider the second-order perturbation solution of Eq. (53) and then on its rhs the \mathbf{K} matrix will be replaced by the \mathbf{V} matrix. In order to express the result of the short-range interaction in terms of phase-shifts, we perform a unitary transformation of our initial basis into a new one, corresponding to eigenchannels, labeled by α , *via* the diagonalization of the reaction matrix \mathbf{K} :

$$\mathbf{K}\mathbf{U} = -\frac{1}{\pi} \tan(\eta) \mathbf{U}. \quad (54)$$

In the external ‘B-region’ [23], characterized by large electron-core distances, the Born-Oppenheimer model is no longer valid for the neutral molecule. Λ is no longer a good quantum number, and a frame transformation [22, 43, 44] is performed, *via* the projection coefficients:

$$\mathcal{C}_{lv^+, \omega\alpha} = \sum_v U_{lv, \alpha}^\omega \langle \chi_{v+} | \cos(\pi\mu_l^\omega + \eta_\alpha^\omega) | \chi_v^\omega \rangle, \quad (55)$$

$$\mathcal{C}_{d, \omega\alpha} = U_{d\alpha}^\omega \cos \eta_\alpha^\omega, \quad (56)$$

$$\mathcal{S}_{lv^+, \omega\alpha} = \sum_v U_{lv, \alpha}^\omega \langle \chi_{v+} | \sin(\pi\mu_l^\omega + \eta_\alpha^\omega) | \chi_v^\omega \rangle, \quad (57)$$

$$\mathcal{S}_{d, \omega\alpha} = U_{d\alpha}^\omega \sin \eta_\alpha^\omega, \quad (58)$$

In practice, in the Equations. (55)-(58), the approximation $\chi_v^\omega \approx \chi_{v+}$ is used, expressing the fact that the vibrational wavefunction of the neutral system in a Rydberg state is almost the same as that of the ion (more the electronic Rydberg state is excited, more this approximation is valid).

The matrices \mathbf{C} and \mathbf{S} , having as elements the coefficients given by (55-58), are eventually used in building the generalized scattering matrix \mathbf{X} , in which all the channels, open (‘o’) and closed (‘c’), are represented, and which can be organized

in 4 sub-matrices:

$$\mathbf{X} = \frac{\mathcal{C} + i\mathcal{S}}{\mathcal{C} - i\mathcal{S}}, \quad \mathbf{X} = \begin{pmatrix} X_{oo} & X_{oc} \\ X_{co} & X_{cc} \end{pmatrix}. \quad (59)$$

The *physical* scattering matrix \mathbf{S} [34] is obtained as a consequence of the boundary conditions:

$$\mathbf{S} = \mathbf{X}_{oo} - \mathbf{X}_{oc} \frac{1}{\mathbf{X}_{cc} - \exp(-i2\pi\boldsymbol{\nu})} \mathbf{X}_{co}, \quad (60)$$

Here the diagonal matrix $\boldsymbol{\nu}$ is formed with the effective quantum numbers (in atomic units),

$$\nu_{v+} = [2(E_{v+} - E)]^{-1/2}, \quad (61)$$

associated with each *closed* channel, i.e. to each vibrational threshold E_{v+} of the ion *larger than* the energy E .

The cross section of Dissociative Recombination (DR, Eq. 1) of an electron of energy ε with an ion initially on the level v^+ , into all the dissociative states d_j of a given ensemble ω of molecular electronic features, writes:

$$\sigma_{d \leftarrow v^+}^\omega(\varepsilon) = \frac{\pi}{4\varepsilon} \rho^\omega \sum_{l,j} |S_{d_j,lv^+}^\omega|^2, \quad (62)$$

whereas the cross section toward an ionization channel v'^+ , describing the VE process in (2), is written as:

$$\sigma_{v' \leftarrow v^+}^\omega(\varepsilon) = \frac{\pi}{4\varepsilon} \rho^\omega \sum_{l,l'} |S_{l',lv^+}^\omega - \delta_{l,l'} \delta_{v^+,v'^+}|^2. \quad (63)$$

The global cross sections are computed by making the sum on all the QNSP sets, ω :

$$\sigma_{d \leftarrow v^+}(\varepsilon) = \sum_{\omega} \sigma_{d \leftarrow v^+}^\omega(\varepsilon) \quad \sigma_{v' \leftarrow v^+}(\varepsilon) = \sum_{\omega} \sigma_{v' \leftarrow v^+}^\omega(\varepsilon) \quad (64)$$

When the indirect process is impossible or inefficient, the \mathbf{X} -matrix from Eq. (59) is reduced to its \mathbf{X}_{oo} component.

Furthermore, provided that:

- (i) one single dissociation channel ' d ' is open only,
- (ii) the first order term of the reaction matrix eq. (53) is the dominant one,
- (iii) the quantum defect is weakly R -dependent,

the DR cross section writes, omitting the collective index ω for sake of simplicity [28]:

$$\sigma_{d\leftarrow v^+} = \sigma_{d\leftarrow v^+}^{(cap)} \cdot f_{d\leftarrow v^+}^{(surv)}, \quad (65)$$

where

$$\sigma_{d\leftarrow v^+}^{(cap)} = \frac{\pi}{\varepsilon} \rho \tilde{\xi}_{v^+}^2, \quad (66)$$

and

$$f_{d\leftarrow v^+}^{(surv)} = \frac{1}{\left[1 + \sum_{v^+} \tilde{\xi}_{v^+}^2\right]^2}. \quad (67)$$

These quantities rely all on the strength of the Rydberg-valence interaction:

$$\tilde{\xi}_{v^+}^2 = \sum_l \xi_{lv^+}^2, \quad (68)$$

where

$$\xi_{lv^+} = \pi \cdot \mathcal{V}_{d,lv^+}. \quad (69)$$

Notice that even if we do not use approximations (ii) and (iii) invoked above, the direct cross section computed using the formulas (53-62) is very close to that given by the simple ones - Eqs. (65-69).

Some applications of this level of theory are presented in the result part of this thesis for electron scattering with ArH^+ molecular cation on chapter (4)

3.4.2.2 Ionization channels built on the ground and excited electronic states of the ion: the "double-core" case (VNR-DC)

The formalism described in the paragraph (3.4.2.1) is able to take into account the vibrational transitions of the target ion in its ground electronic state, as well as the temporary capture of the electron into singly-excited Rydberg states. This is appropriate at low energies of the incident electron, namely *below* the energy necessary to dissociate the ion in its ground electronic state. However, when this energy is exceeded, the theory has to be extended in order to take into account the first excited electronic state of the ion. A detailed description of the theoretical approach was given in [40]. Here the main steps are reproduced by considering two electronic-core state of the ion ($\beta = 1$ for the ground electronic state, *attractive*, and $\beta = 2$ for the lowest excited state, *repulsive*).

At energies higher than the dissociation threshold of the ion we have to take into account the autoionization resulting into states from the continuum part of the

vibrational spectrum, i.e. *dissociative excitation* (DE, equation (47)). These states, representing a free electron in the field of a dissociating ion, can be organized either into dissociation channels, or into ionization ones, but the latter option has been preferred so far. In order to be explicit on the developments implemented here, we will refer concretely to the case of H_2 and HD systems.

For the case of H_2 the two electronic states of the ionic cores are the ground state $^2\Sigma_g^+(1s\sigma_g)$ - referred to as core 1 - and the first excited state $^2\Sigma_u^+(2p\sigma_u)$ - referred to as core 2. The corresponding continua have been discretized by providing a wall of 15 eV height at $R = 25$ a.u. [37]. This corresponds, for every partial wave of the incident electron, to 334 and 291 further ionization channels for the ground cores of HD^+ and H_2^+ respectively - responsible for DE of core 1 - and to 383 and 375 ionization channels for the excited cores of HD^+ and H_2^+ respectively - responsible for DE of core 2. Since the temporary capture into bound Rydberg states AB^* is excluded above the dissociation limit of the ion, the collision process is exclusively driven by the direct mechanism.

When dissociative excitation is included in our approach, the coupling between a given dissociation channel d_j and an ionization one v , built on core 1 - eq. (51) - is extended to the continuum part of the vibrational spectrum (previously discretized as shown in the preceding subsection). On the other hand, every channel v is coupled to the further ionization channels built on the core 2, labelled generically by w . These couplings are quantified at electronic level by the R -dependent interaction term $\tilde{\mathcal{V}}^{(e)\omega}(R)$ - assumed to be energy independent - and they have the following form:

$$V_{wv}^\omega(E, E') = \langle \chi_w^\omega | \tilde{\mathcal{V}}^{(e)\omega}(R) | \chi_v^\omega \rangle. \quad (70)$$

Besides the elements given by eqs. (51) and (70), in which v and w span, for every ω symmetry, *all* the available vibrational levels (bound and discretized continuum), the remaining elements of the interaction matrix - $V_{d_i d_j}^\omega$, $V_{d_i w}^\omega$, $V_{vv'}^\omega$ and $V_{ww'}^\omega$ - vanish, since in the quasidiabatic representation chosen here, they concern pairs of channels associated to the the same ionic core [41]. As for the actual \mathcal{K} -matrix, it is in block form:

$$\mathcal{K} = \begin{pmatrix} \mathcal{K}_{\bar{d}\bar{d}} & \mathcal{K}_{\bar{d}\bar{v}} & \mathcal{K}_{\bar{d}\bar{w}} \\ \mathcal{K}_{\bar{v}\bar{d}} & \mathcal{K}_{\bar{v}\bar{v}} & \mathcal{K}_{\bar{v}\bar{w}} \\ \mathcal{K}_{\bar{w}\bar{d}} & \mathcal{K}_{\bar{w}\bar{v}} & \mathcal{K}_{\bar{w}\bar{w}} \end{pmatrix}. \quad (71)$$

where the collective indices \bar{d} , \bar{v} , \bar{w} in Eq. (71) span the ensembles of all the available individual ones d_j , v and w labeling dissociation channels, ionization channels built on core 1, and ionization channels built on core 2 respectively. Whereas the

matrix formed by the first two rows and columns stand for the DR at low energy, the third row and the third column completes the \mathcal{K} -matrix for the correct description of the DR at high energy, including the DE.

As in the case of DR at low energy, the Lippmann-Schwinger equation can be solved exactly in second order when the interactions $\mathcal{V}_{d_j}^{(e)\omega}$ and $\tilde{\mathcal{V}}^{(e)\omega}$ do not depend on the energy of the incident electron. Whereas the first order solution of equation (28) accounts for the electronic coupling between ionization and dissociation channels, the second order one goes further in accuracy, accounting for electronic coupling between ionization channels, an aspect which was not addressed in older previous studies [45, 46].

The non-vanishing elements, for all the allowed d_i, d_j, v, v', w, w' dissociation and ionization channels, are:

$$K_{vd_j}^\omega = K_{d_jv}^\omega = V_{vd_j}^\omega, \quad (72)$$

$$K_{vw}^\omega = K_{wv}^\omega = V_{vw}^\omega, \quad (73)$$

$$K_{vv'}^\omega = \frac{1}{W} \int \int \left[\chi_v^\omega(R) \mathcal{V}_{d_j}^{(e)\omega}(R) F_d^\Lambda(R_<) G_d^\Lambda(R_>) \mathcal{V}_{d_j}^{(e)\Lambda}(R') \chi_{v'}^\Lambda(R') \right] dR dR'. \quad (74)$$

In eq. (74) W denotes the wronskian of the regular (F_d) and the irregular (G_d) solution of the dissociative state nuclear Schrödinger equation. Due to the previously explained reasons all the other elements will vanish, namely:

$$K_{d_id_j} = 0, \quad K_{d_iw} = K_{wd_j} = 0, \quad K_{ww'} = 0. \quad (75)$$

Taking all of these into account, the second order \mathcal{K} -matrix has the form,

$$\mathcal{K} = \begin{pmatrix} \mathbf{O} & \mathbf{V}_{\bar{d}\bar{v}} & \mathbf{O} \\ \mathbf{V}_{\bar{v}\bar{d}} & \mathcal{K}_{\bar{v}\bar{v}} & \mathbf{V}_{\bar{v}\bar{w}} \\ \mathbf{O} & \mathbf{V}_{\bar{w}\bar{v}} & \mathbf{O} \end{pmatrix} \quad (76)$$

where the elements of each block are given by Eqs. (72), (70) and (74), and \mathbf{O} is the null matrix.

The inclusion of dissociative excitation due to the presence of the discretized continuum levels of the two cores increases not only the dimension of the interaction matrix \mathbf{V} (eq. 70) and the reaction K-matrix (71), but also that of the frame

transformation \mathcal{C} and \mathcal{S} matrices. Consequently, the sum in the right-hand side of eq. (58) is extended to the quasi-continuum levels, and further matrix elements, corresponding to the quasi-continuum levels of the second core, (w), will occur.

The \mathbf{X} -matrix and finally the \mathbf{S} -matrix are eventually built according to Eqs. (59) and (60) respectively. The DE1 and DE2 processes are actually treated as vibrational excitations from an initial vibrational state v_i^+ , to the (discretized) ionization continua of the two cores. The cross sections for these processes are given by:

$$\sigma_{DE1, v_i^+}^{sym, \Lambda} = \frac{\pi}{4\varepsilon} \rho^{sym, \Lambda} \sum_{v_h^+ < v^+ < v_{max}^+(\varepsilon)} |S_{v^+, v_i^+}|^2, \quad (77)$$

and

$$\sigma_{DE2, v_i^+}^{sym, \Lambda} = \frac{\pi}{4\varepsilon} \rho^{sym, \Lambda} \sum_{w^+ < w_{max}^+(\varepsilon)} |S_{w^+, v_i^+}|^2. \quad (78)$$

The total DE cross section has the form:

$$\sigma_{DE, v_i^+} = \sum_{sym, \Lambda} \sigma_{DE, v_i^+}^{sym, \Lambda}, \quad (79)$$

where

$$\sigma_{DE, v_i^+}^{sym, \Lambda} = \sigma_{DE1, v_i^+}^{sym, \Lambda} + \sigma_{DE2, v_i^+}^{sym, \Lambda}. \quad (80)$$

v_h^+ is the highest *bound* vibrational level built on core 1, while $v_{max}^+(\varepsilon)$ and $w_{max}^+(\varepsilon)$ are the highest quasi-continuum vibrational levels situated below the current total energy $E = E_{v_i^+} + \varepsilon$, corresponding to core 1 and core 2 respectively. The cross-sections and rate coefficients calculated using this part of the theory are shown in chapter (5) for the HD^+ electron scattering.

3.4.2.3 Ionization channels built on the ground and excited electronic states of the ion: "triple-core" case (VNR-TC)

A straightforward level of the formalism is the inclusion of another core excited state which includes more couplings of type Rydberg-valence as on equations (49) and (51) for core 2 and 3 :

$$V_{d_j, l_{c2}}^{(el)\omega} = \langle F_{d_j}^\omega(E) | \mathcal{V}_{d_j, l_{v_{c2}^+}}^\omega(E) | \chi_{w^+} \rangle, \quad (81)$$

$$V_{d_j, l_{c3}}^{(el)\omega} = \langle F_{d_j}^\omega(E) | \mathcal{V}_{d_j, l_{v_{c3}^+}}^\omega(E) | \chi_{u^+} \rangle, \quad (82)$$

and some additional Rydberg-Rydberg couplings [47] as on equation (70)

$$V_{vu}^\omega(E, E') = \langle \chi_v^\omega | \tilde{\mathcal{V}}_{c_1, c_3}^{(e)\omega}(R) | \chi_u^\omega \rangle. \quad (83)$$

$$V_{wu}^\omega(E, E') = \langle \chi_w^\omega | \tilde{\mathcal{V}}_{c_2, c_3}^{(e)\omega}(R) | \chi_u^\omega \rangle. \quad (84)$$

Here the vibrational quantum numbers v , w and u are labeled respectively for ionization channels of core 1, 2 and 3.

The consequences of these couplings are the increasing of the dimension of the \mathcal{K} -matrix which is structured in the form :

$$\mathcal{K} = \begin{pmatrix} \mathcal{K}_{\bar{d}\bar{d}} & \mathcal{K}_{\bar{d}\bar{v}} & \mathcal{K}_{\bar{d}\bar{w}} & \mathcal{K}_{\bar{d}\bar{u}} \\ \mathcal{K}_{\bar{v}\bar{d}} & \mathcal{K}_{\bar{v}\bar{v}} & \mathcal{K}_{\bar{v}\bar{w}} & \mathcal{K}_{\bar{v}\bar{u}} \\ \mathcal{K}_{\bar{w}\bar{d}} & \mathcal{K}_{\bar{w}\bar{v}} & \mathcal{K}_{\bar{w}\bar{w}} & \mathcal{K}_{\bar{w}\bar{u}} \\ \mathcal{K}_{\bar{u}\bar{d}} & \mathcal{K}_{\bar{u}\bar{v}} & \mathcal{K}_{\bar{u}\bar{w}} & \mathcal{K}_{\bar{u}\bar{u}} \end{pmatrix}. \quad (85)$$

where \bar{d} , \bar{v} , \bar{w} and \bar{u} are collective indices for indices d , v , w and u wich label respectively for dissociation channel and ionization channels appended on core 1, core 2, and core 3. The \mathcal{C} (55) and \mathcal{S} -matrix (57) increases also respectively with core 2:

$$\mathcal{C}_{w^+, \omega\alpha} = \sum_w U_{lw, \alpha}^\omega \langle \chi_{w^+} | \cos(\pi\mu_{c_2}^\omega + \eta_\alpha^\omega) | \chi_w^\omega \rangle, \quad (86)$$

$$\mathcal{S}_{lw^+, \omega\alpha} = \sum_w U_{lw, \alpha}^\omega \langle \chi_{w^+} | \sin(\pi\mu_{c_2}^\omega + \eta_\alpha^\omega) | \chi_w^\omega \rangle, \quad (87)$$

and with core 3:

$$\mathcal{C}_{u^+, \omega\alpha} = \sum_u U_{lu, \alpha}^\omega \langle \chi_{u^+} | \cos(\pi\mu_{c_3}^\omega + \eta_\alpha^\omega) | \chi_u^\omega \rangle, \quad (88)$$

$$\mathcal{S}_{lu^+, \omega\alpha} = \sum_u U_{lu, \alpha}^\omega \langle \chi_{u^+} | \sin(\pi\mu_{c_3}^\omega + \eta_\alpha^\omega) | \chi_u^\omega \rangle, \quad (89)$$

Using the *physical* \mathcal{S} matrix (60), we can obtain the DR cross section as in equations (62) and (64) the VE cross section :

The DR and VE cross section and rate coefficients using this level of theory are calculated for the molecular cation N_2^+ which has three bound electronic cores and the results are presented in section (6).

Electron scattering on ArH^+

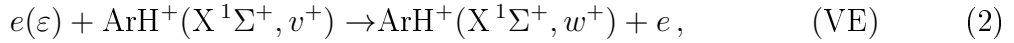
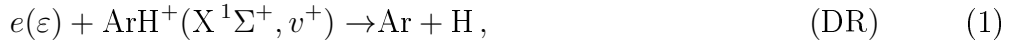
4.1 Introduction

The argonium (ArH^+) is ubiquitous in the interstellar medium (ISM), namely the crab Nebulae where Barlow *et al.* [48] reported detection of $^{36}\text{ArH}^+$ 617.525 GHz ($J = 1 - 0$) and 1234.603 GHz ($J = 2 - 1$) emission lines in spectra from the Crab Nebula using the data from Herschel mission. That supernova remnant is known to contain both molecular hydrogen and regions of enhanced ionized argon emission. After this first noble gas molecular ion detection, Schilke *et al.* [49] realized that the still unidentified absorption transition at 617.5 GHz observed in diffuse gas toward several sources such as Sg B2, and various PRISMA sources (W31C, W49N, W51e, ...), was in fact due to argonium with ^{36}Ar . Moreover, features of $^{38}\text{ArH}^+$ were subsequently found in Sg B2(M) as well and, consequently, Schilke *et al.* suggested that argonium is ubiquitous in the ISM. More recently, Müller *et al.* [50] made extragalactic detections of the ^{36}Ar and ^{38}Ar isotopologues of argonium through absorption studies of a foreground galaxy at $z = 0.89$ along two different lines of sight toward PKS 1830-211 within the band 7 of the ALMA interferometer, including the corresponding redshifted transitions.

The possible formation and destruction processes of ArH^+ are discussed by Neufeld and Wolfire [51]. An important information needed is the unknown value of this dissociative recombination rate coefficient of that molecular ion. An upper limit of $10^{-9} \text{ cm}^3 \text{ s}^{-1}$ for electron collision energies below about 2 eV was reported by Mitchell *et al.* [52] who performed a storage ring measurement. She also gave the corresponding theoretical potential curves. That upper limit value is adopted in the presently available astrochemical models for galactic diffuse clouds [51] whereas Priestley *et al.* [53] introduce a lower value ($10^{-11} \text{ cm}^3 \text{ s}^{-1}$) to inter-

pret the Crab nebula observations. Photodissociation of ArH^+ , another potential destruction mechanism, was studied theoretically by Alekseyev *et al.* [54] and the corresponding photodissociation rate was shown to be moderate, *i.e.* $9.9 \cdot 10^{-12} \text{ s}^{-1}$ in the unshielded mean ultraviolet interstellar radiation field [55, 49]. In addition to this, the rotational excitation due to electron impact has been studied in ref. [56].

In this chapter, we investigate theoretically the dissociative recombination (DR) of ArH^+ through *ab initio* methods, including the dependence on the vibrational excitation of the target molecular ion and, in the same energy range, the competitive process of vibrational excitation (VE) by electron impact, *i.e.*:



where ε is the incident electron energy, v^+ and w^+ represent the initial and final vibrational quantum numbers respectively corresponding to the ground electronic state $\text{X } ^1\Sigma^+$ of ArH^+ . The results presented in this chapter has been published in *Monthly Notices of the Royal Astronomical Society* [57]

4.2 Molecular data

A theoretical study of the ArH^+ electronic excited states was performed by Stolyarov *et al.* [58]; [59] and, more recently, in [60] the ArH Rydberg states have been explored. In the present work we have used, *ab initio* ArH^+ calculations performed using MOLPRO and an aug-cc-pVQZ (AVQZ) Gaussian type orbital (GTO) basis set at the complete active space (CAS) self-consistent field (SCF) level of theory. These calculations provided input orbitals for the electron-ion scattering calculations. All calculations were performed in C_{2v} symmetry, which is the highest allowed by MOLPRO and the polyatomic R-matrix code for an asymmetric linear molecule.

We have also used the potential energy curves and the autoionization widths of the ArH^{**} resonant states calculated using the R-matrix method [3] as implemented in UKRMol code [61]. Our general approach follows closely the treatment of N_2^{**} by [62] which provided the input for N_2^+ DR calculations [63]. The ArH^+ target states were represented using the AVQZ GTO basis set and a CAS in which the $\text{Ar } 1s^2 2s^2 2p^6$ electrons were frozen and the remaining 8 electrons were distributed as $(4\sigma, 5\sigma, 6\sigma, 2\pi)^8$. The 3π virtual orbital was retained to augment the continuum

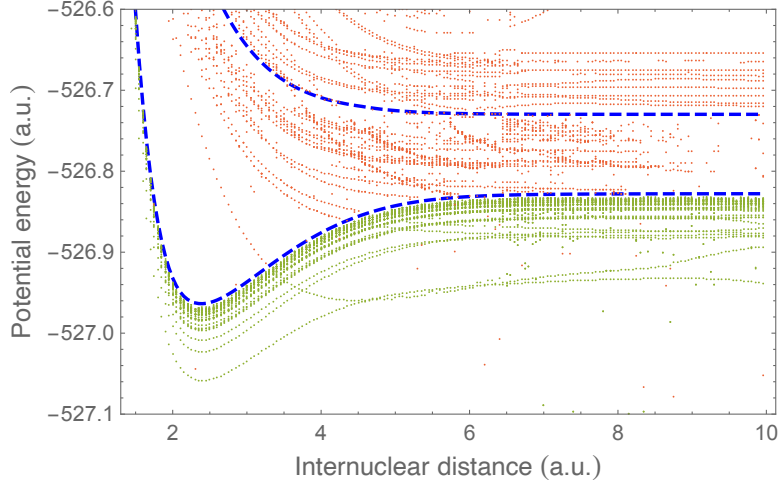


Figure 4.1: R-matrix results for the resonant states of $^2\Pi$ symmetry. The dashed lines are the potential energy curves of the target ground electronic and excited states (blue curves) of ArH^+ . The dotted green curves are those of the Rydberg states converging to the ground electronic state and the red curves converging to the excited electronic states.

orbitals in the scattering calculation.

The scattering calculations used an R-matrix sphere of radius $10 a_0$. Continuum basis functions were represented using GTOs placed at the center of this sphere and contained up to g orbitals ($\ell \leq 4$) [64]. Close-coupling calculations built on the target CAS [65] and an expansion of the 8 lowest states of each (C_{2v}) symmetry were retained for the outer region calculations. In this latter region, calculations were repeated for the internuclear separations $2.2 < R < 15 a_0$ and for symmetries corresponding to $^2\Sigma^+$, $^2\Pi$ and $^2\Delta$ scattering channels.

The outer region calculations explicitly considered the 20 lowest target states. R-matrices were propagated to $100.1 a_0$ and then fitted to an asymptotic form. Resonance positions and widths were determined by automated fitting of the eigenphase sums to a Breit-Wigner form using program RESON [66]. Couplings were determined from the resonance widths Γ using the formula:

$$V(R) = \sqrt{\frac{\Gamma(R)}{2\pi}}. \quad (3)$$

Figure (4.1) is the R-matrix adiabatic potential energy curves for the resonant state of $^2\Pi$. They are used to provide the relevant smoothed quasi-diabatic states shown in Figure (4.2), employed to the study of the DR and VE in this chapter. Couplings and quantum defect are respectively displayed in Figures (4.3) and (4.4).

The molecular data characterizing the ArH^+ ion in its ground state are given in Table 4.1. All these data form the input for the Multichannel Quantum Defect Theory (MQDT) step of the calculations. Linear extrapolation was adopted for the couplings in order to extend the internuclear distances range below $2.2 a_0$ down to $1.6 a_0$.

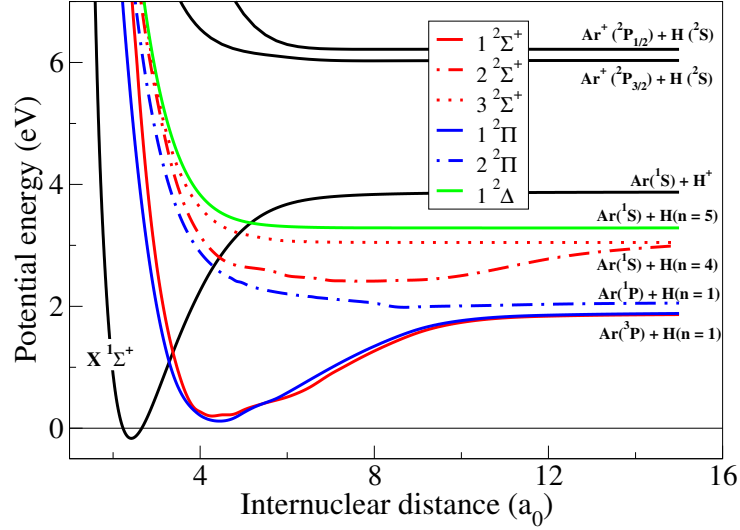


Figure 4.2: Potential energy curves used in the present calculations. The ArH^+ potential curves - ground state, $X^1\Sigma^+$, and the lowest excited electronic states - are displayed as black lines. The molecular data sets for the different symmetries of the neutral system are displayed with different colors: $^2\Sigma$ in red, $^2\Pi$ in blue and $^2\Delta$ in green.

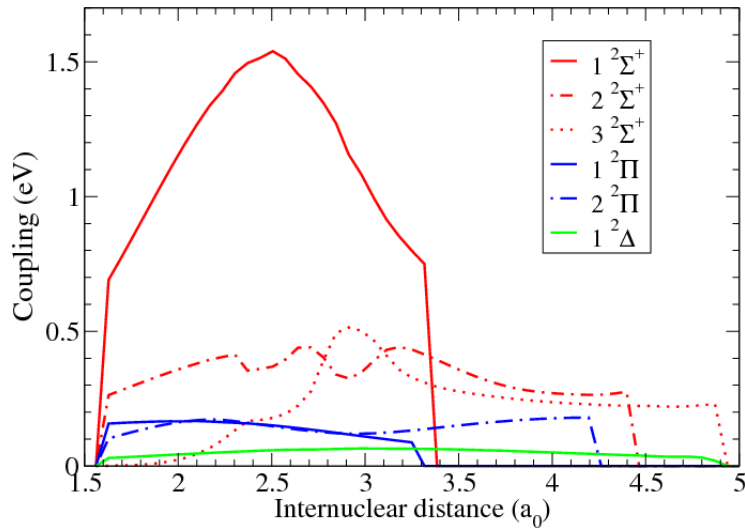


Figure 4.3: Electronic couplings used in the present calculations. The molecular data sets for the different symmetries of the neutral system are displayed with different colors: $^2\Sigma$ in red, $^2\Pi$ in blue and $^2\Delta$ in green.

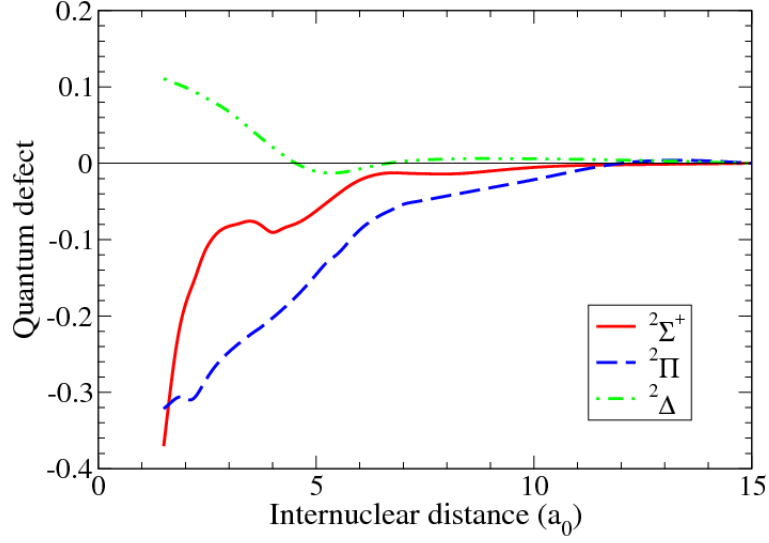


Figure 4.4: Quantum defects used in the present calculations. The molecular data sets for the different symmetries of the neutral system are displayed with different colors: $^2\Sigma$ in red, $^2\Pi$ in blue and $^2\Delta$ in green.

μ (a.u.)		1791.94	
R_{eq} (a_0)		2.419 (2.419)	
D_e (eV)		4.039 (4.025)	
D_0 (eV)		3.8725	
v^+	ϵ_{v^+} (eV)	v^+	ϵ_{v^+} (eV)
0	0.000	12	2.949
1	0.321	13	3.110
2	0.627	14	3.258
3	0.919	15	3.393
4	1.197	16	3.513
5	1.461	17	3.617
6	1.712	18	3.703
7	1.949	19	3.770
8	2.174	20	3.817
9	2.387	21	3.846
10	2.587	22	3.861
11	2.774		

Table 4.1: Molecular constants (reduced mass, equilibrium distance and dissociating energies) for $^{36}\text{ArH}^+$ in its ground electronic state and the energies of the corresponding vibrational levels. The comparison with the experimental data of [67] given in brackets is reported.

ArH^+ is a closed shell system so no spin-orbit (SO) splitting effects are expected in its ro-vibrational levels. Conversely, SO effects may be important in the non- Σ resonances. [68]. However our calculations are non-relativistic and therefore neglect SO effects; we assume the calculated R-matrix resonances converge on the lowest component of the Ar doublets at large internuclear distances. Table 4.2 shows the asymptotic limits of the ArH^{**} resonant states considered below.

Channel	Energy (eV)	Symmetries
$\text{Ar}(^3\text{P}) + \text{H}(n = 1)$	-2.00 (-2.05)	$1^2\Sigma^+, 1^2\Pi$
$\text{Ar}(^1\text{P}) + \text{H}(n = 1)$	-1.81 (-1.87)	$2^2\Pi$
$\text{Ar}(^1\text{S}) + \text{H}(n = 4)$	-0.87 (-0.85)	$2^2\Sigma^+, 3^2\Sigma^+$
$\text{Ar}(^1\text{S}) + \text{H}(n = 5)$	-0.58 (-0.54)	$1^2\Delta$

Table 4.2: Asymptotic limits of the ArH^{**} resonant states relevant for the low-energy impact collisions. The energy is expressed with respect to the asymptotic limit of the ground electronic state of ArH^+ . The experimental energy values from the NIST database [68] are given in brackets for comparison.

The most abundant isotope of argon in the Earth's atmosphere is ^{40}Ar whereas in the ISM ^{36}Ar and ^{38}Ar isotopes are preponderant. In the present work, we deal with vibrational processes and, due to the small relative variation of the reduced mass from one isotopologue to an other - as a consequence of the huge atomic mass of the Ar isotopes - we expect these effects to be negligible. In order to verify this, we performed calculations for different isotopologues of ArH^+ and the relative difference between the rate coefficients was found to be below 1 %.

4.3 Results and discussion

Figure (4.5) displays the DR cross sections for $\text{ArH}^+ v^+ = 0$, namely the total one and the partial contributions corresponding to the asymptotic channels of resonant states. It can be noted that the main contribution arises from the $\text{Ar}(^3\text{P}) + \text{H}(n = 1)$ channel. One reason for this is that, as shown in Table 4.2, this exit channel gathers contributions coming from two states - $1^2\Sigma^+$ and $1^2\Pi$ - instead of one state, as is the case of the exit channels $\text{Ar}(^1\text{P}) + \text{H}(n = 1)$ and $\text{Ar}(^1\text{S}) + \text{H}(n = 5)$. One can argue that - as shown in Table 4.2 - the channel $\text{Ar}(^1\text{S}) + \text{H}(n = 4)$ is the asymptotic limit of two states, as the $\text{Ar}(^3\text{P}) + \text{H}(n = 1)$ one. However, the coupling of the $1^2\Sigma^+$ state with the electron/ion continuum (see Figure 4.2) is about three times larger than the other ones.

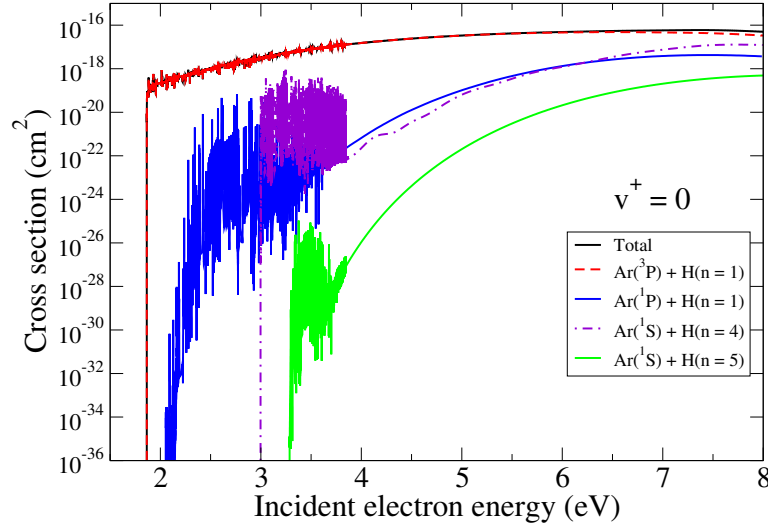


Figure 4.5: Dissociative recombination of vibrationally relaxed ArH^+ . Broken colored lines: The contributions coming from all the dissociative states having the same asymptotic atomic limit. Solid black line (partially hidden by the red curve): Total cross section coming from the sum over all the available dissociative states.

Figures 4.6(a) and (b) display, respectively, the results for DR cross sections and the corresponding rate coefficients for $v^+ = 0, 1, 2$. Two features can be noted:

(i) The resonant structures present in the cross sections correspond to the temporary captures into singly-excited Rydberg states ArH^* , and they cease to appear when the electron energy reaches the dissociation energy of $\text{ArH}^+(v^+ = 0, 1, 2)$;

(ii) For a vibrationally relaxed target, the dissociation channels are closed for energies of the incident electron below 1.8 eV. For the ion situated on one of the next 8 excited vibrational states, the threshold decreases progressively, and the DR becomes exothermic for vibrational levels equal or higher to 9 only. This particular energetic situation explains the particular behavior of the computed rate coefficients displayed in Figure 4.6(b), namely the very low values and the "explosive" increase below 2000 K.

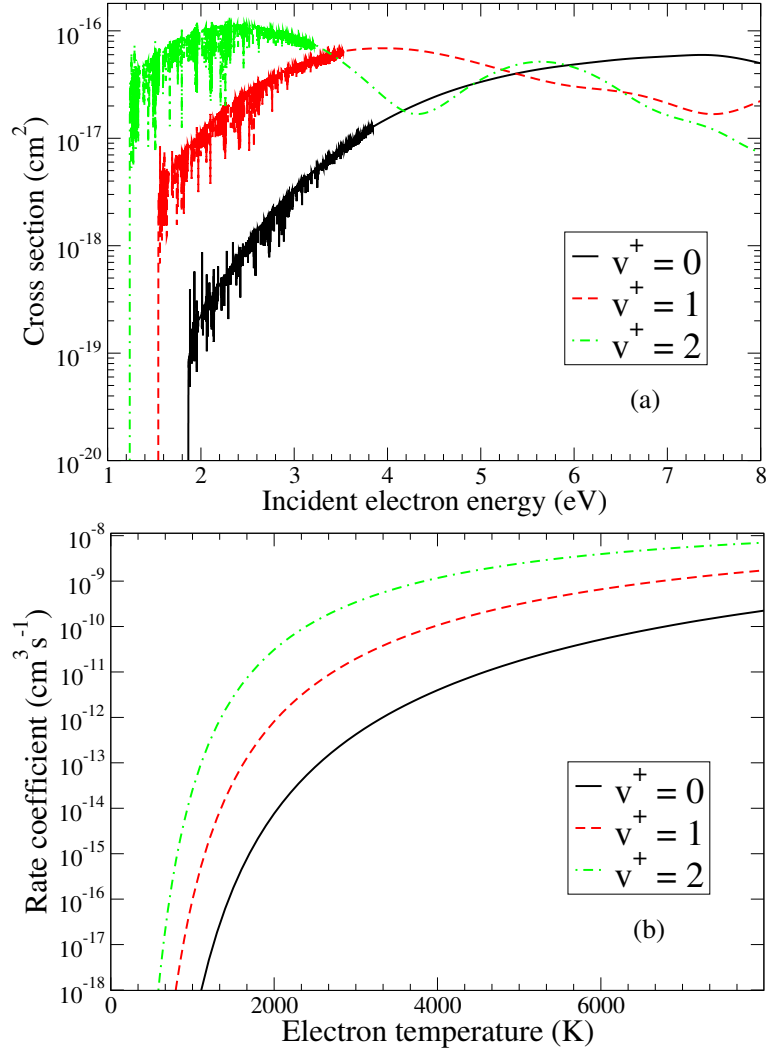


Figure 4.6: Dissociative recombination of ArH^+ on its lowest vibrational levels: (a) global cross sections, coming from the sum over all the available dissociative states; (b) the corresponding Maxwellian-averaged rate coefficients.

In order to validate the results, Figure (4.7) shows the anisotropic DR rate coefficient for $v^+ = 0$, calculated by considering the electron beam with a longitudinal temperature $kT_{\parallel} \approx 0.5 \text{ eV}$ and a transverse temperature $kT_{\perp} \approx 25 \text{ meV}$, compared to the experimental data from the storage ring by [52]. We note that the agreement is quite satisfactory at energies greater than $\sim 3 \text{ eV}$ within the 20% experimental error. At lower energies our calculated rates are smaller than the experimental ones: This can derive from bad detected signal as stated by the authors.

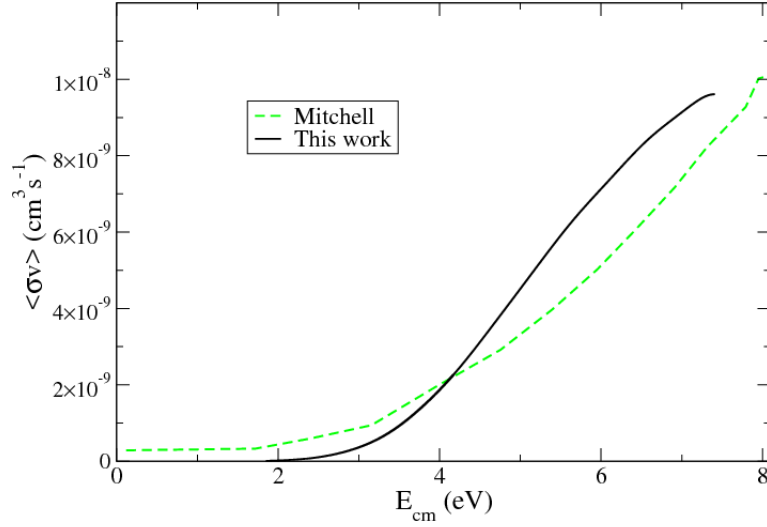


Figure 4.7: Dissociative recombination of vibrationally relaxed ArH^+ . Comparison between the rate coefficient measured in the CRYRING storage ring and the anisotropic rate coefficient obtained by the convolution of our MQDT-computed cross section using the temperatures characterizing the relative velocities of the electrons with respect to the ions in the experiment.

Figure (4.8) displays the DR cross section compared to the competitive process of VE for one quantum excitation in the same energy range. The main feature is that, at energies just above the opening of the dissociative channels, the VE cross section is larger than the corresponding DR starting from the same vibrational level.

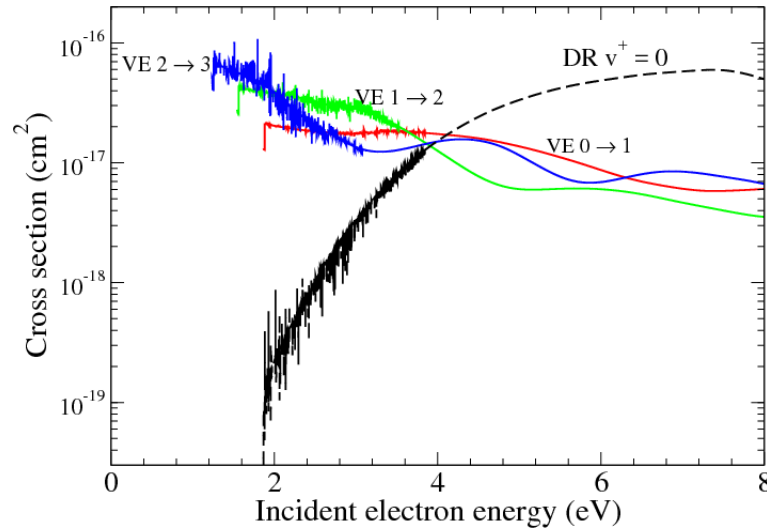


Figure 4.8: Vibrational excitation (VE) of ArH^+ on its lowest vibrational levels: Cross sections for $\Delta v^+ = 1$ (solid lines). The dissociative recombination (DR) cross section are also shown for comparison (broken line).

We also checked the isotopic effect by replacing ArH^+ by ArD^+ , which results

in a variation of the reduced mass by a factor of 2. Figure (4.9) displays this effect for $v^+ = 0$ DR rate coefficient. The rates decrease by a factor between 10 at 1000 K and 3 at 8000 K, due to lowering of the ArD^+ ground state, compared to that of ArH^+ .

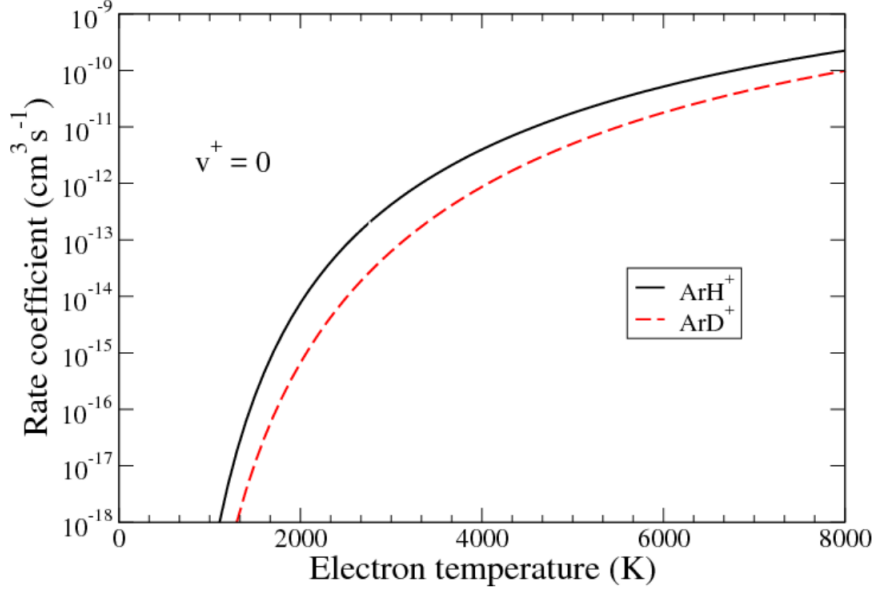


Figure 4.9: Dissociative recombination rate of vibrationally relaxed ArH^+ and ArD^+ as a function of electron temperature: The isotopic effects.

4.4 Astrophysical consequences

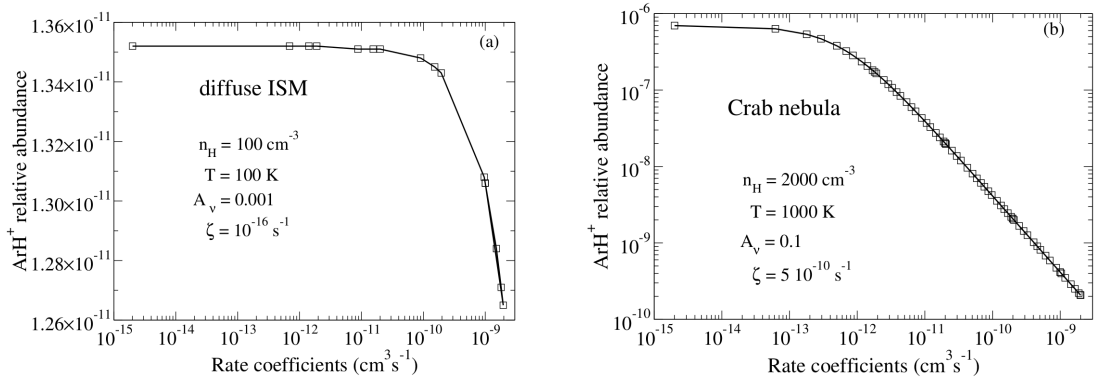


Figure 4.10: Relative abundance of ArH^+ as a function of the rate coefficients for the case of (a) diffuse ISM (temperature $T = 100$ K) and (b) Crab nebula (temperature $T = 1000$ K).

As stated previously, ArH^+ DR is an important destruction mechanism in interstellar conditions. We have examined two different environments where this

molecular ion has been found and have varied the value of the DR rate coefficient over a range of values between 10^{-9} and $10^{-18} \text{ cm}^3 \text{ s}^{-1}$ for a sample of 0D steady state chemical models. We solve the coupled $\frac{d}{dt}[X] = 0$ differential equations where $[X]$ stands for the abundance of a particular X molecule included in the chemical network for a fixed value of density and temperature and different values of the DR chemical rate coefficient of ArH^+ , $k_{\text{DR}}(\text{ArH}^+)$. In Figure 4.10(a), we display the different solutions of the argonium relative abundance as a function of $k_{\text{DR}}(\text{ArH}^+)$ for typical diffuse cloud conditions: Proton density $n_{\text{H}} = 100 \text{ cm}^{-3}$, temperature $T = 100 \text{ K}$, H_2 cosmic ionization rate $\zeta = 10^{-16} \text{ s}^{-1}$, visual extinction $A_v = 0.001$ and standard interstellar radiation field defined by the scaling parameter $\chi = 1$. In Figure 4.10(b), we display the different solutions for physical conditions pertaining to the Crab nebula, as discussed in [53], *i.e.* $n_{\text{H}} = 2000 \text{ cm}^{-3}$, $T = 1000 \text{ K}$, H_2 cosmic ionization rate $\zeta = 5 \cdot 10^{-10} \text{ s}^{-1}$, $\chi = 60$, $A_v = 0.1$ and the elemental abundances displayed in Table 1 of [53]. Each point corresponds to a specific model results and the line connects the different model results. In the standard diffuse cloud conditions, we see that the argonium relative abundance remains constant for values of $k_{\text{DR}}(\text{ArH}^+)$ smaller than some $10^{-11} \text{ cm}^3 \text{ s}^{-1}$, where another destruction mechanism such as photodissociation becomes dominant. It should also be noticed that the scale is linear and the variations are moderate. However, in the extreme conditions of the Crab nebula where the cosmic ionization rate is about 7 orders of magnitude larger, the variation of the relative fractional abundance of argonium is much more spectacular. The limiting value of $k_{\text{DR}}(\text{ArH}^+) = 10^{-13} \text{ cm}^3 \text{ s}^{-1}$, below which the relative abundance of argonium remains almost stable and the destruction by photodissociation and reaction with H_2 take over the dissociative recombination. Our theoretical computations demonstrate that the actual value is significantly below the experimental upper limit $10^{-9} \text{ cm}^3 \text{ s}^{-1}$ and even below the limiting values stressed out by the models (see Figure 4.6(b)). Within these findings, we conclude that DR plays a negligible role in astrophysical media and that photodissociation and reactions with molecular hydrogen become the main destruction processes.

4.5 Quantum defect influence on vibrational excitation

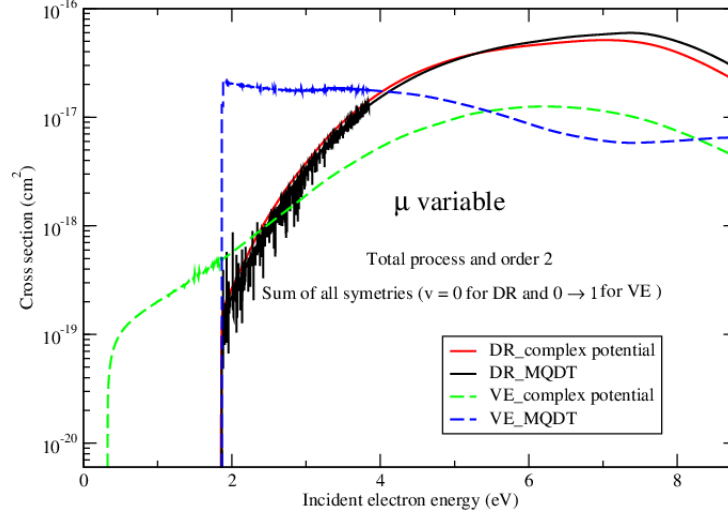


Figure 4.11: Variable quantum defect

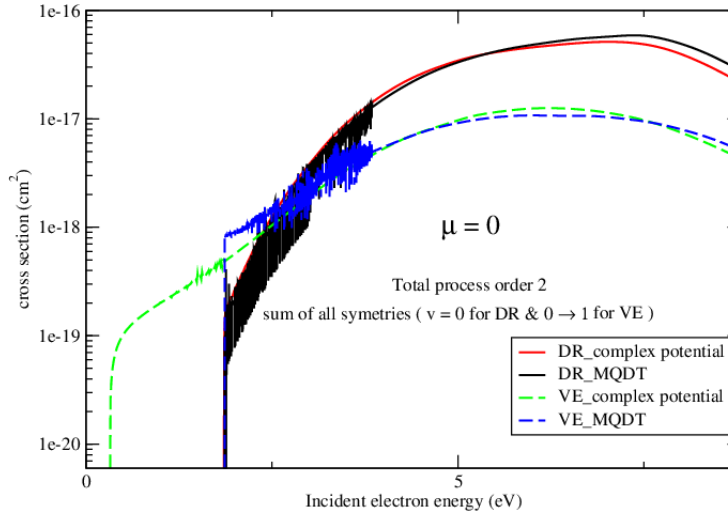


Figure 4.12: Constant quantum defect

In Figures (4.11) and (4.12) we have represented the DR and VE cross sections for the total process at the second order of the \mathcal{K} matrix with a calculation step of 10^{-5} . The quantum defect is considered constant in the Figure (4.12) and this excludes the vibronic coupling between the ionization channels.

The vibrational excitation only is sensitive to this coupling. The complex potential method gives almost the same results as the MQDT method applied for

the constant quantum defect case, except the Rydberg resonances which are not included at all in the former method.

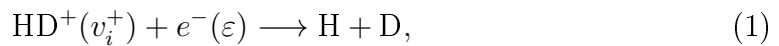
4.6 Conclusions

In this chapter I have described the exploration of the superexcited states of ArH within the R-matrix approach and I have shown how we computed the cross sections and the corresponding rate coefficients for the dissociative recombination and the vibrational excitation of ArH^+ by using Multichannel Quantum Defect Theory. We have explained the very low rate coefficient of DR at low energy, put in evidence by the experimental studies, and we have produced DR, VE and VdE rate-coefficients for the three lowest levels of the argonium ion, in order to be used in the modeling of the kinetics of low temperature ionized media, especially in interstellar molecular clouds.

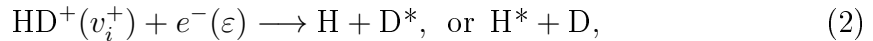
Electron scattering on HD^+

5.1 Introduction

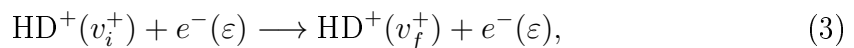
For its simplicity, the hydrogen molecule is one of the most theoretically studied molecule. In the early universe it was the first molecule to be formed [69, 70]. Its isotopologue HD^+ , is the subject of this chapter for fusion plasma application ; the deuterium can easily be founded in water and with tritium are the major reactants on a plasma fusion. In this later, electron induced dissociation of molecular hydrogen plays a major process [71, 72]. The dissociative recombination (DR) of the HD^+ molecular cation, where an electron collide the target and break it up into two neutral fragments as:



in competition with the dissociative excitation (DE) where one of the two fragments is excited:



and the vibrational excitation (VE) and deexcitation (VdE) where the initial vibrational target state is lower and higher respectively:



are the major processes in ionized medias. Theoretically the DR of the HD^+ molecular cation was studied for the last four decades for incident electron energy higher than the dissociation of the molecule, 2.65 eV [73, 74, 75, 76, 77, 78, 45, 46, 33, 40]. The most of these studies was focused on the lowest vibrational states of the molecules except the study of Takagi [45] who made calculations for all the

vibrational states of the molecule and different isotopologues of molecular hydrogen cation and for all the processes mentioned on eqs. (1,2 and 3). The MQDT theory was also the major subject in these studies. The wave packet approach was used in a first time by Ann E. Orel [76] to calculate the direct DR of the molecule and in a second time by Morisset *et. al.* [77] to include the indirect processes where the comparison of the results was in good agreement with the MQDT results. The calculated DR cross section in refs.[79, 45, 46, 33, 40], where the DR was assisted by the DE, was compared with experimental results [80, 81]. The best comparison among all these studies is the MQDT theory developed in our team [40]. The aim of this chapter is to provide more accurate data for all the vibrational states of the molecule and for all the processes in eqs. (1,2 and 3) since the validity of the theory is confirmed. We are using the same theory as in ref. [40] in this chapter.

5.2 Molecular data

The molecular data used in this chapter are the main input data for the theoretical models presented in the sections (3.4.2.2), where the potential energy curve of the target, with some of its vibrational levels, and the lowest dissociative state can be found in Fig. (3.3) and more explicit in Fig. (1) of Refs. [33, 40]. The discrete-to-continuum couplings $V_{d_j,l}^{(e)\Lambda}$ (Eq.(49)) and the quantum defects for the Rydberg states μ_l^Λ (Eqs.(55)-(58)) are the same as on Ref. [40]. In the following calculations, 7 symmetries – $\Lambda = {}^1\Sigma_g^+, {}^1\Sigma_u^+, {}^1\Pi_g, {}^1\Pi_u, {}^3\Sigma_u^+, {}^3\Pi_g, {}^3\Pi_u$ – for the intermediate states HD* and HD** are taken into account and for each symmetry. Four states have been calculated plus one obtained by scaling-law. For the ${}^1\Sigma_g^+$ symmetry two partial waves, corresponding to $l = 0, 2$'s' and 'd' partial waves, were considered whereas for the others ones just for $l = 2$. The discrete-to-continuum coupling $V_{d_j,l}^{(e)\Lambda}$ has been evaluated *via* the width of the corresponding resonance:

$$V_{d_j,l}^{(e)\Lambda} = \sqrt{\frac{\Gamma_{d_j,l}^{(e)\Lambda}}{2\pi}}, \quad (4)$$

Table 5.1 shows the list of vibrational energy levels ϵ_{v^+} of HD⁺ in its ground electronic states with neglecting the rotational effect. Twenty vibrational levels are obtained with the Numerov resolution of the Schrodinger equation. The calculations presented in this chapter are computed for all of these levels and only cross sections and rate coefficients for $v_i^+ = 0, 1, 2, 3, 5, 10, 15$ and 20 are presented.

$$R_{eq} = 1.996 (1.997) \text{ a.u.}$$

$$D_e = 2.793 \text{ eV}$$

$$D_0 = 2.650 \text{ eV}$$

v^+	$\epsilon_{v^+}(\text{eV})$	v^+	$\epsilon_{v^+}(\text{eV})$
0	0.0000	11	1.9233
1	0.2284	12	2.0370
2	0.4454	13	2.1407
3	0.6511	14	2.2340
4	0.8460	15	2.3167
5	1.0306	16	2.3886
6	1.2046	17	2.4492
7	1.3683	18	2.4980
8	1.5219	19	2.5346
9	1.6658	20	2.5583
10	1.7996		

Table 5.1: Vibrational levels of ground state of HD^+ for non rotational case. Dissociation energies D_e and D_0 are shown. In bracket comparison with experimental values from NIST

5.3 Results

We have performed a MQDT calculations of dissociative recombination and excitation cross sections and vibrational transitions of HD^+ ions in it discrete vibrational levels. We explored an energy range between 10^{-5} and 12 eV with an energy step of 0.01 meV. For all studied processes, the calculations were performed including all discrete levels plus 335 discretized from continua which corresponding to a total of 355 vibrational levels for the ground electronic state and 383 discretized levels for the core excited state. The cross sections have been calculated for all the symmetries listed in molecular data section and only the results of the summation of all of these symmetries are plotted. The direct and indirect mechanisms and the second order of the Lippmann-Schwinger equation (53). The rate coefficients of each calculated cross section have been calculated by integrating this cross sections in Maxwell distribution for each level and the results are displayed in the second column of each Figure.

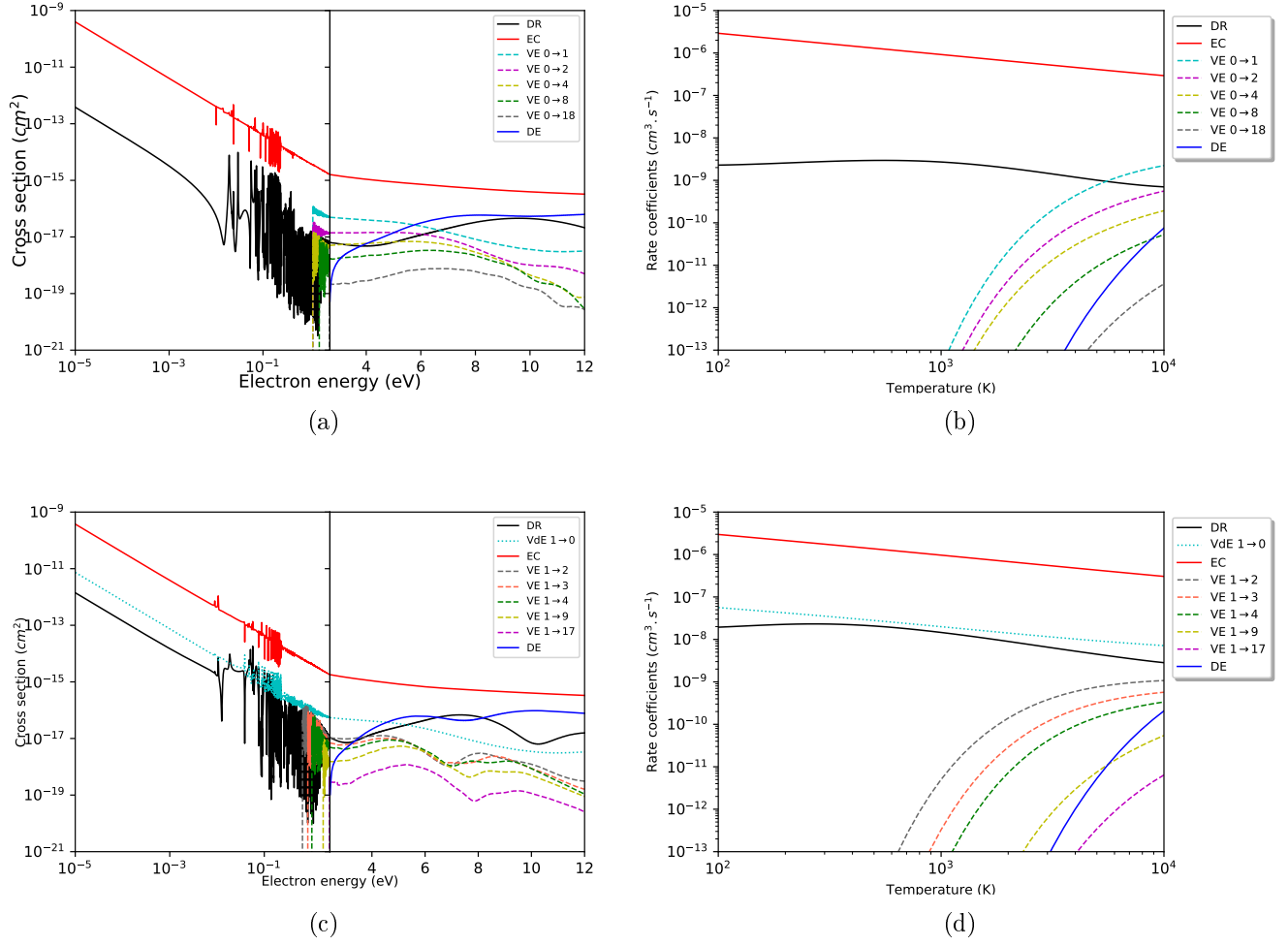


Figure 5.1: Cross section for Dissociative Recombination(DR), Elastic Collisions (EC), Dissociative Excitation (DE) and Vibrational Excitation (VE) of HD^+ on its vibrational levels (left panel) global cross sections, coming from the sum over all the available dissociative states; right panel the corresponding Maxwellian-averaged rate coefficients. (a) and (b) are results for $v_i^+ = 0$ and (c) and (d) for $v_i^+ = 1$

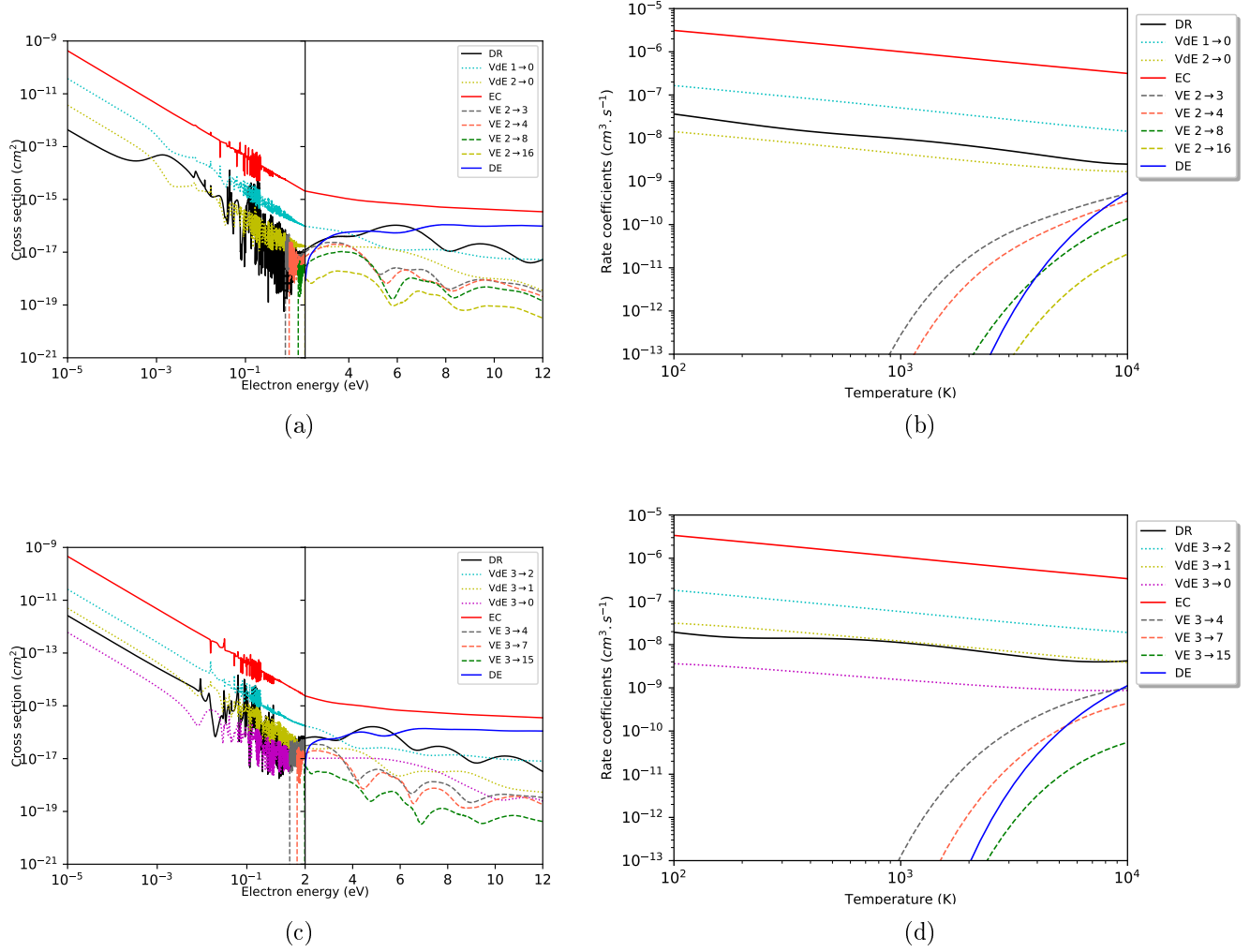


Figure 5.2: Same as figure (5.1) for $v_i^+ = 2$ ((a) and (b)) and $v_i^+ = 3$ ((c) and (d))

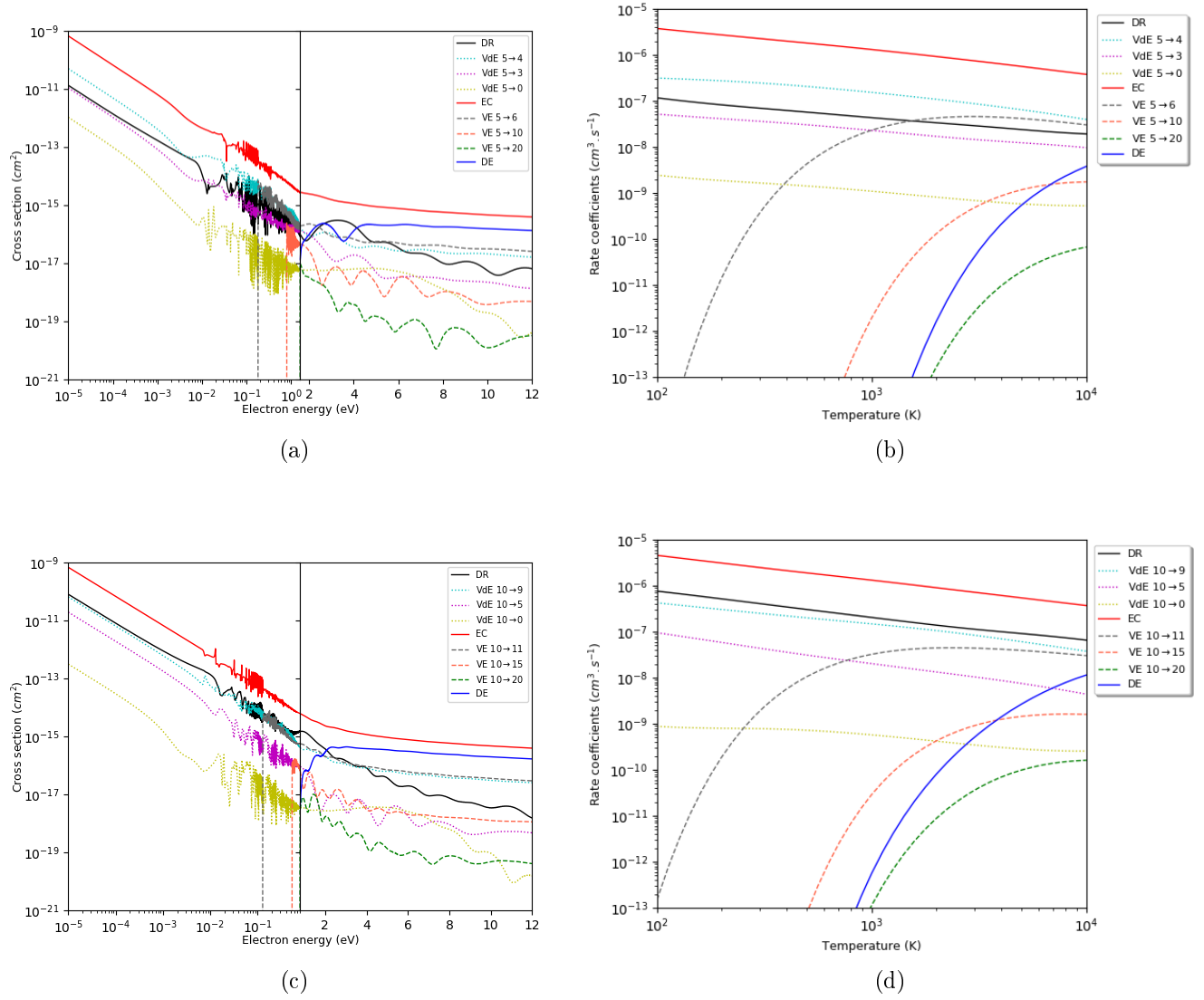


Figure 5.3: Same as figure (5.1) for $v_i^+ = 5$ ((a) and (b)) and $v_i^+ = 10$ ((c) and (d))

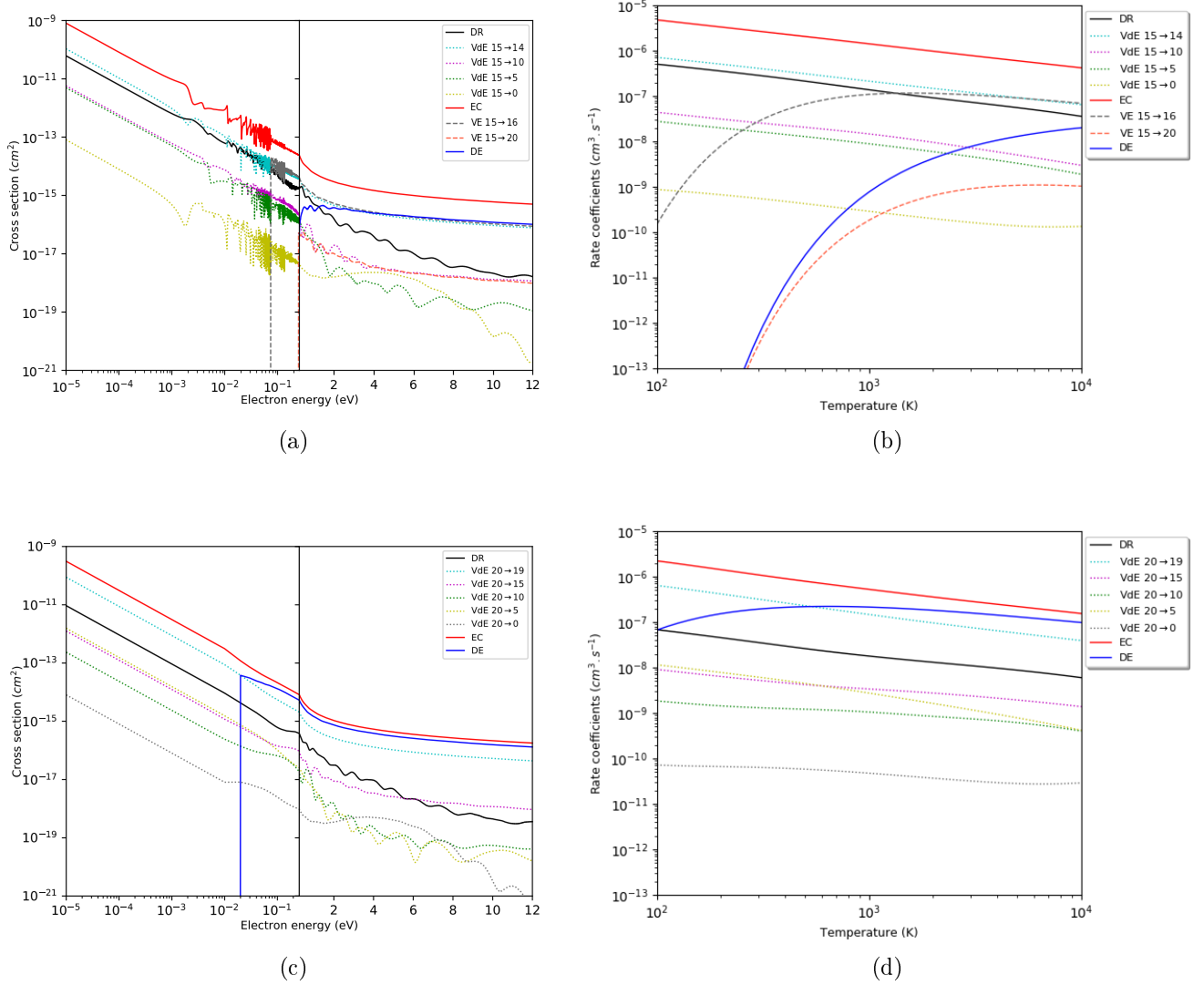


Figure 5.4: Same as figure (5.1) for $v_i^+ = 15$ ((a) and (b)) and $v_i^+ = 20$ ((c) and (d))

Figure (5.1) shows the global cross section and the corresponding rate rate coefficient for each processes , DR, DE, EC, VE and VdE for $v_i^+ = 0$ and $v_i^+ = 1$. And figure (5.2), figure (5.3) and figure (5.4) are results respectively for $v_i^+ = 2$ and 3, 5 and 10 and 15 and 20. For the cross section, results are divided to low and high energy continuously in order to elucidate the total (direct + indirect) mechanisms, at energies below the dissociation limit of the ion, the dissociative states and Rydberg states converging to this limit are sufficient to accurately describe the reactive collision processes at low energies. One can find narrow resonance at low energy. As the electron energy increases, or if reactive collision processes involving the excited vibrational states of the ion are considered, which is the case in this

study, the effect of the indirect process decreases but the contribution excited states is to be considered and these resonances disappear as we approach the dissociation limit where only the direct mechanism govern the processes.

In all the figures, we can see a threshold effect for the VE while for the VdE this effect is not observed which can be explained by the opening of the channels for the VE at each level considered in the calculation. The inverse process does not present this threshold since the channel remains open. The EC predominates compared to the other processes for all levels with a difference between two and three orders of magnitude except the last level $v_i^+ = 20$ where the VdE and DE are in the same order of magnitude. Except the EC, the DE predominates at high energy for all figures except $v_i^+ = 0$ where the DR is in the same order of magnitude as the DE.

The calculated DR rate coefficient as a function of the vibrational levels is displayed in figure (5.5) from the ground vibrational level up to the eleventh one and for different electron temperature. As can be seen in the figure, for a given temperature, the rate coefficient increases as a function of the vibrational level between $v_i^+ = 3$ and $v_i^+ = 10$.

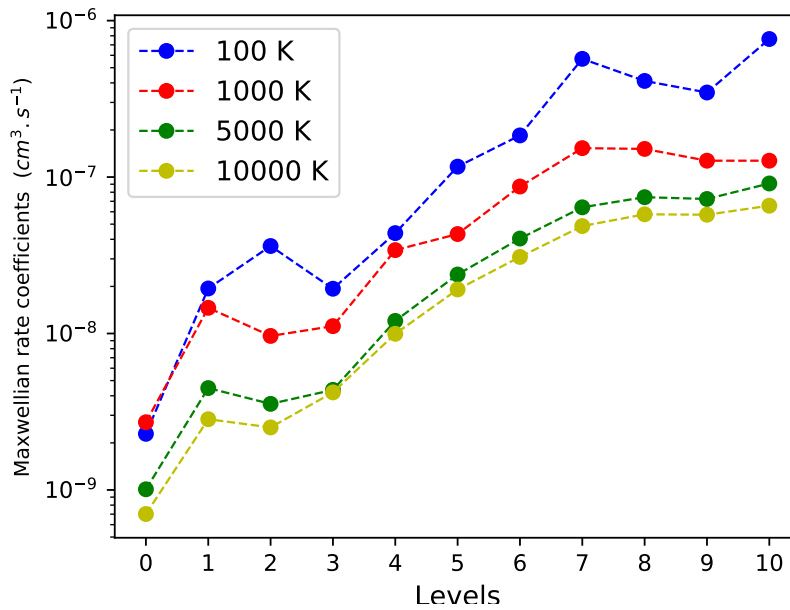


Figure 5.5: Maxwellian-averaged rate coefficients for Dissociative Recombination(DR) over the 11 levels for $T = 100, 1000, 5000$ and $10000K$.

5.4 Conclusion

In this chapter we computed the cross section and rate coefficients for all the discrete levels of reactive collision between electron and HD^+ molecular cation. The MQDT theory is used for energy between 0 and 12 eV. At low energy below the dissociation limit of the molecule the processes are dominated by resonances which are narrow with large amplitude at very low energy and become broad with small amplitudes near the dissociation limit because of the implication of the indirect mechanism where the incident electron is temporary captured in a Rydberg state before dissociating. At high energy the direct mechanism only act in the processes. The theory described in section (3.4.2.2) is used here to calculate the cross section of DR in competition of other DE, EC, VE and VdE. In a perspective to produce an exhaustive database for this system, the exploration of lower energy with the rotational effects is the preoccupation of the team.

Chapter 6

Electron induced reaction on N_2^+

6.1 Introduction

The nitrogen molecule N_2 is one of the most widely studied species so far in plasma physics. Being very stable at low temperature, it is very abundant in the Earth atmosphere, and is notably present in other planetary atmospheres - Titan 98.4 % [82], Triton [83] Pluto [84], Venus 3.5 % and Mars 1.9 % [82] . For other trans-Neptunian objects than Pluto, this molecule is also one of the main component of the ices - spectroscopically observed at their surfaces - and may produce a very thin atmosphere when the temperature increases under solar irradiation [85]. Under the influence of an electric field, the high altitude planetary atmosphere can be crossed by few milliseconds giant discharges called sprites, whose spectroscopic signature is mainly due to spontaneous emission from N_2 excited electronic states [86]. Consequently, the N_2^+ cation is also of huge interest. Due to the solar irradiation, the production of N_2^+ on excited vibrational states plays a significant role in the characteristics of the Earth's thermosphere [87]. It is also the main molecular cation in the atmosphere of Titan [88] and Triton [89]. On the other hand, during the atmospheric entry of a spacecraft in Earth's and Titan's atmospheres, the hypersonic compression of the gases leads to the formation of a plasma departing from local thermodynamic equilibrium [90]. The ionic composition, including N_2^+ , plays a key role in the radiation emitted by the plasma in the near UV spectral region [91]. In many plasma-assisted industrial processes elaborated so far, the plasma reactivity is greatly enhanced by the presence of N_2^+ . This is, for instance, the case in the ammonia synthesis in plasmas/liquid processes [92]. N_2^+ is also very effective in the antibacterial treatment of polyurethane surfaces [93]. Moreover, N_2^+ - as N_2 - is very important in the steel nitriding, resulting in the im-

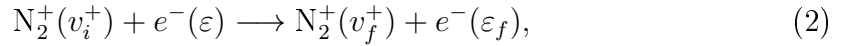
proving of its frictional wear resistance, surface hardness and corrosion resistance [94]. Furthermore, N_2^+ plays a major role in the dermatological treatments based on the nitrogen radio-frequency discharges [95].

The characteristics of the nitrogen-containing plasmas cannot be fully understood without a deep knowledge of the reactivity of N_2^+ , in particular by collisions with electrons.

Dissociative Recombination (DR) is the major molecular cation destruction reaction, that takes place when an electron collides with a the N_2^+ molecular cation, leading to neutral atomic fragments:



In the same time other competitive processes might occur:



i.e. elastic, inelastic and super-elastic collisions.

The elementary non-thermal electron driven processes, in particular dissociative recombination, was experimentally studied using plasmas with laser induced photo-fluorescence techniques [96], shock tubes [97], discharge afterglow experiments [98, 99] and microwave techniques [100]. The most detailed collisional data can be obtained in merged beam [101] and/or storage ring experiments [102].

Two different sets of theoretical calculations have been performed [63, 103, 104, 105] on the DR of N_2^+ . They involved different quantum chemistry and similar nuclear dynamics calculations, and both studies were focusing on the ground and first three vibrational levels of the target.

Our aim with this chapter was to extend as far as possible the calculations started in [63], and to provide DR, EC, VE and VdE cross sections and rate coefficients involving the lowest ten vibrational levels that could be populated in collision with an incoming electron having kinetic energy up to 2.3 eV, relevant for the atmospheric and cold plasma environments. The results presented in this chapter has been published in *Journal of Applied physics* [106]

6.2 Theoretical approach

The MQDT formalism used in this chapter is the same as the one used in chapter (5) valid for the HD^+ system where the dissociative states are coupled to the ionization channels of the ground and excited ion core presented on section (3.4.2.2).

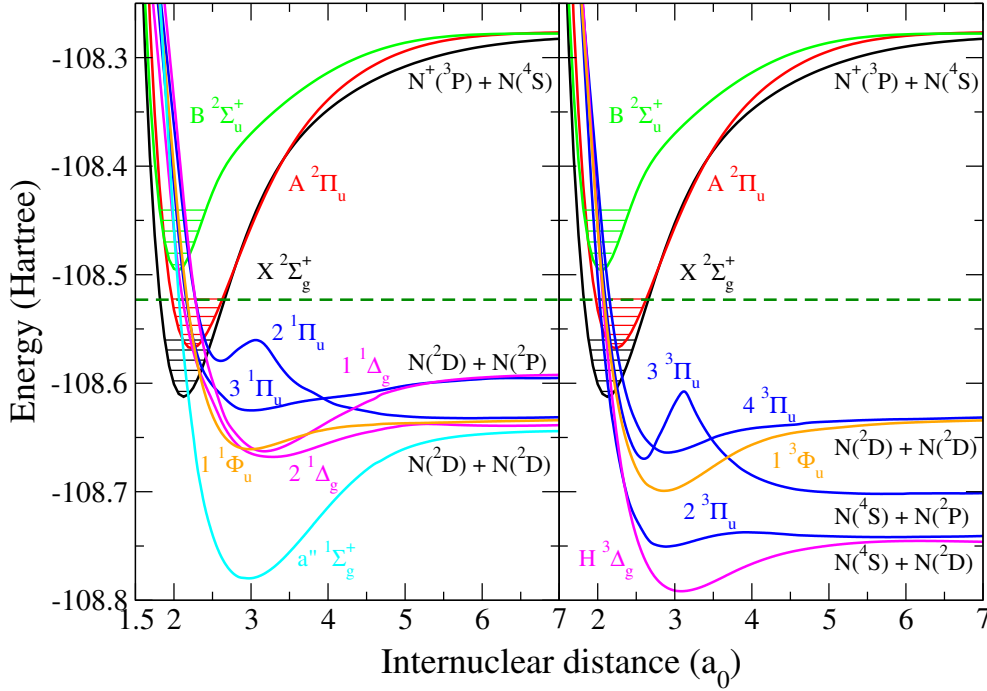


Figure 6.1: Potential energy curves (PEC) relevant for DR of N_2^+ , compiled from Figures. 2 and 3 of Little *et al.*. The color code of the curves is the following: Target cation: ground electronic state ($X^2\Sigma_g^+$): black; 1st excited state ($A^2\Pi_u$): red; 2nd excited state $B^2\Sigma_u^+$: green. Dissociative states of N_2 -left panel: $^1\Pi_u$: blue; $^1\Delta_g$: magenta; $a''^1\Sigma_g^+$: cyan; and $^1\Phi_u$: orange. Dissociative states of N_2 -right panel: $^3\Pi_u$: blue; $H^3\Delta_g$: magenta; and $^3\Phi_u$: orange. The lowest five vibrational levels of each electronic state of the ion and the dissociative asymptotic limits for all states are shown. The green dashed line gives the upper limit of the collision energy.

However, the N_2^+ target cation has two attractive excited states whose ionization continua are coupled to the continuum of the ground core and to neutral dissociative states. The interaction between the elevated number of ionization channels with the dissociation ones result beside the already known electronic couplings to a second type of couplings, namely the Rydberg-Rydberg couplings. The dimension of the *interaction matrix*, and consequently the K-matrix and physical S-matrix is increased with the number of vibrational levels (ionization channels) supported by the two excited ion states. The major steps to arriving to the cross sections remain the same.

6.3 Molecular data

The nuclear dynamics in low-energy electron molecular cation collisions crucially depends on the molecular structure of the colliding partners and on the structure of the formed neutral complex. These calculated molecular data sets include the potential energy curves (PECs) of the target: ground and possibly the excited electronic states of the cation, the PECs of the formed neutral system: doubly excited dissociative molecular states and mono-excited electronically bound Rydberg states, the coupling functions between the ionization and dissociation continua and the generating functions (quantum defects) of the Rydberg series correlating to the electronic states of the target.

One of the few quantum chemistry methods capable to produce the highly excited molecular states at the required accuracy is based on the R-Matrix Theory [3]. The bound and resonant adiabatic potential energy curves of the valence and Rydberg states of N_2 having singlet and triplet symmetries have been published in Refs. [107, 108]. The diabatic curves, couplings and quantum defects relevant for the dissociative recombination of N_2^+ were presented in [63]. The electronic states of the target were calculated using the standard quantum chemistry program suite Molpro [109].

Figures (6.1) and (6.2) contains a compilation of the molecular data used in the present and our previous calculation [63]. Figure 6.1 shows only the molecular states relevant for DR. The PECs of the target cation are given as follows: black curves: $X^2\Sigma_g^+$ ground electronic state; red curves: $A^2\Pi_u$ first excited state and green curves: $B^2\Sigma_u^+$ second excited state. The colour-code for doubly excited dissociative valence states for singlet (left-panel) and triplet (right-panel) symmetries are as follows $^1,3\Pi_u$: blue, $^1,3\Phi_u$: orange, $^1,3\Delta_g$: magenta and $^1\Sigma_g^+$: cyan curves. The dark-green horizontal line gives the upper limit of the collision energy.

Figure (6.2) in contrary contains the complete molecular data relevant for the nuclear dynamics. The figures are restricted to the inter-nuclear distance region between 1.9 and 2.5 a_0 units around the equilibrium geometry of the target cation. The first row of the figure is essentially a repetition of Figure 6.1. The limited inter-nuclear region gives a better view on how favourable the crossings of the dissociative states with the target ones are. The driving interactions of the dynamics are shown in the second row of the figure. The couplings between the dissociative valence states and the Rydberg states for all symmetries - the coupling function that connects the two major decay channels of the neutral: ionization and dissociation - are limited to the chosen inter-nuclear distance region, outside this region they

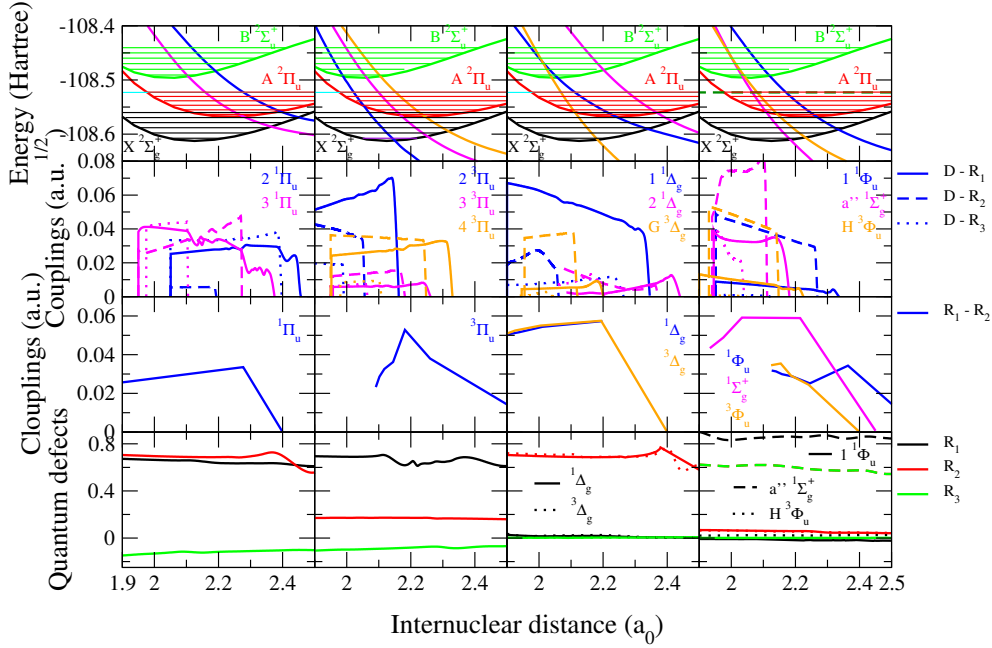


Figure 6.2: Molecular data sets relevant for the DR of N_2^+ limited to internuclear distances around the equilibrium geometry of the ion. 1st row: PECs of the ionic and neutral states for all relevant symmetries. 2nd row: all Rydberg-valence electronic couplings. 3rd row: the relevant Rydberg-Rydberg couplings. 4th row: quantum defects.

vanish. The third row gives the coupling among the different series of Rydberg states. In the present calculation only the couplings among the series correlating to the ground (X) and first excited (A) state of the ion was considered, the other two couplings were taken as zero. And finally the last row of figures represent the quantum defects. For more details on the molecular data set and electron structure calculations, the reader is referred to the reference [63].

6.4 Results and discussions

The present work is a natural continuation of our previous study focusing on the DR of N_2^+ performed for astrophysical applications [63]. Based on the molecular data compiled from [63] and summarized in Figures (6.1) and (6.2), we have performed the nuclear dynamics calculations using the MQDT approach presented in Section 6.2, for the collisions of electrons with N_2^+ target cations. The DR, VE and VdE cross sections have been calculated for the first 10 initial vibrational levels of the ground electronic state of N_2^+ . Table 6.1 shows the energies of the vibrational levels relative to $v_i^+ = 0$ of the target.

Table 6.1: The relevant vibrational levels of the N_2^+ molecular cation - relative to the ground vibrational level - in the present calculations.

v^+	0	1	2	3	4	5	6	7	8	9
E_{v^+} (eV)	0.0	0.266	0.528	0.786	1.040	1.290	1.536	1.777	2.014	2.248

The calculations were performed by taking into account both *direct* (the capture of the incoming electron into a dissociative state of the molecule) and *indirect* (temporary capture of the electron into a highly excited Rydberg state predissociated by the dissociative state) mechanisms at the second order perturbation theory. Three attractive target states (X , A and B) and their vibrational levels (81, 66 and 50) were fully accounted in the calculation.

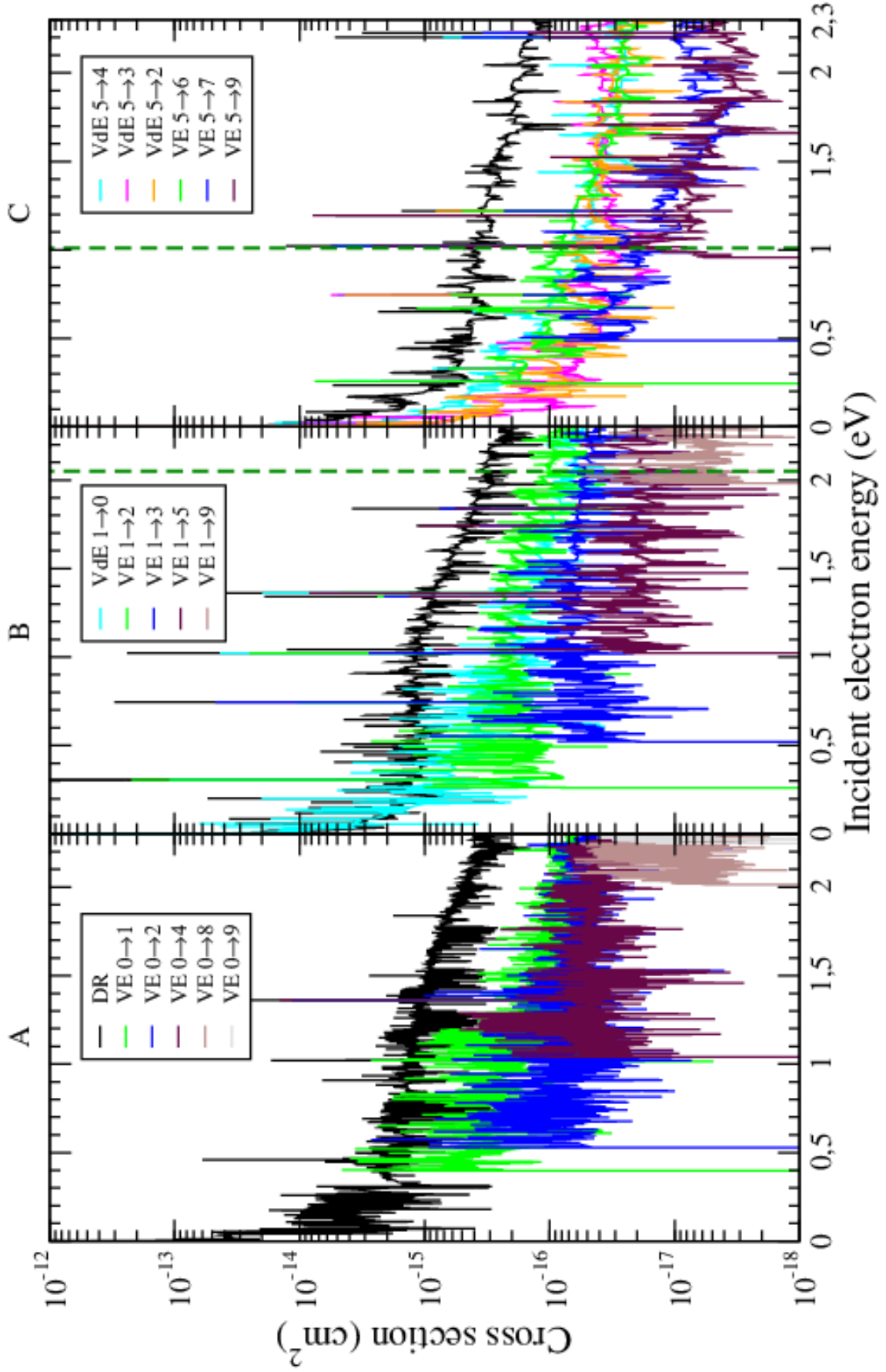


Figure 6.3: Global DR, VE and VdE cross sections of the N_2^+ $v_i^+ = 0$ (A), $v_i^+ = 1$ (B) and $v_i^+ = 5$ (C) as a function of the collision energy. For vibrational transitions (VE and VdE) we label the processes as transitions from the initial to the final vibrational levels of the target. The vertical dashed dark-green line gives the precision limit of the calculations.

The cross sections were calculated for all the relevant symmetries listed in figures. (6.1) and (6.2) for collision energies ranging from $10^{-5} - 2.3$ eV of the incident electron, having an energy step of 0.01 meV. These cross sections were summed up to obtain the global cross sections.

The global DR, VE and VdE cross sections for target cations having initial vibrational levels $v_i^+ = 0, 1$ and 5 are shown in figure (6.3) A, B and C panels respectively. The vertical dark-green dashed lines in the mid and upper panels of figure (6.3) mark the energy below which the calculations are the most accurate. Above these thresholds the calculations neglect the role of the higher lying dissociative states of the neutral. Nevertheless, the data displayed continue to be reasonably correct above these thresholds because these dissociative states penetrate into the ionization continuum above these thresholds, forming favourable/non-vanishing Franck-Condon overlaps with the target electronic states at even higher collision energies. This Franck-Condon overlap is proportional with the first order term of the direct cross section. In addition the couplings of these dissociative states with the Rydberg series are generally weaker, leading to less important cross sections in second order.

The *direct* mechanism is responsible for the background $1/E$ behaviour of the cross sections, while the *indirect* one through the temporary capture into the Rydberg states produces all the resonance structures dominating the cross sections.

The global DR cross section increases as we change the initial vibrational state of the target by unity and starts to decrease as we arrive at $v_i^+ = 5$. While the vibrational de-excitation (cyan curves for initial vibrational levels higher than 0) are in competition with the DR cross section, at higher collision energies their overall cross section values are at least with a factor of 5 smaller than those of the DR. The vibrational excitations (green, blue, violet, maroon,... curves) show threshold effects at the collision energies where they become open. Moreover one can see, that for a given initial vibrational level v_i^+ the $|\Delta v^+| = 1$ vibrational transitions are the most important ones, followed by the higher transitions.

A better view on the vibrational dependence of the processes one can have when the global cross sections are thermally averaged in order to obtain the isotropic Maxwell rate coefficients. Figure 6.4 shows the rate coefficients of all processes for the six lowest initial vibrational levels of N_2^+ . The green dashed line gives the precision limits of our calculation expressed now in electron temperatures.

The DR (solid black line) and VdE (coloured lines with symbols) rates in figure 6.4) show monotonically decreasing patterns as function of the temperature, while the VE (thick coloured lines) ones show increasing behaviour presenting a

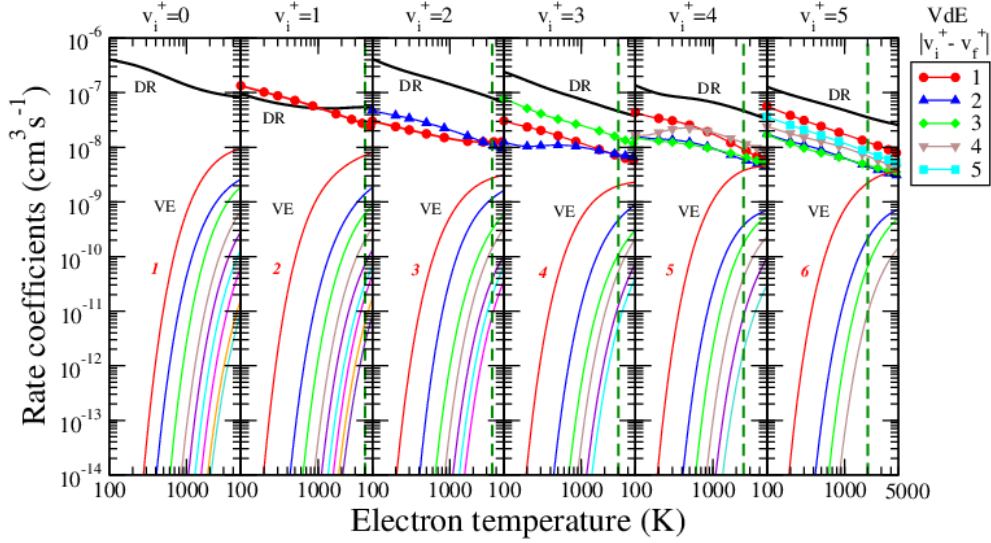


Figure 6.4: Isotropic Maxwell rate coefficients of N_2^+ for $v_i^+ = 0-5$ initial vibrational levels for all relevant electron induced processes: Dissociative recombination (black line), elastic collision (indigo dashed line), vibrational excitation (thin coloured lines) and vibrational de-excitation (symbols and thick coloured lines). For the vibrational excitations all transitions are shown up to $\Delta v^+ = v_f^+ - v_i^+ = 8$ with the lowest transition being labeled on each figure. excitation and de-excitation to final vibrational quantum numbers are given. The green dashed line gives the precision limits of our calculation given in temperatures.

Table 6.2: List of the parameters used in Eq. (3) for the DR rate coefficients of N_2^+ .

	v_i^+	$A_{v_i^+}$	$\alpha_{v_i^+}$	$B_{v_i^+}$
DR	0	$0.168904101 \times 10^{-05}$	$-0.351926202 \times 10^{+00}$	$-0.134370270 \times 10^{+02}$
	1	$0.121053981 \times 10^{-06}$	$-0.107632411 \times 10^{+00}$	$-0.399000690 \times 10^{+02}$
	2	$0.590303124 \times 10^{-05}$	$-0.534570541 \times 10^{+00}$	$0.101278261 \times 10^{+02}$
	3	$0.146929391 \times 10^{-05}$	$-0.431676563 \times 10^{+00}$	$-0.188330434 \times 10^{+02}$
	4	$0.164348890 \times 10^{-05}$	$-0.466246783 \times 10^{+00}$	$0.229753115 \times 10^{+02}$
	5	$0.584851528 \times 10^{-06}$	$-0.365953053 \times 10^{+00}$	$-0.145957453 \times 10^{+02}$

maximum towards higher temperatures. The largest rate coefficients we obtained for the EC process, which is followed by the DR. With the exception of the $v_i^+ = 1$ case the VdE rate coefficients are below the DR. At $v_i^+ = 1$ the DR is in competition with VdE, but for $v_i^+ > 1$ DR exceeds VdE with a factor of 2 – 5. We can see from figure 6.4, that the VE process becomes important at higher electron temperatures. Moreover higher we go with the initial vibrational quantum number of the target cation, more important the VE is becoming.

And finally, in order to allow the versatile implementation of the rate coefficients in kinetics modelling codes, we have fitted them with simple and generalized Arrhenius-type formulas.

The calculated rate coefficients of dissociative recombination rate coefficients of N_2^+

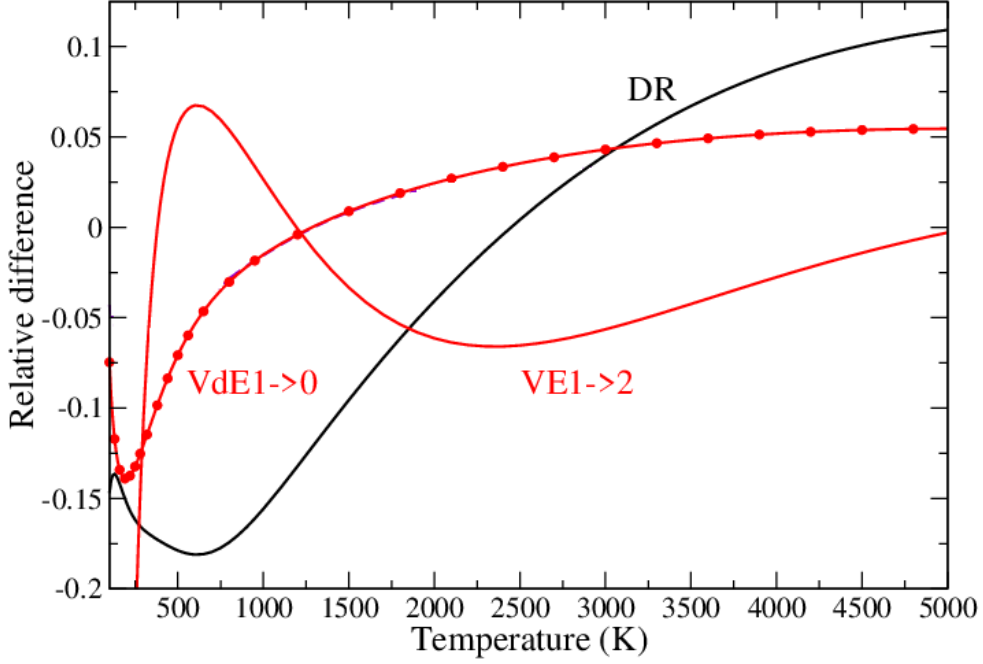


Figure 6.5: Relative difference between the calculated and fitted isotropic Maxwell rate coefficients. The fitting parameters of the (3), and (4) Arrhenius type formulas are listed in tables (6.2) and (6.3). The target vibrational quantum number is $v_i^+ = 1$.

for the lowest 10 vibrational states ($v_i^+ = 0 \rightarrow 9$) have been fitted as:

$$k_{(N_2^+),v_i^+}^{DR}(T_e) = A_{v_i^+} T_e^{\alpha_{v_i^+}} \exp \left[-\frac{B_{v_i^+}}{T_e} \right] \quad (3)$$

over the electron temperature range $100 \text{ K} \leq T_e \leq 12\,000 \text{ K}$. The parameters $A_{v_i^+}$, $\alpha_{v_i^+}$ and $B_{v_i^+}(j)$ are listed in Table 6.2.

The rate coefficients of the vibrational transitions (VE and/or VdE) of N_2^+ have been interpolated under the form

$$k_{(N_2^+),v_i^+ \rightarrow v_f^+}^{VE,VdE}(T_e) = A_{v_i^+ \rightarrow v_f^+} T_e^{\alpha_{v_i^+ \rightarrow v_f^+}} \exp \left[-\frac{B_{v_i^+ \rightarrow v_f^+}}{T_e} \right] \quad (4)$$

over the electron temperature range $450 \text{ K} \leq T_e \leq 12\,000 \text{ K}$. The parameters $A_{v_i^+ \rightarrow v_f^+}$, $\alpha_{v_i^+ \rightarrow v_f^+}$ and $B_{v_i^+ \rightarrow v_f^+}(j)$ are listed in Table 6.3. The values calculated by Eqs. (3)-(4) defer from the referenced values by of a few percent. A representative case figure can be seen in Figure 6.5, where the relative differences among the original and fitted data is presented as function of temperature.

6.5 Conclusions

The present work completes a previous study performed on reactive collisions of N_2^+ with electrons [63]. Making use of the molecular data set calculated in Refs. [107, 108, 63], we have performed a step-wise MQDT calculation for the lowest 6 vibrational levels of the target cation in collisions with electrons having kinetic energy up 2.3 eV. We have provided cross sections and rate coefficients for resonant elastic scattering, dissociative recombination, vibrational excitation and de-excitation of N_2^+ molecular cation, up to collision energies and/or electron temperatures important for the detailed kinetic modelling of cold astrophysical, atmospheric and laboratory plasmas.

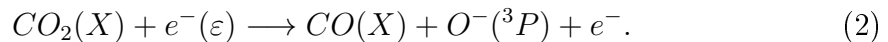
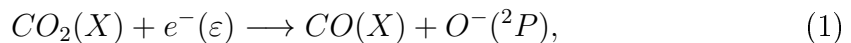
Table 6.3: List of the parameters used in Eq. (4) for the VE and VdE rate coefficients of N_2^+ ($v_i^+ = 0 - 5$). The lines having bold v_f^+ values belong to VdE.

v_i^+	v_f^+	$A_{v_i^+ \rightarrow v_f^+}$	$\alpha_{v_i^+ \rightarrow v_f^+}$	$B_{v_i^+ \rightarrow v_f^+}$
0	1	$0.533344237 \times 10^{-05}$	$-0.639374553 \times 10^{+00}$	$0.456739316 \times 10^{+04}$
	2	$0.658378881 \times 10^{-06}$	$-0.508032807 \times 10^{+00}$	$0.607945515 \times 10^{+04}$
	3	$0.362115898 \times 10^{-05}$	$-0.674156176 \times 10^{+00}$	$0.930893498 \times 10^{+04}$
	4	$0.501855702 \times 10^{-06}$	$-0.500080763 \times 10^{+00}$	$0.120925542 \times 10^{+05}$
	5	$0.235912200 \times 10^{-05}$	$-0.703019757 \times 10^{+00}$	$0.151544255 \times 10^{+05}$
	6	$0.293791457 \times 10^{-05}$	$-0.758069795 \times 10^{+00}$	$0.179532193 \times 10^{+05}$
	7	$0.844921993 \times 10^{-06}$	$-0.636542915 \times 10^{+00}$	$0.207666715 \times 10^{+05}$
	8	$0.138641664 \times 10^{-06}$	$-0.515367652 \times 10^{+00}$	$0.234152751 \times 10^{+05}$
	9	$0.134097811 \times 10^{-08}$	$-0.582687960 \times 10^{-01}$	$0.236665697 \times 10^{+05}$
1	0	$0.295077650 \times 10^{-05}$	$-0.573680535 \times 10^{+00}$	$0.370832440 \times 10^{+02}$
	2	$0.128822963 \times 10^{-06}$	$-0.259330324 \times 10^{+00}$	$0.287067490 \times 10^{+04}$
	3	$0.490705465 \times 10^{-07}$	$-0.246519767 \times 10^{+00}$	$0.603265476 \times 10^{+04}$
	4	$0.289902179 \times 10^{-06}$	$-0.477464964 \times 10^{+00}$	$0.891365876 \times 10^{+04}$
	5	$0.147216051 \times 10^{-06}$	$-0.436923369 \times 10^{+00}$	$0.119542621 \times 10^{+05}$
	6	$0.223367779 \times 10^{-06}$	$-0.521846263 \times 10^{+00}$	$0.147323078 \times 10^{+05}$
	7	$0.133051980 \times 10^{-06}$	$-0.486721650 \times 10^{+00}$	$0.172809300 \times 10^{+05}$
	8	$0.210780119 \times 10^{-06}$	$-0.518354452 \times 10^{+00}$	$0.203265946 \times 10^{+05}$
	9	$0.984869766 \times 10^{-07}$	$-0.477479897 \times 10^{+00}$	$0.229495263 \times 10^{+05}$
2	0	$0.847821462 \times 10^{-06}$	$-0.532998020 \times 10^{+00}$	$0.405352818 \times 10^{+02}$
	1	$0.413063749 \times 10^{-07}$	$-0.143998488 \times 10^{+00}$	$-0.358549186 \times 10^{+02}$
	3	$0.464786859 \times 10^{-07}$	$-0.245777044 \times 10^{+00}$	$0.285862699 \times 10^{+04}$
	4	$0.159108720 \times 10^{-06}$	$-0.391348421 \times 10^{+00}$	$0.585177469 \times 10^{+04}$
	5	$0.360044376 \times 10^{-07}$	$-0.276667604 \times 10^{+00}$	$0.868446216 \times 10^{+04}$
	6	$0.258089123 \times 10^{-06}$	$-0.507330640 \times 10^{+00}$	$0.117566701 \times 10^{+05}$
	7	$0.333098042 \times 10^{-06}$	$-0.605949101 \times 10^{+00}$	$0.144650428 \times 10^{+05}$
	8	$0.613621551 \times 10^{-06}$	$-0.668110981 \times 10^{+00}$	$0.174175232 \times 10^{+05}$
	9	$0.258659482 \times 10^{-06}$	$-0.572706841 \times 10^{+00}$	$0.200428524 \times 10^{+05}$
3	0	$0.164184580 \times 10^{-05}$	$-0.596574164 \times 10^{+00}$	$0.142269951 \times 10^{+02}$
	1	$0.621487443 \times 10^{-07}$	$-0.268738942 \times 10^{+00}$	$0.312326420 \times 10^{+02}$
	2	$0.111782734 \times 10^{-06}$	$-0.336464781 \times 10^{+00}$	$-0.121616700 \times 10^{+02}$
	4	$0.766268279 \times 10^{-07}$	$-0.345400694 \times 10^{+00}$	$0.267682697 \times 10^{+04}$
	5	$0.134606977 \times 10^{-07}$	$-0.179764421 \times 10^{+00}$	$0.574922736 \times 10^{+04}$
	6	$0.535124837 \times 10^{-08}$	$-0.121773603 \times 10^{+00}$	$0.867471070 \times 10^{+04}$
	7	$0.204963902 \times 10^{-07}$	$-0.265769846 \times 10^{+00}$	$0.114419973 \times 10^{+05}$
	8	$0.879364727 \times 10^{-08}$	$-0.224268128 \times 10^{+00}$	$0.142282367 \times 10^{+05}$
	9	$0.814651461 \times 10^{-07}$	$-0.499342338 \times 10^{+00}$	$0.168805145 \times 10^{+05}$
4	0	$0.107606116 \times 10^{-05}$	$-0.575085141 \times 10^{+00}$	$0.145468955 \times 10^{+03}$
	1	$0.248568440 \times 10^{-06}$	$-0.466043134 \times 10^{+00}$	$0.564097946 \times 10^{+02}$
	2	$0.724394585 \times 10^{-07}$	$-0.308511590 \times 10^{+00}$	$0.226809253 \times 10^{+02}$
	3	$0.138222192 \times 10^{-05}$	$-0.640485514 \times 10^{+00}$	$0.561106669 \times 10^{+02}$
	5	$0.239207956 \times 10^{-05}$	$-0.668594861 \times 10^{+00}$	$0.306395333 \times 10^{+04}$
	6	$0.101993424 \times 10^{-05}$	$-0.713594098 \times 10^{+00}$	$0.582189709 \times 10^{+04}$
	7	$0.164341020 \times 10^{-05}$	$-0.729783197 \times 10^{+00}$	$0.861715530 \times 10^{+04}$
	8	$0.125571495 \times 10^{-05}$	$-0.739599323 \times 10^{+00}$	$0.113354172 \times 10^{+05}$
	9	$0.148406106 \times 10^{-06}$	$-0.535162904 \times 10^{+00}$	$0.139439109 \times 10^{+05}$
5	0	$0.611371619 \times 10^{-06}$	$-0.566807382 \times 10^{+00}$	$0.158486274 \times 10^{+02}$
	1	$0.411089882 \times 10^{-06}$	$-0.543865182 \times 10^{+00}$	$0.285127586 \times 10^{+02}$
	2	$0.515303362 \times 10^{-07}$	$-0.315487751 \times 10^{+00}$	$-0.323769106 \times 10^{+02}$
	3	$0.516023387 \times 10^{-07}$	$-0.317535711 \times 10^{+00}$	$-0.246956406 \times 10^{+02}$
	4	$0.791676797 \times 10^{-06}$	$-0.549559034 \times 10^{+00}$	$0.457289565 \times 10^{+01}$
	6	$0.313205750 \times 10^{-06}$	$-0.458006851 \times 10^{+00}$	$0.285255623 \times 10^{+04}$
	7	$0.348715111 \times 10^{-06}$	$-0.594271554 \times 10^{+00}$	$0.575157504 \times 10^{+04}$
	8	$0.303368112 \times 10^{-06}$	$-0.546732721 \times 10^{+00}$	$0.861104543 \times 10^{+04}$
	9	$0.131609694 \times 10^{-06}$	$-0.527503523 \times 10^{+00}$	$0.112079309 \times 10^{+05}$

Chapter 7

Carbon dioxide electron impact reactions

Carbon dioxide is one of the main greenhouse gases and plays a fundamental role in our planetary atmosphere. It helps to control the temperature of the planet by trapping the infrared rays emitted by the sun in the atmosphere. Without greenhouse gases, the Earth's temperature would be very cold. However, the increasing of the human activity increases considerably the amount of CO₂ present in the Earth atmosphere and lead to a disruption of the natural balance which can have unpredictable effects on the Earth's temperature. The excess CO₂ in the atmosphere is one of the main causes of global warming. It is known to play an important fundamental role in the chemistry of the atmospheres of Mars and Venus (most abundant gases with 96 % of the atmospheres) [110] in addition to being involved in respiration mechanisms. The main goal of this chapter was based on the computation of the cross-section of dissociative electronic attachment and dissociative excitation presented in the reactions (1) and (2) below.



Due to the lack of complete data in the literature on the potential energy curves of carbon dioxide, we have set ourselves the main goal of calculating the potential energy curves of the molecule by freezing one CO bond and stretching the other bond, thus bringing our study back to a case of a diatomic molecule. This is justified by the production of carbon monoxide in its fundamental ground electronic state after the collision with electrons.

Configuration	Term	Level (eV)	Configuration	Term	Level (eV)
C ($1s^2 2s^2 2p^2$)	3P	0 .0000000	O ($1s^2 2s^2 2p^4$)	3P	0 .0000000
	1D	1.2637284		1D	1.9673642
	1S	2.6840136		1S	4.1897463
C ($1s^2 2s^2 2p^2$)	3P	0 .0000000	$2 \times$ O ($1s^2 2s^2 2p^4$)	$^3P + ^3P$	0 .0000000
	1D	1.2637284		$^3P + ^1D$	1.9673642
	1S	2.6840136		$^1D + ^1D$	3.9347282

Table 7.1: Energies of spectral atomic terms for Carbon an Oxygen from [NIST](#) [68]

7.1 Step of calculation

In order to describe the adiabatic wave functions of our triatomic molecule, preliminary work must be done to understand well and have the correct wave function and the electronic states to be put in the calculation. The nature of the ground electronic state in our case is done using the *building up principle* [111] based on the Wigner-Witmer correlation rules [112] which consist, for a diatomic molecule, to consider it as a *unified atom*. Using this principle, the molecule may build up from a separated atom or group of atoms, or united atom or molecule. In our case, we choose to build the CO_2 molecule by taking into account the group of two oxygen atoms together with a carbon atom as it is shown in table (7.1). For that, the different spectral terms energy levels of the independent atoms which makes up our molecule have to be checked from atomic spectra database levels form of [NIST](#) website [68]. And several configurations are needed to describe well the real wave function but a huge quantity of molecular state must be putted in the calculation and it can not be possible.

In our study, we are only interested in the lower triplets and singlets spectral terms with minimal energies, i.e, the 0.0000 eV states of oxygen ($^3P + ^3P$) which, according to Bièmont's *table 10.4* [113], correlate to the states ($\Sigma^+(2)$, Σ^- , $\Pi(2)$, Δ) to which we add the triplet 3P at 0.0000eV and the singlet 1D at 1.2637284 eV of carbon to finally reach the final molecular states according to Herzberg's *table 22*[111]:

Molecular state	Energy (eV)
$\Sigma^+(2)$, $\Sigma^-(3)$, $\Pi(5)$, $\Delta(2)$ Φ	0.0000
$\Sigma^+(4)$, $\Sigma^-(3)$, $\Pi(6)$, $\Delta(5)$ $\Phi(2)$, Γ	1.2637284

Table 7.2: Molecular states included in the calculation of potential energy curve of CO_2 molecule

We can see that only with two lowest energies for atomic spectral terms and for triplets and singlets states, we have a total of 34 molecular state (see table (7.2)) which is very big in term of calculation.

7.2 Theoretical approach

The calculation of the potential energy curves was performed taking into account the 34 molecular states shown in the previous section. At this stage, the choice of the basis set to be used in our calculation was crucial. To do this, an optimization of the geometry was carried out.

7.2.1 Basis set choice

To choose the appropriate basis set to use in our calculation of potential energy curves, a convergence study is made for the equilibrium internuclear distance with a geometry optimization with a Hartree Fock and a CASSCF method using the Molpro quantum chemical programs (version 2019.2) [114].

Basis	Hartree Fock	CASSCF
cc-pVDZ	1.14056	1.17124
cc-pVTZ	1.13618	1.16576
cc-pVQZ	1.13448	1.16390
cc-pV5Z	1.13439	1.16378
cc-pV6Z	1.13437	1.16337

Table 7.3: Optimization of CO₂ geometry with a Hartree-Fock and CASSCF method [115]

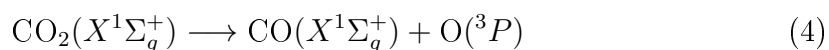
The results of our optimization can be found on table (7.3) for a HF and CASSCF and cc-pVXZ (X = D, T, Q, 5, 6) basis set. Convergence is reached with a cc-pVQZ basis set as is shown on table. The internuclear distance value remains the same with a basis set greater or equal to cc-pVQZ.

7.2.2 Potential Energy Curve of CO₂

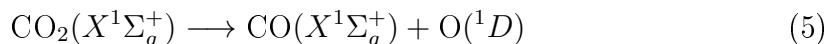
The carbon dioxide molecule is a linear which have 22 electrons and its ground electronic state, in C_{2v} symmetry, is :

$$^1\Sigma_g^+ : (1a_1)^2(2a_1)^2(3a_1)^2(4a_1)^2(5a_1)^2(1b_1)^2(1b_2)^2(6a_1)^2(7a_1)^2(2b_1)^2(2b_2)^2 \quad (3)$$

It is one of the simplest triatomic molecule but the *ab initio* calculations of CO₂ potential energy curve is very scarce for the complexity of the identification of molecular states due to the lack of experimental data. The little theoretical data that can be found in the literature is much more axed on the bent molecule and the debates were more focused on determining how the molecule dissociates. M.C. Lin and S.H. Bauer [116] and M.A.A. Clyne and B.A. Thrush [117] suggested a schematic pathway dissociation for the singlet and triplet states of the molecule. They agreed on a dissociation with a production of a triplet oxygen O(³P) and O(¹D) through two mechanisms:



and



The dissociation involving the second path (5) remains the most logical way to break up the molecule by the conservation of the total spin. Nevertheless, the first path (4) is known to be the lowest dissociation limit since it involves the production of oxygen in a fundamental spectroscopic state O (³P) but it is spin forbidden . It is shown [118, 119] that the dissociation through this latter occur with a step-by-step vibrational excitation which is a non-radiative transition without any kinetic energy. The calculation of the ground and excited state potential energy surface of bent carbon dioxide by Y. Ma et al.[120] did not show any crossing point between triplet and singlet state (¹B₂) and (³B₂) as expected by Abe et al. [121]. In their study of spin-forbidden of carbon dioxide decomposition, D.Y. Hwang and A.M. Mebel [122] show a dissociation mechanism through a bent molecule for the first path and suggest an additional path consisting to product molecular oxygen at higher energy with an atomic carbon (³P). This latter is not the subject of this work and we will focus ourselves onto the two first paths. A large number of singlets and triplets excited states have been identified by [123, 124, 125] and the most of them have a bent structure with conical intersections between them. In this calculation we setting up the whole potential energy curve for a bi-molecular model (*O – CO*) assuming the freeze of one internuclear distance *R*_{*O–CO*} in a range between 1.5 and 8.0 Bohr with an average step of 0.15*a*₀ and 0.05*a*₀ near the equilibrium distance. Complete Active Space Self-Consistent Field (CASSCF) molecular orbitals averaged over 34 molecular symmetries of CO₂, as described before in section (7.1), followed by a Multireference Configuration Interaction (MRCI) calculation for the two lowest molecular states were done with Molpro using the GTO cc-pVQZ Dun-

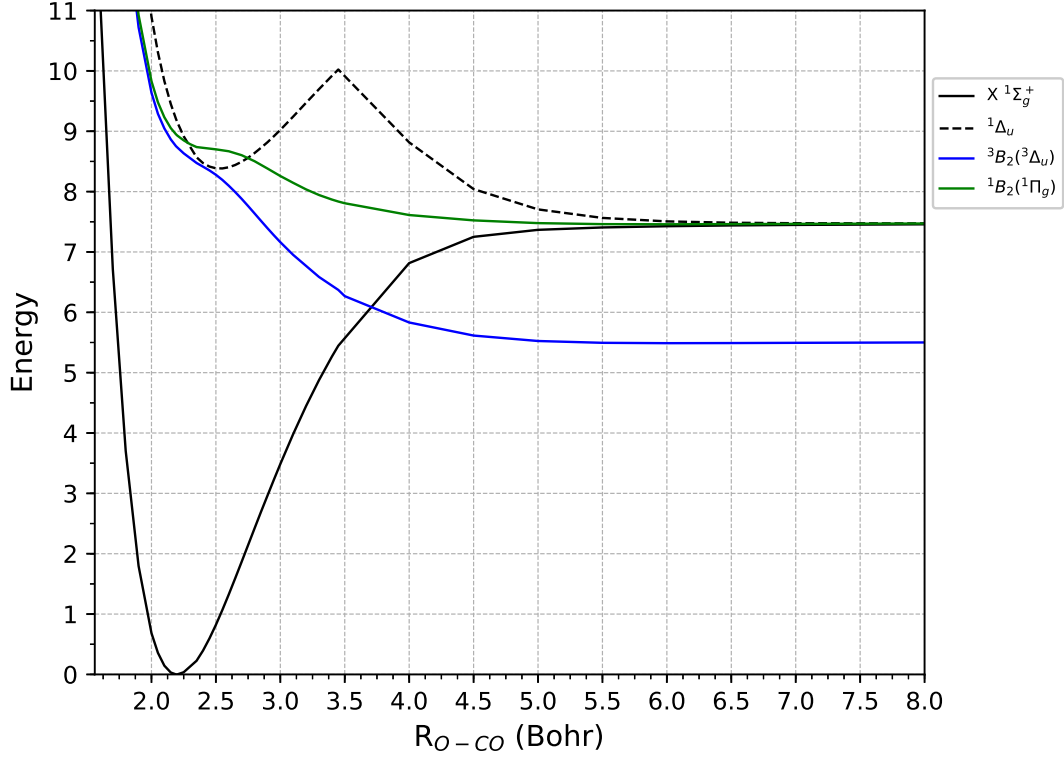


Figure 7.1: Potential energy curves of the ground electronic state of CO_2 as function of the distance between the two oxygen atoms, the CO distance being frozen to its equilibrium value. The black solid curve is the singlet ground electronic state and the dashed one is the singlet excited state. The blue curve is the degenerate excited triplet state.

ning basis set with a Complete Active Space (CAS) of 16 electrons shared between $6a_1$, $3b_1$ and $3b_2$. We can rewrite this CAS as:

$$(core)^6(6 \times a_1, 3 \times b_1, 3 \times b_2, 0 \times a_2)^{16}$$

which gives a total configuration of $(9a_1 \ 3b_1 \ 3b_2 \ 0a_2)^{22}$. Calculations are performed separately for singlets and triplet states to avoid configuration changes errors between them in the calculation. Most of the available works aimed to calculate the dissociation or excitation energy without giving more details on the behavior of the whole potential energy curve. Figure (7.1) displays our complete PEC of the carbon dioxide based on a MRCI cc-pVQZ results for the ground electronic singlet state ($1\Sigma_g^+$) and excited state ($1\Delta_u$ and $1\Pi_g$) and triplet degenerated ($3B_{1/2}$ correlate to $3\Delta_u$) states. An avoided crossing is obvious for the excited singlet state and it is quantified as a combination between a Σ (left part) and Δ (right part)

states. The nature of these states is elucidated by the calculation of the square of the total angular momentum for each molecular state in Molpro. A good agreement between our calculation and the known value of equilibrium geometry. The value of our equilibrium distance is reached at $R_{O-CO} = 2.20$ Bohr while the experiment value is 2.196 Bohr [111]. The dissociation energy of the carbon dioxide is known experimentally to be 5.4533 eV [126] for the ground electronic state. In table (7.4) we show a comparison between our calculated values of the dissociation energy, according to the lowest two asymptotic limits and for the vertical excitation energies with the available values in the literature. A good agreement between our calculation and previous works is obvious. The Spielfeld et al [125] MRCI calculation is done with the same number of electron in the active space and C_{2v} group symmetry as ours. The two calculations differ on the number of configuration and the CAS. Nevertheless the comparison of the excitation energy is done considering a $D_{\infty h}$ calculation which is the real symmetry point group in linear geometry. The calculated dissociation energy is compared to theoretical and experimental values. Considering the dissociation asymptote taken into account, a good agreement can be shown between our calculated D_e value and available D_0 values, knowing that $D_e = D_0 + zpe$, where zpe stand for *zero point energy*. The dissociation correlated to the first asymptote ($CO (X^1\Sigma_g^+) + O (^3P)$) is going through a triplet state as it can be show by the previous works and our calculation. And through the second asymptote ($CO (X^1\Sigma_g^+) + O (^1D)$), the dissociation is directed by a singlet 1A_1 state.

Asymptotes	States	T_e (eV)	D_e (eV)	Method	Taken from
$CO (X^1\Sigma_g^+) + O (^3P)$	3B_2	8.73	5.50	MRCI	This work
	3B_2	8.61	5.45 (D_0)	MRCI	[125]
	$^3A'$	-	5.42 (D_0)	G2(MP2)	[122]
	-	-	5.45 (D_0)	-	Exp. [111]
$CO (X^1\Sigma_g^+) + O (^1D)$	1A_1	-	7.46	MRCI	This work
	1A_1	-	7.41 (D_0)	MRCI	[125]
	-	-	7.63	G2(MP2)	[122]
	1A_1	-	7.53 (D_0)	CASPT2	[120]
	-	-	7.42(D_0)	-	Exp. [116]

Table 7.4: Dissociation and excitation energies for CO_2 .

The resolution of the radial Schrodinger equation by Numerov's method for the CO_2 molecule gives the 'vibrational levels' and the corresponding wave functions.

Table (7.5) gives the discrete spectrum of the 66 considering vibrational levels of CO₂. In this table, v_i is the vibration quantum number and ϵ_{v_i} the energies associated to each vibrational level of the molecule. The ground vibrational state is taken as the reference energy. The unit of energy used here is the electron-Volt (eV). Figure (7.2) shows a zoomed PEC and the wave functions for six first vibrational levels. The PEC values and vibrational levels are referenced to the ground state as on table (7.5)

$R_{eq} = 2.20 (2.196) [111] \text{ a.u.}$			
$D_e \text{ for } ^1A_1 = 7.46 (D_0 = 7.42(\text{Exp.}))\text{eV}$			
v_i	$\epsilon_{v_i}(\text{eV})$	v_i	$\epsilon_{v_i}(\text{eV})$
0	0.0000	33	5.3157
1	0.1888	34	5.4374
2	0.3793	35	5.5566
3	0.5709	36	5.6730
4	0.7600	37	5.7870
5	0.9478	38	5.8983
6	1.1339	39	6.0069
7	1.3181	40	6.1125
8	1.5002	41	6.2154
9	1.6803	42	6.3155
10	1.8583	43	6.4124
11	2.0338	44	6.5060
12	2.2071	45	6.5963
13	2.3783	46	6.6831
14	2.5473	47	6.7664
15	2.7138	48	6.8453
16	2.8779	49	6.9196
17	3.0398	50	6.9892
18	3.1992	51	7.0532
19	3.3568	52	7.1114
20	3.5119	53	7.1634
21	3.6648	54	7.2083
22	3.8153	55	7.2459
23	3.9636	56	7.2758
24	4.1095	57	7.2984
25	4.2531	58	7.3161
26	4.3944	59	7.3297
27	4.5334	60	7.3403
28	4.6697	61	7.3487
29	4.8039	62	7.3555
30	4.9353	63	7.3607
31	5.0646	64	7.3645
32	5.1914	65	7.3675

Table 7.5: Vibrational levels of the CO₂ molecule for non rotational case considering as a diatomic molecule. Dissociation energies D_e and D_0 are shown. In bracket comparison with experimental values from [126]

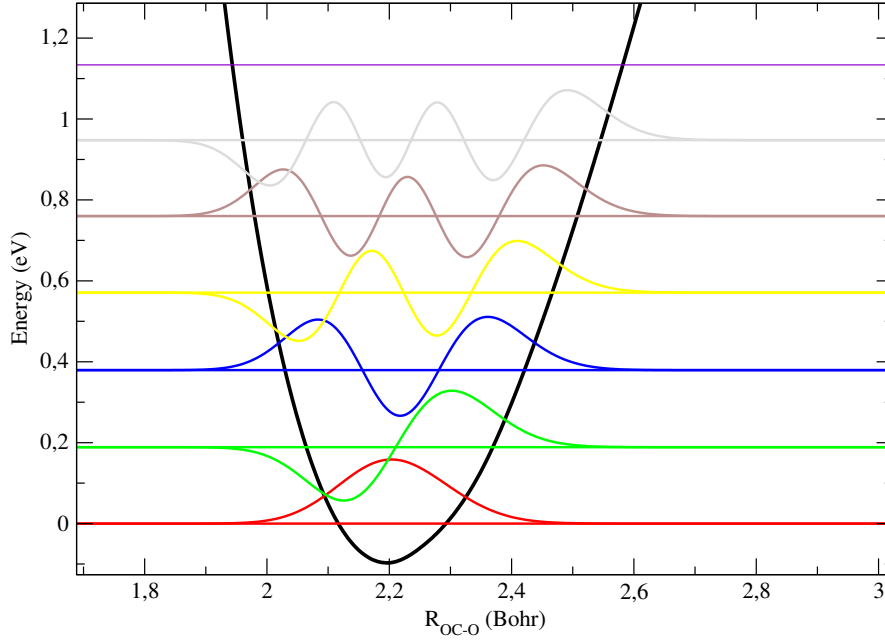


Figure 7.2: Potential energy curves of the ground electronic state of CO_2 as on figure (7.1) and different vibrational wave functions on colors.

7.2.3 Dissociative electron attachment and dissociative excitation on carbon dioxide

Dissociative electron attachment (DEA) (1) and dissociative excitation (DE) (2) of carbon dioxide occurs with an intermediate negative anion or a resonance state as bellow :



For neutral molecules, this dissociation is naturally in competition with the autodetachment which can be followed by a vibrational excitation of the target as explain in the MQDT theory (3) for molecular cations. The DEA of carbon dioxide is a subject of big interest experimentally and theoretically sixty years old. Two majors peaks at 4.4 eV and 8.2 eV have been revealed by the measurements of the O^- production in the DEA of CO_2 ([127, 128] and the O^- ion kinetic energy and CO products was debated to assign the observed broad peaks at 4.2 eV to vibrational states of carbon monoxide and structure of the intermediate state [129, 130, 131, 132, 133, 134] and very recently to vibrationally excited states of the

target molecule [135]. The difference between the oxygen affinity and the asymptotic limit of carbon dioxide provide the asymptotic limit value of the resonant state which must be at 3.988 eV. It is well known that at low energy the resonant state is a $^2\Pi_u$ shape [136, 137, 138] instead of the highest one which is a $^2\Pi_g$ Feshbach state [139, 140]. A conical intersection was suggested by Slaughter *et al* [140] and latter by Morandmand and Slaughter *et al* [141] in order to elucidate the asymptotic limits of the negative anion state. The structure of this latter is never addressed in the previous works. In this study we compute the potential energy curves and the corresponding width of the resonant state using the R-matrix theory.

7.3 R-matrix results

7.3.1 General ideas

In molecular dynamics and in the case of resonant processes as presented previously with MQDT treatment, a number of molecular data are required using *ab initio* calculations such as potential energy curves and autoionization widths from which we can extract the electronic couplings between target and temporary electron capture channels. The R-matrix method is actually one of the powerful theory used in molecular dynamic to provide low energy electron-molecule data for astrophysical and plasma studies. For more details and a complete comprehension about this method, the reader can have more than enough and exhaustive information in the Burke's book [4] for both electron-atom and electron-molecule scattering and in the Tennyson's paper [3] for electron-molecule scattering. in this chapter I show you my brief comprehension in this method.

The main idea of the R-matrix theory is the partition of the coordinate space into an inner and outer regions separated by a spherical boundary of radius a centered at the center-of-mass of the molecule as shown in figure (7.3). For a given molecular system, the inner region is characterized by the target N number of electrons plus the scattering electrons. In this region, the scattering electron and the target electrons are indistinguishable so all electrons are physically identical and the wave function of this region must be anti-symmetric in order to obey to the Pauli principle and then the correlation and exchange are taken into account as for any quantum chemistry calculations. Beyond the spherical radius a in the outer region the incoming electron is distinguishable to those of the target and moves in a long-range interaction with the target. The R-matrix is then the link between the inner region and the outer region at the boundary distances where

the solution of the inner region is derived to the outer region to propagate the short-range interactions to this zone.

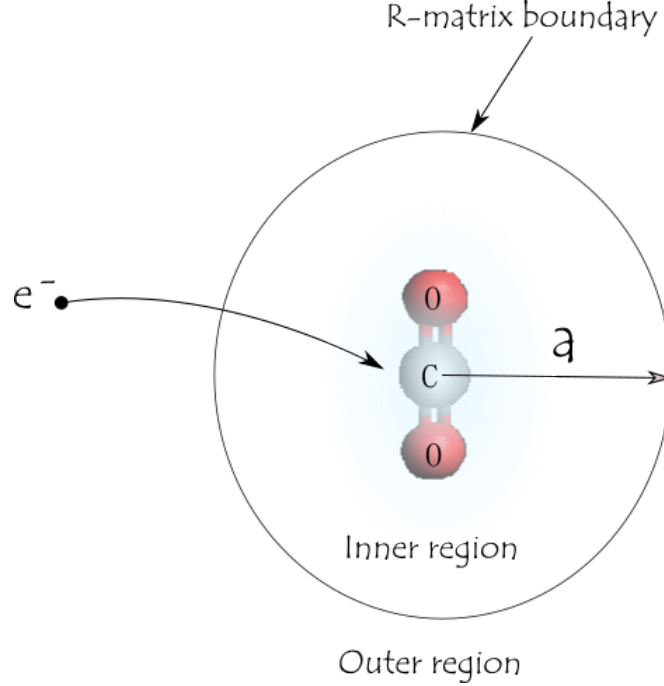


Figure 7.3: Partition of configuration space in fixed-nuclei R-matrix theory for CO_2 molecule. Space is divided into an inner and an outer regions

In the inner region, the R-matrix theory start the problem resolution with a Schrodinger equation taken into account both the target and the scattering electrons where the hermeticity of the Hamiltonian, removed by the introducing spatial restriction at the boundary, is reestablished by a Bloch operator [142] which is added to the first Hamiltonian and form a global hermitic Hamiltonian and result to the canceling of the spatial terms. The inner region total wave function can be written using a close-coupling terms as:

$$\begin{aligned} \Psi_k^{N+1}(q_1 \dots q_{N+1}, R) = & \mathcal{A} \sum_{i,j} a_{i,j,k} \phi_i(q_1 \dots q_{N+1}) u_{i,j}(q_{N+1}) \\ & + \sum_i b_{i,k} \chi_i(q_1 \dots q_{N+1}) \end{aligned} \quad (8)$$

where $q_1 \dots q_{N+1}$ is a set of electronic coordinates for $N + 1$ electrons. \mathcal{A} is an antisymmetrization operator. $u_{i,j}(x_{N+1})$ denotes the extra continuum orbitals used to describe the j^{th} scattering electron with a partial wave up to the maximum value of $l(l_{max} = 4$ in our case), they are only the non zero contribution from the

inner region wave function in the outer region. ϕ_i are wavefunctions for a true or pseudostates of the target molecule. χ_i are known as L^2 - *configurations* and are square integrable functions, constructed from the target occupied and virtual molecular orbitals and they are used to allow the relaxation of the orthogonalization between continuum and target orbitals and also to model the effect of target polarization. The orthogonalization of the total inner region Hamiltonian allow to found the $a_{i,j,k}$ and $b_{i,k}$ expansion coefficients. The target parameters and inner region wave function (8) are used with the associated eigenvalues to built the R-matrix at the boundary in the form of equation (13) of Tennyson [3].

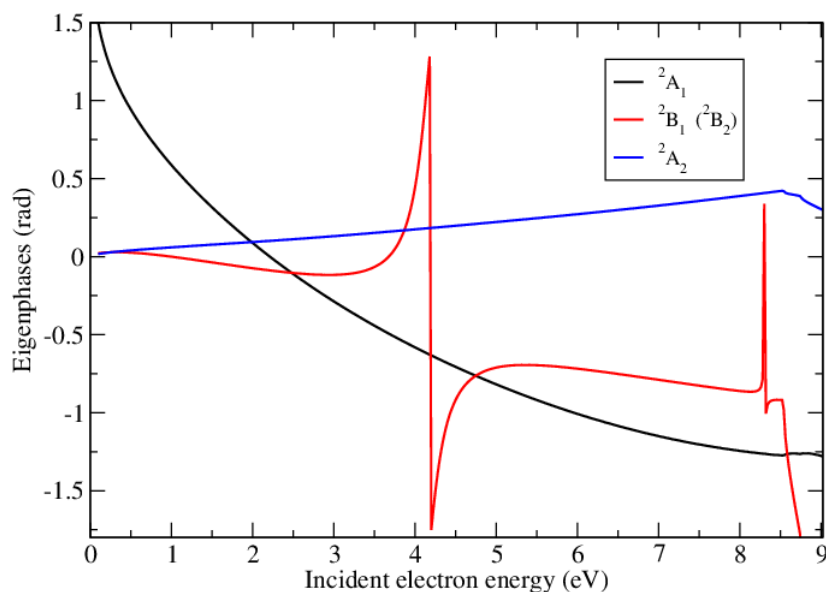
In the outer region, the problem is much more easier than the inner region since the exchange and correlation are neglected. Hence, in this region, electron molecule scattering problem can be solved as an electron-atom problem in term of equations [3, 61, 4]. we must know that there are some differences for molecules since molecular space configurations or symmetries are not the same as those of atoms which make the molecular problem computationally more heavy. The scattered electron behavior can be described by some radial functions which are solution of a set of coupled differential equations used to propagate the R-matrix from boundary to outer region. These radial wave functions have to be matched to asymptotic solutions of known form in order to obtain the K-matrices. This latter is a symmetric matrix and it can be used to extract all the scattering observables such as the scattering matrix \mathcal{S} using the expression:

$$\mathcal{S} = \frac{1 + i\mathcal{K}}{1 - i\mathcal{K}} \quad (9)$$

Also we can calculate the eigenphase sum:

$$\delta(E) = \sum_i \tan^{-1} K_{ii}^D(E) \quad (10)$$

where $K_{ii}^D(E)$ are the diagonal elements of the K-matrices. Within the eigenphase sum we can have information about resonance position which appear as a rapid increasing in π as shown in Figure (7.4)

Figure 7.4: Eigenphase sum for electron-CO₂ scattering

Resonances are very important in reactive processes and it is very crucial to obtain informations for resonance position affected to a symmetry and the corresponding half-width auto-ionization. In our processes we can distinguish two different type of resonances: A *shape resonance* where an electron is trapped behind a centrifugal barrier in the electron-molecule potential; and this barrier is centrifugal which depend on l , which mean that s-wave scattering cannot lead to a shape resonances. From a chemical view, a shape resonance is the occupation of the scattering electron to the lowest unoccupied molecular orbital. In a function of energy, a shape resonances are in generally short lived and usually appear as broad features [3, 39]. and a *Feshbach resonance* which can be explained as the trapping of the scattering electron and the excitation of the target molecules leading to a double excitation simultaneously. The incoming electron is temporarily captured into an unoccupied virtual orbital and the target molecule is excited into a configuration a parent state which is different to the ground electronic state of the molecule. This kind of state decays to the parent state at the end of the resonance's lifetime. Feshbach resonances are prevalent in ionic targets and generally take the form of Rydberg states, there are however also valence states embedded in the continuum which appear as Feshbach resonances.

7.3.2 Calculations

In our R-matrix calculation we started by chose a target model based on a close coupling wave function with a MCSCF method as shown before on section

(7.2) but by lack of time and for numeric complications, the summary of the target states in our CC model on equation (8) is consist on 5 electronic states based on the ground electronic state (1A_1) with excited double degenerated triplet (3B_1 and 3B_2) and singlet (1B_1 and 1B_2) in a C_{2v} symmetry. A cc-pVDZ and cc-pVQZ basis set of Dunning [13] was tested in the beginning and finally the calculation was performed using a cc-pVQZ for the accuracy of the results. A resonance positions of 4.81 eV and 9.72 eV was found for cc-pVDZ basis set against 4.16 eV and 8.29 eV for cc-pVQZ at equilibrium geometry. The scattering calculation was performed for different geometries with the Born-Oppenheimer approximation. Several target models was tested and the model denoted $(6a_1)^{12} (7-8a_1, 1-3b_1, 1-3b_2, 1a_2)^{11}$ was selected; $6a_1$ orbitals was frozen and the Complete Active Space of $(7-8a_1, 1-3b_1, 1-3b_2, 1a_2)^{10} + (9a_1-15a_1, 4b_1-7b_1, 4b_2-7b_2, 1a_2)^1$ where the last set of orbitals are virtuals, was then defined.

Another scattering model based on static exchange plus polarization (SEP) approximation where only Hartree-Fock target wave functions are taken into account with the advantages to better describe Feshbach and shape resonances at low energy by moving one electron from the target into a virtual orbital and which will be added to the scattering electron into a virtual orbital giving two particles. A CAS of $((1-7a_1, 1-2b_1, 1-2b_2, 0a_2)^{21} + (8-14a_1, 3-7b_1, 3-7b_2, 1a_2))^2$, where the second set of orbitals are virtual, and a cc-pVQZ are used in this model. For the CC and SEP model the R-matrix was propagated to $100.1 a_0$ to obtain stable results. To detect resonances and fit them to a Breit-Wigner profile in order to obtain energies and the corresponding width, the program OUTER and RESON [66] in the R-matrix code was used.

The resonance energy is a complex quantity which can be expressed as:

$$E = E^r - i\frac{\Gamma}{2} \quad (11)$$

where E^r is the resonance position and Γ the autoionization width.

The resonance positions are calculated and presented in Figure (7.5) according to the target ground electronic state for close coupling and static exchange plus polarization. the resonant curves are calculated by adding the resonance positions calculated with the R-matrix to the target eigenvalues calculated by MCSCF method in Molpro.

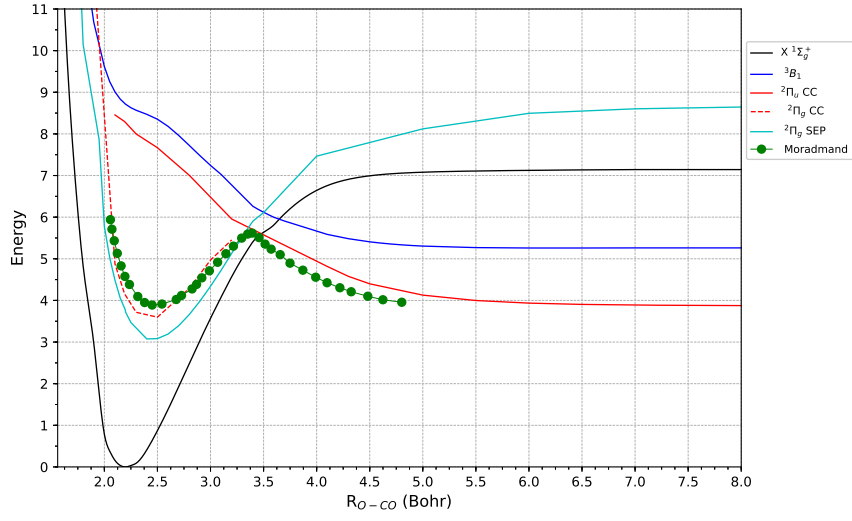


Figure 7.5: Potential energy curves of the ground electronic state of CO_2 as function of distance between the two oxygen atoms, the CO distance being frozen to its equilibrium value. The black solid curve is the singlet ground electronic state and the blue one is the triplet excited state. The red curves are Close Coupling (CC) results and the cyan curve the static exchange plus polarization (SEP) results. The circle marked curve are the results from Moradmand *et al*

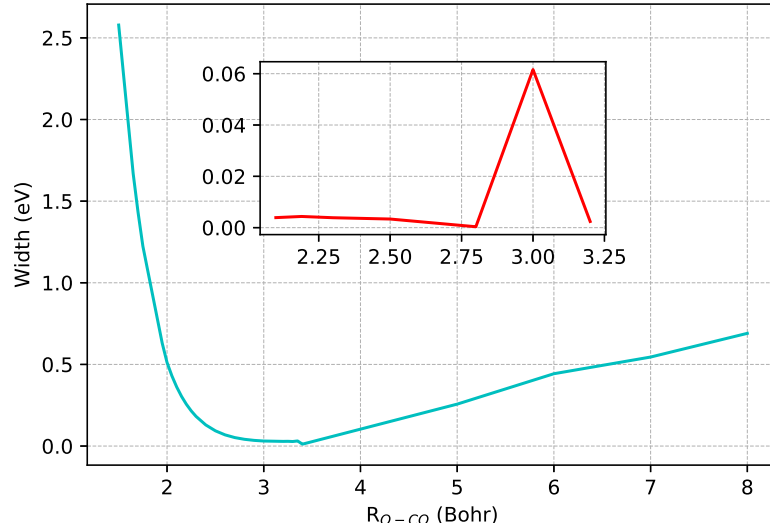


Figure 7.6: Width for CO_2^- as function of the inter-nuclear distance. The dashed curve is the SEP result according to Figure 7.5 and the solid curve, the CC result

On Figure (7.5) we investigate the PEC of the CO_2^- resonant state using R-matrix method [143] and Molpro [114]. We have studied the PEC of CO_2^- resonant state as a function of the asymmetric stretching of one C-O bond and by freezing the

other one in linear geometry. The R-matrix theory is used with CC method from 1.9 to $3.5 a_0$ and the result are completed by a Molpro calculation up to dissociation limit of the anion state. The SEP method is also used to calculate the PEC of the anion state and the calculation is performed from 1.5 to $8.0 a_0$ without Molpro. The target orbitals was obtained using Molpro both for the two R-matrix models. For a long time, it well known that a $^2\Pi_u$ shape resonance [136, 137, 144, 145] govern the low energy electron scattering. A conical intersection between a $^2\Pi_u$ shape resonance and a $^2\Pi_g$ Feshbach resonance was demonstrated in the first time by Slaughter *et al* [140] in their study of dissociative electron attachment to carbon dioxide via a 8.2 eV Feshbach resonance and confirmed by the same team few years after their first study [141]. The behavior of hole resonant state PEC was never addressed before. Our CC results show two resonance positions before the conical intersection point and become numerically unstable beyond this point. A good agreement between our low energy CC result and Moradmand *et al* results. In order to and give a comprehensive resolution of the conical intersection, we combine our SEP low energy results and the high energy CC result. This is why on Figure (7.6), we show only the SEP width and CC result at high energy. The width of this later is very negligible compared to those of SEP method. For DEA calculation, one can expect two principal peaks as discussed before and our equilibrium geometry results (see eigenphase sum on Figure (7.4)) are in good agreement with experimental value for DEA measurement on CO_2 ([127, 128]).

7.4 Conclusion

In this chapter, we compute for the first time the potential energy curves of the carbon dioxide molecule taking into account its ground state as well as the excited states using quantum chemical methods with the Molpro program. With the chosen model, which is close to the asymmetric stretching motion of the molecule and which consists in an assimilation of a diatomic molecule, we determined for the first time the vibrational levels of the molecule. The resonant potential energy curves of CO_2^- were calculated using the R-matrix method. The obtained results are in good agreement with the previous results in terms of resonance position and allowed to confirm the conical intersection that has been demonstrated before on references [140, 141] and also provide the most complete structure of the potential energy curves of the resonant states.

Electron scattering on formylium molecule (HCO^+)

8.1 Introduction

The HCO^+ molecular ion is one of the most abundant species in the ISM and have been the object of a number of detection studies [146, 147, 148, 149, 150, 151]. It is also abundant in the Universe and it is an important constituent of the upper ionosphere of Mars [152]. The DR is known to be the most important molecular cations destruction mechanism. This is the reason why the low energy HCO^+ DR is in the focus of studies for long time both theoretically and experimentally. A major production of carbon monoxide is revealed by the heavy-ion storage ring CRYRING experiment of Geppert *et al* [153] for HCO^+ DR. The DR rate coefficient for this cation was also measured using flowing afterglow [154, 155] and merged-beam [156] experiments and it was found a large DR rate coefficient at low energy. Theoretically, there are a plethora of studies devoted to this ion. The difficulty in studying poly-atomic molecular system compared to the diatomic cations arise from the presence of a multitude of degrees of freedom based on vibrational and rotational motions which have to be taken into account in the calculation. The first pioneering study on the DR of the HCO^+ system was addressed in 2005 by Larson *et al* [157]. They have given an initial comparison with experimental results and open a multitude of questions that where answered are provided in the following studies [158, 159, 160, 161, 162, 163]. Mikailov *et al.* [158] and Jungen and Pratt [159] used a theoretical approach based on reaction matrix K including a non-Born-Oppenheimer Renner-Teller couplings between the doubly-degenerate vibrational modes of the molecule and the degenerate continuum states of the incident electron

and their results was underestimated with a factor lower than two with the merged-beam [156] experimental cross section. The most probable explanation for this was the frozen of CO vibrational modes and the non inclusion of the permanent dipole moment of the molecule. Douguet, Viatcheslav and Greene have added the CO vibrational motion in their first paper [160] and they found a good agreement with Mikhailov *et al* [158] at low energy and a better agreement with the experiments at high energy. In a second study [161] they have included the permanent dipole moment of the molecule and they found an enhancement in the calculated DR cross section, but the discrepancy of about a factor 2 with the experimental cross sections was still persisting. Moreover Larson *et al* [162] have demonstrated that the contribution of a direct mechanism to DR has to be counted only at high energy, above 0.1 eV, since only above this energy one can find a Feshbach resonant state that can derive the direct process. In 2014 dos Santos *et al* [163] has completed these studies with calculations addressing only the indirect mechanism. Their theory consists in the computation of the scattering matrix S in a restricted Renner-Teller coupling scheme by taking into account several types of vibronic couplings through all vibrational modes of the target molecular cation. The S matrix was calculated above the ionization threshold and enables an explicit determination of all diabatic electronic couplings responsible for dissociative recombination. The theoretical framework used in our calculations is based on those presented in dos Santos *et al* [163] and Kokoouline *et al.* [164]. More details can be found in Reference [159] and its major ideas will be presented bellow. The major differences between our calculations and those of dos Santos *et al* [163] are in the computation of the S matrix which is calculated by the R-Matrix method [3, 61, 66] in our calculation and Kohn variational method [165, 166] in dos Santos calculations.

8.2 General ideas on theoretical approach

The present theoretical approach relies on Refs [163] and [164]. In order to calculate cross sections for electron induced processes, a number of approximations has to be taken into account. The rotational energies are negligible comparing to the vibrational ones and resonances caused by a rotational excitation of the molecule in a cross section experiment are taken as an average. The obtained cross sections should be viewed as averaged over initial rotational states and summed over final rotational states of corresponding vibrational levels. Consequently the rotational motion of the molecule is neglected in the theory. Resonances are not resolved individually. The cross section is averaged over the vibrational autoioniz-

ing resonances. The capture of the electron into a Rydberg resonant state allows the conversion of the electron energy to vibrational motion, thus the autoionization lifetime is assumed to be longer than the predissociation lifetime. The cross-section is averaged over the vibrational autoionizing resonances. It is justified because the experimental resolution (storage-ring or merged-beam experiments) is too low to resolve individual Rydberg resonances in the DR spectra. Hence the cross section is obtained using these approximations with the application of an analytical frame transformation. Cross sections obtained at low-energy such as the harmonic approximation is still valid. So the description of the target vibration is done with the harmonic approximation.

8.3 Target properties

The HCO^+ molecular cation is a linear molecule and its ground electronic configuration reads as :

$$X^1\Sigma : (1a_1)^2(2a_1)^2(3a_1)^2(4a_1)^2(5a_1)^2(1b_1)^2(1b_2)^2 \quad (1)$$

It is a closed shell molecule and it has a C_{2v} point group symmetry. It is characterized by $3N - 5 = 4$ vibrational modes, where N is the number of atom. These vibrational modes consist of symmetric stretching(ω_1), the doubly degenerate bending(ω_2) and the asymmetric stretching(ω_3). Figure (8.1) shows these modes. It has to be mentioned that, upon the bending mode, the symmetry of the molecule is broken into a C_s point group.

A first description of the target was done using a multi-reference-configuration-interaction (MRCI) theory in the the Molpro quantum chemical programs (version 2019.2) [114]. The calculation was completed within a wider set of test calculations where different basis sets and theoretical methods were used. Table (8.1) shows our results in comparison with other theoretical and experimental data. 14 electrons of the molecule are distributed in 11 molecular orbitals where 3 cores orbitals were frozen. Our calculated permanent dipole moments are in good agreement with the experimental value of Ref. [167] and the calculated normal modes are also in good agreement with experimental and calculations values as shown in table (8.1) for *cc*-pVTZ basis set. The results for normal modes calculation using a *cc*-pVDZ basis set are not in good agreement with the previous results in table (8.1). Nevertheless the permanent dipole moment value is close to experimental value compare to the one calculated using a *cc*-pVQZ basis set.

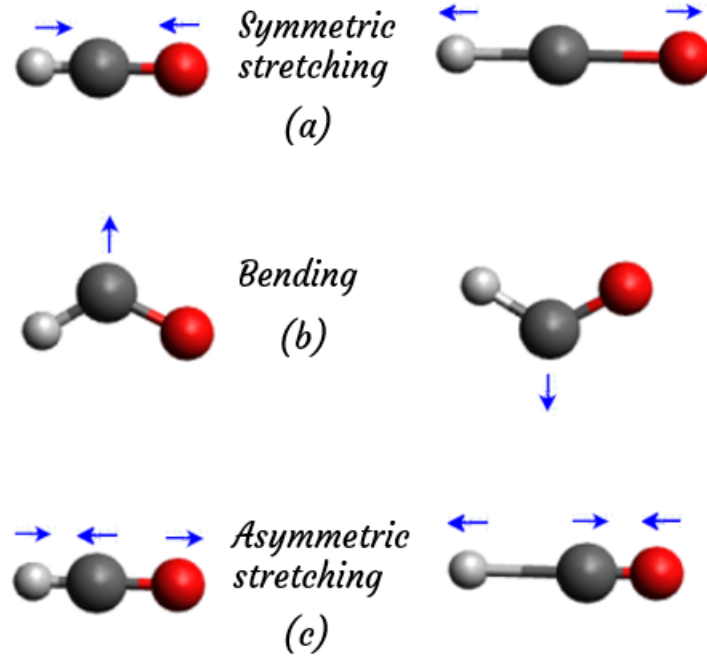


Figure 8.1: Representation of the normal modes of HCO⁺ molecule: Symmetric stretching (a), bending (b) and asymmetric stretching (c). The carbon atom is represented by the black ball, the oxygen by the red ball and the hydrogen by the gray one

ω_1	ω_2	ω_3	μ_e	Method	Taken from
3244	810	2180	3.904	MRCI(<i>cc</i> -pVDZ)	This work
3273	831	2194	3.910	MRCI(<i>cc</i> -pVTZ)	This work
3225	841	2207	3.873	MRCI(<i>cc</i> -pVQZ)	This work
3229	790	2186	...	CEPA	Ref. [163]
3224	863	2212	3.843	CAS-CI	Ref. [163]
3231	845	2215	...	CCSD(T)	Ref. [168]
3224	840	2203	3.888	CCSD(T)	Ref. [169]
...	830	2184	...	Exp.	Ref. [170]
...	3.922	Exp.	Ref. [167]

Table 8.1: Characteristics of the target HCO⁺ from this work compared to those of Tab. 1 of Douguet *et al.* [163]. μ_e is the permanent dipole moment in debye and frequencies are in cm⁻¹

Based on these results, the target energies and geometries are calculated using Molpro and results are showed on table (8.2) for *cc*-pVTZ, *cc*-pVTZ and *cc*-pVQZ basis sets and for different methods. A decreasing of the energy can be seen for the

different method. The calculation starts with the HF method where the molecular orbitals obtained are used to make the CASSCF calculation and the optimization of the MRCI energy is done with molecular orbitals from the CASSCF calculation. The energy optimization is increasing for a big basis set.

Basis	theory	energy (Hartree)	R_{HC} (Å)	R_{CO} (Å)
<i>cc</i> -pVDZ	HF	-112.97984042	1.09405954	1.08320998
	CASSCF	-113.14240827	1.11044919	1.11884714
	MRCI	-113.29025252	1.10729667	1.12199739
<i>cc</i> -pVTZ	HF	-113.01282901	1.08527559	1.07832924
	CASSCF	-113.17917369	1.08265784	1.11027099
	MRCI	-113.38102270	1.08902108	1.11431414
<i>cc</i> -pVQZ	HF	-113.02159952	1.08553544	1.07623707
	CASSCF	-113.18328773	1.10110143	1.11130248
	MRCI	-113.412208080	1.09294535	1.10902872

Table 8.2: characteristics of the linear target HCO^+ : ground state energy and optimized equilibrium geometry for *cc*-pVTZ and *cc*-pVQZ basis sets and for different theoretical models

The scattering calculation was done using the R-Matrix method implemented in UKRMol [3, 61, 66] accessed via Quantemol-N interface [171]. Unfortunately only Hartree-Fock and CASSCF orbitals are available in R-matrix calculation and a close coupling calculation with CASSCF method can be difficult to setting. The multitude of quantum chemistry methods available in Molpro can not be taken into account in the UKRMol codes which means that a balance is needed between the CAS and the basis set. In our R-matrix calculation, it would better to use Molpro molecular orbitals leading to a better characterization of the target. Despite the fact that both software, Molpro and QuantemolN, were installed in the same machine, the molecular orbitals calculated by Molpro could not be taken into account in the diffusion calculation. Many exchanges were initiated with the technical service of Quantemol to solve this problem and solution was to upgrade to the newest version of Quantemol. This most recent version, Quantemol Electron Collision(QEC) [172], has been downloaded and installed. In this new version, we had the possibility to include the orbitals calculated by Molpro in the calculation but we were faced with a limitation on the basis set and on CAS. With this present QEC version, we can not make a calculation with the needed basis set and CAS.

Hence we were forced to do electron scattering calculations using QN with HF orbitals, instead of the MCSCF ones.

Another version of QEC is recently available with the possibility to compute the vibrational excitation using the theoretical model described in this thesis and in refs. [164, 173, 174]

In a first step we have calculated the potential energy curve of the ground electronic state as the function of the normal coordinates using both Molpro and Quantemol-N. On Figure (8.2), we plot the calculated potential energy curve for bending, symmetric stretching and asymmetric stretching normal modes.

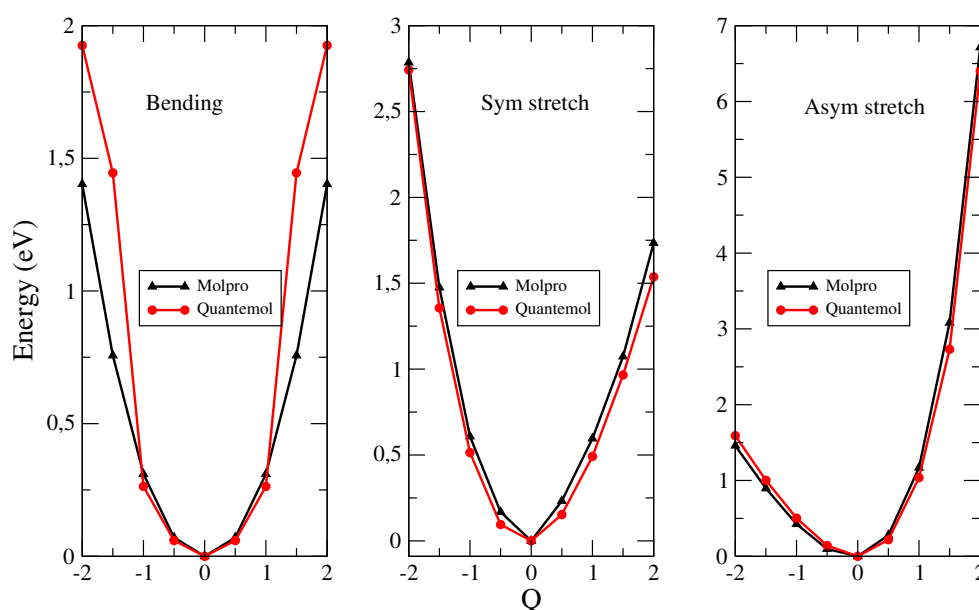


Figure 8.2: Potential energy curves of the ground electronic state of HCO⁺ as function of the dimensionless geometry (Q) for bending (left panel), symmetric stretching (middle) and asymmetric stretching (right panel) modes. Red curves are results from Quantemol-N and black curves from Molpro.

Good agreement can be seen for the symmetric and asymmetric stretching modes for Molpro and Quantemol-N calculations. However for bending mode the agreement is not so good for higher collision energies and/or larger Q values (around ± 1). Despite this disagreement, harmonic curves can be seen for all normal modes. For a good description of the scattering process, the behavior of the eigenphase sum calculated from the reactance K-matrix (10) are obtained for different geometries and their values obtained for 0.1 eV collision energy are plotted on Figure (8.3). The bending mode calculation is done in the C_s point group and for the symmetric and asymmetric modes the C_{2v} point group is used. The variation of eigenphases is linear for these latter, which means that a transition with a quanta will be needed

in the frame transformation and the tendency of the bending mode is slightly curvilinear for different geometries, in this cases, a transition with two quanta will be needed instead of single quanta. In consequence the Taylor expansion of the S-matrix will be used up to second order in the calculation of the cross section. The calculation of this latter consist to take into account the nuclear motion. However in the R-matrix calculation and from the perspective of the incident electron, the Born-Oppenheimer approximation is considered. Thus the approximation is not valid when the speed of the incident electron is in the same order of magnitude with the nuclear motion. This is the case when the distance between the target and incident electron increases causing a deceleration of the electron due to the target attenuation. A vibrational transformation is taken into account to involve the nuclear motion.

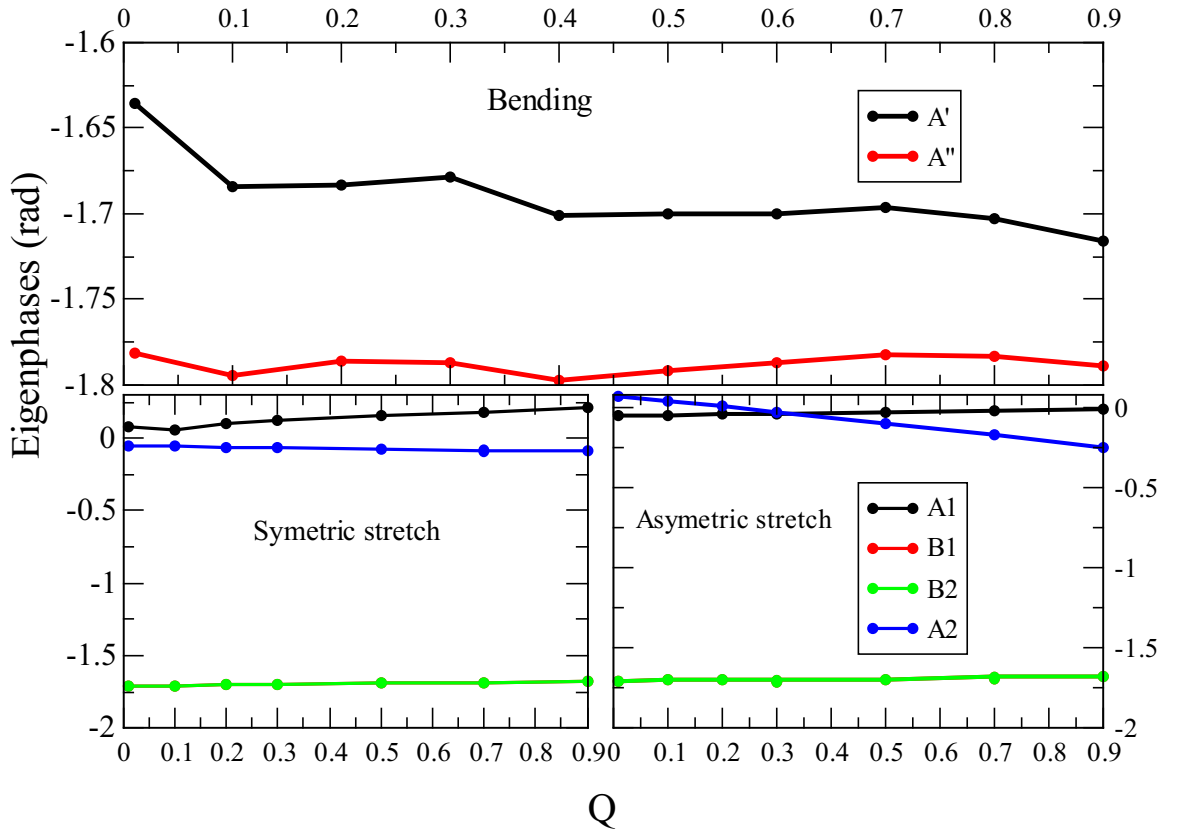


Figure 8.3: Eigenphases as a function of the dimensionless geometry (Q) for electron-scattering energy $E_{el} = 0.1$ eV for the symmetric stretching (left bottom panel), bending (upper panel), and asymmetric stretching (right bottom panel) modes. The curves of different colors correspond to different symmetries

8.4 Probabilities and cross section

Lets define the Ladder operators or raising or lowering operator as increaser or decreaser of the eigenvalue of another operator. These anihilation (lowering) and creation (raising) operators for the quantum harmonic oscillator have the following forms[175]:

$$\hat{a} = \sqrt{\frac{m\omega}{2\hbar}} \left(x + \frac{i}{m\omega} p \right) \quad (2)$$

$$\hat{a}^\dagger = \sqrt{\frac{m\omega}{2\hbar}} \left(x - \frac{i}{m\omega} p \right) \quad (3)$$

The addition of (2) and (3) allow us to write:

$$x\sqrt{\frac{m\omega}{\hbar}} = \frac{1}{\sqrt{2}} (\hat{a}^\dagger + \hat{a}) \quad (4)$$

by letting $q = x\sqrt{\frac{m\omega}{\hbar}}$, we get :

$$q = \frac{1}{\sqrt{2}} (\hat{a}^\dagger + \hat{a}) \quad (5)$$

In the following, the displacement x will be called q . For a given $|v\rangle$ state, the annihilation and creation operators acts as :

$$\hat{a}|v\rangle = \sqrt{v}|v-1\rangle \quad (6)$$

and

$$\hat{a}^\dagger|v\rangle = \sqrt{v+1}|v+1\rangle \quad (7)$$

The vibrational frame transformation consists in evaluating the matrix elements

$$\langle v|S_{l\lambda,l'\lambda'}(\mathbf{q}_i)|\mathbf{v}'\rangle \quad (8)$$

where $S_{l\lambda,l'\lambda'}$ is an element of the scattering matrix obtained from the R-matrix with an initial channel $l\lambda$ and a final channel $l'\lambda'$. Here l is the angular momentum of the electron and λ its projection on the molecular axis. The Taylor expansion

of the S-matrix elements around the equilibrium geometry ($q_i = 0$) reads as :

$$S_{l\lambda,l'\lambda'}(\mathbf{q}) = S_{l\lambda,l'\lambda'}(q)_{\mathbf{q}_0=0,\dots} + \sum_i \left(\frac{\partial S_{l\lambda,l'\lambda'}(q_i)}{\partial q_i} \right)_{q_i=0} q_i + \frac{1}{2} \sum_i \left(\frac{\partial^2 S_{l\lambda,l'\lambda'}(q_i)}{\partial q_i^2} \right)_{q_i=0} q_i^2 + \dots \quad (9)$$

By putting equation (9) into equation (8), we can write:

$$\langle v | S_{l\lambda,l'\lambda'}(q)_{\mathbf{q}_0=0,\dots} | v'_i \rangle + \langle v_i | \sum_i \left(\frac{\partial S_{l\lambda,l'\lambda'}(q_i)}{\partial q_i} \right)_{q_i=0} q_i | v'_i \rangle + \langle v_i | \sum_i \frac{1}{2} \left(\frac{\partial^2 S_{l\lambda,l'\lambda'}(q_i)}{\partial q_i^2} \right)_{q_i=0} q_i^2 | v'_i \rangle \quad (10)$$

which is equivalent to:

$$S_{l\lambda,l'\lambda'}(0) \langle v | v' \rangle + \left(\sum_i \frac{\partial S_{l\lambda,l'\lambda'}(q_i)}{\partial q_i} \right)_{q_i=0} \langle v_i | q_i | v'_i \rangle + \frac{1}{2} \left(\sum_i \frac{\partial^2 S_{l\lambda,l'\lambda'}(q_i)}{\partial q_i^2} \right)_{q_i=0} \langle v_i | q_i^2 | v'_i \rangle \quad (11)$$

Lets evaluate term by term the equation (11) using equations (6) and (7).

$$S_{l\lambda,l'\lambda'}(0) \langle v | v' \rangle = S_{l\lambda,l'\lambda'}(0) \delta_{v,v'} \quad (12)$$

$$\begin{aligned} \left(\sum_i \frac{\partial S_{l\lambda,l'\lambda'}(q_i)}{\partial q_i} \right)_{q_i=0} \langle v_i | q_i | v'_i \rangle &= \frac{1}{\sqrt{2}} \left(\sum_i \frac{\partial S_{l\lambda,l'\lambda'}(q_i)}{\partial q_i} \right)_{q_i=0} \langle v_i | (a^\dagger + a) | v'_i \rangle \\ &= \frac{1}{\sqrt{2}} \left(\sum_i \frac{\partial S_{l\lambda,l'\lambda'}(q_i)}{\partial q_i} \right)_{q_i=0} \langle v_i | (a^\dagger | v' \rangle + a | v'_i \rangle) \\ &= \frac{1}{\sqrt{2}} \left(\sum_i \frac{\partial S_{l\lambda,l'\lambda'}(q_i)}{\partial q_i} \right)_{q_i=0} \langle v | \left(\sqrt{v'_i + 1} | v'_i + 1 \rangle + \sqrt{v'_i} | v'_i - 1 \rangle \right) \\ &= \frac{1}{\sqrt{2}} \left(\sum_i \frac{\partial S_{l\lambda,l'\lambda'}(q_i)}{\partial q_i} \right)_{q_i=0} \left(\sqrt{v + 1} \delta_{v_i, v'_i + 1} + \sqrt{v'_i} \delta_{v_i, v'_i - 1} \right) \end{aligned} \quad (13)$$

$$\begin{aligned}
\frac{1}{2} \sum_i \frac{\partial^2 S_{l\lambda, l'\lambda'}(q_i)}{\partial q_i^2} \langle v_i | q_i^2 | v'_i \rangle &= \frac{1}{2} \left(\sum_i \frac{\partial^2 S_{l\lambda, l'\lambda'}(q_i)}{\partial q_i^2} \right)_{q_i=0} \langle v_i | \left(\frac{a^\dagger + a}{\sqrt{2}} \right)^2 | v'_i \rangle \\
&= \frac{1}{4} \left(\sum_i \frac{\partial^2 S_{l\lambda, l'\lambda'}(q_i)}{\partial q_i^2} \right)_{q_i=0} \langle v_i | (a^{\dagger 2} + a^2 + a^\dagger a + a a^\dagger) | v'_i \rangle \\
&= \frac{1}{4} \left(\sum_i \frac{\partial^2 S_{l\lambda, l'\lambda'}(q_i)}{\partial q_i^2} \right)_{q_i=0} \langle v_i | (a^{\dagger 2} | v'_i \rangle + a^2 | v'_i \rangle + a^\dagger a | v'_i \rangle + a a^\dagger | v'_i \rangle) \\
&= \frac{1}{4} \left(\sum_i \frac{\partial^2 S_{l\lambda, l'\lambda'}(q_i)}{\partial q_i^2} \right)_{q_i=0} \left(\sqrt{(v'_i + 1)(v'_i + 2)} \delta_{v_i, v'_i+2} + \sqrt{v'_i(v'_i - 1)} \delta_{v_i, v'_i-2} \right) \\
&+ \frac{1}{4} \left(\sum_i \frac{\partial^2 S_{l\lambda, l'\lambda'}(q_i)}{\partial q_i^2} \right)_{q_i=0} (v'_i \delta_{v_i, v'_i} + (v'_i + 1) \delta_{v_i, v'_i}) \quad (14)
\end{aligned}$$

By considering the ion in its vibrational ground state and an excitation with one vibrational quanta, the electron can be captured only in the first vibrational excited state of each mode. Hence for $v = v' + 1$, equations (12) and (14) cancels out and equation (10) can be written as:

$$\left(\sum_i \frac{\partial S_{l\lambda, l'\lambda'}(q_i)}{\partial q_i} \right)_{q_i=0} \langle v_i | q_i | v'_i \rangle = \frac{\sqrt{v_i + 1}}{\sqrt{2}} \left(\sum_i \frac{\partial S_{l\lambda, l'\lambda'}(q_i)}{\partial q_i} \right)_{q_i=0} \quad (15)$$

for vibrational excitation (VE) and:

$$\left(\sum_i \frac{\partial S_{l\lambda, l'\lambda'}(q_i)}{\partial q_i} \right)_{q_i=0} \langle v_i | q_i | v'_i \rangle = \frac{\sqrt{v_i}}{\sqrt{2}} \left(\sum_i \frac{\partial S_{l\lambda, l'\lambda'}(q_i)}{\partial q_i} \right)_{q_i=0} \times 1 \quad (16)$$

for vibrational de-excitation (VDE). In the case of an excitation with two quanta in the second order, equations (12) and (13) canceled out and equation (10) becomes :

$$\frac{1}{2} \sum_i \frac{\partial^2 S_{l\lambda, l'\lambda'}(q_i)}{\partial q_i^2} \langle v_i | q_i^2 | v'_i \rangle = \frac{\sqrt{(v'_i + 1)(v'_i + 2)}}{4} \left(\sum_i \frac{\partial^2 S_{l\lambda, l'\lambda'}(q_i)}{\partial q_i^2} \right)_{q_i=0} \times 1 \quad (17)$$

for the excitation and

$$\frac{1}{2} \sum_i \frac{\partial^2 S_{l\lambda, l'\lambda'}(q_i)}{\partial q_i^2} \langle v_i | q_i^2 | v'_i \rangle = \frac{\sqrt{v'_i(v'_i - 1)}}{4} \left(\sum_i \frac{\partial^2 S_{l\lambda, l'\lambda'}(q_i)}{\partial q_i^2} \right)_{q_i=0} \times 1 \quad (18)$$

for the de-excitation.

For a given incident electron energy (E_{el}), the dissociative recombination (DR) cross section in the first order, is defined as :

$$\sigma^{DR}(E_{el}) = \frac{\pi}{k^2} P_i \quad (19)$$

where k is the wavevector corresponding to $E_{el} = \frac{\hbar^2 k^2}{2\mu}$ and by using the frame transformation in equation (8), and according to equations (15) we can rewrite equation (19) as:

$$\begin{aligned} \sigma^{DR}(E_{el}) &= \frac{\pi \hbar^2}{2mE_{el}} \sum_i \sum_{ll', \lambda\lambda'} |\langle v_i | S_{l\lambda, l'\lambda'}(q_i) | v'_i \rangle|^2 g_i \theta(\hbar\omega_i - E_{el}) \\ &= \frac{\pi \hbar^2}{2mE_{el}} \sum_i \sum_{ll', \lambda\lambda'} \left| \left(\sum_i \frac{\partial S_{l\lambda, l'\lambda'}(q_i)}{\partial q_i} \right)_{q_i=0} \langle v_i | q_i | v'_i \rangle \right|^2 g_i \theta(\hbar\omega_i - E_{el}) \\ &= \frac{\pi \hbar^2}{4mE_{el}} \sum_i \sum_{ll', \lambda\lambda'} \left| \frac{\partial S_{l\lambda, l'\lambda'}(q_i)}{\partial q_i} \right|^2 g_i \theta(\hbar\omega_i - E_{el}) \end{aligned} \quad (20)$$

here $\theta(\hbar\omega_i - E_{el})$ is the Heaviside step function open that when ($E_{el} \geq \hbar\omega_i$), the sum over i is for different normal modes, g_i the degeneracy of the mode i and the sum over $ll', \lambda\lambda'$ for initial and final angular momentum quantum number and their projections. Equation (20) can be expressed in term of probability as: and for the Vibrational de-Excitaitaion (VdE) of one quanta is :

$$\sigma^{DR}(E_{el}) = \sum_i \frac{\pi \hbar^2 g_i}{2mE_{el}} \theta(\hbar\omega_i - E_{el}) P_i \quad (21)$$

where

$$P_i = \frac{g_i}{2} \sum_{ll', \lambda\lambda'} \left| \frac{\partial S_{l\lambda, l'\lambda'}(q_i)}{\partial q_i} \right|^2 \quad (22)$$

According to equation (14) at the second order and for a transition with two quanta,

the cross section can be expressed as:

$$\begin{aligned}
 \sigma^{DR}(E_{el}) &= \frac{\pi \hbar^2}{2mE_{el}} \sum_i \sum_{l', \lambda \lambda'} |\langle v | S_{l\lambda, l'\lambda'}(q_i) | v' \rangle|^2 g_i \theta(\hbar\omega_i - E_{el}) \\
 &= \frac{\pi \hbar^2}{2mE_{el}} \sum_i \sum_{l', \lambda \lambda'} \left| \frac{1}{2} \sum_i \frac{\partial^2 S_{l\lambda, l'\lambda'}(q_i)}{\partial q_i^2} \langle v | q_i^2 | v' \rangle \right|^2 g_i \theta(\hbar\omega_i - E_{el}) \\
 &= \frac{\pi \hbar^2}{2mE_{el}} \sum_i \sum_{l', \lambda \lambda'} \left| \frac{1}{4} \left(\sum_i \frac{\partial^2 S_{l\lambda, l'\lambda'}(q_i)}{\partial q_i^2} \right)_{q_i=0} \times \sqrt{2} \right|^2 g_i \theta(\hbar\omega_i - E_{el}) \\
 &= \frac{\pi \hbar^2}{16mE_{el}} \sum_i \sum_{l', \lambda \lambda'} \left| \frac{\partial^2 S_{l\lambda, l'\lambda'}(q_i)}{\partial q_i^2} \right|^2 g_i \theta(\hbar\omega_i - E_{el}) \tag{23}
 \end{aligned}$$

8.5 Results

The cross section calculation requires a continuous verification of the results obtained during the scattering calculation. One way is to plot the eigenphase sum obtained after collision in the R-matrix calculation. A necessary and obvious condition concerning the use of the method developed above evokes the absence of resonant states at low energy before applying the derivative of the S matrix. For a geometry corresponding to a very small displacement from equilibrium along the different normal modes of the molecule ($q_i = 0.001$), we show the eigenphase sum in figure (8.4). The calculations were performed in C_s group symmetry for the bending mode, C_{2v} point group for symmetric and asymmetric stretching. At low collision energies, below 2 eV, we can see that the eigenphase sums are smooth as a functions of the electron energy, which is a criteria to use the previously presented method to calculate the cross section.

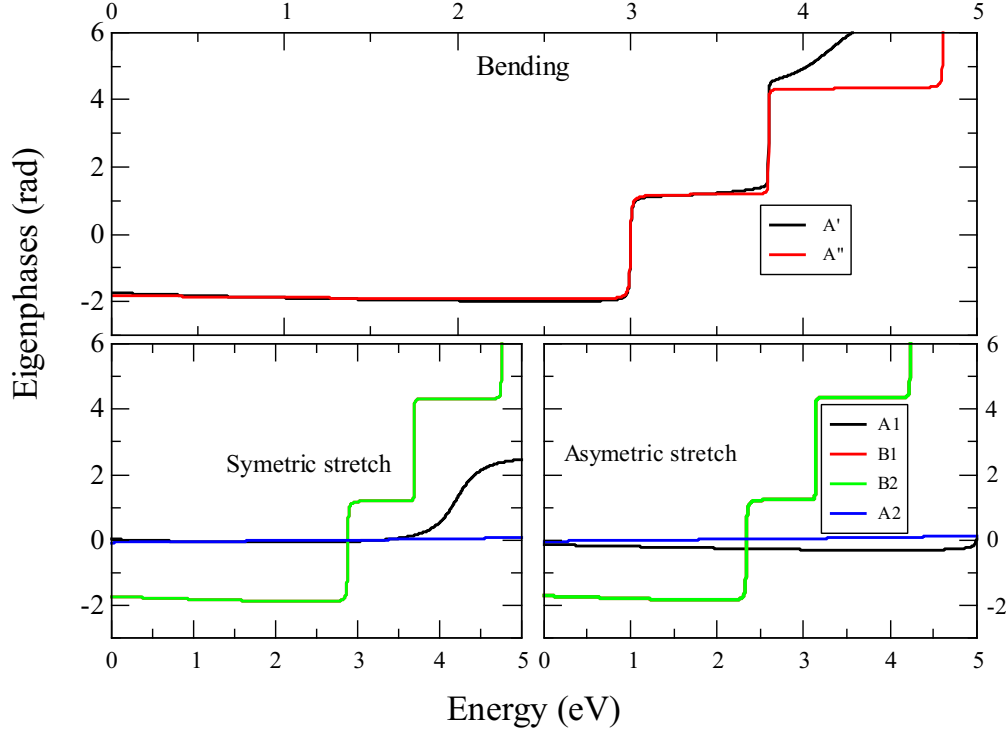


Figure 8.4: Eigenphase sums as a function of the incident electron energy for $q = 0.001$ (dimensionless) for the bending mode in C_s group symmetry (upper panel), symmetric stretching (left bottom panel) and asymmetric stretching (right bottom panel) modes in C_{2v} point group. The curves of different colors correspond to different symmetries of the electron HCO^+ scattering. For bending mode, black curve is for A' symmetry and the red one for A'' . For symmetric and asymmetric stretching, the black curve is for A_1 , red and green curves are for doublet degenerate symmetries B_1 and B_2 and the blue curve is for A_2 symmetry

The e^- - HCO^+ DR cross-section is computed using equation (20) and the results are shown on figure (8.5). Our calculated cross section overestimates by a factor 2 the previous calculations of Refs. [156, 158, 160, 163]. In order to understand the origin of this discrepancy a number of auxiliary test calculations were performed using different CAS, basis but the results remain the same. The present investigations tend to attribute to the nature of the molecular orbitals used in the fixed nuclei calculation. In this work the calculations were done with Hartree-Fock orbitals and the target is well described by this method as it can be seen with drops corresponding to each vibrational threshold. A proof of concept/methodology we obtained when we have used the capture probabilities calculated by Ref [163] in our model.

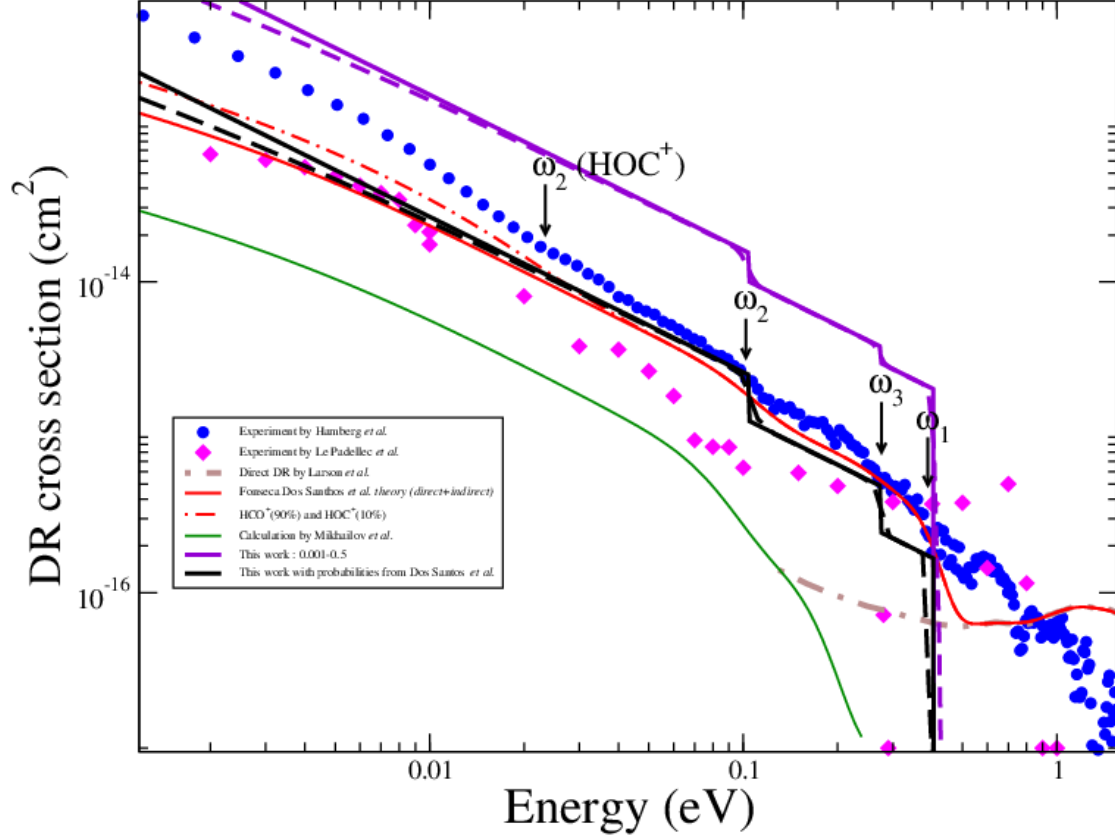


Figure 8.5: DR cross section as on figure (6) of dos Santo *et al.*. The violet solid and dashed curves are respectively the calculated cross section and its convolution compared to previous works. Black curves are cross section calculation obtained with probabilities from dos Santo *et al.*

8.6 Conclusion

In this chapter, we compute the DR cross-section of a linear triatomic molecular cation HCO⁺ using a theoretical approach based on harmonic approximation and frame transformation. The Molpro program is used to describe the target molecule while the R-matrix method is used, via the Quantemol-N interface, to describe the nuclear dynamics. A good description is shown with frequencies and angular dipole moment in agreement with previous experience and calculation. The DR cross-section is over-estimated and the model must be improved by the inclusion of molecular orbitals from CASSCF calculation. The overestimation of our calculated cross-section with S matrix from R-matrix calculation can be explained also with the phase shift difference between our results and the Kohn calculation of dos Santo *et al.* [163]. Another assumption of this overestimation may be explained by the probability values in equation (22) which are not constant against the incident electron energy for the bending and asymmetric stretching modes as shown in

Figure(8.6).

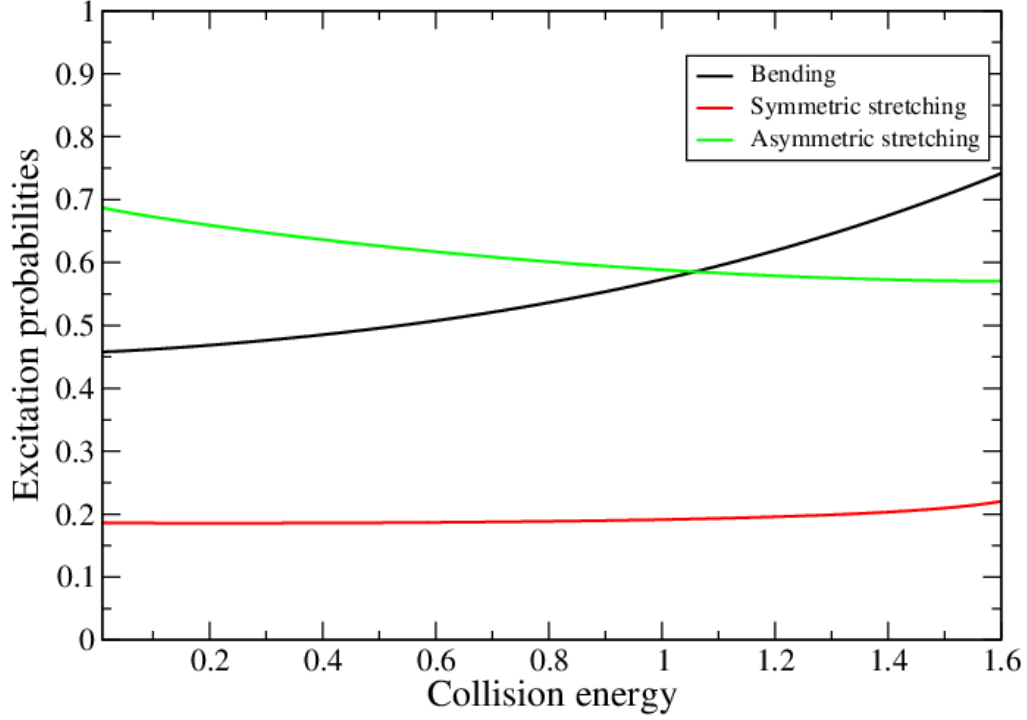


Figure 8.6: Excitation probabilities

As a perspective in this work and to understand well the discrepancy between our results and those of dos Santos *et al.* [163], we can evaluate the phase shift by fitting and identifying the relevant S matrix element. The phase shift can be obtained using the S matrix as the following:

$$S_i = e^{2i(\delta_i)} \quad (24)$$

$$\frac{\log(S_i)}{2i} = \delta_i \quad (25)$$

The S matrix can be fitted for different value of q_i , and we can identify the relevant S matrix element as in Figure 1 of dos Santo *et al.* [163] and then calculate the derivative of the scattering matrix.

Conclusion and perspectives

In this thesis, the electron-molecule reactive collision processes have been studied. These collisions are important in ionized media, plasmas used for technological applications, in the ISM and planetary atmospheres. In this thesis, we have focused on collisions between electrons and diatomic molecular cations with different versions of theory based on MQDT and on two triatomic molecules.

We have also studied the competitive processes: VE, VdE and DE.

Before the quantum dynamics study, the description of the relevant electronic states is a prerequisite. This is why the first theoretical chapter of this thesis was dedicated to the description of the relevant quantum chemical theory used for the different electronic states.

We have neglected the rotational effects of the molecules. The application of a first approach of this theory with a single-core was dedicated to ArH^+ molecular cation [57] where the DR and VE cross-section and corresponding rate coefficient for the three first vibrational levels are computed and DE is not taken into account. Results are in good agreement with merged beams measurement of Mitchell *et al.*[52]. The continuation of this work can be the inclusion of more dissociative PECs in the calculation and take into account the DE process in order to have a realistic database of this system at high energy. In a second approach of the theory with a double-core, we show the results for electron scattering with HD^+ molecular cation in chapter (5). The cross-section and rate coefficients for all processes are calculated for all vibrational levels up to electron energy equal to 12 eV. Results shown in this chapter are the work continuation of Chakrabarti *et al.* [40] In near future, a better approach, taking into account the numerous dissociative highly-excited states and using the grid method for the modeling of the continuum rather than the Numerov one will be implemented in order to extend our exploration.

The last MQDT application is based on an approach of the theory where multiple excited-core are taken into account for N_2^+ molecular cation [106] in chapter (6). Cross-sections and thermal rate coefficients are computed for electron-impact DR, VE, and VdE of the N_2^+ molecular ion in its lowest six vibrational levels, for collision energies up to 2.3 eV. *Ab initio* calculations for still higher neutral states will be initiated.

Poly-atomic molecules have been studied in the two last chapters. In a perspective to computing the cross-section of the DEA and VE of the carbon dioxide, the potential energy curves of this molecule for different resonant states using quantum chemistry and R-matrix [3, 4] Finally, In chapter (8) the DR cross-section for electron scattering with formylium molecule (HCO^+) is calculated using a theoretical approach based on the MQDT where the scattering matrix has been obtained in an R-matrix calculation for different geometries considering the normal mode coordinates and frame transformation. More investigations on the CAS or the nature of molecular orbitals may be done in order to have a good agreement with previous calculations. Most of the data - cross-section and rate coefficients - that we have obtained will be used in the improvement of powerful collisional-radiative models needed in the kinetics of various ionized cold media.

Chapter 10

Appendix A

The $a(E', E)$ is a coefficient which can be determined using the Schrödinger equation:

$$H(r)\varphi_E(r) = [H_0 + V(r)]\varphi_E(r) = E\varphi_E(r) \quad (1)$$

Putting equation (1) on equation (1) lead to

$$[H_0 + V(r)] \int dE' a(E', E) f_{E'}(r) = E \int dE' a(E', E) f_{E'}(r) \quad (2)$$

Making the scalar product of $f_{E'}(r)$ on the left of equation (2) and integrate on all radial coordinates give:

$$\langle f_{E'}(r) | H_0 + V(r) - E | \int dE'' a(E'', E) f_{E''}(r) \rangle = 0 \quad (3)$$

The expansion of this equation (3) give terms as:

$$\begin{aligned} \langle f_{E'}(r) | H_0 | \int dE'' a(E'', E) f_{E''}(r) \rangle + \langle f_{E'}(r) | V(r) | \int dE'' a(E'', E) f_{E''}(r) \rangle \\ - \langle f_{E'}(r) | E | \int dE'' a(E'', E) f_{E''}(r) \rangle = 0 \end{aligned} \quad (4)$$

and by expanding these terms one by one we can write the first one as:

$$\begin{aligned} \langle f_{E'}(r) | H_0 | \int dE'' a(E'', E) f_{E''}(r) \rangle &= \int dE'' a(E'', E) \langle f_{E'}(r) | H_0 | f_{E''}(r) \rangle \\ &= \int dE'' a(E'', E) E'' \langle f_{E'}(r) | f_{E''}(r) \rangle \\ &= \int dE'' a(E'', E) E'' \delta(E' - E'') \\ &= a(E'', E) E' \end{aligned} \quad (5)$$

the second one is the definition of the \mathcal{K} which will be explicitly explain on the next part:

$$\begin{aligned} \langle f_{E'}(r)|V(r)| \int dE'' a(E'', E) f_{E''}(r) \rangle &= \langle f_{E'}(r)|V(r)|\varphi_E(r) \rangle \\ &= K(E', E) \end{aligned} \quad (6)$$

and the last one as:

$$\begin{aligned} -\langle f_{E'}(r)|E| \int dE'' a(E'', E) f_{E''}(r) \rangle &= -E \int dE'' a(E'', E) \langle f_{E'}(r)|f_{E''}(r) \rangle \\ &= -E \int dE'' a(E'', E) \delta(E' - E'') \\ &= -E a(E'', E) \end{aligned} \quad (7)$$

The sum of these different terms hold on the relation:

$$a(E'', E)E' + K(E', E) - E a(E'', E) = 0 \quad (8)$$

whhich can be rewrite as:

$$a(E'', E) = \frac{K(E', E)}{E - E'} \quad (9)$$

Here $E - E'$ may vanish when energy is conserved and it can be happen when $E = E'$. Dividing equation (9) by $E - E'$ is then accordingly nontrivial. The general solution of (9) is nevertheless expressed by a mathematical notation due to Dirac [31]

$$a(E'', E) = \mathcal{P} \int \frac{1}{E - E'} K(E', E) + \delta(E - E') \quad (10)$$

where $\delta(E - E')$ is the Dirac delta function, and the symbol \mathcal{P} specifies the principal part integration which should be taken over the singularity of $\frac{1}{E - E'}$ on the summation.

According to relation (6) we can write the reaction matrix \mathcal{K} by inserting the wave function established in (13) and expand it:

$$\begin{aligned} K(E', E) &= \langle f_{E'}(r)|V(r)|\varphi_E(r) \rangle \\ &= \langle f_{E'}(r)|V(r) \left[|f_E(r) + \mathcal{P} \int dE'' \frac{1}{E - E''} K(E'', E) f_{E''}(r) \right] \rangle \\ &= \langle f_{E'}(r)|V(r)|f_E(r) \rangle + \mathcal{P} \int dE'' \frac{\langle f_{E'}(r)|V(r)|f_{E''}(r) \rangle}{E - E''} K(E'', E) \end{aligned} \quad (11)$$

to obtain the Lippmann-Schwinger equation :

$$K(E', E) = \langle f_{E'}(r) | V(r) | f_{E'}(r) \rangle + \mathcal{P} \int dE'' \frac{\langle f_{E'}(r) | V(r) | f_{E''}(r) \rangle}{E - E''} K(E'', E) \quad (12)$$

Published papers

Theoretical study of ArH⁺ dissociative recombination and electron-impact vibrational excitation

A. Abdoulanziz,¹ F. Colboc,¹ D. A. Little,² Y. Moulane,^{3,4} J. Zs. Mezei,^{1,5,6} E. Roueff,⁷ J. Tennyson,² I. F. Schneider^{1,8} and V. Laporta^{1,2*}

¹Laboratoire Ondes et Milieux Complexes, CNRS–Université du Havre–Normandie Université, 76058 Le Havre, France

²Department of Physics and Astronomy, University College London, London WC1E 6BT, UK

³Oukaimden Observatory, High Energy Physics and Astrophysics Laboratory, Cadi Ayyad University, Marrakech, Morocco

⁴Space sciences, Technologies & Astrophysics Research Institute, University of Liège, Liège, Belgium

⁵Laboratoire des Sciences des Procédés et des Matériaux, CNRS–Université Paris 13–USPC, 93430 Villetaneuse, France

⁶Institute of Nuclear Research, Hungarian Academy of Sciences, Debrecen, Hungary

⁷Sorbonne Université, Observatoire de Paris, Université PSL, CNRS, LERMA, F-92190, Meudon, France

⁸Laboratoire Aimé-Cotton, CNRS–Université Paris-Sud–ENS Cachan–Université Paris-Saclay, 91405 Orsay, France

Accepted XXX. Received YYY; in original form ZZZ

ABSTRACT

Cross sections are presented for dissociative recombination and electron-impact vibrational excitation of the ArH⁺ molecular ion at electron energies appropriate for the interstellar environment. The R-matrix method is employed to determine the molecular structure data, *i.e.* the position and width of the resonance states. The cross sections and the corresponding Maxwellian rate coefficients are computed using a method based on the Multichannel Quantum Defect Theory. The main result of the paper is the very low dissociative recombination rate found at temperatures below 1000K. This is in agreement with the previous upper limit measurement in merged beams and offers a realistic explanation to the presence of ArH⁺ in exotic interstellar conditions.

Key words: ArH⁺ – dissociative recombination – vibrational excitation – interstellar medium

1 INTRODUCTION

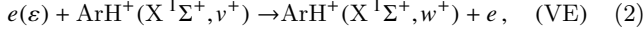
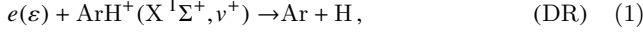
The presence of the ArH⁺ molecular cation, argonium, in interstellar medium (ISM) was reported for the first time by Barlow *et al.* (2013), who detected ³⁶ArH⁺ 617.525 GHz ($J = 1 - 0$) and 1234.603 GHz ($J = 2 - 1$) emission lines in spectra from the Crab Nebula using the data from Herschel mission. That supernova remnant is known to contain both molecular hydrogen and regions of enhanced ionized argon emission. After this first noble gas molecular ion detection, Schilke *et al.* (2014) realized that the still unidentified absorption transition at 617.5 GHz observed in diffuse gas toward several sources such as Sg B2, and various PRISMA sources (W31C, W49N, W51e, ...), was in fact due to argonium with ³⁶Ar. Moreover, features of ³⁸ArH⁺ were subsequently found in Sg B2(M) as well and, consequently, Schilke *et al.* suggested that argonium is ubiquitous in the ISM. More recently, Müller *et al.* (2015) made extragalactic detections of the ³⁶Ar and ³⁸Ar isotopologues of argonium through absorption studies of a foreground galaxy at $z = 0.89$ along two different lines of sight toward PKS

1830-211 within the band 7 of the ALMA interferometer, including the corresponding redshifted transitions.

The possible formation/destruction processes linked to ArH⁺ are discussed by Neufeld & Wolfire (2016) who emphasized that ArH⁺ is a good tracer of the almost purely atomic diffuse ISM in the Milky Way. However, an important missing piece of information remains the unknown value of the dissociative recombination rate coefficient of that molecular ion. An upper limit of $10^{-9} \text{ cm}^3 \text{ s}^{-1}$ for electron collision energies below about 2 eV was reported by Mitchell *et al.* (2005) who performed a storage ring measurement. Mitchell *et al.* also gave the corresponding theoretical potential curves. That upper limit value is adopted in the presently available astrochemical models for galactic diffuse clouds (Neufeld & Wolfire 2016) whereas Priestley *et al.* (2017) introduce a lower value ($10^{-11} \text{ cm}^3 \text{ s}^{-1}$) to interpret the Crab nebula observations. Photodissociation of ArH⁺, another potential destruction mechanism, was studied theoretically by Alekseyev *et al.* (2007) and the corresponding photodissociation rate was shown to be moderate, *i.e.* $9.9 \cdot 10^{-12} \text{ s}^{-1}$ in the unshielded mean ultraviolet interstellar radiation field (Roueff *et al.* 2014). In addition to these, the rotational excitation due to electron impact has been studied by Hamilton *et al.* (2016).

* E-mail: vincenzo.laporta@univ-lehavre.fr (VL)

In this paper, we investigate theoretically the dissociative recombination (DR) process of ArH^+ through *ab initio* methods, including the dependence on the vibrational excitation of the target molecular ion and, in the same energy range, the competitive process of vibrational excitation (VE) by electron impact, *i.e.*:



where ε is the incident electron energy, v^+ and w^+ represent the initial and final vibrational quantum numbers respectively corresponding to the ground electronic state $X^1\Sigma^+$ of ArH^+ .

The manuscript is organized as follows: in Section 2 the theoretical model used to characterize the ArH^{**} resonant states is presented and in Section 3 the results concerning the cross sections and the corresponding rate coefficients are discussed. Finally the conclusions, in Section 4, close the paper.

2 THEORETICAL MODEL

A theoretical study of the ArH^+ electronic excited states was performed by [Stolyarov & Child \(2005\)](#); [Jungen et al. \(1997\)](#), and more recently [Kirrander et al. \(2006\)](#), explored ArH Rydberg states.

In the present work, *ab initio* ArH^+ calculations were performed using MOLPRO and an aug-cc-pVQZ (AVQZ) Gaussian type orbital (GTO) basis set at the complete active space (CAS) self-consistent field (SCF) level of theory. These calculations provided input orbitals for the electron-ion scattering calculations. All calculations were performed in C_{2v} symmetry, which is the highest allowed by MOLPRO and the polyatomic R-matrix code for an asymmetric linear molecule.

The potential energy curves and the widths for the ArH^{**} resonant states were calculated using the R-matrix method ([Tennyson 2010](#)) as implemented in UKRMol code ([Carr et al. 2012](#)). The general approach follows closely the treatment of N_2^{**} by [Little & Tennyson \(2014\)](#) which provided the input for N_2^+ DR calculations ([Little et al. 2014](#)). The ArH^+ target states were represented using the AVQZ GTO basis set and a CAS in which the Ar $1s^2 2s^2 2p^6$ electrons were frozen and the remaining 8 electrons were distributed as $(4\sigma, 5\sigma, 6\sigma, 2\pi)^8$. The 3π virtual orbital was retained to augment the continuum orbitals in the scattering calculation.

The scattering calculations used an R-matrix sphere of radius $10 a_0$. Continuum basis functions were represented using GTOs placed at the center of this sphere and contained up to g orbitals ($\ell \leq 4$) ([Faure et al. 2002](#)). Close-coupling calculations built on the target CAS ([Tennyson 1996](#)) and an expansion of the 8 lowest states of each (C_{2v}) symmetry were retained for the outer region calculations. In this latter region, calculations were repeated for the internuclear separations $2.2 < R < 15 a_0$ and for symmetries corresponding to $^2\Sigma^+$, $^2\Pi$ and $^2\Delta$ scattering channels.

The outer region calculations explicitly considered the 20 lowest target states. R-matrices were propagated to $100.1 a_0$ and then fitted to an asymptotic form. Resonance positions and widths were determined by automated fitting

μ (a.u.)	1791.94		
R_{eq} (a_0)	2.419 (2.419)		
D_e (eV)	4.039 (4.025)		
D_0 (eV)	3.8725		
v^+	ϵ_{v^+} (eV)	v^+	ϵ_{v^+} (eV)
0	0.000	12	2.949
1	0.321	13	3.110
2	0.627	14	3.258
3	0.919	15	3.393
4	1.197	16	3.513
5	1.461	17	3.617
6	1.712	18	3.703
7	1.949	19	3.770
8	2.174	20	3.817
9	2.387	21	3.846
10	2.587	22	3.861
11	2.774		

Table 1. Molecular constants (reduced mass, equilibrium distance and dissociating energies) for $^{40}\text{ArH}^+$ in its ground electronic state and the energies of the corresponding vibrational levels. The comparison with the experimental data of [Hotop et al. \(1998\)](#) given in brackets is reported.

of the eigenphase sums to a Breit-Wigner form using program RESON ([Tennyson & Noble 1984](#)). Couplings were determined from the resonance widths Γ using the formula:

$$V(R) = \sqrt{\frac{\Gamma(R)}{2\pi}}. \quad (3)$$

Figure 1 shows the R-matrix results for resonance positions (upper panel), couplings (middle panel) and quantum defect (lower panel). The corresponding molecular data are given in Table 1. These data form the input for the Multi-channel Quantum Defect Theory (MQDT) step of the calculations. Linear extrapolation was adopted for the couplings in order to extend the internuclear distances range below $2.2 a_0$ to $1.6 a_0$.

ArH^+ is a closed shell system so no spin-orbit (SO) splitting effects are expected in its ro-vibrational levels. Conversely, SO effects may be important in the non- Σ resonances and are well characterized for the Ar asymptotic states. In particular, the $\text{Ar}(^2P_{3/2}^0 4s)$ and $\text{Ar}(^2P_{1/2}^0 4s)$ show SO splittings of 0.075 eV and 0.105 eV, respectively ([Kramida et al. 2018](#)). Our calculations are non-relativistic and therefore neglect SO effects; we assume the calculated R-matrix resonances converge on the lowest component of the Ar doublets at large internuclear distances. Table 2 shows the asymptotic limits of the ArH^{**} resonant states considered below.

The MQDT method ([Giusti 1980](#); [Guberman & Giusti-Suzor 1991](#); [Chakrabarti et al. 2013](#); [Motapon et al. 2014](#); [Little et al. 2014](#); [Epée Epée et al. 2015](#)) was used to study the processes (1) and (2). Within this approach, the corresponding cross sections are

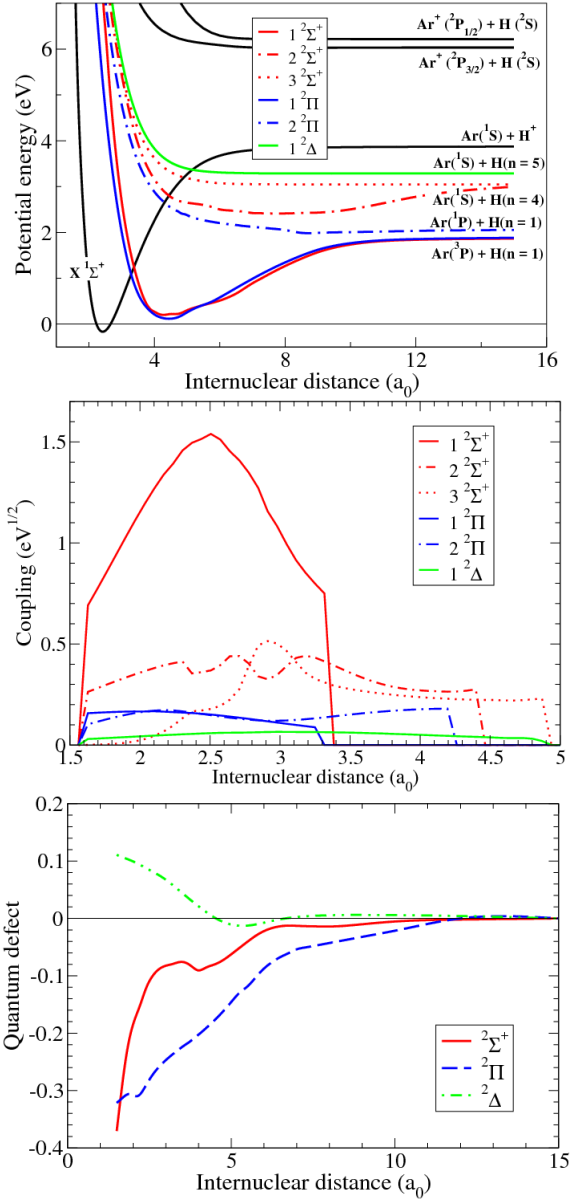


Figure 1. Potential energy curves, couplings and quantum defects used in the present calculations. The ArH⁺ potential curves - ground state, X¹Σ⁺, and the lowest excited electronic states - are displayed as black lines. The molecular data sets for the different symmetries of the neutral system are displayed with different colors: 2²Σ in red, 2²Π in blue and 2²Δ in green.

Channel	Energy (eV)	Symmetries
Ar(³ P) + H(n = 1)	-2.00 (-2.05)	1 ² Σ ⁺ , 1 ² Π
Ar(¹ P) + H(n = 1)	-1.81 (-1.87)	2 ² Π
Ar(¹ S) + H(n = 4)	-0.87 (-0.85)	2 ² Σ ⁺ , 3 ² Σ ⁺
Ar(¹ S) + H(n = 5)	-0.58 (-0.54)	1 ² Δ

Table 2. Asymptotic limits of the ArH⁺ resonant states relevant for the low-energy impact collisions. The energy is expressed with respect to the asymptotic limit of the ground electronic state of ArH⁺. The experimental energy values from the NIST database (Kramida et al. 2018) are given in brackets for comparison.

expressed in terms of S-matrix elements as:

$$\sigma_{v^+}(\varepsilon) = \frac{\pi}{4\varepsilon} \sum_{sym, \Lambda, l, j} \rho^{sym, \Lambda} |S_{d_j, l v^+}^{sym, \Lambda}|^2, \quad (4)$$

$$\sigma_{v^+, w^+}(\varepsilon) = \frac{\pi}{4\varepsilon} \sum_{sym, \Lambda, l, l'} \rho^{sym, \Lambda} |S_{l' w^+, l v^+}^{sym, \Lambda} - \delta_{l, l'} \delta_{v^+, w^+}|^2, \quad (5)$$

where the summation is extended over all symmetries (*sym*: spin, inversion for homonuclear molecules) of the neutral system, projection of the total electronic angular momentum on the internuclear axis Λ , and partial waves l/l' of the incident/scattered electron, and $\rho^{sym, \Lambda}$ is the ratio between the multiplicities of the neutral system and of the target ion.

The most abundant isotope of argon in the Earth's atmosphere is ⁴⁰Ar whereas in the ISM ³⁶Ar and ³⁸Ar isotopes are preponderant. In the present work, we deal with vibrational processes and, due to the small relative variation of the reduced mass from one isotopologue to another - as a consequence of the huge atomic mass of the Ar isotopes - we expect these effects to be negligible. In order to verify this, we performed calculations for different isotopologues of ArH⁺ and the relative difference between the rate coefficients was found to be below 1%.

3 RESULTS AND DISCUSSION

Figure 2 displays the DR cross sections for ArH⁺ $v^+ = 0$, namely the total one and the partial contributions corresponding to the asymptotic channels of resonant states. It can be noted that the main contribution arises from the Ar(³P) + H(n = 1) channel. One reason for this is that, as shown in Table 2, this exit channel gathers contributions coming from two states - 1²Σ⁺ and 1²Π - instead of one state, as is the case of the exit channels Ar(¹P) + H(n = 1) and Ar(¹S) + H(n = 5). One can argue that - as shown in Table 2 - the channel Ar(¹S) + H(n = 4) is the asymptotic limit of two states, as the Ar(³P) + H(n = 1) one. However, the coupling of the 1²Σ⁺ state with the electron/ion continuum (see Fig. 1) is about three times larger than the other ones.

Figures 3(a) and (b) display, respectively, the results for DR cross sections and the corresponding rate coefficients for $v^+ = 0, 1, 2$. Two features can be noted:

(i) The resonant structures present in the cross sections correspond to the temporary captures into singly-excited Rydberg states ArH*, and they cease to appear when the electron energy reaches the dissociation energy of ArH⁺ ($v^+ = 0, 1, 2$);

(ii) For a vibrationally relaxed target, the dissociation channels are closed for energies of the incident electron below 1.8 eV. For the ion situated on one of the next 8 excited vibrational states, the threshold decreases progressively, and the DR becomes exothermic for vibrational levels equal or higher to 9 only. This particular energetic situation explains the particular behavior of the computed rate coefficients displayed in Fig. 3(b), namely the very low values and the "explosive" increase below 2000 K.

In order to validate the results, Fig. 4 shows the anisotropic DR rate coefficient for $v^+ = 0$, calculated by considering the electron beam with a longitudinal temperature

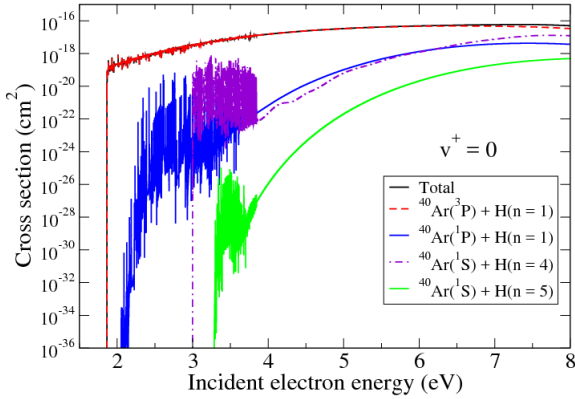


Figure 2. Dissociative recombination of vibrationally relaxed ArH^+ . Broken colored lines: The contributions coming from all the dissociative states having the same asymptotic atomic limit. Solid black line (partially hidden by the red curve): Total cross section coming from the sum over all the available dissociative states.

$kT_{\parallel} \approx 0.5$ eV and a transverse temperature $kT_{\perp} \approx 25$ meV, compared to the experimental data from the storage ring by Mitchell et al. (2005). We note that the agreement is quite satisfactory at energies greater than ~ 3 eV within the 20% experimental error. At lower energies our calculated rates are smaller than the experimental ones: This can derive from bad detected signal as stated by the authors.

Figure 5 displays the DR cross section compared to the competitive process of VE for one quantum excitation in the same energy range. The main feature is that, at energies just above the opening of the dissociative channels, the VE cross section is larger than the corresponding DR starting from the same vibrational level.

We also checked the isotopic effect by replacing ArH^+ by ArD^+ , which results in a variation of the reduced mass by a factor of 2. Fig. 6 displays this effect for $v^+ = 0$ DR rate coefficient. The rates decrease by a factor between 10 at 1000 K and 3 at 8000 K, due to lowering of the ArD^+ ground state, compared to that of ArH^+ .

3.1 Astrophysical consequences

As stated previously, ArH^+ DR is an important destruction mechanism in interstellar conditions. We have examined two different environments where this molecular ion has been found and have varied the value of the DR rate coefficient over a range of values between 10^{-9} and 10^{-18} $\text{cm}^3 \text{s}^{-1}$ for a sample of 0D steady state chemical models. We solve the coupled $\frac{d}{dt}[X] = 0$ differential equations where $[X]$ stands for the abundance of a particular X molecule included in the chemical network for a fixed value of density and temperature and different values of the DR chemical rate coefficient of ArH^+ , $k_{\text{DR}}(\text{ArH}^+)$. In Fig. 7(a), we display the different solutions of the argonium relative abundance as a function of $k_{\text{DR}}(\text{ArH}^+)$ for typical diffuse cloud conditions: Proton density $n_{\text{H}} = 100 \text{ cm}^{-3}$, temperature $T = 100$ K, H_2 cosmic ionization rate $\zeta = 10^{-16} \text{ s}^{-1}$, visual extinction $A_{\text{V}} = 0.001$ and standard interstellar radiation field defined by the scaling parameter $\chi = 1$. In Fig. 7(b), we display the different solutions for physical conditions pertaining to the Crab nebula, as discussed in Priestley et al. (2017), *i.e.* $n_{\text{H}} = 2000 \text{ cm}^{-3}$,

$T = 1000$ K, H_2 cosmic ionization rate $\zeta = 5 \cdot 10^{-10} \text{ s}^{-1}$, $\chi = 60$, $A_{\text{V}} = 0.1$ and the elemental abundances displayed in Table 1 of Priestley et al. (2017). Each point corresponds to a specific model results and the line connects the different model results. In the standard diffuse cloud conditions, we see that the argonium relative abundance remains constant for values of $k_{\text{DR}}(\text{ArH}^+)$ smaller than some $10^{-11} \text{ cm}^3 \text{s}^{-1}$, where another destruction mechanism such as photodissociation becomes dominant. It should also be noticed that the scale is linear and the variations are moderate. However, in the extreme conditions of the Crab nebula where the cosmic ionization rate is about 7 orders of magnitude larger, the variation of the relative fractional abundance of argonium is much more spectacular. The limiting value of $k_{\text{DR}}(\text{ArH}^+) = 10^{-13} \text{ cm}^3 \text{s}^{-1}$, below which the relative abundance of argonium remains almost stable and the destruction by photodissociation and reaction with H_2 take over the dissociative recombination. Our theoretical computations demonstrate that the actual value is significantly below the experimental upper limit $10^{-9} \text{ cm}^3 \text{s}^{-1}$ and even below the limiting values stressed out by the models (see Fig. 3(b)). Within these findings, we conclude that DR plays a negligible role in astrophysical media and that photodissociation and reactions with molecular hydrogen become the main destruction processes.

4 CONCLUSIONS

In this paper we explored the superexcited states of ArH^+ within the R-matrix approach and we computed the cross sections and the corresponding rate coefficients for the dissociative recombination and the vibrational excitation of ArH^+ by using Multichannel Quantum Defect Theory. The very low values of the dissociative recombination rate coefficients leads to the conclusion that the only significant ArH^+ destruction mechanisms in the interstellar medium are the collisions with H_2 molecules and the photodissociation.

ACKNOWLEDGEMENTS

ER, IFS and VL acknowledge the Programme National “Physique et Chimie du Milieu Interstellaire” (PCMI) of CNRS/INSU with INC/INP co-funded by CEA and CNES. They also thank for generous financial support from La Région Haute-Normandie *via* the GRR Electronique, Energie et Matériaux, from the “Fédération de Recherche Energie, Propulsion, Environnement”, and from the LabEx EMC³ and FEDER *via* the projects PicoLIBS (ANR-10-LABEX-09-01), EMOPlaF and CO₂-VIRIDIS. IFS and VL thank PHC GALILEE 2018 PROJET (39379SF) and the GdR THEMIS. IFS and JZM acknowledge support from the IAEA *via* the Coordinated Research Project “Light Element Atom, Molecule and Radical Behaviour in the Divertor and Edge Plasma Regions”. JZM acknowledges support from USPC *via* ENUMPP and Labex SEAM. This work is supported by BATTUTA Project (Building Academic Ties Towards Universities through Training Activities) in the frame of the Erasmus Mundus program, at LOMC UMR-CNRS-6294 of Le Havre University. YM thanks the SRI department, especially Mrs. Martine Currie, for outstanding hospitality.

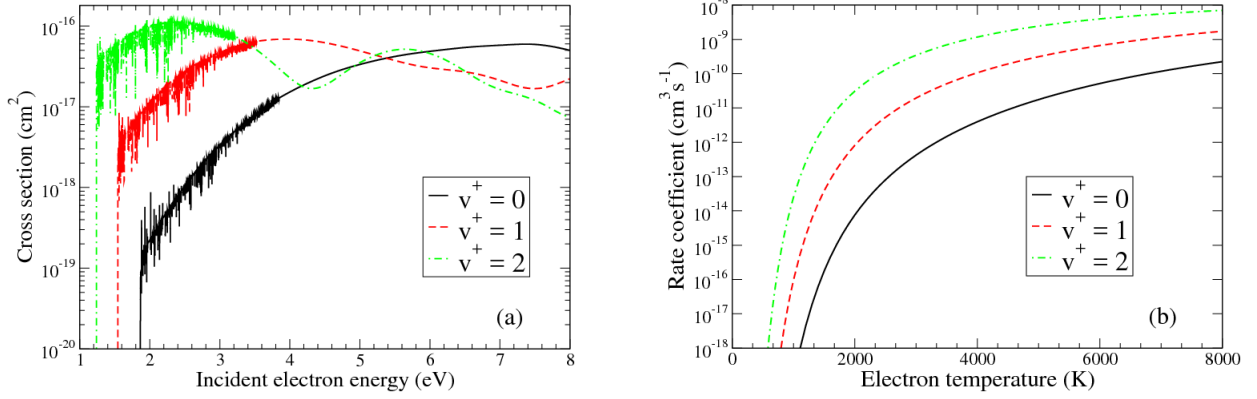


Figure 3. Dissociative recombination of ArH⁺ on its lowest vibrational levels: (a) global cross sections, coming from the sum over all the available dissociative states; (b) the corresponding Maxwellian-averaged rate coefficients.

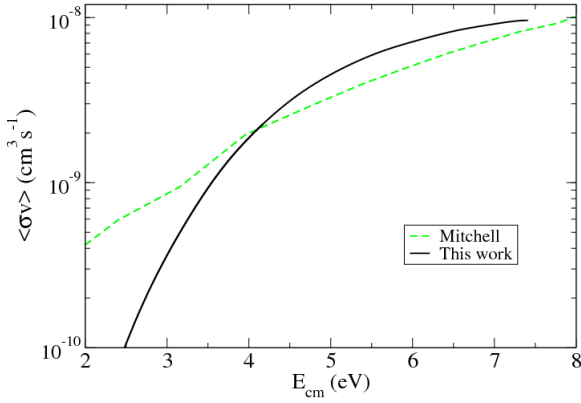


Figure 4. Dissociative recombination of vibrationally relaxed ArH⁺. Comparison between the rate coefficient measured in the CRYRING storage ring Mitchell et al. (2005) and the anisotropic rate coefficient obtained by the convolution of our MQDT-computed cross section using the temperatures characterizing the relative velocities of the electrons with respect to the ions in the experiment.

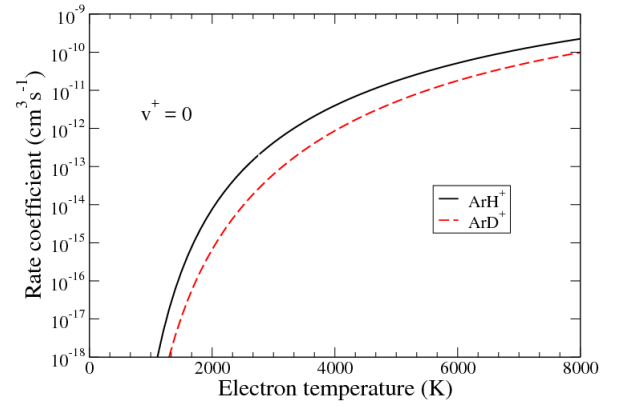


Figure 6. Dissociative recombination rate of vibrationally relaxed ArH⁺ and ArD⁺ as a function of electron temperature: The isotopic effects.

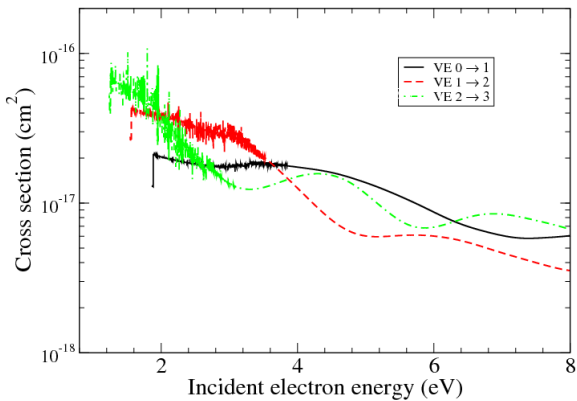


Figure 5. Vibrational excitation (VE) of ArH⁺ on its lowest vibrational levels: Cross sections for $\Delta v^+ = 0$ (solid lines). The dissociative recombination (DR) cross section are also shown for comparison (broken line).

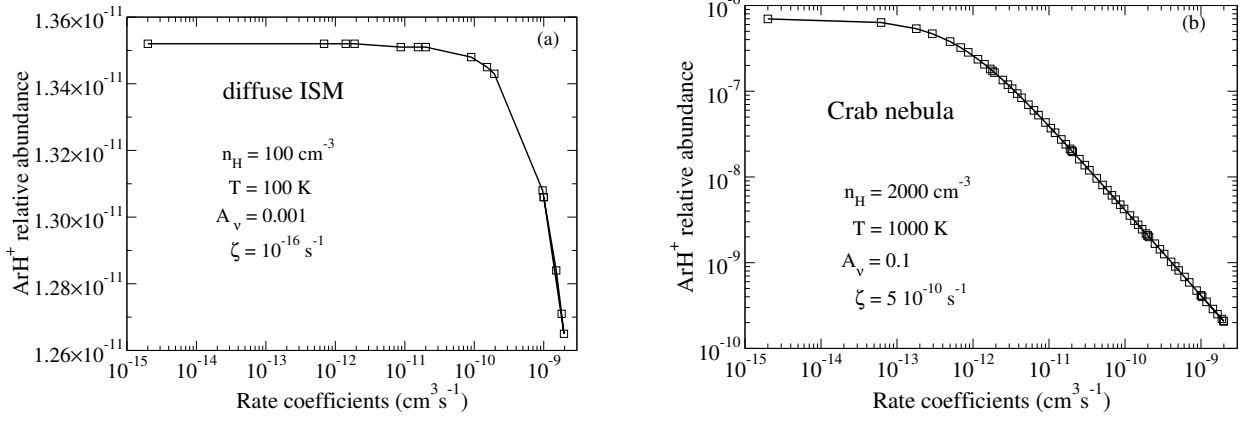


Figure 7. Relative abundance of ArH^+ as a function of the rate coefficients for the case of (a) diffuse ISM (temperature $T = 100 \text{ K}$) and (b) Crab nebula (temperature $T = 1000 \text{ K}$).

REFERENCES

- Alekseyev A. B., Liebermann H., Buenker R. J., 2007, *Physical Chemistry Chemical Physics*, 9, 5088
- Barlow M. J., et al., 2013, *Science*, 342, 1343
- Carr J. M., et al., 2012, *The European Physical Journal D*, 66, 58
- Chakrabarti K., et al., 2013, *Phys. Rev. A*, 87, 022702
- Epée Epée M. D., Mezei J. Z., Motapon O., Pop N., Schneider I. F., 2015, *MNRAS*, 455, 276
- Faure A., Gorfinkiel J. D., Morgan L. A., Tennyson J., 2002, *Computer Physics Communications*, 144, 224
- Giusti A., 1980, *Journal of Physics B: Atomic and Molecular Physics*, 13, 3867
- Guberman S. L., Giusti-Suzor A., 1991, *The Journal of Chemical Physics*, 95, 2602
- Hamilton J. R., Faure A., Tennyson J., 2016, *Monthly Notices of the Royal Astronomical Society*, 455, 3281
- Hotop H., Roth T. E., Ruf M.-W., Yench A. J., 1998, *Theoretical Chemistry Accounts*, 100, 36
- Jungen C., Roche A. L., Arif M., 1997, [Philosophical Transactions of the Royal Society of London A: Mathematical, Physical and Engineering Sciences] 10.1098/rsta.1997.0072, 355, 1481
- Kirrander A., Child M. S., Stolyarov A. V., 2006, *Phys. Chem. Chem. Phys.*, 8, 247
- Kramida A., Yu. Ralchenko Reader J., and NIST ASD Team 2018, NIST Atomic Spectra Database (ver. 5.5.2), NIST Atomic Spectra Database (ver. 5.5.2), [Online]. Available: <https://physics.nist.gov/asd> [2018, January 30]. National Institute of Standards and Technology, Gaithersburg, MD.
- Little D. A., Tennyson J., 2014, *Journal of Physics B: Atomic, Molecular and Optical Physics*, 47, 105204
- Little D. A., Chakrabarti K., Mezei J. Z., Schneider I. F., Tennyson J., 2014, *PHYSICAL REVIEW A*, 90, 052705
- Mitchell J. B. A., et al., 2005, *Journal of Physics B: Atomic, Molecular and Optical Physics*, 38, L175
- Motapon O., et al., 2014, *Phys. Rev. A*, 90, 012706
- Müller H. S. P., et al., 2015, *Astronomy & Astrophysics*, 582, L4
- Neufeld D. A., Wolfire M. G., 2016, *The Astrophysical Journal*, 826, 183
- Priestley F. D., Barlow M. J., Viti S., 2017, *Monthly Notices of the Royal Astronomical Society*, 472, 4444
- Roueff E., Alekseyev A. B., Bourlot J. L., 2014, *Astronomy & Astrophysics*, 566, A30
- Schilke P., et al., 2014, *Astronomy & Astrophysics*, 566, A29
- Stolyarov A. V., Child M. S., 2005, *Phys. Chem. Chem. Phys.*, 7, 2259
- Tennyson J., 1996, *Journal of Physics B: Atomic, Molecular and Optical Physics*, 29, 6185
- Tennyson J., 2010, *Physics Reports*, 491, 29
- Tennyson J., Noble C. J., 1984, *Computer Physics Communications*, 33, 421

APPENDIX A: SOME EXTRA MATERIAL








The numerical data for ArH⁺ dissociative recombination rate coefficients corresponding to the Fig. 3(b) can be found as supplementary material to this paper.

This paper has been typeset from a T_EX/L^AT_EX file prepared by the author.

Low-energy electron impact dissociative recombination and vibrational transitions of N_2^+

Cite as: J. Appl. Phys. 129, 053303 (2021); <https://doi.org/10.1063/5.0038609>

Submitted: 24 November 2020 . Accepted: 14 January 2021 . Published Online: 02 February 2021

 A. Abdoulanziz, C. Argentin,  V. Laporta,  K. Chakrabarti,  A. Bultel,  J. Tennyson,  I. F. Schneider, and  J. Zs. Mezei

COLLECTIONS

Paper published as part of the special topic on [Fundamentals and Applications of Atmospheric Pressure Plasmas](#) [ATMPP2021](#)



View Online



Export Citation



CrossMark

ARTICLES YOU MAY BE INTERESTED IN

[Self-organized pattern formation in radio frequency capacitively coupled discharges](#)

Journal of Applied Physics **129**, 053304 (2021); <https://doi.org/10.1063/5.0028599>





Your Qubits. Measured.

Meet the next generation of quantum analyzers

- Readout for up to 64 qubits
- Operation at up to 8.5 GHz, mixer-calibration-free
- Signal optimization with minimal latency

[Find out more](#)

 **Zurich Instruments**

Low-energy electron impact dissociative recombination and vibrational transitions of N_2^+

Cite as: J. Appl. Phys. **129**, 053303 (2021); doi: [10.1063/5.0038609](https://doi.org/10.1063/5.0038609)

Submitted: 24 November 2020 · Accepted: 14 January 2021 ·

Published Online: 2 February 2021



A. Abdoulanziz,¹  C. Argentin,^{1,2} V. Laporta,³  K. Chakrabarti,⁴  A. Bultel,²  J. Tennyson,^{1,5} 
I. F. Schneider,^{1,6,a)}  and J. Zs. Mezei^{1,7,b)} 

AFFILIATIONS

¹LOMC-UMR6294 CNRS-Université Le Havre Normandie, 76058 Le Havre, France

²CORIA-UMR6614 CNRS-Université de Rouen Normandie, 76800 Saint-Etienne du Rouvray, France

³Istituto per la Scienza e Tecnologia dei Plasmi, CNR, 70126 Bari, Italy

⁴Department of Mathematics, Scottish Church College, 700006 Kolkata, India

⁵Department of Physics and Astronomy, University College London, WC1E 6BT London, United Kingdom

⁶LAC-FRE2038, CNRS-Université Paris-Saclay, 91405 Orsay, France

⁷Institute for Nuclear Research, 4001 Debrecen, Hungary

Note: This paper is part of the Special Topic on Fundamentals and Applications of Atmospheric Pressure Plasmas.

a) Electronic mail: ioan.schneider@univ-lehavre.fr

b) Author to whom correspondence should be addressed: mezei.zsolt@atomki.hu

ABSTRACT

Cross sections and thermal rate coefficients are computed for electron-impact dissociative recombination and vibrational excitation/de-excitation of the N_2^+ molecular ion in its lowest six vibrational levels, for collision energies/temperatures up to 2.3 eV/5000 K.

Published under license by AIP Publishing. <https://doi.org/10.1063/5.0038609>

I. INTRODUCTION

The nitrogen molecule N_2 is one of the most widely studied species so far in plasma physics. Being very stable at low temperature, it is very abundant in the Earth atmosphere and is notably present in other planetary atmospheres—Titan 98.4%,¹ Triton² Pluto,³ Venus 3.5%, and Mars 1.9%.¹ For trans-Neptunian objects other than Pluto, this molecule is also one of the main components of the ices—spectroscopically observed at their surfaces—and may produce a very thin atmosphere when the temperature increases under solar irradiation.⁴ Under the influence of an electric field, high altitude planetary atmosphere can be crossed by giant discharges of a few milliseconds duration called sprites, whose spectroscopic signature is mainly due to spontaneous emission from N_2 excited electronic states.⁵ The application of N_2 as seeding gas in magnetically confined fusion plasmas (ITER and JET equipments) will help in the reduction of power loads on the tungsten divertor region. Nitrogen may be preferable as an extrinsic radiator to noble gases (neon) as it

mostly affects the divertor radiation without significantly increasing core radiation.^{6,7}

All these facts justify the various studies of the role of the N_2 molecule in the cold plasmas, from the state-to-state description of its electron impact induced reactivity^{8–10} to the detailed modeling of its contribution to the plasma kinetics.^{11–14}

Consequently, the N_2^+ cation is also of huge interest. Due to the solar irradiation, the production of N_2^+ on excited vibrational states plays a significant role in the characteristics of the Earth's thermosphere.¹⁵ It is also the main molecular cation in the atmosphere of Titan¹⁶ and Triton.¹⁷ On the other hand, during the atmospheric entry of a spacecraft in Earth's and Titan's atmospheres, the hypersonic compression of the gases leads to the formation of a plasma departing from local thermodynamic equilibrium.¹⁸ The ionic composition, including N_2^+ , plays a key role in the radiation emitted by the plasma in the near UV spectral region.¹⁹ In many plasma-assisted industrial processes elaborated so far, the plasma reactivity is greatly enhanced by the presence of N_2^+ . This is, for instance, the case in the ammonia synthesis in plasmas/liquid processes.²⁰ N_2^+ is also very

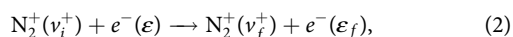
effective in the antibacterial treatment of polyurethane surfaces.²¹ Moreover, N_2^+ —like N_2 —is a key ingredient in the steel nitriding, resulting in improving its frictional wear resistance, surface hardness, and corrosion resistance.²² Furthermore, N_2^+ also plays a major role in the dermatological treatments based on the nitrogen radio-frequency discharges.²³

The characteristics of the nitrogen-containing plasmas cannot be fully understood without a deep knowledge of the reactivity of N_2^+ , in particular, by collisions with electrons.

Dissociative Recombination (DR) is the major molecular cation destruction reaction that takes place when an electron collides with the N_2^+ molecular cation, leading to neutral atomic fragments,



Here, ϵ is the kinetic energy of the incident electron and v_i^+ is the initial vibrational quantum number of the target. Alongside DR, other competitive processes can occur,



i.e., elastic (EC) ($v_f^+ = v_i^+$), inelastic (IC) ($v_f^+ > v_i^+$) and super-elastic (SEC) collisions ($v_f^+ < v_i^+$), v_f^+ standing for the final vibrational quantum number of the target ion. These processes are also known as Elastic Scattering (ES), Vibrational Excitation (VE), and Vibrational deExcitation (VdE), respectively.

The elementary non-thermal electron driven processes, in particular, dissociative recombination, have been studied experimentally using plasmas with laser induced photo-fluorescence techniques,²⁴ shock tubes,²⁵ discharge afterglow experiments,^{26,27} and microwave techniques.²⁸ The most detailed collisional data can be obtained in merged beam²⁹ and/or storage ring experiments.³⁰

Two different sets of theoretical calculations have been performed^{31–34} on the DR of N_2^+ . They involved different underlying quantum chemistry but rather similar nuclear dynamics calculations; both these studies focused on the ground and the lowest three vibrational levels of the N_2^+ target.

While both results show good agreement with the experiment for the ground vibrational level, the rates for the higher vibrational levels calculated in Ref. 31, contrary to those of Refs. 32–34, indicate less strong vibrational dependence on temperature, in agreement with the experimental results.

Our aim with this paper is to extend as far as possible the calculations started in Ref. 31. This extension refers to

- The kinetic energy of the incoming electron: up to 2.3 eV vs 1 eV previously.
- The elementary processes explored: besides the DR studied in the past, the VE and VdE cross sections and rate coefficients are computed.
- The vibrational levels considered in the vibrational transitions: up to the fifth excited level of the target vs the third previously and the lowest ten vibrational levels as the final ones.

The rotational effects have been neglected since they are important only at very low collision energies.

All these extensions make our results relevant for the atmospheric and cold plasma environments, at electron temperatures where the rotational effects can be neglected.

The paper is organized as follows: After a brief description of the theoretical approach (Sec. II), we present in more detail the molecular data used in the calculations (Sec. III) followed by the presentation of the results (Sec. IV). The paper is ended with conclusions.

II. THEORETICAL APPROACH

The efficiency of our method of modeling the electron/diatom cation collisions based on the Multichannel Quantum Defect Theory (MQDT) has been proved in many previous studies on different species, including H_2^+ and its isotopologues,^{35–37} ArH^+ ,³⁸ CH^+ ,³⁹ SH^+ ,⁴⁰ etc. The general ideas of our approach were already presented in detail in our previous study of the N_2^+ dissociative recombination³¹ and, therefore, here we restrict ourselves to its major steps.

The reactive processes (1) and (2) involve *ionization* channels—describing the scattering of an electron on the target cation—and *dissociation* channels—accounting for atom–atom scattering. The mixing of these channels results in quantum interference of the *direct* mechanism—in which the capture takes place into a doubly excited dissociative state of the neutral system—and the *indirect* one—in which the capture occurs via a Rydberg bound state of the molecule belonging to a *closed* channel, this state being predissociated by the dissociative one. In both mechanisms, the autoionization—based on the existence of *open* ionization channels—is

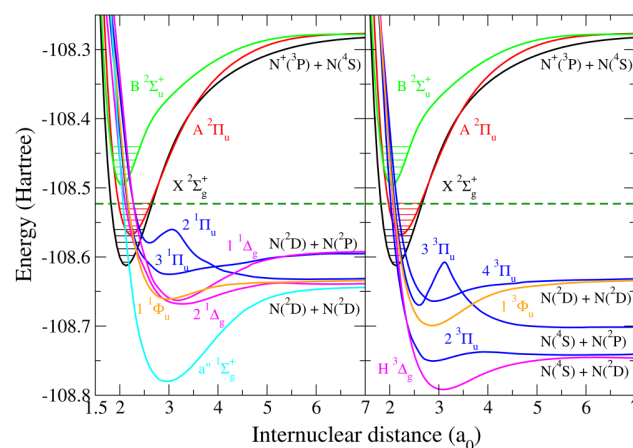


FIG. 1. Potential energy curves (PECs) relevant for the DR of N_2^+ .³¹ Target cation N_2^+ : ground electronic state ($X^2\Sigma_g^+$) black, first excited state ($A^2\Pi_u$) red, and second excited state ($B^2\Sigma_u^+$) green. Neutral system N_2 : Left panel, singlet states of different symmetries—blue for $1\Pi_u$, magenta for $1\Delta_g$, cyan for $a''1\Sigma_g^+$, and orange for $1\Phi_u$. Right panel, triplet states of different symmetries—blue for $3\Pi_u$, magenta for $H^3\Delta_g$, and orange for $3\Phi_u$. The lowest five vibrational levels of each electronic state of the ion and the dissociative asymptotic limits for all states are shown. The green dashed line gives the upper limit of the total energy of the system, above which our results are still reasonably correct (see the text).

in competition with the predissociation and can lead to the excitation or to the de-excitation of the cation.

One starts with the building of the *interaction matrix* \mathcal{V} that drives the collision, whose elements quantify the couplings between the different channels—ionization and/or dissociation ones.

More specifically, each of the ionization channels, built on the N_2^+ ion in one of its three lowest electronic states— $X^2\Sigma_g^+$, $A^2\Pi_u$, or $B^2\Sigma_u^+$, see Fig. 1—in a particular vibrational level, interacts not only with all the dissociation exit channels (Rydberg–valence interaction), but also with the other ionization channels (Rydberg–Rydberg interactions)—Fig. 2. Depending on the total energy of the system, these ionization channels can be *open*—either as entrance channels, describing the incident electron colliding the ion in its ground electronic state, or as exit channels, describing the autoionization, i.e., elastic scattering, vibrational excitation, and de-excitation—or *closed*—describing the resonant temporary captures into Rydberg states.

Once the \mathcal{V} -matrix is elaborated, we build the short-range reaction matrix \mathcal{K} of the collision, as a second order perturbative solution of the Lippmann–Schwinger equation. The diagonalized version of the \mathcal{K} -matrix (in the eigenchannel representation), whose eigenvalues are expressed in terms of long range phase-shifts of the eigenfunctions, together with the vibronic couplings between the ionization channels, serves for the building of the frame transformation matrices.

Applying a Cayley transformation on these latter matrices, we can setup the generalized scattering matrix X . The Seaton’s method

of “eliminating” the closed channels⁴¹ is then employed, resulting in the physical scattering matrix \mathcal{S} ,

$$S = X_{oo} - X_{oc} \frac{1}{X_{cc} - \exp(-i 2 \pi \nu)} X_{co}, \quad (3)$$

relying on the block-matrices involving open (X_{oo}), open and closed (X_{oc} and X_{co}), and closed (X_{cc}) channels. The diagonal matrix ν in the denominator of Eq. (3) contains the effective quantum numbers corresponding to the vibrational thresholds of the closed ionization channels at a given total energy of the system.

Finally, the cross section for the dissociative recombination and for the vibrational transitions—vibrational excitation/de-excitation and elastic scattering write, respectively, as

$$\sigma_{diss \leftarrow v_i^+} = \frac{\pi}{4\epsilon} \rho^{sym} \sum_{l,j} \left| S_{d_j, l v_i^+}^A \right|^2 \quad (4)$$

and

$$\sigma_{v_j^+ \leftarrow v_i^+} = \frac{\pi}{4\epsilon} \rho^{sym} \sum_{l,l'} \left| S_{l' v_j^+, l v_i^+}^A - \delta_{l,l'} \delta_{v_i^+, v_j^+} \right|^2, \quad (5)$$

where d_j stands for a given dissociative state and ρ^{sym} the ratio between the state multiplicities of the neutral and the target ion.

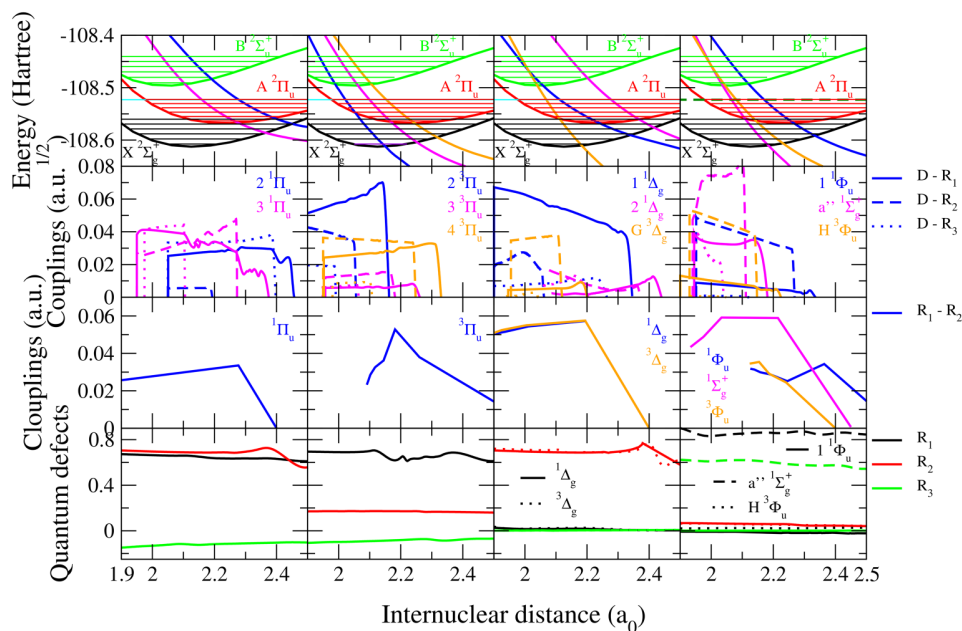


FIG. 2. Molecular data sets for the modeling of reactive collisions between electrons and N_2^+ .³¹ First row: PECs of the relevant states of the ion and of the neutral for all relevant symmetries. Second row: Rydberg–valence electronic couplings. Third row: Rydberg–Rydberg electronic couplings. Fourth row: Quantum defects characterizing the Rydberg series of states.

TABLE I. The energies of the vibrational levels of the N_2^+ molecular cation—relative to the ground one—involved either as initial or as final levels in the present calculations.

v^+	0	1	2	3	4	5	6	7	8	9
E_{v^+} (eV)	0.0	0.266	0.528	0.786	1.040	1.290	1.536	1.777	2.014	2.248

III. MOLECULAR DATA

The nuclear dynamics in low-energy electron/molecular cation collisions crucially depends on the molecular structure of the target and of the formed neutral—often superexcited—complex. The relevant molecular data sets consist in the potential energy curves (PECs) of the target cation—for the ground and for the excited electronic states—the PECs of the doubly excited bound or dissociative molecular states of the neutral, the quantum defect-functions characterizing the bound mono-excited Rydberg series of the neutral, and the coupling functions between the several—ionization and dissociation—continua.

One of the few quantum chemistry methods capable of producing the highly excited molecular states at the required accuracy is based on the R-Matrix Theory.⁴² Bound and resonant adiabatic potential energy curves of the valence and Rydberg states of N_2 having singlet and triplet symmetries were obtained by Little and Tennyson^{43,44} using R-matrix calculations on fine grid of internuclear separations. The diabatic curves, couplings, and quantum

defects relevant for the dissociative recombination of N_2^+ were presented in Ref. 31. The electronic states of the target were calculated using the standard quantum chemistry program suite Molpro.⁴⁵ Figure 1 shows the PECs of the dissociative molecular states of N_2 , as well as those of the relevant states of N_2^+ , involved in our previous³¹ and present calculations.

The same PECs are displayed by symmetries on the first row of Fig. 2, which contains the whole ensemble of molecular data relevant for the modeling of the internuclear dynamics. Whereas its first row illustrates how favorable the crossings are between the PECs of the dissociative states with those of the target ones—i.e., the Franck–Condon effect—the driving interactions of the dynamics—the Rydberg–valence couplings—are shown in the second row. The third row gives the Rydberg–Rydberg couplings: In the present calculation, only the couplings among the series correlating to the ground (X) and first excited (A) state of the ion have been considered. And finally, the last row of the figure displays the quantum defects characterizing the Rydberg series built, each of them, on one of the three cores X, A, and B.

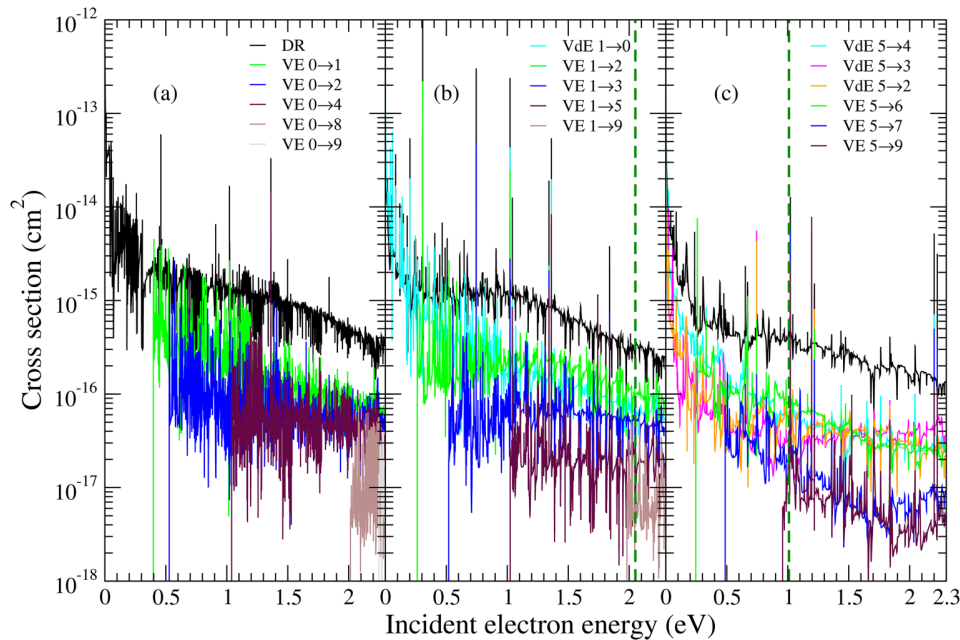


FIG. 3. Global DR, VE, and VdE cross sections of the N_2^+ $v_i^+ = 0$ (a), $v_i^+ = 1$ (b), and $v_i^+ = 5$ (c) as a function of the collision energy. For vibrational transitions (VE and VdE), we label the processes as transitions from the initial to the final vibrational levels of the target. The vertical dashed dark-green line gives the precision limit of the calculations (for details, see the text).

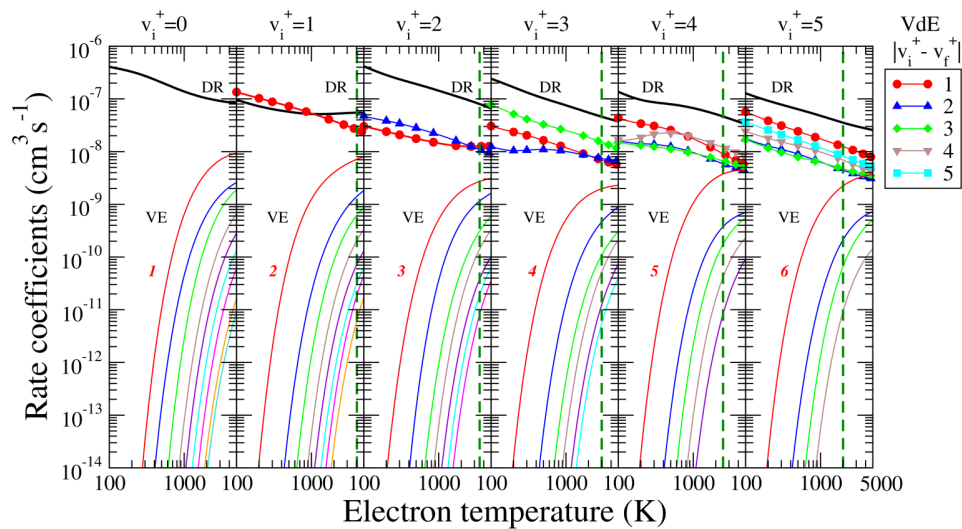


FIG. 4. Maxwell rate coefficients for all the relevant electron-induced processes on N_2^+ initially on $v_i^+ = 0-5$ vibrational levels: Dissociative recombination (black line), vibrational excitation (thin colored lines), and vibrational de-excitation (symbols and thick colored lines). For the vibrational excitations, all the transitions are shown up to $v_f^+ = 9$ with the lowest transition being labeled on each figure. The excitation and the de-excitation up to the final vibrational quantum numbers are given. The green dashed line gives the precision limit of our calculation given in temperatures (for details, see the text).

IV. RESULTS AND DISCUSSIONS

Based on the molecular data already presented in Fig. 2, we have performed nuclear dynamics calculations using the MQDT approach presented in Sec. II. The DR, VE, and VdE cross sections have been calculated considering the N_2^+ target in one of its lowest six vibrational states and focusing on the vibrational transitions to the lowest ten vibrational levels, when energetically accessible. Table I shows the energies of these latter levels relative to $v_i^+ = 0$ of the target.

The calculations have been performed by taking into account both the *direct* and the *indirect* mechanisms, the reaction matrix being evaluated in the second order, and all their vibrational levels—81, 66, and 50, respectively, associated with *open* or *closed*

ionization channels, according to the total energy of the system—have been fully accounted for.

The cross sections have been calculated for all the relevant symmetries listed in Figs. 1 and 2, for collision energies of the incident electron ranging between 10^{-5} and 2.3 eV, with an energy step of 0.01 meV. These cross sections have been summed up to obtain the global cross sections.

The global DR, VE, and VdE cross sections for target cations having initial vibrational levels $v_i^+ = 0, 1$, and 5 are shown in Figs. 3(a)–3(c), respectively. The vertical dark-green dashed lines in the mid and upper panels of Fig. 3 mark the energy below which the calculations are the most accurate. Above these thresholds, the calculations neglect the role of the higher lying dissociative states of the neutral.

TABLE II. List of the fitting parameters used in formula (6), temperature regions, and root mean squares for the DR rate coefficients of N_2^+ ($v_i^+ = 0-5$).

	v_i^+	Temperature range K	A ($\text{cm}^3 \text{s}^{-1} \text{K}^{-\alpha}$)	α	B (K)	RMS
DR	0	$100 \leq T \leq 700$	1.56020×10^{-5}	-0.679449	53.0333	0.0051
		$700 < T \leq 5000$	2.27099×10^{-7}	-0.129049	-388.399	0.0040
	1	$100 \leq T \leq 900$	1.11178×10^{-7}	-0.120373	-41.6843	0.0049
		$900 < T \leq 5000$	2.60704×10^{-8}	0.086645	-85.4307	0.0055
	2	$100 \leq T \leq 1000$	1.54430×10^{-6}	-0.345836	-28.1712	0.0053
		$1000 < T \leq 5000$	7.09592×10^{-6}	-0.544674	145.630	0.0030
	3	$100 \leq T \leq 5000$	1.53033×10^{-6}	-0.438705	-19.1368	0.0088
	4	$100 \leq T \leq 460$	5.25573×10^{-8}	0.042384	-76.5345	0.0032
		$460 < T \leq 5000$	3.42600×10^{-6}	-0.539469	208.028	0.0031
	5	$100 \leq T \leq 5000$	7.20627×10^{-7}	-0.394354	-7.90548	0.0106

TABLE III. List of the fitting parameters used in formula (6), temperature regions and root mean squares for the VE and VdE rate coefficients of N_2^+ ($v_i^+ = 0 - 5$ and $v_f^+ = 9$). The lines having bold v_f^+ values belong to VdE.

v_i^+	v_f^+	Temperature range (K)	A ($cm^3 s^{-1} K^{-\alpha}$)	α	B (K)	RMS
0	1	$270 \leq T \leq 5000$	$3.354\,76 \times 10^{-6}$	-0.584 062	4525.43	0.0073
		$400 \leq T \leq 1000$	$9.136\,78 \times 10^{-7}$	-0.553 899	6100.88	0.0021
		$1000 < T \leq 5000$	$3.045\,96 \times 10^{-7}$	-0.420 925	5907.02	0.0028
	3	$600 \leq T \leq 1500$	$9.670\,70 \times 10^{-7}$	-0.509 170	3228.55	0.0062
		$1500 < T \leq 5000$	$4.984\,32 \times 10^{-6}$	-0.699 380	9626.89	0.0040
		$850 \leq T \leq 2000$	$9.306\,28 \times 10^{-8}$	-0.292 379	119 89.3	0.0054
	4	$2000 < T \leq 5000$	$8.814\,69 \times 10^{-7}$	-0.546 342	126 51.0	0.0033
		$1000 \leq T \leq 5000$	$8.924\,93 \times 10^{-7}$	-0.596 125	14871.8	0.0066
		$1200 \leq T \leq 2500$	$1.447\,02 \times 10^{-6}$	-0.667 566	179 80.5	0.0022
	6	$2500 < T \leq 5000$	$5.491\,26 \times 10^{-6}$	-0.815 886	184 22.2	0.0009
		$1500 \leq T \leq 5000$	$1.655\,52 \times 10^{-6}$	-0.696 318	213 45.0	0.0190
		$1800 \leq T \leq 5000$	$9.867\,09 \times 10^{-8}$	-0.470 871	235 04.3	0.0071
	8	$2000 \leq T \leq 5000$	$1.340\,02 \times 10^{-6}$	-0.780 327	263 09.7	0.0025
		$100 \leq T \leq 5000$	$1.453\,41 \times 10^{-6}$	-0.478 820	19.3876	0.0195
		$190 \leq T \leq 900$	$3.828\,42 \times 10^{-6}$	-0.706 740	3146.96	0.0154
	2	$900 < T \leq 5000$	$1.451\,26 \times 10^{-8}$	-0.015 912	2326.31	0.0076
		$420 \leq T \leq 900$	$1.790\,64 \times 10^{-7}$	-0.420 497	6137.15	0.0011
		$900 < T \leq 5000$	$1.143\,29 \times 10^{-8}$	-0.080 877	5736.89	0.0040
1	0	$600 \leq T \leq 1500$	$5.536\,86 \times 10^{-8}$	-0.277 018	8726.55	0.0040
		$1500 < T \leq 5000$	$4.120\,85 \times 10^{-7}$	-0.506 359	9262.99	0.0065
		$850 \leq T \leq 5000$	$1.382\,79 \times 10^{-7}$	-0.426 255	120 08.4	0.0031
	6	$1100 \leq T \leq 2500$	$9.873\,96 \times 10^{-7}$	-0.707 100	148 13.1	0.0035
		$2500 < T \leq 5000$	$3.024\,02 \times 10^{-8}$	-0.318 434	136 84.3	0.0017
		$1300 \leq T \leq 5000$	$3.250\,83 \times 10^{-8}$	-0.336 661	167 32.0	0.0157
	8	$1500 \leq T \leq 5000$	$1.395\,45 \times 10^{-7}$	-0.467 278	203 48.3	0.0062
		$1800 \leq T \leq 5000$	$3.505\,37 \times 10^{-8}$	-0.362 041	226 92.0	0.0027
		$100 \leq T \leq 1500$	$1.046\,03 \times 10^{-7}$	-0.287 973	-9.07849	0.0073
	2	$1500 < T \leq 5000$	$4.350\,37 \times 10^{-9}$	0.116 715	-377.074	0.0027
		$100 \leq T \leq 5000$	$6.634\,40 \times 10^{-7}$	-0.498 417	38.4238	0.0193
		$200 \leq T \leq 700$	$1.791\,99 \times 10^{-7}$	-0.415 799	2977.42	0.0005
	3	$700 < T \leq 5000$	$7.478\,37 \times 10^{-8}$	-0.306 566	2843.67	0.0089
		$400 \leq T \leq 1300$	$4.275\,98 \times 10^{-6}$	-0.800 392	6144.90	0.0036
		$1300 < T \leq 5000$	$4.375\,39 \times 10^{-8}$	-0.268 995	5056.36	0.0148
	5	$600 \leq T \leq 1500$	$7.029\,48 \times 10^{-8}$	-0.367 691	8687.59	0.0076
		$1500 < T \leq 5000$	$8.342\,12 \times 10^{-9}$	-0.117 668	8217.86	0.0022
		$850 \leq T \leq 5000$	$9.678\,64 \times 10^{-8}$	-0.401 678	114 29.0	0.0164
2	7	$1000 \leq T \leq 2500$	$9.385\,61 \times 10^{-7}$	-0.733 592	145 27.8	0.0013
		$2500 < T \leq 5000$	$1.752\,59 \times 10^{-7}$	-0.547 538	139 60.8	0.0012
		$1300 \leq T \leq 5000$	$1.130\,24 \times 10^{-6}$	-0.737 221	175 18.6	0.0117
	9	$1500 \leq T \leq 5000$	$1.462\,92 \times 10^{-7}$	-0.513 870	197 32.3	0.0137
		$100 \leq T \leq 5000$	$3.601\,61 \times 10^{-7}$	-0.490 909	23.3038	0.0108
		$100 \leq T < 700$	$2.526\,73 \times 10^{-9}$	0.215 750	-58.7472	0.0174
	1	$700 \leq T < 5000$	$7.862\,65 \times 10^{-8}$	-0.292 543	41.8077	0.0060
		$100 \leq T \leq 700$	3.69265×10^{-7}	-0.399 263	-29.4462	0.0087
		$700 < T \leq 5000$	$1.889\,55 \times 10^{-6}$	-0.594 995	205.425	0.0045
	4	$100 \leq T \leq 560$	$3.679\,69 \times 10^{-7}$	-0.546 948	2807.96	0.0290
		$560 < T \leq 5000$	$1.291\,98 \times 10^{-7}$	-0.410 534	2682.71	0.0112
		$440 \leq T \leq 1300$	$4.829\,97 \times 10^{-7}$	-0.335 457	5887.42	0.0106
	5	$1300 < T \leq 5000$	$8.499\,83 \times 10^{-9}$	-0.137 448	5427.34	0.0084
		$650 \leq T \leq 1700$	$1.541\,45 \times 10^{-7}$	-0.532 191	9039.15	0.0032
		$1300 < T \leq 5000$	$9.065\,25 \times 10^{-10}$	0.052 019	7617.98	0.0111
	7	$850 \leq T \leq 2000$	$2.496\,01 \times 10^{-8}$	-0.300 658	113 33.8	0.0091

TABLE III. (Continued.)

v_i^+	v_f^+	Temperature range (K)	A ($\text{cm}^3\text{s}^{-1}\text{K}^{-\alpha}$)	α	B (K)	RMS
4	8	$2000 < T \leq 5000$	$4.154\,24 \times 10^{-9}$	$-0.093\,853$	$108\,88.7$	0.0003
		$1100 \leq T \leq 5000$	$2.275\,58 \times 10^{-9}$	$-0.079\,760$	$137\,23.8$	0.0189
		$1300 \leq T \leq 5000$	$3.068\,56 \times 10^{-7}$	$-0.645\,208$	$172\,78.8$	0.0034
		$100 \leq T \leq 400$	$6.378\,63 \times 10^{-8}$	$-0.145\,968$	-28.4720	0.0082
	3	$400 < T \leq 5000$	$6.361\,81 \times 10^{-6}$	$-0.825\,697$	192.216	0.0072
		$100 \leq T \leq 900$	$6.554\,02 \times 10^{-8}$	$-0.262\,797$	23.6274	0.0227
		$900 < T \leq 5000$	$1.058\,21 \times 10^{-7}$	$-0.378\,427$	-214.371	0.0140
	2	$100 \leq T \leq 440$	$2.329\,72 \times 10^{-8}$	$-0.116\,666$	$-8.972\,62$	0.0057
		$440 \leq T \leq 5000$	$2.270\,97 \times 10^{-7}$	$-0.444\,141$	124.096	0.0044
		$100 \leq T \leq 400$	$2.129\,11 \times 10^{-9}$	$0.389\,295$	-22.4417	0.0183
	1	$400 < T \leq 5000$	$2.100\,16 \times 10^{-6}$	$-0.645\,580$	264.431	0.0066
		$190 \leq T \leq 900$	$7.698\,58 \times 10^{-7}$	$-0.525\,187$	2964.92	0.0217
		$900 < T \leq 5000$	$2.432\,98 \times 10^{-6}$	$-0.666\,480$	3146.71	0.0028
	0	$400 \leq T \leq 1200$	$4.497\,41 \times 10^{-6}$	$-0.896\,475$	5955.41	0.0017
		$1200 < T \leq 5000$	$8.844\,87 \times 10^{-7}$	$-0.708\,372$	5563.92	0.0076
		$580 \leq T \leq 1500$	$1.179\,91 \times 10^{-5}$	$-0.974\,002$	8780.06	0.0036
	7	$1500 < T \leq 5000$	$7.346\,77 \times 10^{-7}$	$-0.655\,786$	8053.50	0.0084
		$800 \leq T \leq 2000$	$4.107\,91 \times 10^{-6}$	$-0.886\,512$	$11\,434.1$	0.0015
		$2000 < T \leq 5000$	$3.732\,24 \times 10^{-7}$	$-0.615\,368$	$107\,37.3$	0.0026
	6	$1000 \leq T \leq 2500$	$1.137\,54 \times 10^{-7}$	$-0.519\,202$	$136\,77.4$	0.0126
		$2500 < T \leq 5000$	$1.251\,00 \times 10^{-8}$	$-0.269\,595$	$130\,39.9$	0.0002
5	4	$100 \leq T \leq 5000$	$4.509\,70 \times 10^{-7}$	$-0.474\,388$	-11.0566	0.0125
		$100 \leq T \leq 500$	$5.830\,98 \times 10^{-8}$	$-0.304\,037$	-19.8859	0.0073
		$500 < T \leq 5000$	$1.317\,81 \times 10^{-7}$	$-0.447\,966$	-55.6242	0.0132
	3	$100 \leq T \leq 5000$	$6.216\,86 \times 10^{-8}$	$-0.340\,696$	-27.4858	0.0101
		$100 \leq T \leq 900$	$8.495\,09 \times 10^{-8}$	$-0.310\,555$	-17.4355	0.0022
		$900 < T \leq 5000$	$1.089\,34 \times 10^{-6}$	$-0.653\,000$	198.309	0.0031
	2	$100 \leq T \leq 5000$	$3.732\,56 \times 10^{-7}$	$-0.501\,538$	$2.803\,63$	0.0122
		$190 \leq T \leq 5000$	$1.476\,02 \times 10^{-7}$	$-0.367\,489$	2789.39	0.0150
		$400 \leq T \leq 1200$	$3.158\,77 \times 10^{-8}$	$-0.292\,229$	5543.78	0.0036
	1	$1200 < T \leq 5000$	$1.105\,25 \times 10^{-6}$	$-0.712\,115$	6289.63	0.0090
		$600 \leq T \leq 5000$	$4.107\,24 \times 10^{-7}$	$-0.585\,006$	8593.14	0.0153
		$850 \leq T \leq 2000$	$7.616\,66 \times 10^{-7}$	$-0.744\,946$	$113\,07.6$	0.0038
	0	$2000 < T \leq 5000$	$7.878\,95 \times 10^{-8}$	$-0.489\,941$	$106\,18.0$	0.0036

Nevertheless, the data displayed continue to be reasonably correct above these thresholds because these dissociative states penetrate into the ionization continuum well above these thresholds, forming favorable/non-vanishing Franck–Condon overlaps with the target electronic states at even higher collision energies. This Franck–Condon overlap is proportional to the first order term of the direct cross section. In addition, the couplings of these dissociative states with the Rydberg series are generally weaker, leading to less important cross sections in second order.

The *direct* mechanism is responsible for the background $1/E$ behavior of the cross sections, while the *indirect* one through the temporary capture into the Rydberg states produces all the resonance structures dominating the cross sections.

Among all the processes studied here, dissociative recombination (black curves in Fig. 3) predominates. The global DR cross section increases as we change the initial vibrational state of the target by unity and starts to decrease as we arrive at $v_i^+ = 5$. While

the vibrational de-excitation (cyan curves for initial vibrational levels higher than 0) is in competition with the DR cross section, at higher collision energies their overall cross section values are at least with a factor of 5 smaller than those of the DR. The vibrational excitations (green, blue, violet, maroon, etc., curves) show threshold effects at the collision energies where they become open. Moreover, one can see that for a given initial vibrational level v_i^+ the $|\Delta v^+| = 1$ vibrational transitions are the most probable ones, decreasing monotonically with $|\Delta v^+|$ for the transitions between more distant levels.

Figure 4 shows the thermal rate coefficients of all processes for the six lowest initial vibrational levels of N_2^+ . The green dashed line gives the precision limits of our calculation expressed now in electron temperatures.

The DR (solid black line in Fig. 4) and VdE (symbols and thick colored lines) rate coefficients decrease monotonically with the temperature, while the VE (thin colored lines) ones increase, partly because of the threshold behavior of their corresponding

cross sections. The largest rate coefficients we obtained are those for the DR. With the exception of the $v_i^+ = 1$ case, the VdE rate coefficients are smaller than those for the DR. At $v_i^+ = 1$, the DR is in competition with VdE but, for $v_i^+ > 1$, DR exceeds VdE by a factor of 2–5. We can see from Fig. 4 that the VE process is relatively important at high electron temperatures only. Moreover, the higher we go with the initial vibrational quantum number of the target cation, the more probable VE becomes.

And finally, in order to allow the versatile implementation of the rate coefficients in kinetics modeling codes, we have fitted them with Arrhenius-type formulas. The calculated rate coefficients for the dissociative recombination of electrons with N_2^+ in each of its lowest 6 vibrational levels ($v_i^+ = 0, 1, \dots, 5$) have been interpolated using the mathematical form,

$$k^{fit}(T) = A T^\alpha \exp\left[-\frac{B}{T}\right] \quad (6)$$

over the electron temperature range $100 \text{ K} \leq T_e \leq 5000 \text{ K}$ and/or for rate coefficients larger than $10^{-14} \text{ cm}^3 \text{ s}^{-1}$, as displayed in Fig. 4. The A , α , and B fitting parameters used in Eq. (6) together with the temperature regions are listed in Table II for DR and in Table III for VE and VdE processes. The efficiency of the fitting is characterized by the root mean squares, and we were able to reproduce the MQDT rate coefficients with a precision higher than 97%.

V. CONCLUSIONS

The present work extends considerably our previous study of the dissociative recombination of N_2^+ with electrons.³¹ Making use of the molecular data set calculated in Refs. 31, 43, and 44 and of our stepwise MQDT method, we have performed calculations for the lowest 6 vibrational levels of the target cation in collision with electrons having kinetic energy up to 2.3 eV and, in the case of thermal equilibrium, electronic temperature up to 5000 K. We have provided cross sections and rate coefficients for dissociative recombination, vibrational excitation, and de-excitation of the N_2^+ molecular cation, important for the detailed kinetic modeling of cold astrophysical, atmospheric, and laboratory plasmas. The calculated cross sections and rate coefficients are available on request.

ACKNOWLEDGMENTS

The authors acknowledge support from Fédération de Recherche Fusion par Confinement Magnétique (CNRS and CEA), La Région Normandie, FEDER, and LabEx EMC3 via the projects PTOLEMEE, Bioengine, EMoPlaF, COMUE Normandie Université, the Institute for Energy, Propulsion and Environment (FR-IEPE), the European Union via COST (European Cooperation in Science and Technology) action MD-GAS (CA18212), and ERASMUS-plus conventions between Université Le Havre Normandie and University College London. This work has received funding from the Euratom Research and Training Programme 2014–2018 and 2019–2020 under Grant Agreement No. 633053. The views and opinions expressed herein do not necessarily reflect those of the European Commission. The authors are indebted to Agence Nationale de la Recherche (ANR) via the project MONA, Centre National de la Recherche Scientifique via the GdR TheMS and the DYMCOM

project, and the Institute Pascal, University Paris-Saclay for the warm hospitality during the DYMCOM workshop. This work was supported by the Programme National “Physique et Chimie du Milieu Interstellaire” (PCMI) of CNRS/INSU with INC/INP co-funded by CEA and CNES. J.Zs.M. thanks the financial support of the National Research, Development and Innovation Fund of Hungary, under the K18 funding scheme with Project No. K128621.

DATA AVAILABILITY

The data that support the findings of this study are available from the corresponding author upon reasonable request.

REFERENCES

- V. A. Krasnopolsky, “Chemical composition of Titan’s atmosphere and ionosphere: Observations and the photochemical model,” *Icarus* **236**, 83–91 (2014).
- J. L. Elliot, D. F. Strobel, X. Zhu, J. A. Stansberry, L. H. Wasserman, and O. G. Franz, “The thermal structure of Triton’s middle atmosphere,” *Icarus* **143**, 425–428 (2020).
- V. A. Krasnopolsky, “A photochemical model of Pluto’s atmosphere and ionosphere,” *Icarus* **335**, 113374 (2020).
- L. A. Young, F. Braga-Ribas, and R. E. Johnson, “Volatile evolution and atmospheres of trans-neptunian objects,” in *The Trans-Neptunian Solar System*, edited by D. Prialnik, M. A. Barucci, and L. A. Young (Elsevier, The Netherlands, 2020), Chap. 6, pp. 127–151.
- R. A. Armstrong, D. M. Suszcynsky, W. A. Lyons, and T. E. Nelson, “Multi-color photometric measurements of ionization and energies in sprites,” *Geophys. Res. Lett.* **27**, 653–656 (2000).
- M. Oberkofler *et al.*, “First nitrogen-seeding experiments in jet with the ITER-like wall,” *J. Nucl. Mater.* **438**, S258 (2013).
- C. Giroud and JET-EFDA Contributors *et al.*, “(Exc/p3-02) integration of a radiative divertor for heat load control into jet operational scenarios,” in *Proceedings of the 23rd IAEA Fusion Energy Conference, Daejeon, 11–16 October 2010* (International Atomic Energy Agency, 2010).
- V. Laporta, R. Celiberto, and J. M. Wadehra, “Theoretical vibrational-excitation cross sections and rate coefficients for electron-impact resonant collisions involving rovibrationally excited N_2 and NO molecules,” *Plasma Sources Sci. Technol.* **21**, 055018 (2012).
- V. Laporta, D. A. Little, R. Celiberto, and J. Tennyson, “Electron-impact resonant vibrational excitation and dissociation processes involving vibrationally excited N_2 molecules,” *Plasma Sources Sci. Technol.* **23**, 065002 (2014).
- M. Kitajima, T. Kishino, T. Okumura, N. Kobayashi, A. Sayama, Y. Mori, K. Hosaka, T. Odagiri, M. Hoshino, and H. Tanaka, “Low-energy and very-low energy total cross sections for electron collisions with N_2 ,” *Eur. Phys. J. D* **71**, 139 (2017).
- V. Guerra, P. A. Sa, and J. Loureiro, “Kinetic modeling of low-pressure nitrogen discharges and post-discharges,” *Eur. Phys. J. Appl. Phys.* **28**, 125 (2004).
- M. Panesi, T. E. Magin, A. Bourdon, A. Bultel, and O. Chazot, “Electronic excitation of atoms and molecules for the FIRE II flight experiment,” *J. Thermophys. Heat Trans.* **25**, 361 (2011).
- M. Capitelli, G. Colonna, G. D’Ammando, V. Laporta, and A. Laricchiuta, “Nonequilibrium dissociation mechanisms in low temperature nitrogen and carbon monoxide plasmas,” *Chem. Phys.* **438**, 31 (2014).
- K. L. Heritier, R. L. Jaffe, V. Laporta, and M. Panesi, “Energy transfer models in nitrogen plasmas: Analysis of $N_2(x^1\sigma_g^+) - n(^1s_u) - e^-$ interaction,” *J. Chem. Phys.* **141**, 184302 (2014).
- M. R. Torr, “Neutral and ion chemistry and solar fluxes,” *J. Geomag. Geoelectr.* **35**, 131–153 (1983).
- H. Lammer, W. Stumpner, G. Molina-Cuberos, S. Bauer, and T. Owen, “Nitrogen isotope fractionation and its consequence for Titan’s atmospheric evolution,” *Planet. Space Sci.* **48**, 529–543 (2000).

- ¹⁷Y. L. Yung and J. R. Lyons, "Triton: Topside ionosphere and nitrogen escape," *Geophys. Res. Lett.* **17**, 1717–1720 (1990).
- ¹⁸J. Annaloro and A. Bultel, "Vibrational and electronic collisional-radiative model in air for earth entry problems," *Phys. Plasmas* **21**, 123512 (2020).
- ¹⁹Y. Plastinin, G. Karabadzak, B. Khmelinin, B. Zemliansky, A. Gorshkov, and G. Zalogin, "Measurements of the UV radiation generated by the Soyuz spacecraft transport capsule during reentry," in *45th AIAA Aerospace Sciences Meeting and Exhibit* (AIAA, 2007/2012), <https://arc.aiaa.org/doi/pdf/10.2514/6.2007-815>.
- ²⁰T. Sakakura, N. Murakami, Y. Takatsuji, M. Morimoto, and T. Haruyama, "Contribution of discharge excited atomic N, N₂⁺, and N₂⁺ to a plasma/liquid interfacial reaction as suggested by quantitative analysis," *Chem. Phys. Chem.* **20**, 1467–1474 (2019).
- ²¹I. A. Morozov, A. S. Mamaev, I. V. Osorgina, L. M. Lemkina, V. P. Korobov, A. Y. Belyaev, S. E. Porozova, and M. G. Sherban, "Structural-mechanical and antibacterial properties of a soft elastic polyurethane surface after plasma immersion N₂⁺ implantation," *Mater. Sci. Eng. C* **62**, 242–248 (2016).
- ²²M. K. Sharma and B. K. Saikia, "Discharge conditions and emission spectroscopy of N₂ and N₂⁺ active species in a variable power DC pulsed plasma used for steel nitriding," *Indian J. Pure Appl. Phys.* **46**, 463–470 (2008); available at <http://nopr.niscair.res.in/handle/123456789/1889>.
- ²³J. D. Holcomb and A. Schucker, "Helium plasma skin regeneration: Evaluation of skin tissue effects in a porcine model and comparison to nitrogen plasma skin regeneration," *Lasers Surg. Med.* **52**, 23–32 (2020).
- ²⁴E. C. Zipf, "The dissociative recombination of vibrationally excited N₂⁺ ions," *Geophys. Res. Lett.* **7**, 645–648 (1980).
- ²⁵A. J. Cunningham and R. M. Hobson, "Dissociative recombination at elevated temperatures. IV. N₂⁺ dominated afterglows," *J. Phys. B At. Mol. Phys.* **5**, 2328–2331 (1972).
- ²⁶S. K. Mitra, "Active nitrogen," *Phys. Rev.* **90**, 516–521 (1953).
- ²⁷J. Kaplan, "Active nitrogen," *Phys. Rev.* **73**, 494–496 (1948).
- ²⁸M. A. Biondi and S. C. Brown, "Measurement of electron-ion recombination," *Phys. Rev.* **76**, 1697–1700 (1949).
- ²⁹C. Noren, F. B. Yousif, and J. B. A. Mitchell, "Dissociative recombination and excitation of N₂⁺," *J. Chem. Soc. Faraday Trans. 2* **85**, 1697 (1989).
- ³⁰J. R. Peterson, A. L. Padellec, H. Danared, G. H. Dunn, M. Larsson, A. Larson, R. Peverall, C. Strömholm, S. Rosén, M. af Ugglas, and W. J. van der Zande, "Dissociative recombination and excitation of N₂⁺: Cross sections and product branching ratios," *J. Chem. Phys.* **108**, 1978–1988 (1998).
- ³¹D. A. Little, K. Chakrabarti, J. Z. Mezei, I. F. Schneider, and J. Tennyson, "Dissociative recombination of N₂⁺: An ab initio study," *Phys. Rev. A* **90**, 052705 (2014).
- ³²S. L. Guberman, "Spectroscopy above the ionization threshold: Dissociative recombination of the ground vibrational level of N₂⁺," *J. Chem. Phys.* **137**, 074309 (2012).
- ³³S. L. Guberman, "The vibrational dependence of dissociative recombination: Cross sections for N₂⁺," *J. Chem. Phys.* **139**, 124318 (2013).
- ³⁴S. L. Guberman, "The vibrational dependence of dissociative recombination: Rate constants for N₂⁺," *J. Chem. Phys.* **141**, 204307 (2014).
- ³⁵K. Chakrabarti, D. R. Backodissa-Kiminou, N. Pop, J. Z. Mezei, O. Motapon, F. Lique, O. Dulieu, A. Wolf, and I. F. Schneider, "Dissociative recombination of electrons with diatomic molecular cations above dissociation threshold: Application to H₂⁺ and HD⁺," *Phys. Rev. A* **87**, 022702 (2013).
- ³⁶O. Motapon, N. Pop, F. Argoubi, J. Z. Mezei, M. D. Epee Epee, A. Faure, M. Telnini, J. Tennyson, and I. F. Schneider, "Rotational transitions induced by collisions of HD⁺ ions with low-energy electrons," *Phys. Rev. A* **90**, 012706 (2014).
- ³⁷M. D. Epée Epée, J. Z. Mezei, O. Motapon, N. Pop, and I. F. Schneider, "Reactive collisions of very low-energy electrons with H₂⁺: Rotational transitions and dissociative recombination," *Mon. Not. R. Astron. Soc.* **455**, 276–281 (2016).
- ³⁸A. Abdoulanziz, F. Colboc, D. A. Little, Y. Moulane, J. Z. Mezei, E. Roueff, J. Tennyson, I. F. Schneider, and V. Laporta, "Theoretical study of ArH⁺ dissociative recombination and electron-impact vibrational excitation," *Mon. Not. R. Astron. Soc.* **479**, 2415–2420 (2018).
- ³⁹J. Z. Mezei, K. Chakrabarti, M. D. Epée Epée, O. Motapon, C. H. Yuen, M. A. Ayouz, N. Douguet, S. F. dos Santos, V. Kokoouline, and I. F. Schneider, "Electron-induced excitation, recombination, and dissociation of molecular ions initiating the formation of complex organic molecules," *ACS Earth Space Chem.* **3**, 2376 (2019).
- ⁴⁰D. O. Kashinski, D. Talbi, A. P. Hickman, O. E. Di Nallo, F. Colboc, K. Chakrabarti, I. F. Schneider, and J. Z. Mezei, "A theoretical study of the dissociative recombination of SH⁺ with electrons through the ²π states of SH," *J. Chem. Phys.* **146**, 204109 (2017).
- ⁴¹M. J. Seaton, "Quantum defect theory," *Rep. Prog. Phys.* **46**, 167 (1983).
- ⁴²J. Tennyson, "Electron-molecule collision calculations using the *R*-matrix method," *Phys. Rep.* **491**, 29–76 (2010).
- ⁴³D. A. Little and J. Tennyson, "An ab initio study of singlet and triplet Rydberg states of N₂," *J. Phys. B At. Mol. Opt. Phys.* **46**, 145102 (2013).
- ⁴⁴D. A. Little and J. Tennyson, "An *R*-matrix study of singlet and triplet continuum states of N₂," *J. Phys. B At. Mol. Opt. Phys.* **47**, 105204 (2014).
- ⁴⁵H.-J. Werner, P. J. Knowles, G. Knizia, F. R. Manby, and M. Schütz, "Molpro: A general-purpose quantum chemistry program package," *WIREs Comput. Mol. Sci.* **2**, 242–253 (2012).



Contents lists available at ScienceDirect

Atomic Data and Nuclear Data Tables

journal homepage: www.elsevier.com/locate/adtReactive collisions between electrons and BeT^+ : Complete set of thermal rate coefficients up to 5000 KN. Pop^a, F. Iacob^{b,*}, S. Niyonzima^c, A. Abdoulanziz^d, V. Laporta^e, D. Reiter^f, I.F. Schneider^{d,g}, J.Zs. Mezei^{d,h}^a Department of Physical Foundations of Engineering, Politehnica University of Timisoara, 300223 Timisoara, Romania^b Department of Physics, West University of Timisoara, 300223 Timisoara, Romania^c Département de Physique, Fac. des Sciences, Université du Burundi, B.P. 2700 Bujumbura, Burundi^d LOMC-UMR 6294 CNRS-Université Le Havre Normandie, BP 540-76 058 Le Havre, France^e Istituto per la Scienza e Tecnologia dei Plasmi, CNR, Bari, Italy^f Institute for Laser and Plasma Physics, Heinrich-Heine-University, D-40225 Düsseldorf, Germany^g LAC-UMR 8199, CNRS, Université Paris-Saclay, ENS Cachan, 91405 Orsay, France^h Institute for Nuclear Research, 4001 Debrecen, Hungary

ARTICLE INFO

Article history:

Received 10 November 2020

Received in revised form 11 January 2021

Accepted 13 January 2021

Available online 16 February 2021

Keywords:

Dissociative recombination

Plasma-wall interaction

Beryllium monohydride

Vibrational excitation

Isotopic effect

ABSTRACT

Rate coefficients for the dissociative recombination, vibrational excitation and vibrational de-excitation of the BeT^+ ion for all vibrational levels of its ground electronic state ($X^1\Sigma^+, v_i^+ = 0, \dots, 27$) are reported, including in the calculation the contribution of super-excited states of the BeT complex pertaining to three electronic symmetries - $^2\Pi$, $^2\Sigma^+$, and $^2\Delta$. These data are suitable for the kinetic modeling of beryllium and tritium containing plasma, as encountered in magnetic fusion devices with beryllium walls (JET, ITER). In the present study we restrict ourselves to incident electron energies from 10^{-3} up to 2.7 eV, and to electron temperatures between 100 and 5000 K, respectively. Together with our earlier and closely related studies on the BeH^+ and BeD^+ systems, this present work completes the isotopic coverage for the beryllium monohydride ions. The vibrational energy (rather than the vibrational quantum state) is identified as a proper isotopic similarity parameter, e.g., for reduced but still isotopically correct plasma chemistry models.

© 2021 Elsevier Inc. All rights reserved.

* Corresponding author.

E-mail address: felix.iacob@e-uvr.ro (F. Iacob).

Contents

1. Introduction.....	2
2. Theoretical approach of the dynamics.....	3
3. Results and discussions.....	3
4. Conclusions.....	4
Declaration of competing interest.....	5
Acknowledgments.....	5
Appendix A. Supplementary data.....	5
References.....	5
Explanation of Graphs.....	6
Graph 1–5. Dissociative recombination, vibrational excitation and de-excitation Maxwell rate coefficients for all the vibrational levels of BeH ⁺ in its ground electronic state.....	6
Graph 6. Ratios of the dissociative recombination rate coefficients for BeD ⁺ vs BeH ⁺ (left), and for BeT ⁺ vs BeH ⁺ (right) molecular cations, as function of the quantum number of the initial vibrational level of the target and of temperature.....	6
Graph 7. Dissociative recombination rate coefficient for the three beryllium monohydride isotopologue cations as function of the energy of the initial vibrational level of the target – relative to the ground vibrational level – for three different electron temperatures.....	6
Explanation of Tables.....	7
Table 1. List of fitting parameters according to Eq. (8), minimum and maximum values of relative difference and root mean squares calculated for dissociative recombination for the $v_i^+ = 0 - 10$ vibrational levels of the ground electronic state of BeT ⁺	7
Tables 2–12. List of fitting parameters according to Eq. (8), minimum and maximum values of relative difference and root mean squares calculated for vibrational transitions ($\Delta v_{max} = 10$) for the $v_i^+ = 0 - 10$ vibrational levels of the ground electronic state of BeT ⁺	7
Table 13. List of dissociative recombination rate coefficient showing the isotopic effects displayed in Graph 7.....	7

1. Introduction

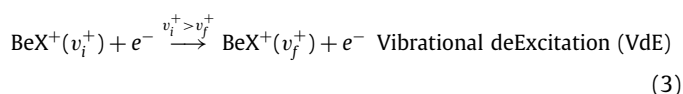
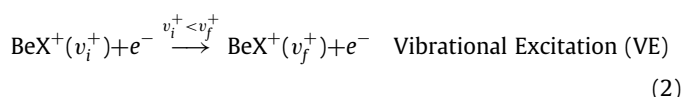
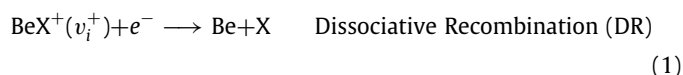
The plasma in the peripheral region (plasma boundary) of the ITER fusion reactor [1] necessarily interacts with the first wall materials, which are mostly covered with the low Z metal beryllium in the main chamber. In the outer (near wall) plasma domains this leads to a complex diversity of interconnected physical and chemical elementary processes [2]. The fuel used in the activated phases in next step magnetic fusion reactors consists of deuterium and the tritium at equal concentrations. The d-t fusion reaction leads to helium and neutrons as products, which carry the excess energy from these fusion processes as kinetic energy. While the neutrons leave the plasma flame, the helium ash is confined and therefore magnetically guided out (together with the other plasma constituents) from the main plasma chamber into the so called divertor [1,2]. The latter is equipped with pumps and high heat flux components (currently envisaged there: tungsten target surfaces).

Beryllium and tungsten are therefore considered as major plasma-facing materials for the ITER reactor [3–5] which, once released, act as plasma impurities. Thus it is of great importance to quantitatively understand their release, the transport, and the chemical reactivity of these metals in the plasma. The main chamber beryllium wall is exposed to plasma heat and particle bombardment from the outer boundary plasma region. Identification and quantification of the various release candidate mechanisms, such as physical, chemical sputtering or other such processes, is still an active field of ongoing research in magnetic confinement fusion [3,6,7]. Chemically assisted physical sputtering contributes to the formation of beryllium atoms at surfaces; release mechanisms of molecular forms BeH or BeH₂ may also play a role. The beryllium atoms or beryllium hydrides in turn will enter into the plasma, fragment (dissociate) and radiate there, and/or form further molecular species like BeH, BeD and BeT (or their ions) in chemical reactions with the atoms of the fuel (H, D, T) or their molecules.

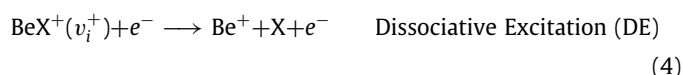
Besides the experimentally confirmed presence of Be containing neutral atomic and molecular species in magnetic fusion plasma, their ionic counterparts (Be⁺, BeX⁺, where X stands

for H, D, or T) were also presumed early [8–10] and meanwhile also been experimentally confirmed by spectroscopic methods [11–15]. Even though the fuel hydrogen isotopes remain, by far, the dominant gas and charged components, in the colder edge/divertor regions collisions between comparatively low energy (0.1 – 100 eV) electrons and BeX⁺ ions can play a significant role for the overall transport and fragmentation pathways of these impurities and hence, globally, for the fusion plasma flame purity. Typically, in current fusion devices related impurity wall release rates are inferred only rather indirectly, via intensity of light emission from the Be and BeX containing plasma constituents. However, this experimental procedure combines two unknowns: firstly the surface release mechanisms and rates, and, secondly, the (mostly) electron collision driven volumetric collisional processes (incl. fragmentation, excitation, etc.). Our present computational work on the BeX⁺ family of ions contributes to a wider effort to separate these two unknowns, by isolating the latter with detailed theoretical cross section calculations, hence to make the former then better experimentally accessible.

The most relevant reactive collisions starting from BeX⁺ ions that can take place are the following:



and, at high collision energies – which will be a range addressed in future work:



where v_i^+ and v_f^+ denote the initial and final vibrational quantum numbers of the target cation.

In the framework of the Multichannel Quantum Defect Theory (MQDT) [16–21] we have performed nuclear dynamics calculations using previously computed molecular data [20,22] updated for the heaviest beryllium monohydride isotopologue. The present work continues and ends a series of studies we performed on the DR, VE and VdE – Eqs. (1)–(3) – of BeH^+ [10,20,23] and BeD^+ [24–26] with electrons of low to moderate collision energy. Here we first present a complete study on the vibrational dependence of the DR, VdE and VE rate coefficients of BeT^+ cation. Having thus completed the set of monohydride BeX^+ ion isotopologues enables us now to also derive an isotopic scaling law from this data-set (see Section 3), which greatly facilitates the use of this detailed information inside the physically and numerically already demanding multi-physics multi-scale fusion boundary plasma computational tools, such as the current ITER boundary plasma suite of codes SOLPS-ITER [27].

The paper is organized as follows: The introduction is followed by a brief description of the employed theoretical approach and some computational details. Section 3 presents our calculated rate coefficients. The paper ends with conclusions.

2. Theoretical approach of the dynamics

In the present study, we used an MQDT-based method to study the electron-impact collision processes given by Eqs. (1)–(3). Along with other methods we use [28], MQDT has proven to be a powerful and successful method when applied to several diatomic systems like H_2^+ [29], N_2^+ [30], CO^+ [31]. This approach, combined with the R-matrix technique, was also used to model satisfactorily – although less accurately – electronic collisions with poly-atomic ions like BF_2^+ [32] and $\text{NH}_2\text{CH}_2\text{O}^+$ [33].

The processes studied in the present paper involve ionization channels, describing the scattering of an electron on the molecular cation, and dissociation channels, accounting for atom-atom scattering. The mixing of these channels results in quantum interference of the *direct* mechanism – in which the capture takes place into a doubly excited dissociative state of the neutral system – and the *indirect* one – in which the capture occurs *via* a Rydberg state of the molecule, predissociated by the dissociative state. The direct mechanism dominates the reactive collisions in the cases of favorable crossings (in accordance with the Franck-Condon principle) between the potential energy curves of the dissociative states and that of the target ion. In both mechanisms the autoionization is in competition with the predissociation, and leads to the excitation/de-excitation of the cation. In the present calculations we account for vibrational structure for the target ion's ground electronic state and for the neutral's relevant electronic states, and neglect the rotational effects. A detailed description of our theoretical approach has been given in our previous articles – see for example [20] and [21] and references therein. Here the general ideas and major steps are recalled only. Within a quasi-diabatic representation of the molecular states, and for a given set of conserved quantum numbers of the neutral system – Λ (projection of the electronic angular momentum on the internuclear axis), S (total electronic spin) – the interaction matrix is built based on the couplings between *ionization* channels – associated to the vibrational levels v^+ of the cation and to the orbital quantum number l of the incident/Rydberg electron – and *dissociation* channels d_j . By adopting the second-order perturbative solution for the Lippman-Schwinger integral equation [34], we compute the reaction matrix of our collision system in the reaction zone.

A frame transformation is performed eventually, from the Born-Oppenheimer (short range) representation, characterized

by v and Λ quantum numbers, valid for small electron-ion and nucleus-nucleus distances, to the close-coupling (long-range) representation, characterized by v^+ , Λ^+ (for the ion) and l (orbital quantum number of the incident/Rydberg electron), valid for both large distances. This frame transformation relies on the quantum defects $\mu_l^A(R)$ describing the relevant Rydberg series built on the ionic core, and on the eigenvectors and eigenvalues of the K-matrix.

Based on the frame-transformation coefficients, we then build the physical scattering matrix organized in blocks associated to energetically *open* and/or *closed* (O and/or C respectively) channels:

$$S = X_{OO} - X_{OC} \frac{1}{X_{CC} - \exp(-i2\pi v)} X_{CO}. \quad (5)$$

The first term in Eq. (5) is restricted to the open channels, resulting in the *direct* mechanism, and the second takes into account their mixing with the closed ones, resulting in the *total*, i.e. direct and indirect mechanism, the denominator being responsible for the resonant patterns in the shape of the cross section [17]. Here the matrix $\exp(-i2\pi v)$ is diagonal and relies on the effective quantum numbers v_{v^+} associated to the vibrational thresholds of the closed ionization channels.

Once we have the scattering matrix the *computation of the cross-sections* is straightforward. For a given target cation on vibrational level v_i^+ and for a given energy of the incident electron ε , the dissociative recombination and the vibrational transition – elastic scattering, excitation, de-excitation – cross sections are computed using, respectively:

$$\sigma_{\text{diss} \leftarrow v_i^+} = \frac{\pi}{4\varepsilon} \sum_{l,\Lambda} \rho^\Lambda \sum_j \left| S_{d_j,lv_i^+}^\Lambda \right|^2, \quad (6)$$

$$\sigma_{v_f^+ \leftarrow v_i^+} = \frac{\pi}{4\varepsilon} \sum_{l,l',\Lambda} \rho^\Lambda \left| S_{l'v_f^+,lv_i^+}^\Lambda - \delta_{ll'} \delta_{v_f^+v_i^+} \right|^2. \quad (7)$$

Here ρ^Λ is the ratio between the spin and angular momentum multiplicities of the neutral and the target ion.

3. Results and discussions

Neglecting the very slight effects related to the change of the nuclear mass when Tritium replace Hydrogen, we have used the molecular data given in Figure 1 of Ref. [20] – namely:

- (i) the potential energy curve (PEC) of the ground electronic state of the cation and, for each of the dominant symmetries $^2\Sigma^+$, $^2\Pi$ and $^2\Delta$,
- (ii) the PECs of the valence dissociative states of the neutral,
- (iii) the quantum defects corresponding to the PECs of the bound Rydberg singly-excited states of the neutral,
- (iv) the Rydberg-valence couplings.

Relying on these molecular data, we have performed the inter-nuclear dynamics calculations using the MQDT approach presented in Section 2, for the collisions of low-energy electrons with BeT^+ molecular ions. The DR, VE and VdE cross sections have been calculated for all 28 vibrational levels of the target cation. Table A shows the energies of the vibrational levels of the cation relative to $v_i^+ = 0$ as well as its two spectroscopic dissociation energies (D_e and D_0).

The cross sections have been calculated with the inclusion of both direct and indirect mechanisms for the Σ and Π symmetries, and only the direct mechanism for the Δ symmetry at the highest (i.e. second) order of theory. The cross sections were calculated for each symmetry for the energy range $10^{-5} - 2.7$ eV of the incident electron, having an energy step of 0.01 meV. Thus, we managed to cover the energy range up to the dissociation

Table A

BeT⁺ vibrational levels relative to the $v_i^+ = 0$. The values of dissociation energies are $D_e = 2.795$ eV and $D_0 = 2.704$ eV.

v_i^+	$E_{v_i^+}$ (eV)	v_i^+	$E_{v_i^+}$ (eV)	v_i^+	$E_{v_i^+}$ (eV)	v_i^+	$E_{v_i^+}$ (eV)
0	0.000	7	1.078	14	1.921	21	2.477
1	0.167	8	1.214	15	2.017	22	2.532
2	0.327	9	1.347	16	2.107	23	2.578
3	0.486	10	1.475	17	2.193	24	2.617
4	0.641	11	1.597	18	2.273	25	2.648
5	0.792	12	1.712	19	2.348	26	2.674
6	0.937	13	1.819	20	2.416	27	2.693

limit of the ion, i.e. 2.704 eV. The global cross sections – Eqs. (6) and (7) – summed up over all symmetries were averaged over a Maxwellian electron energy distribution in order to obtain the thermal rate coefficients up to a maximum electron temperature of 5000 K.

Graphs 1–5 show the rate coefficients for DR, VE and VdE of BeT⁺ for all the 28 vibrational levels of the electronic ground state. For a given vibrational level of BeT⁺ the DR and the VdE rate coefficients have mainly monotonically decreasing tendencies as function of the electron temperature, while the VE ones increase. Moreover, the vibrational dependence of the DR rate coefficients show a monotonically decreasing behavior presenting local maxima for $v_i^+ = 3, 8, 17, 23$ initial target vibrational levels. The DR rate coefficients dominate for $v_i^+ \leq 16$, while for $v_i^+ > 16$ the monovibrational de-excitations become more important.

The excitations are getting important for higher electron temperatures for each vibrational level of the target. For the lower vibrational levels of the BeT⁺ cation ($v_i^+ \leq 16$), the VE rates are a notable competitor for DR or the de-excitation processes above 1000 K electron temperature only. For $v_i^+ > 16$, the competition starts at lower temperatures (even below 300 K) and, for the highest vibrational levels ($v_i^+ \geq 24$) and temperatures above 1000 K, VE becomes the dominant process. Notice that the vibrational excitation and de-excitation channels are not necessarily simply connected via detailed balancing, because they involve intermediate states and multi-step processes.

Finally, in order to facilitate kinetic modeling of the beryllium and hydrogen containing plasma and to illustrate the isotopic effect for the beryllium monohydride, we have displayed the rate coefficients for all three isotopologues in the same graph, in two versions.

Graph 6 shows the ratio of the DR rate coefficients for BeD⁺ [24] vs BeH⁺ [10,20,23], and for BeT⁺ vs BeH⁺ molecular cations, as function of the quantum number of the initial vibrational level of the target and of temperature.

In this representation, the isotopic effect increases with the vibrational quantum number of the target, from very weak for v_i^+ smaller than 5 to very significant for v_i^+ larger than 8, being stronger for BeT⁺ than for BeD⁺. This is entirely do to the dependence of the positions of the vibrational levels with respect to the points of crossing between the dissociative PECs and the PEC of the ground state of the target cation.

Graph 7 shows the DR rate coefficients for BeH⁺, BeD⁺ and BeT⁺ molecular cations as function of the energy of the current vibrational level – relative to the ground ($v_i^+ = 0$) vibrational level (see Table A) – for three different electron temperatures, 300, 1000 and 5000 K respectively. Each point or symbol on these curves belongs to a vibrational level of a different isotopologue. The slight shift in each point is due to the slightly different vibrational level spacing induced by the mass difference of the three isotopologues.

Distinct from the common way of plotting such rate coefficients versus vibrational quantum numbers, which in our case leads to a set of three different curves for each considered elec-

tron temperature, we now find that the rate coefficients for the three isotopologues versus vibrational energy instead collapse to a very similar (nearly identical) functional form. With the exception of a few points they are essentially the same. This is a very interesting outcome, similar to the one observed already by Capitelli et al. [35] for pure neutral hydrogen isotopologues. This similarity law provides scalable rate coefficient functions for all isotopologues with reasonable accuracy starting from rate coefficients calculated for one of them only.

In order to allow the versatile implementation of the rate coefficients shown in Graphs 1–5 in kinetics modeling codes, unlike our previous studies [10,24] where we have used generalized Arrhenius formula, here we considered that the original Arrhenius formula is quite suitable for this (cold) plasma application. We also found that this is falling within the range of accuracy provided by quantum chemistry data. As in [30] we will use Arrhenius formula as follows:

$$k^{\text{fit}}(T) = A T^\alpha \exp \left[-\frac{B}{T} \right], \quad (8)$$

for DR and VT (VE and VdE) processes over the electron temperature range $100 \text{ K} \leq T \leq 5000 \text{ K}$. Assuming a Maxwell–Boltzmann vibrational level distribution we have found that vibrational levels up to $v_{\text{max}}^+ = 10$ and vibrational transition with $\Delta v_{\text{max}} = 10$ are of importance at 5000K electron temperatures. The fitting parameters (A, α, B) are displayed in Tables 1–12. The numerical values, obtained using Eq. (8), agree with the MQDT-computed ones within a range of errors specified in the caption of each table. A maximal relative deviation and an average Root Mean Square (RMS) were provided per data set.

4. Conclusions

The present work completes a large series of studies performed on reactive collisions of the beryllium monohydride cation and its isotopologues with low energy electrons, namely for BeH⁺ [10,20,23], for BeD⁺ [24] and for BeT⁺. Making use of the molecular data set calculated in Ref. [20,22] and by adjusting the nuclear masses, we have performed an MQDT calculation for all 28 vibrational levels of the heaviest beryllium monohydride cation in collisions with electrons having kinetic energy up to the dissociation limit of the ion.

We have provided rate coefficients for dissociative recombination, vibrational excitation and de-excitation of BeT⁺ molecular cation, relevant for detailed kinetic plasma-chemical modeling of the cold edge plasma in fusion devices and for aiding and improving interpretation of spectroscopic beryllium wall release rate experiments. Our present and previously-calculated rate coefficients for the beryllium monohydride isotopologues have been alternatively represented in a comparative way as functions of the target vibrational energy – rather than of the target vibrational quantum number – for different electron temperatures. We found a quite close qualitative and quantitative behavior for all three of these species. This provides a hitherto apparently unexpected similarity scaling law, significantly reducing complexity of the underlying plasma chemical databases for kinetic plasma chemistry models, to be employed in the above mentioned fusion applications. A quite natural but important extension of this finding, left to future work, would be identification (or disproof) of a similar scaling also for the pure hydrogen molecular ions, which is currently already used in fusion boundary codes merely for simplicity, but so far without a posteriori theoretical confirmation.

It is known that beryllium and its compounds are toxic, so no experimental data are provided yet. In this regard, our calculations can be considered as reference. The accuracy of the

calculated data is based on our method, which was tested and calibrated with other molecular ions where experimental data can be found. However, we are aware that the main source of error comes from the data obtained from quantum chemistry calculations, which provides us potential energy curves and couplings.

The present article completes the study of *low-energy* collisions of electrons with beryllium monohydride cations. Computations of the high-energy cross sections will start soon, relying on the inclusion of further excited dissociative paths and of the vibrational continuum of the ion, this latter element being at the origin of the dissociative excitation.

Finally we must mention that all the data in tables 1–13 are provided in the Supplementary Materials as ASCII files. Furthermore, the raw data sets of cross sections and rate coefficients are additionally added. Along the way, the data will be uploaded to the LxCat database [36] website.

Declaration of competing interest

The authors declare that they have no known competing financial interests or personal relationships that could have appeared to influence the work reported in this paper.

Acknowledgments

The authors acknowledge support from Fédération de Recherche Fusion par Confinement Magnétique, France (CNRS, CEA and Eurofusion), La Région Normandie, France, FEDER, France and LabEx EMC3, France via the projects PTOLEEMEE, Bioengine, EMoPlaF, COMUE Normandie Université, the Institute for Energy, Propulsion and Environment (FR-IEPE), the European Union via COST (European Cooperation in Science and Technology) actions TUMIEE (CA17126), MW-Gaia (CA18104) and MD-GAS (CA18212), and ERASMUS-plus conventions between Université Le Havre Normandie and Politehnica University Timisoara, West University Timisoara and University College London. We are indebted to Agence Nationale de la Recherche (ANR) via the project MONA, Centre National de la Recherche Scientifique via the GdR TheMS and the DYMCOM project, and the Institute Pascal, University Paris-Saclay for the warm hospitality during the DYMCOM workshop. NP, FI and JZsM acknowledge support from the UEFISCDI, Romania through the mobility project no. PN-III-P1-1.1-MCD-2019-0163. NP is grateful for the support of the Romanian Ministry of Research and Innovation, project no. 10PFE/16.10.2018, PERFORM-TECH-UPT. JZsM thanks the financial support of the National Research, Development and Innovation Fund of Hungary, under the FK 19 funding scheme with project no. FK 132989. The work of DR was carried out under the auspices of the ITER scientists fellow network (ISFN) program, ITER Organization, Route de Vinon-sur-Verdon, CS 90 046 13067 St. Paul-lez-Durance (France).

Appendix A. Supplementary data

Supplementary material related to this article can be found online at <https://doi.org/10.1016/j.adt.2021.101414>.

References

- [1] A.W. Kleyn, N.J. Lopes Cardozo, U. Samm, *Phys. Chem. Chem. Phys.* **8** (2006) 1761.
- [2] R.E.H. Clark, D. Reiter (Eds.), *Springer Series in Chemical Physics*, vol. 78, Springer, Berlin, 2005.
- [3] R. Celiberto, R.K. Janev, D. Reiter, *Plasma Phys. Control. Fusion* **54** (2012) 035012.
- [4] O. Motojima, *Nucl. Fusion* **55** (2015) 104023.
- [5] R. Mitteau, R. Eaton, A. Gervash, V. Kuznetsov, V. Davydov, R. Rulev, *Nucl. Mater. Energy* **12** (2017) 1067.
- [6] J. Paméla, G.F. Matthews, V. Philipps, R. Kamendje, *JET Contributors*, *J. Nucl. Mater.* **363–365** (2007) 1.
- [7] Borodin, et al., *Nucl. Mater. Energy* **9** (2016) 604–609.
- [8] G. Duxbury, M.F. Stamp, H.P. Summers, *Plasma Phys. Control. Fusion* **40** (1998) 361.
- [9] D. Darby-Lewis, J. Tennyson, K.D. Lawson, S.N. Yurchenko, M.F. Stamp, A. Shaw, S. Brezinsek, *JET Contributors*, *J. Phys. B: At. Mol. Opt. Phys.* **51** (2018) 185701.
- [10] S. Niyonzima, S. Ilie, N. Pop, J.Zs. Mezei, K. Chakrabarti, V. Morel, B. Peres, D.A. Little, K. Hassouni, A. Larson, A.E. Orel, D. Benredjem, A. Bultel, J. Tennyson, D. Reiter, I.F. Schneider, *At. Data Nucl. Data Tables* **115–116** (2017) 287.
- [11] S. Brezinsek, et al., *Nucl. Fusion* **54** (2014) 103001.
- [12] S. Brezinsek, et al., *JET Contributors*, *Nucl. Fusion* **55** (2015) 063021.
- [13] K. Krieger, et al., *JET Contributors*, *J. Nucl. Mater.* **438** (2013) S262.
- [14] D. Nishijima, R.P. Doerner, M.J. Baldwin, G. De Temmerman, E.M. Hollmann, *Plasma Phys. Control. Fusion* **50** (2008) 125007.
- [15] R.P. Doerner, M.J. Baldwin, D. Buchenauer, G. De Temmerman, D. Nishijima, *J. Nucl. Mater.* **390–391** (2009) 681.
- [16] A. Giusti, *J. Phys. B: At. Mol. Phys.* **13** (1980) 3867.
- [17] M.J. Seaton, *Rep. Progr. Phys.* **46** (1983) 16.
- [18] I.F. Schneider, O. Dulieu, A. Giusti-Suzor, *J. Phys. B: At. Mol. Phys.* **24** (1991) L289.
- [19] Ch. Jungen, in: M. Quack, F. Merkt (Eds.), *Handbook of High Resolution Spectroscopy*, Wiley, Chichester, New York, 2011, pp. 471–510.
- [20] S. Niyonzima, F. Lique, K. Chakrabarti, A. Larson, A.E. Orel, I.F. Schneider, *Phys. Rev. A* **87** (2013) 022713.
- [21] J.Zs. Mezei, K. Chakrabarti, M.D. Epée Epée, O. Motapon, Ch.H. Yuen, M.A. Ayouz, N. Douguet, S. Fonseca dos Santos, V. Kokoouline, I.F. Schneider, *ACS Earth Space Chem.* **3** (2019) 2376.
- [22] J.B. Roos, M. Larsson, A. Larson, A.E. Orel, *Phys. Rev. A* **80** (2009) 012501.
- [23] V. Laporta, K. Chakrabarti, R. Celiberto, R.K. Janev, J.Zs. Mezei, S. Niyonzima, J. Tennyson, I.F. Schneider, *Plasma Phys. Control. Fus.* **59** (2017) 045008.
- [24] S. Niyonzima, N. Pop, F. Iacob, A. Larson, A.E. Orel, J.Zs. Mezei, K. Chakrabarti, V. Laporta, K. Hassouni, D. Benredjem, A. Bultel, J. Tennyson, D. Reiter, I.F. Schneider, *Plasma Sources. Sci. Technol.* **27** (2018) 025015.
- [25] F. Iacob, N. Pop, J.Zs. Mezei, M.D. Epée Epée, O. Motapon, S. Niyonzima, V. Laporta, I.F. Schneider, *AIP Conf. Proc.* **2071** (2019) 020007.
- [26] N. Pop, F. Iacob, J.Z. Mezei, O. Motapon, S. Niyonzima, D. Kashinski, D. Talbi, A.P. Hickman, I.F. Schneider, *AIP Conf. Proc.* **1916** (2017) 020013.
- [27] R.A. Pitts, et al., *Nucl. Mater. Energy* **20** (2019) 100696.
- [28] Felix Iacob, *Phys. Lett. A* **384**, **35** (2020) 126888.
- [29] O. Motapon, N. Pop, F. Argoubi, J.Zs. Mezei, M.D. Epée Epée, A. Faure, M. Telmini, J. Tennyson, I.F. Schneider, *Phys. Rev. A* **90** (2014) 012706.
- [30] D.A. Little, K. Chakrabarti, J.Zs. Mezei, I.F. Schneider, J. Tennyson, *Phys. Rev. A* **90** (2014) 052705.
- [31] Y. Moulane, J.Zs. Mezei, V. Laporta, E. Jehin, Z. Benkhaldoun, I.F. Schneider, *Astron. Astrophys.* **613** (2018) A53.
- [32] V. Kokoouline, M.A. Ayouz, J.Zs. Mezei, K. Hassouni, I.F. Schneider, *Plasma Sources. Sci. Technol.* **27** (2018) 115007.
- [33] M.A. Ayouz, Ch.H. Yuen, N. Balucani, C. Ceccarelli, I.F. Schneider, V. Kokoouline, *Mon. Not. R. Astron. Soc.* **490** (2019) 1325.
- [34] V. Ngassam, A. Florescu, L. Pichl, I.F. Schneider, O. Motapon, A. Suzor-Weiner, *Eur. Phys. J. D* **26** (2003) 165.
- [35] M. Capitelli, et al., *Nucl. Fusion* **46** (2006) S260.
- [36] S. Pancheshnyi, S. Biagi, M.C. Bordage, G.J.M. Hagelaar, W.L. Morgan, A.V. Phelps, L.C. Pitchford, *Chem. Phys.* **398** (2012) 148.

Explanation of Graphs

Graphs 1–5.	Dissociative recombination, vibrational excitation and de-excitation Maxwell rate coefficients for all the vibrational levels of BeH⁺ in its ground electronic state.
Ordinate	Maxwell rate coefficient in cm ³ s ^{−1}
Abscissa	Electron temperature in K
Thick black line	DR Maxwell rate coefficient
Thin colored lines	Vibrational excitation rate coefficients
Colored lines with symbols	Vibrational de-excitation rate coefficients
Graph 6.	Ratios of the dissociative recombination rate coefficients for BeD⁺ vs BeH⁺ (left), and for BeT⁺ vs BeH⁺ (right) molecular cations, as function of the quantum number of the initial vibrational level of the target and of temperature.
Ordinate	Ratios of dissociative recombination Maxwell rate coefficients
Abscissa	Electron temperature in K
Graph 7.	Dissociative recombination rate coefficient for the three beryllium monohydride isotopologue cations as function of the energy of the initial vibrational level of the target – relative to the ground vibrational level – for three different electron temperatures.
Ordinate	Dissociative recombination Maxwell rate coefficient in cm ³ s ^{−1}
Abscissa	Vibrational energy relative to the ground level in eV.
Black curves	DR rate coefficients for BeH ⁺ .
Blue curves	DR rate coefficients for BeD ⁺ .
Red curves	DR rate coefficients for BeT ⁺ .
Dashed colored curves with symbols	DR rate coefficients at $T = 300$ K electron temperature.
Continuous colored curves with symbols	DR rate coefficients at $T = 1000$ K electron temperature.
Dashed-dotted colored curves with symbols	DR rate coefficients at $T = 5000$ K electron temperature.

Explanation of Tables

Table 1. List of fitting parameters according to Eq. (8), minimum and maximum values of relative difference and root mean squares calculated for dissociative recombination for the $v_i^+ = 0 - 10$ vibrational levels of the ground electronic state of BeT^+ .

v_i^+	Initial vibrational level of BeT^+
Temperature range	in K
A, α, B	Fitting parameters
$\text{rd}_{\max} = \max_{i=1, \dots, n} \left \frac{k_i(T) - k_i^{\text{fit}}(T)}{k_i(T)} \right $	maximum of relative difference
$\text{RMS} = \sqrt{\sum_{i=1}^n \frac{1}{n} \left \frac{k_i(T) - k_i^{\text{fit}}(T)}{k_i(T)} \right ^2}$	root mean square

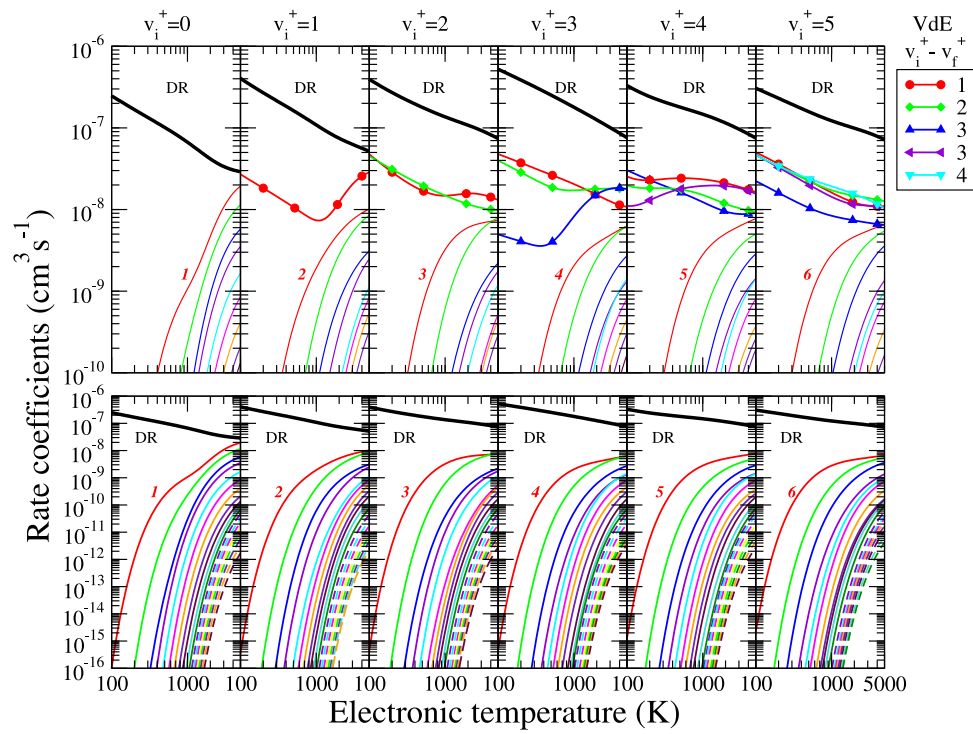
Tables 2–12. List of fitting parameters according to Eq. (8), minimum and maximum values of relative difference and root mean squares calculated for vibrational transitions ($\Delta v_{\max} = 10$) for the $v_i^+ = 0 - 10$ vibrational levels of the ground electronic state of BeT^+ .

$v_i^+ \rightarrow v_j^+$	Vibrational transition of BeT^+
$v_i^+ \rightarrow v_j^+$	Stands for VdE
Temperature range	in K
A, α, B	Fitting parameters
$\text{rd}_{\max} = \max_{i=1, \dots, n} \left \frac{k_i(T) - k_i^{\text{fit}}(T)}{k_i(T)} \right $	maximum of relative difference
$\text{RMS} = \sqrt{\sum_{i=1}^n \frac{1}{n} \left \frac{k_i(T) - k_i^{\text{fit}}(T)}{k_i(T)} \right ^2}$	root mean square

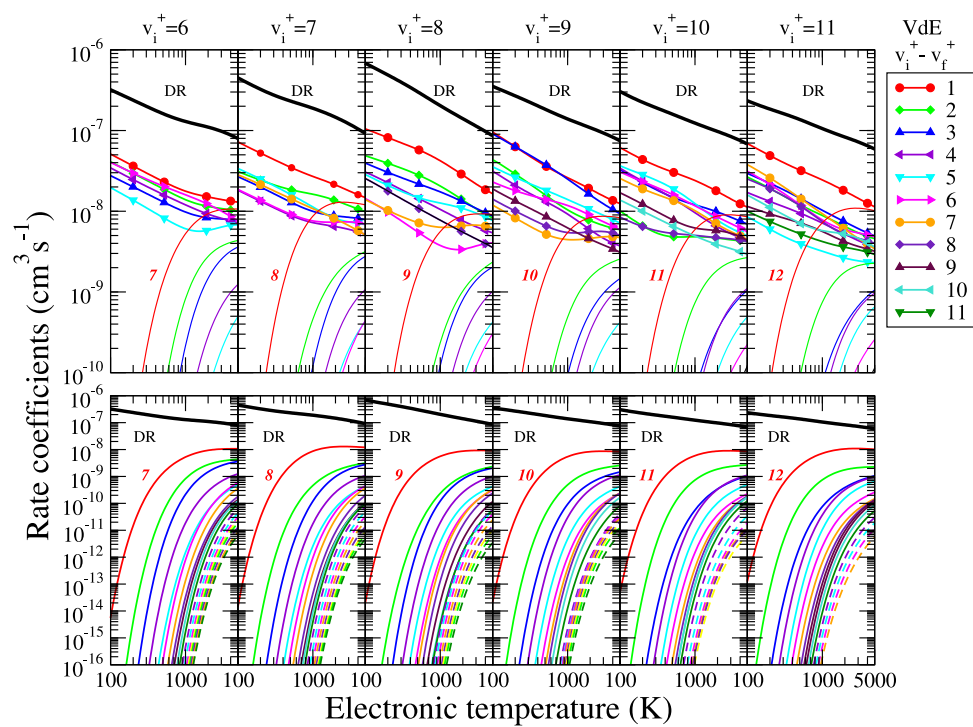
Note: In Tables 1–12 the coefficients were given taking into account a wider temperature range in order to prevent boundary errors. The temperature range was increased with 10% of the boundary values. The global maximal value of relative difference was taken as the maximum among all DR maximum relative differences and the maximum among all VT values for a given target. The average RMS was calculated as the arithmetic mean of the temperature weighted process RMS values.

Table 13. List of dissociative recombination rate coefficient showing the isotopic effects displayed in Graph 7.

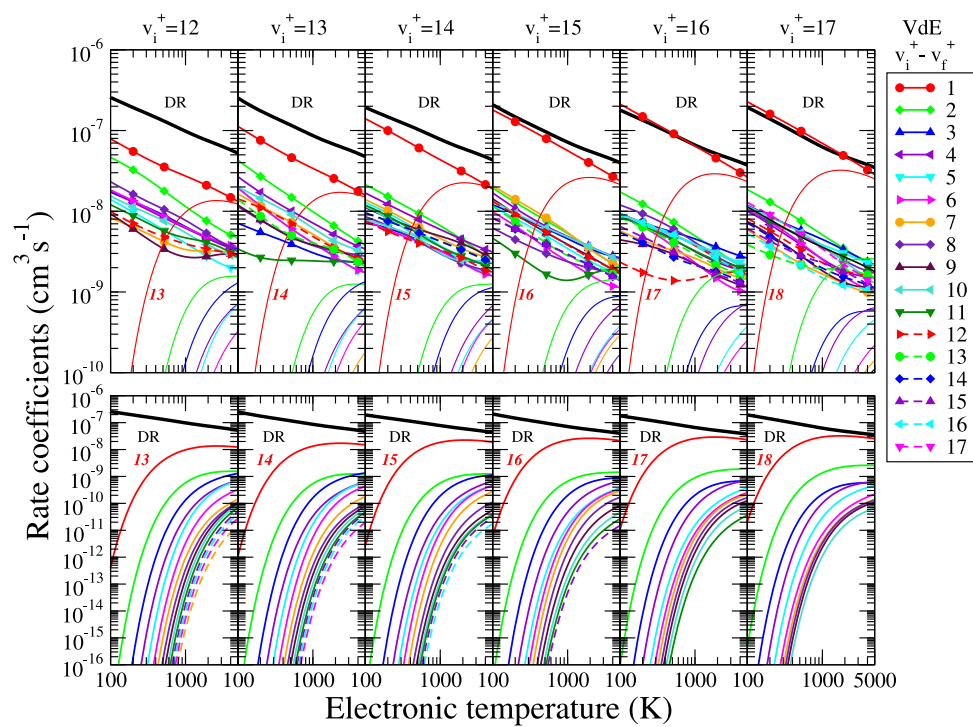
Temperature range	in K
v_i^+	Initial vibrational level of BeX^+
$E_{v_i^+} - E_0$	Energy difference relative to the ground state
Rate coefficient	in (cm^3/s)
Data by columns corresponding to isotopologues	$\text{BeX}^+ \in \{\text{BeH}^+, \text{BeD}^+, \text{BeT}^+\}$



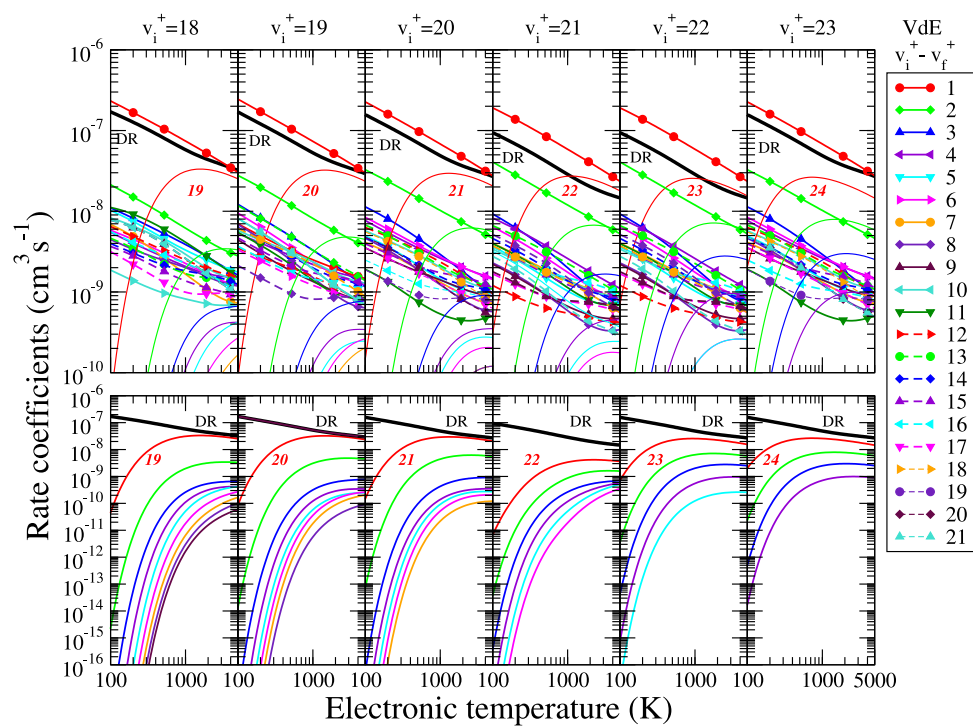
Graph 1. Dissociative recombination (DR, thick black line), vibrational excitation (VE, thin colored solid and dashed lines) and vibrational de-excitation (VdE, symbols and thick colored lines) rate coefficients of BeT^+ in its electronic ground state and for the initial vibrational levels $v_i^+ = 0 - 5$. Upper panels: for each v_i^+ of BeT^+ , all possible de-excitation final vibrational quantum numbers are given, while for the excitation only the first one is labeled. The VE rate coefficients decrease monotonically with the increase of the final vibrational quantum numbers of the target ion. Lower panels: DR and VE rate coefficients only, with the panels extended down to $10^{-16} \text{ cm}^3 \text{ s}^{-1}$.



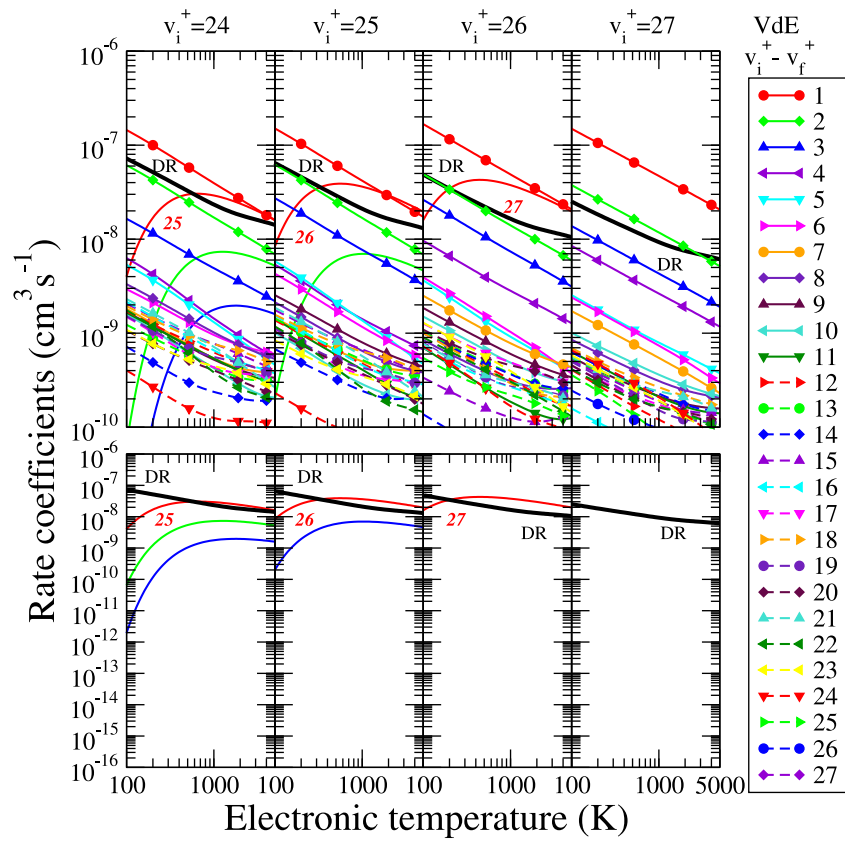
Graph 2. Same as in [Graph 1](#) for $v_i^+ = 6 - 11$.



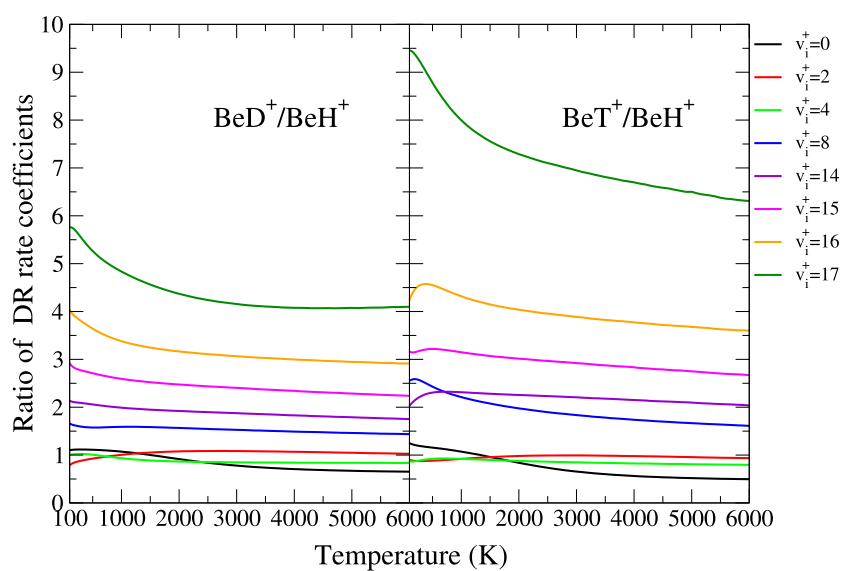
Graph 3. Same as in Graph 1 for $v_i^+ = 12 - 17$.



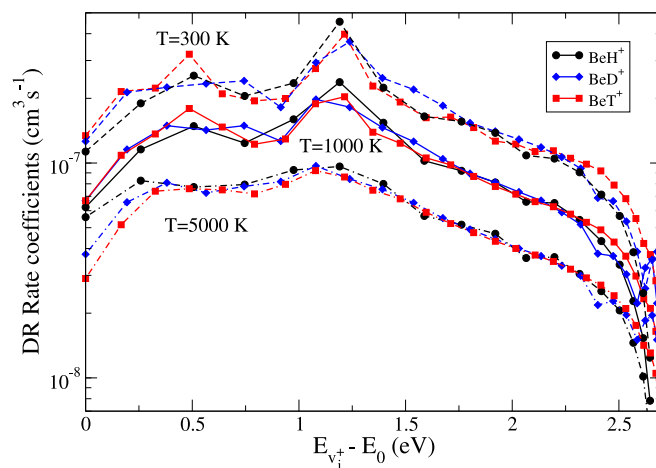
Graph 4. Same as in [Graph 1](#) for $v_i^+ = 18 - 23$.



Graph 5. Same as in Graph 1 for $v_i^+ = 24 - 27$.



Graph 6. Isotopic effects: Ratios of the dissociative recombination rate coefficients for BeD^+ [24] vs BeH^+ [10,20,23] (left), and for BeT^+ vs BeH^+ (right) molecular cations, as function of the quantum number of the initial vibrational level of the target and of temperature.



Graph 7. Isotopic effects: Dissociative recombination rate coefficient of the BeH^+ (black curves with circles), BeD^+ (blue curves with diamonds) and BeT^+ (red curves with squares) molecular cations as function of the energy of the initial vibrational level of the target – relative to the ground vibrational level – for three electron temperatures.

In order to facilitate the use of the rate coefficients given in [Graph 7](#) we have presented them in [Table 13](#). The data obtained for each of the three isotopologues are suitable to represent the behavior as a function of the vibrational energy.

Table 1

Fitting parameters for the DR Maxwell rate coefficients of $\text{BeT}^+(v_l^+ = 0, \dots, 10)$, for temperatures ranging between 100 K and 5000 K as displayed in [Graph 1–5](#). The calculated rate coefficients are reproduced with a maximal relative deviation of 3.242% and with an average Root Mean Square (RMS) of 0.0064.

v_l^+	Temperature range (K)	A (cm^3/s)	α	B (K)
0	$100 \leq T \leq 1000$	$3.28197 \cdot 10^{-6}$	−0.560182	1.28522
	$1000 < T \leq 5000$	$1.2742 \cdot 10^{-7}$	−0.193793	−715.096
1	$100 \leq T \leq 1500$	$4.93965 \cdot 10^{-6}$	−0.551551	−3.05762
	$1500 < T \leq 5000$	$5.54357 \cdot 10^{-7}$	−0.286297	−345.175
2	$100 \leq T \leq 1500$	$1.59139 \cdot 10^{-6}$	−0.359808	−26.6809
	$1500 < T \leq 5000$	$8.88933 \cdot 10^{-6}$	−0.551753	429.823
3	$100 \leq T \leq 5000$	$6.41436 \cdot 10^{-6}$	−0.517293	13.1328
4	$100 \leq T \leq 1000$	$6.98686 \cdot 10^{-7}$	−0.228439	−30.1691
	$1000 < T \leq 5000$	$8.75990 \cdot 10^{-6}$	−0.551726	279.519
5	$100 \leq T \leq 1000$	$1.81880 \cdot 10^{-6}$	−0.393492	−3.40054
	$1000 < T \leq 5000$	$2.01551 \cdot 10^{-6}$	−0.386694	140.669
6	$100 \leq T \leq 5000$	$8.97394 \cdot 10^{-7}$	−0.281268	−28.9724
7	$100 \leq T \leq 1000$	$1.08752 \cdot 10^{-6}$	−0.258424	−31.4290
	$100 \leq T \leq 5000$	$1.82852 \cdot 10^{-5}$	−0.612179	350.171
8	$100 \leq T \leq 1000$	$8.0781 \cdot 10^{-6}$	−0.539215	0.11067
	$1000 < T \leq 5000$	$1.0082 \cdot 10^{-5}$	−0.561074	11.15700
9	$100 \leq T \leq 1000$	$1.7769 \cdot 10^{-6}$	−0.360498	−3.68476
	$1000 < T \leq 5000$	$2.0542 \cdot 10^{-6}$	−0.388174	−3.37710
10	$100 \leq T \leq 1000$	$2.7190 \cdot 10^{-6}$	−0.467593	−0.13565
	$1000 \leq T \leq 5000$	$2.6040 \cdot 10^{-6}$	−0.423590	128.7260

Table 2
Fitting parameters for the VT ($\Delta v_{max} = 10$) Maxwell rate coefficients of $\text{BeT}^+(v_i^+ \rightarrow v_f^+)$, for temperatures ranging between 100 K and 5000 K, as displayed in Graph 1. The calculated rate coefficients are reproduced with a maximal relative deviation of 6.073% and with an average RMS of 0.0108.

$v_i^+ \rightarrow v_f^+$	Temperature range (K)	A (cm^3/s)	α	B (K)
$0 \rightarrow 1$	$100 \leq T \leq 800$	$5.55127 \cdot 10^{-7}$	-0.631862	1946.6
	$800 < T \leq 1700$	$6.82095 \cdot 10^{-20}$	3.19051	-1420.11
	$1700 < T \leq 5000$	$2.18465 \cdot 10^{-6}$	-0.41325	6020.8
$0 \rightarrow 2$	$200 \leq T \leq 540$	$5.61 \cdot 10^{-8}$	-0.277382	3703.32
	$540 < T \leq 1700$	$1.69648 \cdot 10^{-14}$	1.71428	2320.49
	$1700 < T \leq 5000$	$1.8088 \cdot 10^{-6}$	-0.439072	6608.15
$0 \rightarrow 3$	$320 \leq T \leq 700$	$1.96702 \cdot 10^{-16}$	2.42111	4758.72
	$700 < T \leq 1500$	$4.0198 \cdot 10^{-9}$	0.242131	6595.09
	$1500 < T \leq 5000$	$1.94918 \cdot 10^{-5}$	-0.755523	8455.75
$0 \rightarrow 4$	$400 \leq T \leq 1500$	$7.19563 \cdot 10^{-8}$	-0.156832	7658.54
	$1500 < T \leq 5000$	$7.81868 \cdot 10^{-6}$	-0.696791	8849.87
$0 \rightarrow 5$	$460 \leq T \leq 1500$	$2.62787 \cdot 10^{-7}$	-0.367603	9262.82
	$1500 < T \leq 5000$	$5.20392 \cdot 10^{-6}$	-0.710329	10044.6
$0 \rightarrow 6$	$560 \leq T \leq 1500$	$5.36862 \cdot 10^{-7}$	-0.486471	11014.8
	$1500 < T \leq 5000$	$8.72782 \cdot 10^{-6}$	-0.808104	11756.5
$0 \rightarrow 7$	$650 \leq T \leq 1500$	$2.72072 \cdot 10^{-7}$	-0.460102	12561.0
	$1500 < T \leq 5000$	$3.60645 \cdot 10^{-6}$	-0.753226	13304.5
$0 \rightarrow 8$	$750 \leq T \leq 1500$	$2.22274 \cdot 10^{-7}$	-0.487693	14077.8
	$1500 < T \leq 5000$	$1.37401 \cdot 10^{-6}$	-0.685974	14745.6
$0 \rightarrow 9$	$850 \leq T \leq 1700$	$7.47373 \cdot 10^{-8}$	-0.37838	15497.4
	$1700 < T \leq 5000$	$1.16235 \cdot 10^{-6}$	-0.678763	16486.9
$0 \rightarrow 10$	$950 \leq T \leq 2000$	$1.76168 \cdot 10^{-8}$	-0.212531	16919.9
	$2000 < T \leq 5000$	$2.31428 \cdot 10^{-6}$	-0.755505	18522.3

Table 3

Same as Table 2 for $v_i^+ = 1$, as displayed in Graph 1, maximal relative deviation of 6.459% and average RMS of 0.0098.

$v_i^+ \rightarrow v_f^+$	Temperature range (K)	A (cm ³ /s)	α	B (K)
$1 \rightarrow 0$	$100 \leq T \leq 1000$	$4.50249 \cdot 10^{-7}$	-0.599873	5.30000
	$1000 < T \leq 2500$	$2.43483 \cdot 10^{-16}$	2.21315	-1823.33
	$2500 < T \leq 5000$	$1.8544 \cdot 10^{-5}$	-0.643767	4975.26
$1 \rightarrow 2$	$100 \leq T \leq 300$	$2.55835 \cdot 10^{-7}$	-0.467812	1818.6
	$300 < T \leq 900$	$4.45218 \cdot 10^{-9}$	0.102817	1562.25
	$900 < T \leq 5000$	$5.70154 \cdot 10^{-9}$	0.112954	1901.61
$1 \rightarrow 3$	$190 \leq T \leq 400$	$7.33653 \cdot 10^{-8}$	-0.243628	3630.72
	$400 < T \leq 1300$	$3.59106 \cdot 10^{-9}$	0.303087	3419.43
	$1300 < T \leq 5000$	$4.92087 \cdot 10^{-8}$	-0.110554	4050.88
$1 \rightarrow 4$	$280 \leq T \leq 1500$	$6.03362 \cdot 10^{-7}$	-0.507352	5686.01
	$1500 < T \leq 5000$	$1.92775 \cdot 10^{-8}$	-0.096070	5036.37
$1 \rightarrow 5$	$360 \leq T \leq 1000$	$9.45769 \cdot 10^{-8}$	-0.295715	7099.65
	$1000 < T \leq 2500$	$9.96048 \cdot 10^{-10}$	0.267671	6422.72
	$2500 < T \leq 5000$	$2.40339 \cdot 10^{-7}$	-0.344658	8178.08
$1 \rightarrow 6$	$480 \leq T \leq 1000$	$1.60089 \cdot 10^{-9}$	-0.127208	8485.23
	$1000 < T \leq 2500$	$2.88654 \cdot 10^{-11}$	0.636106	8003.94
	$2500 < T \leq 5000$	$2.48387 \cdot 10^{-7}$	-0.378268	10844.1
$1 \rightarrow 7$	$560 \leq T \leq 1700$	$1.02492 \cdot 10^{-9}$	0.234332	10195.0
	$1700 < T \leq 5000$	$8.8946 \cdot 10^{-7}$	-0.535633	12076.0
$1 \rightarrow 8$	$650 \leq T \leq 1700$	$7.23629 \cdot 10^{-10}$	0.273121	11880.6
	$1700 < T \leq 5000$	$3.37484 \cdot 10^{-6}$	-0.692863	14159.8
$1 \rightarrow 9$	$750 \leq T \leq 1800$	$8.58581 \cdot 10^{-10}$	0.230284	13453.3
	$1800 < T \leq 5000$	$7.40756 \cdot 10^{-6}$	-0.804795	15920.4
$1 \rightarrow 10$	$800 \leq T \leq 1700$	$7.91052 \cdot 10^{-9}$	-0.045485	15121.1
	$1700 < T \leq 5000$	$2.45025 \cdot 10^{-5}$	-0.965532	17280.1
$1 \rightarrow 11$	$900 \leq T \leq 1800$	$5.55123 \cdot 10^{-8}$	-0.295216	16841.5
	$1800 < T \leq 5000$	$5.33313 \cdot 10^{-5}$	-1.0799	18708.8

Table 4

Same as Table 2 for $v_i^+ = 2$, as displayed in Graph 1, maximal relative deviation of 5.369% and average RMS of 0.0079.

$v_i^+ \rightarrow v_f^+$	Temperature range (K)	A (cm ³ /s)	α	B (K)
$2 \rightarrow 1$	$100 \leq T \leq 650$	$1.98340 \cdot 10^{-7}$	-0.410144	-47.2313
	$650 < T \leq 2500$	$2.67382 \cdot 10^{-9}$	0.217131	-221.517
	$2500 < T \leq 5000$	$1.03204 \cdot 10^{-5}$	-0.743861	1679.41
$2 \rightarrow 0$	$100 \leq T \leq 1000$	$2.65852 \cdot 10^{-7}$	-0.422904	-18.0281
	$1000 < T \leq 5000$	$1.41619 \cdot 10^{-8}$	-0.055055	-438.763
$2 \rightarrow 3$	$100 \leq T \leq 750$	$2.98556 \cdot 10^{-7}$	-0.385583	1857.56
	$750 < T \leq 5000$	$1.52063 \cdot 10^{-7}$	-0.317954	1649.34
$2 \rightarrow 4$	$180 \leq T \leq 460$	$5.39078 \cdot 10^{-8}$	-0.108704	3706.07
	$460 < T \leq 1500$	$1.79330 \cdot 10^{-7}$	-0.270308	3810.89
	$1500 < T \leq 5000$	$4.21512 \cdot 10^{-7}$	-0.373900	3955.53
$2 \rightarrow 5$	$280 \leq T \leq 750$	$1.47486 \cdot 10^{-8}$	-0.104801	5239.98
	$750 < T \leq 5000$	$1.07730 \cdot 10^{-8}$	-0.064429	5185.79
$2 \rightarrow 6$	$360 \leq T \leq 950$	$1.63766 \cdot 10^{-7}$	-0.383215	7049.35
	$950 < T \leq 5000$	$4.35176 \cdot 10^{-8}$	-0.214698	6932.32
$2 \rightarrow 7$	$460 \leq T \leq 1000$	$5.07710 \cdot 10^{-7}$	-0.548890	8732.22
	$1000 < T \leq 2500$	$2.29574 \cdot 10^{-9}$	0.108113	7824.24
	$2500 < T \leq 5000$	$3.27557 \cdot 10^{-8}$	-0.181104	8832.80
$2 \rightarrow 8$	$560 \leq T \leq 1200$	$3.04328 \cdot 10^{-10}$	0.265882	9619.67
	$1200 < T \leq 2500$	$4.32959 \cdot 10^{-12}$	0.789060	8969.37
	$2500 < T \leq 5000$	$7.05150 \cdot 10^{-8}$	-0.293284	12085.2
$2 \rightarrow 9$	$650 \leq T \leq 1900$	$4.62304 \cdot 10^{-10}$	0.282399	11528.0
	$1900 < T \leq 5000$	$5.15463 \cdot 10^{-7}$	-0.509966	13597.4
$2 \rightarrow 10$	$750 \leq T \leq 2000$	$6.43134 \cdot 10^{-9}$	-0.046700	13239.8
	$2000 < T \leq 5000$	$3.16506 \cdot 10^{-7}$	-0.479755	14524.7
$2 \rightarrow 11$	$800 \leq T \leq 1900$	$3.04332 \cdot 10^{-8}$	-0.276149	14504.1
	$1900 < T \leq 5000$	$9.65857 \cdot 10^{-8}$	-0.392462	15116.6
$2 \rightarrow 12$	$850 \leq T \leq 2000$	$3.35235 \cdot 10^{-8}$	-0.308151	15744.6
	$2000 < T \leq 5000$	$3.55228 \cdot 10^{-7}$	-0.565695	16623.0

Table 5

Same as Table 2 for $v_i^+ = 3$, as displayed in Graph 1, maximal relative deviation of 4.869% and average RMS of 0.0064.

$v_i^+ \rightarrow v_f^+$	Temperature range (K)	A (cm ³ /s)	α	B (K)
3 \rightarrow 2	100 \leq T \leq 5000	$3.46715 \cdot 10^{-7}$	-0.410553	9.90469
3 \rightarrow 1	100 \leq T \leq 650	$2.12157 \cdot 10^{-7}$	-0.394035	-15.1628
	650 < T \leq 5000	$1.58371 \cdot 10^{-8}$	0.015527	18.2980
3 \rightarrow 0	100 \leq T \leq 380	$8.75244 \cdot 10^{-9}$	-0.163227	-19.2090
	380 < T \leq 1000	$1.36004 \cdot 10^{-15}$	2.15314	-751.922
	1000 < T \leq 5000	$2.54536 \cdot 10^{-6}$	-0.531187	2127.30
3 \rightarrow 4	100 \leq T \leq 400	$1.73997 \cdot 10^{-7}$	-0.378735	1800.43
	400 < T \leq 1500	$2.53625 \cdot 10^{-7}$	-0.435000	1813.83
	1500 < T \leq 5000	$2.33805 \cdot 10^{-10}$	0.397347	443.964
3 \rightarrow 5	180 \leq T \leq 540	$1.91749 \cdot 10^{-7}$	-0.357808	3511.67
	540 < T \leq 1500	$1.85672 \cdot 10^{-8}$	-0.046832	3300.15
	1500 < T \leq 5000	$7.81031 \cdot 10^{-8}$	-0.210848	3672.47
3 \rightarrow 6	270 \leq T \leq 750	$8.51869 \cdot 10^{-8}$	-0.324917	5161.45
	750 < T \leq 2000	$2.54974 \cdot 10^{-9}$	0.122469	4737.41
	2000 < T \leq 5000	$2.16745 \cdot 10^{-8}$	-0.117307	5390.10
3 \rightarrow 7	360 \leq T \leq 1000	$4.41787 \cdot 10^{-9}$	0.036043	6626.28
	1000 < T \leq 2500	$5.03471 \cdot 10^{-8}$	-0.258383	7048.81
	2500 < T \leq 5000	$3.83663 \cdot 10^{-7}$	-0.487105	7658.27
3 \rightarrow 8	440 \leq T \leq 1200	$5.57754 \cdot 10^{-8}$	-0.212691	8466.71
	1200 < T \leq 5000	$1.46301 \cdot 10^{-6}$	-0.599417	9162.28
3 \rightarrow 9	520 \leq T \leq 1500	$1.24894 \cdot 10^{-6}$	-0.630400	10297.4
	1500 < T \leq 5000	$3.04057 \cdot 10^{-7}$	-0.460993	10053.8
3 \rightarrow 10	650 \leq T \leq 1500	$1.48874 \cdot 10^{-6}$	-0.698783	11634.5
	1500 < T \leq 5000	$1.54147 \cdot 10^{-7}$	-0.417352	11387.4
3 \rightarrow 11	700 \leq T \leq 1200	$8.17357 \cdot 10^{-8}$	-0.385387	12622.1
	1200 < T \leq 2500	$1.27242 \cdot 10^{-9}$	0.121714	11933.6
	2500 < T \leq 5000	$4.55953 \cdot 10^{-7}$	-0.532978	13861.3
3 \rightarrow 12	800 \leq T \leq 2000	$8.98344 \cdot 10^{-11}$	0.416906	13704.7
	2000 < T \leq 5000	$9.46224 \cdot 10^{-7}$	-0.628390	16455.0
3 \rightarrow 13	900 \leq T \leq 2500	$2.32460 \cdot 10^{-9}$	0.002630	15463.8
	2500 < T \leq 5000	$5.98830 \cdot 10^{-7}$	-0.614689	17301.9

Table 6

Same as Table 2 for $v_i^+ = 4$, as displayed in Graph 1, maximal relative deviation of 6.067% and average RMS of 0.0047.

$v_i^+ \rightarrow v_f^+$	Temperature range (K)	A (cm^3/s)	α	B (K)
$4 \rightarrow 3$	$100 \leq T \leq 200$	$1.06736 \cdot 10^{-9}$	0.494538	-89.1826
	$200 < T \leq 700$	$3.68736 \cdot 10^{-8}$	-0.056086	37.2856
	$700 < T \leq 5000$	$3.40362 \cdot 10^{-7}$	-0.349760	255.420
$4 \rightarrow 2$	$100 \leq T \leq 400$	$9.47838 \cdot 10^{-9}$	0.0986899	-26.4064
	$400 < T \leq 1000$	$4.68070 \cdot 10^{-7}$	-0.4725691	170.016
	$1000 < T \leq 5000$	$3.33750 \cdot 10^{-8}$	-0.157519	-307.015
$4 \rightarrow 1$	$100 \leq T \leq 1000$	$1.59446 \cdot 10^{-7}$	-0.368440	-3.36955
	$1000 < T \leq 2500$	$1.29462 \cdot 10^{-8}$	-0.069683	-437.410
	$2500 < T \leq 5000$	$1.38102 \cdot 10^{-10}$	0.455216	-1536.81
$4 \rightarrow 0$	$100 \leq T \leq 400$	$7.22006 \cdot 10^{-10}$	0.514608	-32.8827
	$400 < T \leq 1000$	$8.18946 \cdot 10^{-7}$	-0.447542	666.741
	$1000 < T \leq 5000$	$2.46285 \cdot 10^{-10}$	0.391802	-1330.58
$4 \rightarrow 5$	$120 \leq T \leq 400$	$5.49606 \cdot 10^{-7}$	-0.512713	1754.28
	$400 < T \leq 800$	$3.72401 \cdot 10^{-7}$	-0.457827	1729.88
	$800 < T \leq 5000$	$2.82849 \cdot 10^{-7}$	0.139895	973.706
$4 \rightarrow 6$	$240 \leq T \leq 500$	$3.76215 \cdot 10^{-7}$	-0.480352	3439.51
	$500 < T \leq 1700$	$1.23983 \cdot 10^{-8}$	-0.003322	3097.05
	$1700 < T \leq 5000$	$4.55290 \cdot 10^{-8}$	-0.176574	3510.89
$4 \rightarrow 7$	$240 \leq T \leq 650$	$7.06310 \cdot 10^{-8}$	-0.297187	4995.04
	$650 < T \leq 2000$	$4.11467 \cdot 10^{-9}$	0.075303	4708.91
	$2000 < T \leq 5000$	$6.05544 \cdot 10^{-8}$	-0.230307	5456.78
$4 \rightarrow 8$	$360 \leq T \leq 1000$	$3.44101 \cdot 10^{-7}$	-0.501357	6677.32
	$1000 < T \leq 2500$	$7.49936 \cdot 10^{-8}$	-0.317387	6409.92
	$2500 < T \leq 5000$	$4.83064 \cdot 10^{-8}$	-0.264485	6349.28
$4 \rightarrow 9$	$440 \leq T \leq 1100$	$2.87446 \cdot 10^{-7}$	-0.434330	8217.24
	$1100 < T \leq 5000$	$6.37019 \cdot 10^{-7}$	-0.520453	8494.59
	$520 \leq T \leq 1500$	$2.54007 \cdot 10^{-7}$	-0.450098	9647.51
$4 \rightarrow 10$	$1500 < T \leq 5000$	$5.21684 \cdot 10^{-7}$	-0.527340	9919.87
	$600 \leq T \leq 1500$	$3.52393 \cdot 10^{-7}$	-0.548614	10917.4
	$1500 < T \leq 5000$	$5.21684 \cdot 10^{-7}$	-0.527340	9919.87
$4 \rightarrow 12$	$700 \leq T \leq 2000$	$9.41697 \cdot 10^{-7}$	-0.675116	12596.2
	$2000 < T \leq 5000$	$5.88904 \cdot 10^{-7}$	-0.609756	12639.5
	$800 \leq T \leq 2000$	$9.80478 \cdot 10^{-9}$	-0.148876	13089.3
$4 \rightarrow 13$	$2000 < T \leq 5000$	$4.90592 \cdot 10^{-7}$	-0.582882	14390.0
	$900 \leq T \leq 2000$	$2.60260 \cdot 10^{-11}$	0.522764	13703.4
	$2000 < T \leq 5000$	$8.71549 \cdot 10^{-7}$	-0.652413	16809.2

Table 7

Same as Table 2 for $v_i^+ = 5$, as displayed in Graph 1, maximal relative deviation of 4.841% and average RMS of 0.0047.

$v_i^+ \rightarrow v_f^+$	Temperature range (K)	A (cm^3/s)	α	B (K)
5 \rightarrow 4	100 $\leq T \leq$ 1000	$5.56989 \cdot 10^{-7}$	-0.513528	3.53340
	1000 $< T \leq$ 2500	$2.01375 \cdot 10^{-8}$	-0.094742	-436.759
	2500 $< T \leq$ 5000	$6.94136 \cdot 10^{-10}$	0.295339	-1236.46
5 \rightarrow 3	100 $\leq T \leq$ 1000	$3.10058 \cdot 10^{-7}$	-0.423326	-4.96023
	1000 $< T \leq$ 5000	$3.62360 \cdot 10^{-8}$	-0.125478	-116.229
5 \rightarrow 2	100 $\leq T \leq$ 1000	$1.06655 \cdot 10^{-7}$	-0.366370	-18.3113
	1000 $< T \leq$ 5000	$1.29558 \cdot 10^{-8}$	-0.084856	-152.314
5 \rightarrow 1	100 $\leq T \leq$ 800	$5.14091 \cdot 10^{-7}$	-0.521073	-1.52554
	800 $< T \leq$ 5000	$4.26149 \cdot 10^{-9}$	0.096789	-537.599
5 \rightarrow 0	100 $\leq T \leq$ 1000	$1.48856 \cdot 10^{-7}$	-0.300884	-23.0870
	1000 $< T \leq$ 5000	$1.00448 \cdot 10^{-6}$	-0.528422	313.166
5 \rightarrow 6	100 $\leq T \leq$ 400	$4.37146 \cdot 10^{-7}$	-0.483497	1694.15
	400 $< T \leq$ 1500	$5.91892 \cdot 10^{-7}$	-0.529020	1704.15
	1500 $< T \leq$ 5000	$1.05782 \cdot 10^{-9}$	0.225184	472.374
5 \rightarrow 7	180 $\leq T \leq$ 650	$1.21009 \cdot 10^{-7}$	0.014402	3269.17
	650 $< T \leq$ 1700	$1.21516 \cdot 10^{-7}$	-0.284733	3516.74
	1700 $< T \leq$ 5000	$3.54698 \cdot 10^{-8}$	-0.144782	3187.95
5 \rightarrow 8	260 $\leq T \leq$ 650	$1.83759 \cdot 10^{-8}$	-0.090440	4793.12
	650 $< T \leq$ 2100	$5.73937 \cdot 10^{-9}$	0.059712	4662.73
	2100 $< T \leq$ 5000	$7.20070 \cdot 10^{-8}$	-0.224701	5421.46
5 \rightarrow 9	380 $\leq T \leq$ 1200	$1.37355 \cdot 10^{-9}$	0.149154	6364.13
	1200 $< T \leq$ 2500	$7.66743 \cdot 10^{-10}$	0.222468	6290.03
	2500 $< T \leq$ 5000	$6.81228 \cdot 10^{-8}$	-0.279019	7715.95
5 \rightarrow 10	460 $\leq T \leq$ 900	$1.73377 \cdot 10^{-10}$	0.440321	7689.34
	900 $< T \leq$ 2500	$2.58850 \cdot 10^{-8}$	-0.162749	8416.55
	2500 $< T \leq$ 5000	$4.18396 \cdot 10^{-7}$	-0.490630	9309.77
5 \rightarrow 11	540 $\leq T \leq$ 1000	$5.21803 \cdot 10^{-10}$	0.299906	9102.53
	1000 $< T \leq$ 2500	$5.32106 \cdot 10^{-8}$	-0.265705	9855.20
	2500 $< T \leq$ 5000	$6.50276 \cdot 10^{-7}$	-0.546073	10637.9
5 \rightarrow 12	650 $\leq T \leq$ 1200	$2.30279 \cdot 10^{-10}$	0.336866	10621.2
	1200 $< T \leq$ 2500	$2.45953 \cdot 10^{-8}$	-0.233982	11391.3
	2500 $< T \leq$ 5000	$1.56872 \cdot 10^{-7}$	-0.439112	12002.3
5 \rightarrow 13	750 $\leq T \leq$ 1500	$2.54628 \cdot 10^{-9}$	-0.031512	12035.7
	1500 $< T \leq$ 5000	$2.24958 \cdot 10^{-8}$	-0.279178	12675.0
5 \rightarrow 14	800 $\leq T \leq$ 2000	$6.65399 \cdot 10^{-9}$	-0.137991	12985.0
	2000 $< T \leq$ 5000	$5.58883 \cdot 10^{-8}$	-0.372194	13735.0
5 \rightarrow 15	850 $\leq T \leq$ 2500	$1.04228 \cdot 10^{-9}$	0.084524	13778.2
	2500 $< T \leq$ 5000	$1.23324 \cdot 10^{-7}$	-0.444019	15405.9

Table 8

Same as Table 2 for $v_i^+ = 6$, as displayed in Graph 2, maximal relative deviation of 4.706% and average RMS of 0.0053.

$v_i^+ \rightarrow v_f^+$	Temperature range (K)	A (cm ³ /s)	α	B (K)
6 \rightarrow 5	100 \leq T \leq 900	$3.70942 \cdot 10^{-7}$	-0.446045	-7.63342
	900 $<$ T \leq 5000	$2.79129 \cdot 10^{-8}$	-0.094844	-201.478
6 \rightarrow 4	100 \leq T \leq 1000	$3.46289 \cdot 10^{-7}$	-0.467495	-2.18171
	1000 $<$ T \leq 5000	$1.47926 \cdot 10^{-8}$	-0.051965	-289.979
6 \rightarrow 3	100 \leq T \leq 1000	$2.16284 \cdot 10^{-7}$	-0.451211	-2.10319
	1000 $<$ T \leq 5000	$4.54736 \cdot 10^{-9}$	0.054518	-382.150
6 \rightarrow 2	100 \leq T \leq 1500	$2.25277 \cdot 10^{-7}$	-0.426085	-8.75750
	1500 $<$ T \leq 5000	$2.52568 \cdot 10^{-8}$	-0.154857	-337.870
6 \rightarrow 1	100 \leq T \leq 800	$2.50619 \cdot 10^{-7}$	-0.545479	3.32825
	800 $<$ T \leq 1700	$8.66864 \cdot 10^{-11}$	0.497744	-808.696
	1700 $<$ T \leq 5000	$5.97457 \cdot 10^{-9}$	0.027004	461.581
6 \rightarrow 0	100 \leq T \leq 1500	$1.78058 \cdot 10^{-7}$	-0.351516	-13.7935
	1500 $<$ T \leq 5000	$2.93734 \cdot 10^{-6}$	-0.688251	503.043
6 \rightarrow 7	100 \leq T \leq 460	$4.35370 \cdot 10^{-7}$	-0.408248	1624.97
	460 $<$ T \leq 5000	$4.93604 \cdot 10^{-7}$	-0.411277	1691.35
6 \rightarrow 8	160 \leq T \leq 400	$5.53976 \cdot 10^{-7}$	-0.466277	3252.76
	400 $<$ T \leq 1500	$3.24117 \cdot 10^{-6}$	-0.707137	3392.23
	1500 $<$ T \leq 5000	$2.29274 \cdot 10^{-7}$	-0.401535	2749.01
6 \rightarrow 9	230 \leq T \leq 600	$2.75278 \cdot 10^{-6}$	-0.672536	4802.44
	600 $<$ T \leq 2000	$2.46122 \cdot 10^{-6}$	-0.662899	4763.01
	2000 $<$ T \leq 5000	$3.21817 \cdot 10^{-7}$	-0.426979	4277.31
6 \rightarrow 10	320 \leq T \leq 950	$9.81810 \cdot 10^{-7}$	-0.663553	6282.91
	950 $<$ T \leq 5000	$3.49419 \cdot 10^{-8}$	-0.257514	5717.87
6 \rightarrow 11	420 \leq T \leq 1300	$2.12516 \cdot 10^{-8}$	-0.277995	7628.75
	1300 $<$ T \leq 5000	$1.97566 \cdot 10^{-9}$	0.006899	7193.40
6 \rightarrow 12	480 \leq T \leq 5000	$3.07918 \cdot 10^{-8}$	-0.259332	8791.81
6 \rightarrow 13	560 \leq T \leq 1500	$3.83568 \cdot 10^{-9}$	-0.043277	9957.15
	1500 $<$ T \leq 5000	$2.59324 \cdot 10^{-8}$	-0.254134	10597.6
6 \rightarrow 14	650 \leq T \leq 1600	$9.86322 \cdot 10^{-9}$	-0.214461	11127.2
	1600 $<$ T \leq 5000	$1.41149 \cdot 10^{-8}$	-0.245719	11390.3
6 \rightarrow 15	700 \leq T \leq 1700	$1.99330 \cdot 10^{-7}$	-0.558820	12607.5
	1700 $<$ T \leq 5000	$4.11509 \cdot 10^{-7}$	-0.639626	12839.7
6 \rightarrow 16	750 \leq T \leq 2000	$1.80570 \cdot 10^{-7}$	-0.527551	13787.9
	2000 $<$ T \leq 5000	$2.31377 \cdot 10^{-6}$	-0.815269	14547.0

Table 9

Same as Table 2 for $v_i^+ = 7$, as displayed in Graph 2, maximal relative deviation of 4.507% and average RMS of 0.0049.

$v_i^+ \rightarrow v_f^+$	Temperature range (K)	A (cm^3/s)	α	B (K)
7 \rightarrow 6	$100 \leq T \leq 5000$	$3.37418 \cdot 10^{-7}$	-0.367396	-16.0055
7 \rightarrow 5	$100 \leq T \leq 700$	$6.89753 \cdot 10^{-8}$	-0.217932	-21.4795
	$700 < T \leq 1700$	$2.20433 \cdot 10^{-7}$	-0.355737	150.159
	$1700 < T \leq 5000$	$2.18723 \cdot 10^{-7}$	-0.362567	50.2353
7 \rightarrow 4	$100 \leq T \leq 900$	$2.28672 \cdot 10^{-7}$	-0.458909	2.53416
	$900 < T \leq 5000$	$1.05626 \cdot 10^{-8}$	-0.037530	-200.131
	$100 \leq T \leq 700$	$1.05779 \cdot 10^{-7}$	-0.400270	-8.90257
7 \rightarrow 3	$700 < T \leq 2000$	$7.32901 \cdot 10^{-9}$	-0.028179	-182.674
	$2000 < T \leq 5000$	$2.22962 \cdot 10^{-7}$	-0.428072	577.902
	$100 \leq T \leq 1500$	$4.48329 \cdot 10^{-7}$	-0.529847	14.8007
7 \rightarrow 2	$1500 < T \leq 5000$	$2.83299 \cdot 10^{-9}$	0.085167	-826.414
	$100 \leq T \leq 700$	$1.00443 \cdot 10^{-7}$	-0.386590	-10.0161
	$700 < T \leq 1700$	$9.68579 \cdot 10^{-10}$	0.240321	-398.928
7 \rightarrow 1	$1700 < T \leq 5000$	$1.28210 \cdot 10^{-7}$	-0.323788	789.265
	$100 \leq T \leq 1000$	$2.23629 \cdot 10^{-7}$	-0.439551	4.12887
	$1000 < T \leq 5000$	$5.92475 \cdot 10^{-7}$	-0.553455	189.878
7 \rightarrow 8	$100 \leq T \leq 400$	$6.80708 \cdot 10^{-7}$	-0.392035	1590.04
	$400 < T \leq 1000$	$4.87541 \cdot 10^{-6}$	-0.667102	1721.04
	$1000 < T \leq 5000$	$1.47057 \cdot 10^{-6}$	-0.531807	1429.38
7 \rightarrow 9	$160 \leq T \leq 400$	$1.37265 \cdot 10^{-6}$	-0.709983	3138.77
	$400 < T \leq 1000$	$1.75384 \cdot 10^{-7}$	-0.428938	2981.03
	$1000 < T \leq 5000$	$1.58164 \cdot 10^{-8}$	-0.127625	2640.45
7 \rightarrow 10	$240 \leq T \leq 700$	$2.95504 \cdot 10^{-8}$	-0.146963	4487.15
	$700 < T \leq 5000$	$3.18819 \cdot 10^{-7}$	-0.444849	4811.26
	$320 \leq T \leq 1000$	$2.63726 \cdot 10^{-7}$	-0.512544	6088.15
7 \rightarrow 11	$1000 < T \leq 5000$	$4.07183 \cdot 10^{-8}$	-0.294606	5560.91
	$400 \leq T \leq 1000$	$2.14375 \cdot 10^{-7}$	-0.573817	7364.27
	$1000 < T \leq 2500$	$6.02160 \cdot 10^{-8}$	-0.422393	7123.42
7 \rightarrow 12	$2500 < T \leq 5000$	$8.85182 \cdot 10^{-10}$	0.054397	5893.89
	$460 \leq T \leq 1400$	$3.46987 \cdot 10^{-7}$	-0.600761	8655.21
	$1400 < T \leq 5000$	$5.22711 \cdot 10^{-9}$	-0.109419	7716.82
7 \rightarrow 14	$560 \leq T \leq 1500$	$4.47577 \cdot 10^{-8}$	-0.348135	9650.12
	$1500 < T \leq 5000$	$8.57693 \cdot 10^{-9}$	-0.151472	9339.79
	$600 \leq T \leq 2000$	$4.05949 \cdot 10^{-9}$	-0.109537	10670.0
7 \rightarrow 15	$2000 < T \leq 5000$	$4.20558 \cdot 10^{-9}$	-0.106801	10810.7
	$700 \leq T \leq 1000$	$1.17187 \cdot 10^{-7}$	-0.559309	12044.6
	$1000 < T \leq 5000$	$4.20426 \cdot 10^{-9}$	-0.166911	11348.1
7 \rightarrow 17	$700 \leq T \leq 1000$	$8.31094 \cdot 10^{-7}$	-0.762056	13081.4
	$1000 < T \leq 5000$	$2.65219 \cdot 10^{-7}$	-0.630184	12803.8

Table 10

Same as Table 2 for $v_i^+ = 8$, as displayed in Graph 2, maximal relative deviation of 3.697% and average RMS of 0.0054.

$v_i^+ \rightarrow v_f^+$	Temperature range (K)	A (cm ³ /s)	α	B (K)
8 → 7	100 ≤ T ≤ 500	5.78241·10 ⁻⁷	-0.536410	2.54953
	500 < T ≤ 1500	6.89449·10 ⁻⁶	-0.712737	172.842
	1500 < T ≤ 5000	8.52219·10 ⁻⁷	-0.471517	-331.533
8 → 6	100 ≤ T ≤ 500	3.16466·10 ⁻⁷	-0.383842	10.6386
	500 < T ≤ 1500	2.60307·10 ⁻⁶	-0.679387	149.899
	1500 < T ≤ 5000	2.87412·10 ⁻⁷	-0.426602	-396.479
8 → 5	100 ≤ T ≤ 500	1.63510·10 ⁻⁷	-0.325893	-8.18654
	500 < T ≤ 1500	4.22095·10 ⁻⁷	-0.450519	79.3021
	1500 < T ≤ 5000	3.29429·10 ⁻⁷	-0.427530	-41.4880
8 → 4	100 ≤ T ≤ 500	3.37039·10 ⁻⁷	-0.502840	8.13046
	500 < T ≤ 1500	3.27948·10 ⁻⁷	-0.495167	16.8707
	1500 < T ≤ 5000	3.56897·10 ⁻⁸	-0.231563	-423.381
8 → 3	100 ≤ T ≤ 500	1.04359·10 ⁻⁷	-0.321301	-18.8331
	500 < T ≤ 1500	3.17592·10 ⁻⁸	-0.142575	-61.4199
	1500 < T ≤ 5000	9.16946·10 ⁻⁷	-0.548129	547.126
8 → 2	100 ≤ T ≤ 500	3.85687·10 ⁻⁷	-0.677221	17.1568
	500 < T ≤ 1500	2.62968·10 ⁻⁹	-0.003202	-388.783
	1500 < T ≤ 5000	6.05370·10 ⁻¹⁰	0.223618	-62.8571
8 → 1	100 ≤ T ≤ 500	5.19264·10 ⁻⁸	-0.324035	-18.0165
	500 < T ≤ 1500	5.95451·10 ⁻¹⁰	0.293257	-341.671
	1500 < T ≤ 5000	5.95451·10 ⁻¹⁰	0.293257	-341.671
8 → 0	100 ≤ T ≤ 500	3.09423·10 ⁻⁷	-0.536410	2.54953
	500 < T ≤ 1500	2.19437·10 ⁻⁷	-0.486125	-14.5982
	1500 < T ≤ 5000	2.04734·10 ⁻⁷	-0.475431	2.70393
8 → 9	100 ≤ T ≤ 400	9.49750·10 ⁻⁷	-0.530662	1516.89
	400 < T ≤ 1000	2.83633·10 ⁻⁷	-0.359254	1443.77
	1000 < T ≤ 5000	4.07622·10 ⁻⁷	-0.413605	1410.77
8 → 10	170 ≤ T ≤ 400	4.15169·10 ⁻¹⁰	0.325430	2808.01
	400 < T ≤ 1000	3.35729·10 ⁻⁹	0.048405	2993.08
	1000 < T ≤ 5000	5.58929·10 ⁻⁹	-0.035381	2866.01
8 → 11	240 ≤ T ≤ 400	5.35457·10 ⁻⁷	-0.569165	4472.53
	400 < T ≤ 1000	2.73894·10 ⁻⁷	-0.477771	4420.27
	1000 < T ≤ 5000	9.80430·10 ⁻⁸	-0.357002	4192.51
8 → 12	320 ≤ T ≤ 400	1.35568·10 ⁻⁷	-0.449477	5765.65
	400 < T ≤ 1000	9.19102·10 ⁻⁸	-0.396388	5735.52
	1000 < T ≤ 5000	2.88488·10 ⁻⁸	-0.266229	5409.83
8 → 13	400 ≤ T ≤ 1000	1.47058·10 ⁻⁷	-0.527347	6967.98
	1000 < T ≤ 5000	5.13127·10 ⁻⁹	-0.152644	5990.70
8 → 14	480 ≤ T ≤ 1000	2.18512·10 ⁻⁷	-0.589139	8345.45
	1000 < T ≤ 5000	1.39150·10 ⁻⁹	-0.014322	7001.90
8 → 15	520 ≤ T ≤ 1000	1.63717·10 ⁻⁶	-0.807889	9435.76
	1000 < T ≤ 5000	4.53125·10 ⁻⁹	-0.117374	8117.49
8 → 16	600 ≤ T ≤ 1000	5.91540·10 ⁻⁷	-0.706951	10448.0
	1000 < T ≤ 5000	2.64262·10 ⁻⁹	-0.062595	9368.17
8 → 17	700 ≤ T ≤ 1000	3.30687·10 ⁻⁸	-0.442046	11199.8
	1000 < T ≤ 5000	3.21768·10 ⁻¹⁰	0.127603	10540.1
8 → 18	750 ≤ T ≤ 1000	2.60829·10 ⁻⁹	-0.174712	12243.2
	1000 < T ≤ 5000	3.60844·10 ⁻¹⁰	0.068440	12019.2

Table 11

Same as Table 2 for $v_i^+ = 9$, as displayed in Graph 2, maximal relative deviation of 4.062% and average RMS of 0.0038.

$v_i^+ \rightarrow v_f^+$	Temperature range (K)	A (cm^3/s)	α	B (K)
$9 \rightarrow 8$	$100 \leq T \leq 500$	$1.44871 \cdot 10^{-6}$	-0.593333	-1.62306
	$500 < T \leq 1500$	$3.65915 \cdot 10^{-7}$	-0.392892	-69.8892
	$1500 < T \leq 5000$	$2.67847 \cdot 10^{-7}$	-0.367149	-264.834
$9 \rightarrow 7$	$100 \leq T \leq 500$	$1.24170 \cdot 10^{-6}$	-0.695805	14.5189
	$500 < T \leq 1500$	$9.79737 \cdot 10^{-8}$	-0.351667	-189.513
	$1500 < T \leq 5000$	$1.44986 \cdot 10^{-8}$	-0.117823	-505.359
$9 \rightarrow 6$	$100 \leq T \leq 500$	$1.24407 \cdot 10^{-6}$	-0.558619	4.63465
	$500 < T \leq 1500$	$3.89262 \cdot 10^{-6}$	-0.719476	76.8211
	$1500 < T \leq 5000$	$4.21510 \cdot 10^{-7}$	-0.456587	-381.530
$9 \rightarrow 5$	$100 \leq T \leq 500$	$2.06640 \cdot 10^{-7}$	-0.448587	-18.4794
	$500 < T \leq 1500$	$2.17823 \cdot 10^{-6}$	-0.766914	168.897
	$1500 < T \leq 5000$	$1.99507 \cdot 10^{-8}$	-0.218426	-872.766
$9 \rightarrow 4$	$100 \leq T \leq 500$	$1.70925 \cdot 10^{-7}$	-0.362443	-9.96986
	$500 < T \leq 1500$	$2.95153 \cdot 10^{-7}$	-0.437449	29.4370
	$1500 < T \leq 5000$	$4.01500 \cdot 10^{-7}$	-0.469641	143.683
$9 \rightarrow 3$	$100 \leq T \leq 500$	$4.32221 \cdot 10^{-8}$	-0.188273	-24.1836
	$500 < T \leq 1500$	$4.48697 \cdot 10^{-7}$	-0.502495	171.029
	$1500 < T \leq 5000$	$2.22533 \cdot 10^{-7}$	-0.426892	-50.0461
$9 \rightarrow 2$	$100 \leq T \leq 500$	$1.02774 \cdot 10^{-7}$	-0.483004	-7.30020
	$500 < T \leq 1500$	$3.06525 \cdot 10^{-10}$	0.330319	-395.902
	$1500 < T \leq 5000$	$3.26279 \cdot 10^{-8}$	-0.208900	725.828
$9 \rightarrow 1$	$100 \leq T \leq 500$	$8.86504 \cdot 10^{-8}$	-0.420146	-9.85374
	$500 < T \leq 1500$	$3.83639 \cdot 10^{-10}$	0.322306	-430.712
	$1500 < T \leq 5000$	$4.67244 \cdot 10^{-7}$	-0.502120	1216.24
$9 \rightarrow 0$	$100 \leq T \leq 500$	$1.38755 \cdot 10^{-7}$	-0.446860	-6.22064
	$500 < T \leq 1500$	$1.72365 \cdot 10^{-7}$	-0.481270	-3.16788
	$1500 < T \leq 5000$	$7.12289 \cdot 10^{-8}$	-0.369724	-100.655
$9 \rightarrow 10$	$100 \leq T \leq 400$	$1.20071 \cdot 10^{-7}$	-0.234322	1439.04
	$400 < T \leq 1000$	$4.95822 \cdot 10^{-7}$	-0.430412	1539.01
	$1000 < T \leq 5000$	$6.58499 \cdot 10^{-7}$	-0.479700	1459.11
$9 \rightarrow 11$	$160 \leq T \leq 400$	$2.11543 \cdot 10^{-7}$	-0.466053	2885.60
	$400 < T \leq 1000$	$1.24949 \cdot 10^{-7}$	-0.388771	2861.73
	$1000 < T \leq 5000$	$3.20005 \cdot 10^{-8}$	-0.239367	2473.46
$9 \rightarrow 12$	$230 \leq T \leq 400$	$2.59073 \cdot 10^{-7}$	-0.528059	4271.87
	$400 < T \leq 1000$	$2.59555 \cdot 10^{-7}$	-0.531444	4261.73
	$1000 < T \leq 5000$	$8.74783 \cdot 10^{-9}$	-0.125368	3613.08
$9 \rightarrow 13$	$300 \leq T \leq 400$	$1.85508 \cdot 10^{-7}$	-0.474054	5459.09
	$400 < T \leq 1000$	$2.46768 \cdot 10^{-7}$	-0.512874	5481.55
	$1000 < T \leq 5000$	$3.72732 \cdot 10^{-8}$	-0.290945	5066.43
$9 \rightarrow 14$	$400 \leq T \leq 1000$	$4.04717 \cdot 10^{-7}$	-0.676035	6685.63
	$1000 < T \leq 5000$	$1.88103 \cdot 10^{-9}$	-0.047674	5464.71
	$460 \leq T \leq 1000$	$8.55868 \cdot 10^{-8}$	-0.523497	7733.14
$9 \rightarrow 15$	$1000 < T \leq 5000$	$5.12315 \cdot 10^{-10}$	0.058287	6354.33
	$520 \leq T \leq 1000$	$9.83633 \cdot 10^{-8}$	-0.505568	8961.72
	$1000 < T \leq 5000$	$1.71131 \cdot 10^{-9}$	-0.044699	7889.40
$9 \rightarrow 16$	$560 \leq T \leq 1000$	$3.44385 \cdot 10^{-7}$	-0.645044	9929.37
	$1000 < T \leq 5000$	$2.87160 \cdot 10^{-9}$	-0.084483	8860.52
	$650 \leq T \leq 1000$	$3.83691 \cdot 10^{-7}$	-0.693580	10839.3
$9 \rightarrow 17$	$1000 < T \leq 5000$	$9.37271 \cdot 10^{-10}$	0.022107	9636.56
	$650 \leq T \leq 1000$	$6.27368 \cdot 10^{-8}$	-0.562797	11532.9
	$1000 < T \leq 5000$	$1.85441 \cdot 10^{-14}$	1.152320	7032.37

Table 12

Same as Table 2 for $v_i^+ = 10$, as displayed in Graph 2, maximal relative deviation of 3.541% and average RMS of 0.0038.

$v_i^+ \rightarrow v_f^+$	Temperature range (K)	A (cm^3/s)	α	B (K)
$10 \rightarrow 9$	$100 \leq T \leq 500$	$1.92577 \cdot 10^{-7}$	-0.305078	-26.8405
	$500 < T \leq 1500$	$9.22604 \cdot 10^{-7}$	-0.512261	111.699
	$1500 < T \leq 5000$	$4.18158 \cdot 10^{-7}$	-0.429462	-175.701
$10 \rightarrow 8$	$100 \leq T \leq 650$	$1.10611 \cdot 10^{-8}$	-0.160095	-66.0942
	$650 < T \leq 1500$	$6.14458 \cdot 10^{-9}$	-0.031534	25.8044
	$1500 < T \leq 5000$	$4.20322 \cdot 10^{-9}$	-0.003797	-252.871
$10 \rightarrow 7$	$100 \leq T \leq 500$	$1.73636 \cdot 10^{-7}$	-0.401646	-18.5255
	$500 < T \leq 1500$	$4.87697 \cdot 10^{-8}$	-0.213395	-71.3638
	$1500 < T \leq 5000$	$3.15820 \cdot 10^{-7}$	-0.443674	207.158
$10 \rightarrow 6$	$100 \leq T \leq 500$	$3.60732 \cdot 10^{-7}$	-0.516145	-1.65344
	$500 < T \leq 1500$	$7.79404 \cdot 10^{-7}$	-0.632888	23.7802
	$1500 < T \leq 5000$	$3.27638 \cdot 10^{-8}$	-0.250421	-543.330
$10 \rightarrow 5$	$100 \leq T \leq 500$	$3.52024 \cdot 10^{-7}$	-0.460535	15.1393
	$500 < T \leq 1500$	$4.77314 \cdot 10^{-6}$	-0.839672	147.701
	$1500 < T \leq 5000$	$3.13883 \cdot 10^{-8}$	-0.234609	-763.686
$10 \rightarrow 4$	$100 \leq T \leq 500$	$1.80921 \cdot 10^{-7}$	-0.387829	-0.99888
	$500 < T \leq 1500$	$3.81103 \cdot 10^{-7}$	-0.501019	22.6404
	$1500 < T \leq 5000$	$2.89393 \cdot 10^{-7}$	-0.462745	31.7006
$10 \rightarrow 3$	$100 \leq T \leq 500$	$7.58313 \cdot 10^{-8}$	-0.281289	-20.6885
	$500 < T \leq 1500$	$2.03004 \cdot 10^{-6}$	-0.736521	210.870
	$1500 < T \leq 5000$	$5.68021 \cdot 10^{-8}$	-0.308307	-456.762
$10 \rightarrow 2$	$100 \leq T \leq 500$	$7.31922 \cdot 10^{-9}$	-0.067803	-46.7249
	$500 < T \leq 1500$	$1.09392 \cdot 10^{-8}$	-0.109858	20.2654
	$1500 < T \leq 5000$	$2.86504 \cdot 10^{-8}$	-0.217551	302.217
$10 \rightarrow 1$	$100 \leq T \leq 500$	$1.77418 \cdot 10^{-7}$	-0.501015	3.90605
	$500 < T \leq 1500$	$1.64880 \cdot 10^{-9}$	0.142933	-339.635
	$1500 < T \leq 5000$	$1.89084 \cdot 10^{-6}$	-0.683998	1184.11
$10 \rightarrow 0$	$100 \leq T \leq 500$	$1.13041 \cdot 10^{-7}$	-0.456875	0.21805
	$500 < T \leq 1500$	$4.54531 \cdot 10^{-8}$	-0.330801	-65.4893
	$1500 < T \leq 5000$	$4.86730 \cdot 10^{-8}$	-0.327513	84.7081
$10 \rightarrow 11$	$100 \leq T \leq 400$	$2.78742 \cdot 10^{-7}$	-0.356049	1385.68
	$400 < T \leq 1000$	$4.46097 \cdot 10^{-7}$	-0.419660	1422.69
	$1000 < T \leq 5000$	$8.10946 \cdot 10^{-7}$	-0.501366	1445.19
$10 \rightarrow 12$	$140 \leq T \leq 400$	$2.13203 \cdot 10^{-6}$	-0.753681	2786.00
	$400 < T \leq 1000$	$1.04984 \cdot 10^{-6}$	-0.655861	2735.17
	$1000 < T \leq 5000$	$8.91478 \cdot 10^{-8}$	-0.359020	2283.81
$10 \rightarrow 13$	$230 \leq T \leq 400$	$4.10433 \cdot 10^{-8}$	-0.373744	4005.04
	$400 < T \leq 1000$	$2.41232 \cdot 10^{-8}$	-0.306044	3948.51
	$1000 < T \leq 5000$	$5.04050 \cdot 10^{-10}$	0.163101	3267.37
$10 \rightarrow 14$	$290 \leq T \leq 400$	$1.06117 \cdot 10^{-7}$	-0.419498	5166.32
	$400 < T \leq 1000$	$1.19855 \cdot 10^{-7}$	-0.434089	5182.09
	$1000 < T \leq 5000$	$3.45317 \cdot 10^{-8}$	-0.289256	4896.40
$10 \rightarrow 15$	$360 \leq T \leq 400$	$1.94581 \cdot 10^{-7}$	-0.578360	6313.66
	$400 < T \leq 1000$	$1.77365 \cdot 10^{-7}$	-0.569324	6293.84
	$1000 < T \leq 5000$	$2.27823 \cdot 10^{-9}$	-0.053242	5386.11
$10 \rightarrow 16$	$420 \leq T \leq 1000$	$2.65598 \cdot 10^{-7}$	-0.688741	7328.40
	$1000 < T \leq 5000$	$2.90340 \cdot 10^{-10}$	0.103411	5706.67
$10 \rightarrow 17$	$500 \leq T \leq 1000$	$1.33379 \cdot 10^{-8}$	-0.315155	8238.91
	$1000 < T \leq 5000$	$3.48882 \cdot 10^{-10}$	0.090272	7160.36
$10 \rightarrow 18$	$560 \leq T \leq 1000$	$4.78249 \cdot 10^{-8}$	-0.444997	9369.07
	$1000 < T \leq 5000$	$1.08039 \cdot 10^{-9}$	-0.010176	8414.03
$10 \rightarrow 19$	$600 \leq T \leq 1000$	$1.51702 \cdot 10^{-7}$	-0.584259	10253.4
	$1000 < T \leq 5000$	$1.50933 \cdot 10^{-9}$	-0.040020	9279.58
$10 \rightarrow 20$	$600 \leq T \leq 1000$	$1.51702 \cdot 10^{-7}$	-0.584259	10253.4
	$1000 < T \leq 5000$	$1.50933 \cdot 10^{-9}$	-0.040020	9279.58

Table 13

Isotopic effects: Dissociative recombination rate coefficient of the BeH^+ , BeD^+ and BeT^+ molecular cations as function of the energy of the initial vibrational level of the target $E_{v_i^+} - E_0$ (relative to the ground vibrational level) for three electron temperatures: 300 K, 1000 K and 5000 K.

Temperature (K)	BeH^+			BeD^+			BeT^+		
	v_i^+	$E_{v_i^+} - E_0$ (eV)	Rate coefficient (cm^3/s)	v_i^+	$E_{v_i^+} - E_0$ (eV)	Rate coefficient (cm^3/s)	v_i^+	$E_{v_i^+} - E_0$ (eV)	Rate coefficient (cm^3/s)
300	0	0.000	$1.13043 \cdot 10^{-7}$	0	0.000	$1.26201 \cdot 10^{-7}$	0	0.000	$1.34068 \cdot 10^{-7}$
	1	0.259	$1.89605 \cdot 10^{-7}$	1	0.194	$2.13453 \cdot 10^{-7}$	1	0.167	$2.15156 \cdot 10^{-7}$
	2	0.507	$2.55119 \cdot 10^{-7}$	2	0.381	$2.25027 \cdot 10^{-7}$	2	0.327	$2.23157 \cdot 10^{-7}$
	3	0.746	$2.05097 \cdot 10^{-7}$	3	0.565	$2.34042 \cdot 10^{-7}$	3	0.486	$3.20841 \cdot 10^{-7}$
	4	0.975	$2.35437 \cdot 10^{-7}$	4	0.743	$2.41174 \cdot 10^{-7}$	4	0.641	$2.09956 \cdot 10^{-7}$
	5	1.191	$4.54551 \cdot 10^{-7}$	5	0.915	$1.81772 \cdot 10^{-7}$	5	0.792	$1.947060 \cdot 10^{-7}$
	6	1.396	$2.24184 \cdot 10^{-7}$	6	1.080	$2.93495 \cdot 10^{-7}$	6	0.937	$1.996350 \cdot 10^{-7}$
	7	1.588	$1.64762 \cdot 10^{-7}$	7	1.238	$3.67180 \cdot 10^{-7}$	7	1.078	$2.752180 \cdot 10^{-7}$
	8	1.762	$1.55939 \cdot 10^{-7}$	8	1.391	$2.48675 \cdot 10^{-7}$	8	1.214	$3.978330 \cdot 10^{-7}$
	9	1.921	$1.38102 \cdot 10^{-7}$	9	1.538	$2.19837 \cdot 10^{-7}$	9	1.347	$2.280440 \cdot 10^{-7}$
	10	2.066	$1.08544 \cdot 10^{-7}$	10	1.675	$1.84860 \cdot 10^{-7}$	10	1.475	$1.922060 \cdot 10^{-7}$
	11	2.198	$1.04839 \cdot 10^{-7}$	11	1.802	$1.53598 \cdot 10^{-7}$	11	1.597	$1.624550 \cdot 10^{-7}$
	12	2.316	$0.90535 \cdot 10^{-7}$	12	1.921	$1.403460 \cdot 10^{-7}$	12	1.712	$1.636260 \cdot 10^{-7}$
	13	2.418	$0.71285 \cdot 10^{-7}$	13	2.031	$1.289540 \cdot 10^{-7}$	13	1.819	$1.462200 \cdot 10^{-7}$
	14	2.503	$0.56714 \cdot 10^{-7}$	14	2.135	$1.184330 \cdot 10^{-7}$	14	1.921	$1.264430 \cdot 10^{-7}$
	15	2.568	$0.38451 \cdot 10^{-7}$	15	2.232	$0.1065160 \cdot 10^{-7}$	15	2.017	$1.224940 \cdot 10^{-7}$
	16	2.614	$0.248093 \cdot 10^{-7}$	16	2.321	$0.942660 \cdot 10^{-7}$	16	2.107	$1.131190 \cdot 10^{-7}$
	17	2.646	$0.12415 \cdot 10^{-7}$	17	2.401	$0.688125 \cdot 10^{-7}$	17	2.193	$1.140570 \cdot 10^{-7}$
				18	2.473	$0.664439 \cdot 10^{-7}$	18	2.273	$1.05216 \cdot 10^{-7}$
				19	2.535	$0.53440 \cdot 10^{-7}$	19	2.348	$0.98783 \cdot 10^{-7}$
				20	2.586	$0.38638 \cdot 10^{-7}$	20	2.416	$0.91899 \cdot 10^{-7}$
				21	2.624	$0.26081 \cdot 10^{-7}$	21	2.477	$0.78952 \cdot 10^{-7}$
				22	2.656	$0.35449 \cdot 10^{-7}$	22	2.532	$0.68255 \cdot 10^{-7}$
				23	2.679	$0.38637 \cdot 10^{-7}$	23	2.578	$0.55167 \cdot 10^{-7}$
							24	2.617	$0.42227 \cdot 10^{-7}$
							25	2.648	$0.37486 \cdot 10^{-7}$
							26	2.673	$0.28288 \cdot 10^{-7}$
							27	2.693	$0.15356 \cdot 10^{-7}$
1000	0	0.000	$0.62273 \cdot 10^{-7}$	0	0.000	$0.6676 \cdot 10^{-7}$	0	0.000	$0.66745 \cdot 10^{-7}$
	1	0.259	$1.15746 \cdot 10^{-7}$	1	0.194	$1.15668 \cdot 10^{-7}$	1	0.167	$1.08648 \cdot 10^{-7}$
	2	0.507	$1.48471 \cdot 10^{-7}$	2	0.381	$1.49232 \cdot 10^{-7}$	2	0.327	$1.3651 \cdot 10^{-7}$
	3	0.746	$1.23833 \cdot 10^{-7}$	3	0.565	$1.42339 \cdot 10^{-7}$	3	0.486	$1.79330 \cdot 10^{-7}$
	4	0.975	$1.59735 \cdot 10^{-7}$	4	0.743	$1.49176 \cdot 10^{-7}$	4	0.641	$1.47070 \cdot 10^{-7}$
	5	1.191	$2.37894 \cdot 10^{-7}$	5	0.915	$1.26522 \cdot 10^{-7}$	5	0.792	$1.22328 \cdot 10^{-7}$
	6	1.396	$1.54019 \cdot 10^{-7}$	6	1.080	$1.97732 \cdot 10^{-7}$	6	0.937	$1.29393 \cdot 10^{-7}$
	7	1.588	$1.02440 \cdot 10^{-7}$	7	1.238	$1.81918 \cdot 10^{-7}$	7	1.078	$1.88718 \cdot 10^{-7}$
	8	1.762	$0.91984 \cdot 10^{-7}$	8	1.391	$1.46238 \cdot 10^{-7}$	8	1.214	$2.03371 \cdot 10^{-7}$
	9	1.921	$0.81237 \cdot 10^{-7}$	9	1.538	$1.25893 \cdot 10^{-7}$	9	1.347	$1.39099 \cdot 10^{-7}$
	10	2.066	$0.66003 \cdot 10^{-7}$	10	1.675	$1.04380 \cdot 10^{-7}$	10	1.475	$1.23618 \cdot 10^{-7}$
	11	2.198	$0.65134 \cdot 10^{-7}$	11	1.802	$0.89330 \cdot 10^{-7}$	11	1.597	$1.05604 \cdot 10^{-7}$
	12	2.316	$0.54343 \cdot 10^{-7}$	12	1.921	$0.81329 \cdot 10^{-7}$	12	1.712	$0.980590 \cdot 10^{-7}$
	13	2.418	$0.43323 \cdot 10^{-7}$	13	2.031	$0.73243 \cdot 10^{-7}$	13	1.819	$0.86606 \cdot 10^{-7}$
	14	2.503	$0.33629 \cdot 10^{-7}$	14	2.135	$0.66925 \cdot 10^{-7}$	14	1.921	$0.77773 \cdot 10^{-7}$
	15	2.568	$0.22762 \cdot 10^{-7}$	15	2.232	$0.59011 \cdot 10^{-7}$	15	2.017	$0.71660 \cdot 10^{-7}$
	16	2.614	$0.15309 \cdot 10^{-7}$	16	2.321	$0.51745 \cdot 10^{-7}$	16	2.107	$0.66103 \cdot 10^{-7}$
	17	2.646	$0.12415 \cdot 10^{-7}$	17	2.401	$0.37836 \cdot 10^{-7}$	17	2.193	$0.62597 \cdot 10^{-7}$
				18	2.473	$0.36924 \cdot 10^{-7}$	18	2.273	$0.57802 \cdot 10^{-7}$
				19	2.535	$0.30333 \cdot 10^{-7}$	19	2.348	$0.52977 \cdot 10^{-7}$
				20	2.586	$0.22249 \cdot 10^{-7}$	20	2.416	$0.48865 \cdot 10^{-7}$
				21	2.624	$0.32560 \cdot 10^{-7}$	21	2.477	$0.42874 \cdot 10^{-7}$
				22	2.656	$0.36031 \cdot 10^{-7}$	22	2.532	$0.36855 \cdot 10^{-7}$
				23	2.679	$0.22243 \cdot 10^{-7}$	23	2.578	$0.29787 \cdot 10^{-7}$
							24	2.617	$0.23348 \cdot 10^{-7}$
							25	2.648	$0.21063 \cdot 10^{-7}$
							26	2.673	$0.16473 \cdot 10^{-7}$
							27	2.693	$0.09307 \cdot 10^{-7}$
5000	0	0.000	$0.55998 \cdot 10^{-7}$	0	0.000	$0.37608 \cdot 10^{-7}$	0	0.000	$0.29001 \cdot 10^{-7}$
	1	0.259	$0.82794 \cdot 10^{-7}$	1	0.194	$0.65690 \cdot 10^{-7}$	1	0.167	$0.51597 \cdot 10^{-7}$
	2	0.507	$0.77280 \cdot 10^{-7}$	2	0.381	$0.80984 \cdot 10^{-7}$	2	0.327	$0.73925 \cdot 10^{-7}$
	3	0.746	$0.79359 \cdot 10^{-7}$	3	0.565	$0.72617 \cdot 10^{-7}$	3	0.486	$0.75943 \cdot 10^{-7}$
	4	0.975	$0.92771 \cdot 10^{-7}$	4	0.743	$0.77806 \cdot 10^{-7}$	4	0.641	$0.74990 \cdot 10^{-7}$
	5	1.191	$0.96326 \cdot 10^{-7}$	5	0.915	$0.81876 \cdot 10^{-7}$	5	0.792	$0.71843 \cdot 10^{-7}$
	6	1.396	$0.79917 \cdot 10^{-7}$	6	1.080	$0.96890 \cdot 10^{-7}$	6	0.937	$0.79576 \cdot 10^{-7}$
	7	1.588	$0.56721 \cdot 10^{-7}$	7	1.238	$0.84272 \cdot 10^{-7}$	7	1.078	$0.92157 \cdot 10^{-7}$
	8	1.762	$0.51647 \cdot 10^{-7}$	8	1.391	$0.75447 \cdot 10^{-7}$	8	1.214	$0.86090 \cdot 10^{-7}$
	9	1.921	$0.46885 \cdot 10^{-7}$	9	1.538	$0.65267 \cdot 10^{-7}$	9	1.347	$0.74701 \cdot 10^{-7}$
	10	2.066	$0.36131 \cdot 10^{-7}$	10	1.675	$0.55439 \cdot 10^{-7}$	10	1.475	$0.68115 \cdot 10^{-7}$
	11	2.198	$0.36483 \cdot 10^{-7}$	11	1.802	$0.49067 \cdot 10^{-7}$	11	1.597	$0.58977 \cdot 10^{-7}$
	12	2.316	$0.30467 \cdot 10^{-7}$	12	1.921	$0.44263 \cdot 10^{-7}$	12	1.712	$0.52260 \cdot 10^{-7}$

(continued on next page)

Table 13 (continued)

Temperature (K)	BeH ⁺			BeD ⁺			BeT ⁺		
	v_i^+	$E_{v_i^+} - E_0$ (eV)	Rate coefficient (cm ³ /s)	v_i^+	$E_{v_i^+} - E_0$ (eV)	Rate coefficient (cm ³ /s)	v_i^+	$E_{v_i^+} - E_0$ (eV)	Rate coefficient (cm ³ /s)
	13	2.418	$0.25328 \cdot 10^{-7}$	13	2.031	$0.39992 \cdot 10^{-7}$	13	1.819	$0.47411 \cdot 10^{-7}$
	14	2.503	$0.20608 \cdot 10^{-7}$	14	2.135	$0.36903 \cdot 10^{-7}$	14	1.921	$0.43223 \cdot 10^{-7}$
	15	2.568	$0.14556 \cdot 10^{-7}$	15	2.232	$0.33269 \cdot 10^{-7}$	15	2.017	$0.40022 \cdot 10^{-7}$
	16	2.614	$0.10140 \cdot 10^{-7}$	16	2.321	$0.29882 \cdot 10^{-7}$	16	2.107	$0.37307 \cdot 10^{-7}$
	17	2.646	$0.053571 \cdot 10^{-7}$	17	2.401	$0.21835 \cdot 10^{-7}$	17	2.193	$0.34827 \cdot 10^{-7}$
				18	2.473	$0.22794 \cdot 10^{-7}$	18	2.273	$0.32048 \cdot 10^{-7}$
				19	2.535	$0.19643 \cdot 10^{-7}$	19	2.348	$0.29209 \cdot 10^{-7}$
				20	2.586	$0.15036 \cdot 10^{-7}$	20	2.416	$0.27011 \cdot 10^{-7}$
				21	2.624	$0.18515 \cdot 10^{-7}$	21	2.477	$0.24116 \cdot 10^{-7}$
				22	2.656	$0.19536 \cdot 10^{-7}$	22	2.532	$0.21027 \cdot 10^{-7}$
				23	2.679	$0.15037 \cdot 10^{-7}$	23	2.578	$0.17552 \cdot 10^{-7}$
							24	2.617	$0.14177 \cdot 10^{-7}$
							25	2.648	$0.13063 \cdot 10^{-7}$
							26	2.673	$0.10503 \cdot 10^{-7}$
							27	2.693	$0.06095 \cdot 10^{-7}$

ELECTRON DRIVEN REACTIVE PROCESSES INVOLVING H_2^+ AND HD^+ MOLECULAR CATIONS IN THE EARLY UNIVERSE

EMERANCE DJUISSI¹, RĂZVAN BOGDAN², ABDILLAH ABDOULANZIZ¹, NICOLINA POP³,
FELIX IACOB⁴, CLÉMENT ARGENTIN¹, MICHEL DOUGLAS EPÉE EPÉE⁵, OUSMANOU
MOTAPON^{5,6}, VINCENZO LAPORTA⁷, JÁNOS ZSOLT MEZEI^{1,8}, IOAN F. SCHNEIDER^{1,9}

¹LOMC CNRS-UMR6294, Université Le Havre Normandie, 53 rue Prony, 76058 Le Havre, France

²Dept. of Comput. & Informat. Technol., Politehnica University Timișoara, 2 blvd Vasile Pârvan,
300223 Timișoara, Romania

³Dept. Physical Foundations of Engineering, Politehnica University Timișoara, 2 blvd Vasile Pârvan,
300223 Timișoara, Romania Email: nicolina.pop@upt.ro

⁴Dept. of Physics, West University of Timișoara, 4 blvd Vasile Pârvan, 300223 Timișoara, Romania

⁵LPF, UFD Mathématiques, Informatique Appliquée et Physique Fondamentale, University of Douala,
P. O. Box 24157 Douala, Cameroon

⁶Faculty of Science, University of Maroua, P. O. Box 814 Maroua, Cameroon

⁷Istituto per la Scienza e Tecnologia dei Plasmi, CNR, Bari, Italy

⁸Institute for Nuclear Research, Bem sqr. 18/c, 4026 Debrecen, Hungary

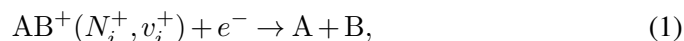
⁹LAC CNRS-FRE2038, Université Paris-Saclay, ENS Cachan, Campus d'Orsay, Bat. 305, 91405
Orsay, France

Abstract. We describe the major low-energy electron-impact processes involving H_2^+ and HD^+ , relevant for the astrochemistry of the early Universe: Dissociative recombination, elastic, inelastic and superelastic scattering. We report cross sections and Maxwellian rate coefficients of both rotational and vibrational transitions, and outline several important features, like isotopic, rotational and resonant effects.

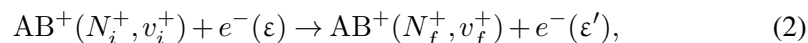
Key words: Astrochemistry – Dissociative recombination – Vibrational excitation – Early Universe .

1. INTRODUCTION

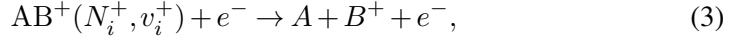
The models of the early Universe (Lepp *et al.*, 2002; Coppola *et al.*, 2016) state that atomic hydrogen, helium and lithium - and their cations - have been the very first species produced by the nucleosynthetic activity which followed the Big Bang. Later on, atoms reacted to form simple molecules, like HeH^+ , H_2 , HD , LiH and their cations. These latter ones face *Dissociative Recombination* (DR):



Ro-Vibrational Transitions (RVT):



and *Dissociative Excitation* (DE):



where N_i^+/N_f^+ and v_i^+/v_f^+ are the initial/final rotational and vibrational quantum numbers of the target ion, and ε/ε' the energy of the incident/scattered electron.

The dissociative recombination was first bravely proposed as elementary process in the Earth's ionosphere, as a competitor to the photoionisation providing free electrons (Bates and Massey, 1947). Currently, it is considered a corner-stone reaction in the synthesis of interstellar molecules and plays an important role in the ionized layers of other planets, exoplanets and their satellites. In the modeling of the kinetics of cold dilute gases, the ro-vibrational distribution of molecular species is governed by competition between formation and destruction processes, absorption, fluorescence, radiative cascades, and low-energy collisions involving neutral and ionized atomic and molecular species as well as electrons. Rate coefficients for such elementary reactions are badly needed, in particular for the chemical models of the early Universe, interstellar medium, and planetary atmospheres.

Within a semiclassical scenario, a two-step process characterizes the DR. First, the electron is captured by the molecular cation while exciting an electron, similarly to the dielectronic recombination of atomic cations. A neutral molecule is formed, for many species in a doubly-excited, repulsive electronic state, located above the lowest ionization potential. Second, the molecule dissociates rapidly along the potential energy curve of this dissociative state. The (re-)ejection of an electron may occur – autoionization – with low probability due to rapid dissociation which lowers the electronic energy below the lowest ionization limit. The molecule stabilizes then the electron capture by dissociating.

The spectroscopic information, given by the output of RVT reactions (2), is sensitive to the quantum numbers of the target ion (initial: $\{N_i^+, v_i^+\}$ and final: $\{N_f^+, v_f^+\}$) and consequently it provides the structure of the ionized media. As for the RVT, they are called *Elastic Collisions* (EC), *Inelastic Collisions* and *Super-Elastic Collisions* (SEC) when the final energy of the electron is equal, smaller or larger respectively than the initial one.

This paper aims to illustrate our theoretical approach of the reactive collisions of electrons with H_2^+ and HD^+ cations at low – below 1 eV – energy, from basic ideas to computation of cross sections and rate coefficients, *via* details of the methods we use. The results we show are a part of a huge series of data we are about to produce, relevant for the kinetic modelling of the early Universe. This data generation was initiated by previous publications of our group (Motapon *et al.*, 2014; Epée *et al.*, 2016). In the present study, the accent is put on HD^+ rather than on H_2^+ , since most of the latest experiments – performed in storage rings – focused on this isotopomer, is subject of quick vibrational relaxation and, consequently, more easy to

vibrationally resolve than the homonuclear species. We have to notice that, whereas for this latter isotopomer, the rotational transitions involve rotational quantum numbers of strictly the same parity (even or odd), this rule is not valid for the deuterated variant. However, we have assumed it for HD^+ too, since no data are so far available for the *gerade/ungerade* mixing, and since the transitions between rotational quantum numbers of different parity are much less intense than the others (Shafir *et al.*, 2009).

Our paper is organized as follows: The introduction is followed – Section 2 – by a brief description of the employed theoretical approach and of the major computational details. In section 3 we present and discuss our calculated cross sections and rate coefficients. The paper ends with conclusions – Section 4.

2. THEORETICAL APPROACH

We presently use a stepwise version of the Multichannel Quantum Defect Theory (MQDT) to study the electron-induced reactions described in Eqs. (1–3). In the last decade, we made evolve this approach and applied it successfully for computing the dissociative recombination, ro-vibrational and dissociative excitation cross sections of H_2^+ and its isotopologues (Waffeu *et al.*, 2011; Chakrabarti *et al.*, 2013; Motapon *et al.*, 2014; Epée *et al.*, 2016), CH^+ (Mezei *et al.*, 2019), SH^+ (Kashinski *et al.*, 2017), BeH^+ and its isotopologues (Niyonzima *et al.*, 2017; Pop *et al.*, 2017; Niyonzima *et al.*, 2018), etc.

The reactive collision between an electron and a diatomic cation target can follow two pathways, a *direct* one when the electron is captured into a (most often doubly-excited) dissociation state of the neutral and an *indirect* one where the electron is captured in a bound mono-excited Rydberg state which in turn is predissociated by the dissociative one. Both pathways involve ionization and dissociation channels, *open* if the total energy of the molecular system is higher than the energy of its fragmentation threshold, and *closed* in the opposite case. The open channels are responsible for the direct mechanism and for the autoionization/predissociation, while the closed ionization channels imply the electron capture into series of Rydberg states (Giusti, 1980; Schneider *et al.*, 1994). The quantum interference between the indirect and the direct mechanisms results in the *total* processes.

A detailed description of method has been given in previous articles (Motapon *et al.*, 2014; Mezei *et al.*, 2019), and here, the main ideas and steps will be recalled.

1. *Building the interaction matrix:* Within a quasidiabatic representation, for a given set of conserved quantum numbers of the neutral system, Λ (projection of the electronic angular momentum on the internuclear axis) and N (total rotational quantum number), the interaction matrix is based on the couplings between ionization channels – associated with the ro-vibrational levels N^+, v^+

of the cation and with the orbital quantum number l of the incident/Rydberg electron – and dissociation channels.

2. *Computation of the reaction matrix:* We adopt the second-order perturbative ‘exact’ solution (Ngassam *et al.*, 2003) of the Lippmann-Schwinger integral equation (Florescu *et al.*, 2003; Motapon *et al.*, 2006).
3. *Diagonalization of the reaction matrix:* We end up in building the *eigenchannel* short-range representation.
4. *Frame transformation* We switch from the *Born-Oppenheimer* (short-range) representation, characterized by N , v , and Λ to the close-coupling (long-range) representation, characterized by N^+ , v^+ , Λ^+ for the ion, and l (orbital quantum number) for the incident/Rydberg electron.
5. *Building of the generalized scattering matrix:* Based on the frame-transformation coefficients and on the Cayley transform, we obtain the generalized scattering matrix, organized in blocks associated with energetically open (o) and/or closed (c) channels:

$$\mathbf{X} = \begin{pmatrix} \mathbf{X}_{oo} & \mathbf{X}_{oc} \\ \mathbf{X}_{co} & \mathbf{X}_{cc} \end{pmatrix}. \quad (4)$$

6. *Building of the physical scattering matrix:* Applying the method of “elimination of the closed channels” (Seaton, 1983) we get the scattering matrix:

$$\mathbf{S} = \mathbf{X}_{oo} - \mathbf{X}_{oc} \frac{1}{\mathbf{X}_{cc} - \exp(-i2\pi\mathbf{v})} \mathbf{X}_{co}. \quad (5)$$

The diagonal matrix \mathbf{v} in the denominator above contains the effective quantum numbers corresponding to the vibrational thresholds of the closed ionisation channels at the current total energy of the system.

7. *Computation of the cross-sections:* For the target initially in a state characterized by the quantum numbers N_i^+ , v_i^+ , Λ_i^+ , and for the energy of the incident electron ϵ , the dissociative recombination and the ro-vibrational transitions global cross-

sections read respectively

$$\sigma_{diss \leftarrow N_i^+ v_i^+} = \sum_{\Lambda, sym} \sigma_{diss \leftarrow N_i^+ v_i^+}^{(sym, \Lambda)}, \quad (6)$$

$$\sigma_{diss \leftarrow N_i^+ v_i^+}^{(sym, \Lambda)} = \frac{\pi}{4\epsilon} \rho^{(sym, \Lambda)} \sum_N \frac{2N+1}{2N_i^++1} \sum_{l,j} |S_{d_j, N_i^+ v_i^+ l}^{(sym, \Lambda, N)}|^2, \quad (7)$$

$$\sigma_{N_f^+ v_f^+ \leftarrow N_i^+ v_i^+} = \sum_{\Lambda, sym} \sigma_{N_f^+ v_f^+ \leftarrow N_i^+ v_i^+}^{(sym, \Lambda)}, \quad (8)$$

$$\begin{aligned} \sigma_{N_f^+ v_f^+ \leftarrow N_i^+ v_i^+}^{(sym, \Lambda)} &= \frac{\pi}{4\epsilon} \rho^{(sym, \Lambda)} \sum_N \frac{2N+1}{2N_i^++1} \sum_{l, l'} |S_{N_f^+ v_f^+ l', N_i^+ v_i^+ l}^{(sym, \Lambda, N)}| \\ &\quad - \delta_{N_i^+ N_f^+} \delta_{v_i^+ v_f^+} \delta_{ll'}|^2, \end{aligned} \quad (9)$$

where *sym* is referring to the inversion symmetry – gerade/ungerade – and to the spin quantum number of the neutral system, N is standing for its total rotational quantum number, and $\rho^{(sym, \Lambda)}$ is the ratio between the multiplicities of the neutral system and of the ion.

3. RESULTS AND DISCUSSIONS

The results presented in this work are the first ones going beyond our previous studies performed on HD^+ (Waffeu *et al.*, 2011; Motapon *et al.*, 2014) and H_2^+ (Epée *et al.*, 2016) for low collision energies relevant for astrophysical applications. Indeed, not only we extended the range of the incident energy of the electron but, furthermore, we considered for the first time simultaneous rotational and vibrational transitions (excitations and/or de-excitations).

The calculations were performed using the step-wise MQDT method including rotation, briefly outlined in the previous section. We have used the same molecular structure data sets as those from our previous studies (Waffeu *et al.*, 2011; Motapon *et al.*, 2014; Epée *et al.*, 2016). The cross sections have been calculated with the inclusion of both *direct* and *indirect* mechanisms for the Σ^+ , Π and Δ – singlet and triplet, gerade and ungerade – symmetries at the highest (second) order of perturbation theory. The energy range considered here was $10^{-5} - 1.7$ eV, while the energy step was taken as 0.01 meV.

Our results are presented in Figures 1–4, where we have chosen three different initial ro-vibrational levels of the ground electronic state of both target systems, namely $(N_i^+, v_i^+) = (0, 0)$, $(1, 0)$ and $(0, 1)$, corresponding to *ground* state, lowest rotationally *excited* state and lowest *vibrationally* excited state respectively. The calculated cross sections (Figs. 1–3) are restricted to low collision energies – $\epsilon \leq 0.5$

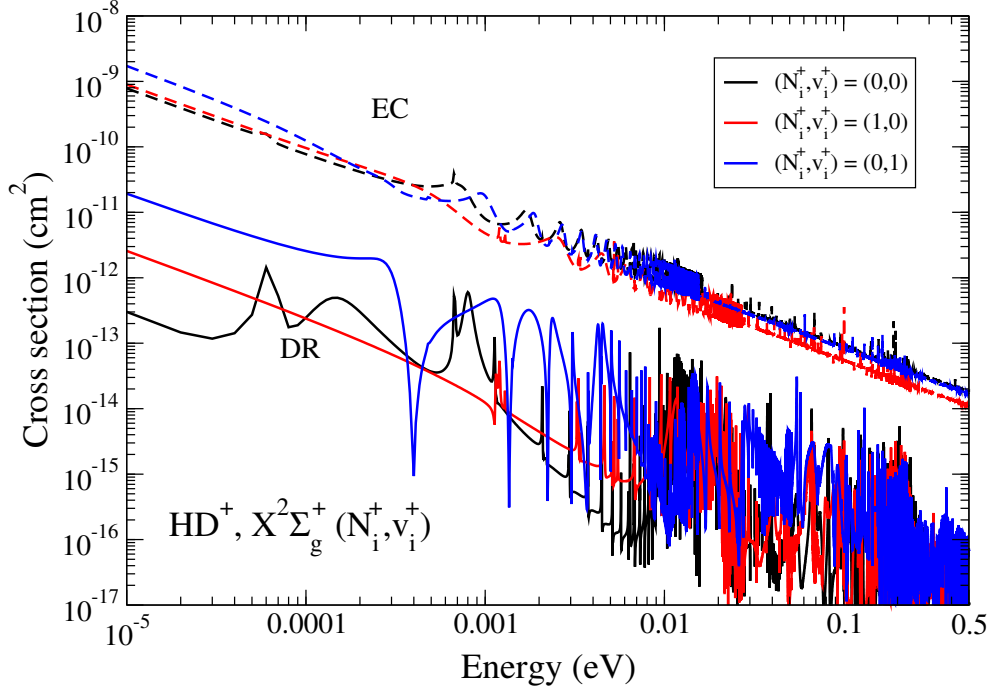


Fig. 1 – *Dissociative Recombination (DR) and Elastic Collisions (EC) of $\text{HD}^+(\text{X}^2\Sigma_g^+)$* , effect of the excitation of the target. Black: target in its ground state ($N_i^+ = 0, v_i^+ = 0$). Red: target rotationally excited ($N_i^+ = 1, v_i^+ = 0$). Blue: target vibrationally excited ($N_i^+ = 0, v_i^+ = 1$).

eV – where the rotational effects are the most relevant, while for calculating the rate coefficients (Fig. 4) we have used the cross sections on the whole energy range.

Figure 1 shows the dissociative recombination (solid lines) and resonant elastic scattering (dashed lines) cross sections of HD^+ for the previously defined three initial target states. The background $\frac{1}{\epsilon}$ trend is due to the direct mechanism, while the resonant structures correspond to the temporary captures of the incident electron into ro-vibrational levels of Rydberg states - indirect mechanism. The cross section of EC exceeds the DR by at least two orders of magnitudes, and we found that the importance of resonances and of the target-excitation effects are much less pronounced than in the case of the DR, both on order of magnitude and on position and number density of resonances.

Figure 2 illustrates the dependence of the ro-vibrational excitation – $\Delta N^+ = 0, 2, 4$ and $\Delta v^+ = 0, 1$ – cross section on the excitation of the target. While the most prominent $\Delta N^+ = 2, \Delta v^+ = 0$ transition shows very little dependence, those involving more change in the ro-vibrational state are more sensitive to the target state.

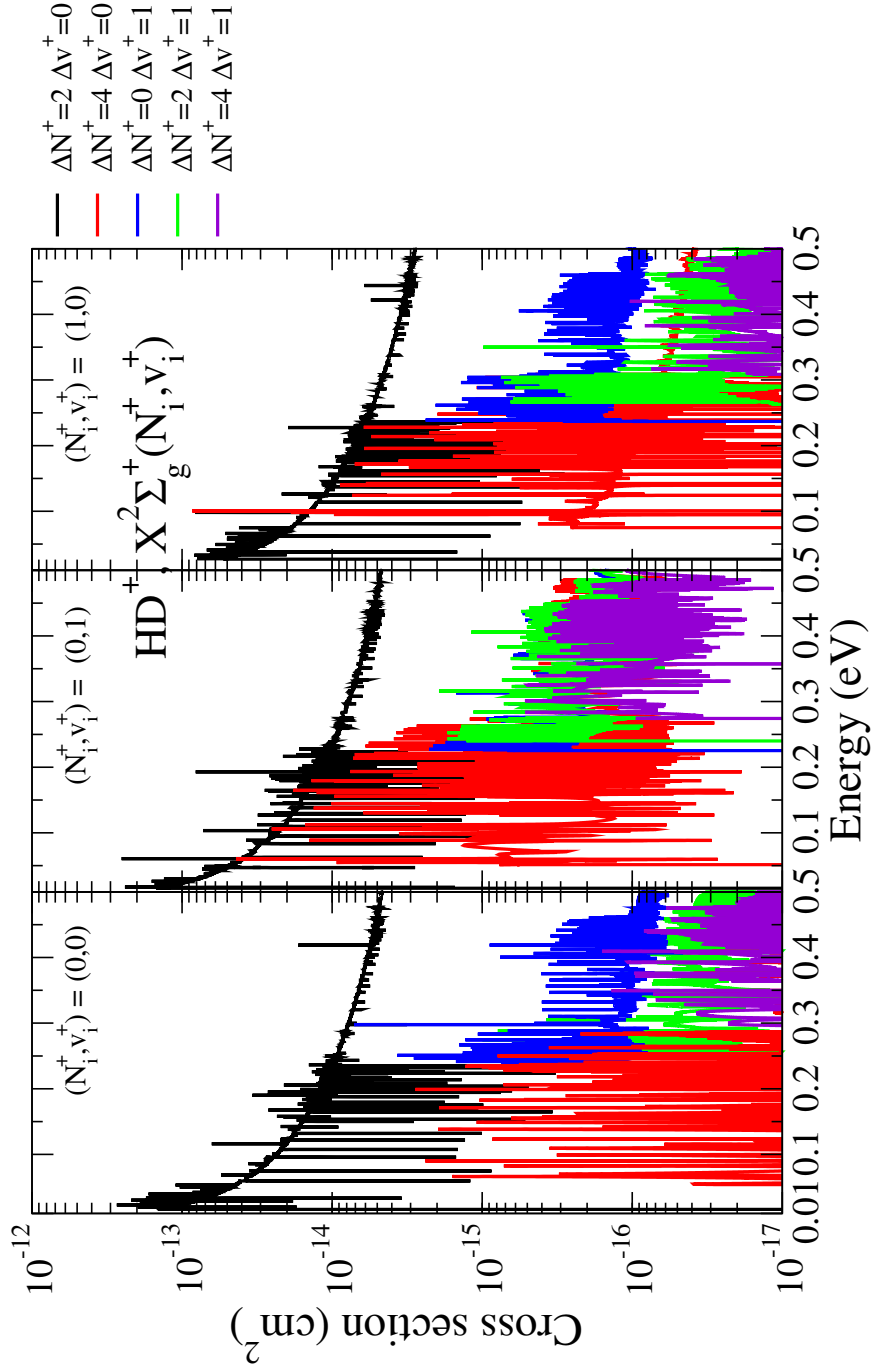


Fig. 2 – *Ro-Vibrational Excitation (RVE) of HD^+ ($X^2\Sigma_g^+$), effect of the excitation of the target. Left: target in its ground state ($N_i^+ = 0, v_i^+ = 0$). Middle: target vibrationally excited ($N_i^+ = 0, v_i^+ = 1$). Right: target rotationally excited ($N_i^+ = 1, v_i^+ = 0$).*

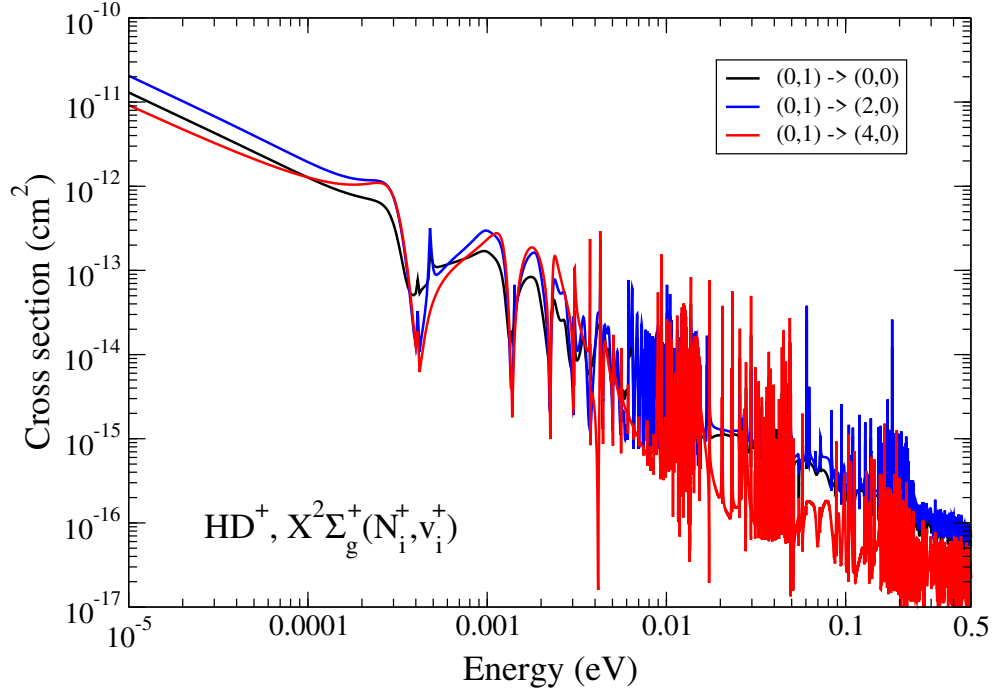


Fig. 3 – De-excitation of the lowest vibrationally-excited level ($N_i^+ = 0, v_i^+ = 1$) of $\text{HD}^+(\text{X}^2\Sigma_g^+)$, dependence on the *final* ro-vibrational state: ($N_i^+ = 0, v_i^+ = 0$) - vibrational de-excitation, black, ($N_i^+ = 2, v_i^+ = 0$) and ($N_i^+ = 4, v_i^+ = 0$) - rotational excitation and vibrational de-excitation, blue and red respectively.

The largest sensitivity corresponds to the $\Delta N^+ = 4$ transition, where a unity change in either and/or both rotational and vibrational quanta increases the cross section with more than one order of magnitude.

The cross sections display threshold effects and, similarly to DR, prominent resonances. On the other hand, concerning the intensity of the transitions, the $\Delta N^+ = 2, \Delta v^+ = 0$ one is followed by the $\Delta v^+ = 1$ purely vibrational (blue curves) and by either the $\Delta N^+ = 4$ purely rotational (red curves) or $\Delta N^+ = 2, \Delta v^+ = 1$ (green curves) 'mixed' ro-vibrational excitations. The smallest cross sections characterize the $\Delta N^+ = 4, \Delta v^+ = 1$ excitations.

Figure 3 is an illustration of the dependence of the de-excitation cross section on the *final* ro-vibrational state of the target ion. We have chosen as example the case of $\text{HD}^+(\text{X}^2\Sigma_g^+)$ initially on its ($N_i^+ = 0, v_i^+ = 1$) level. The black, blue and red curves correspond to the ($\Delta v^+ = -1, \Delta N^+ = 0$), ($\Delta v^+ = -1, \Delta N^+ = 2$), and ($\Delta v^+ = -1, \Delta N^+ = 4$) transitions respectively. While below 10 meV of collision energy the three cross sections have roughly the same shape and magnitude, above 10

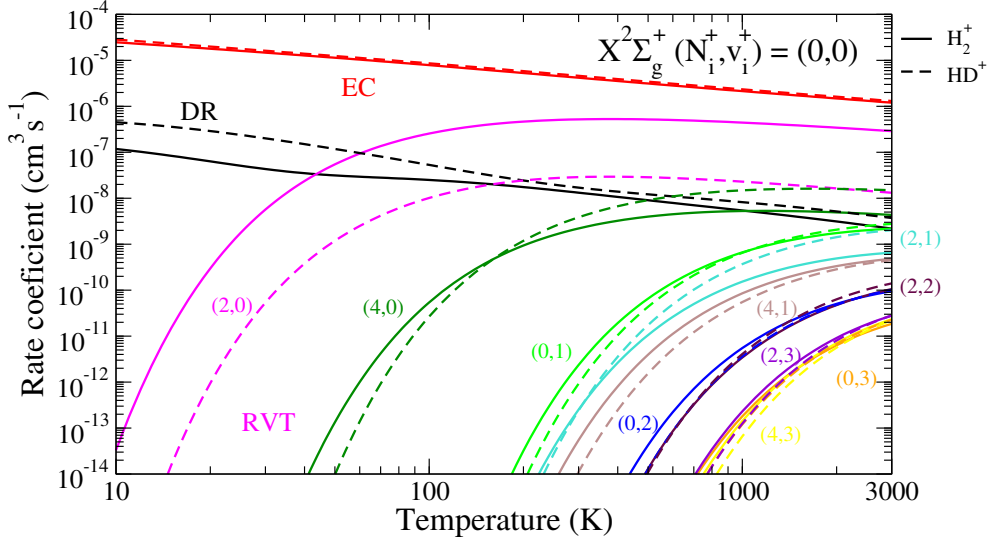


Fig. 4 – Electron-impact dissociative recombination and ro-vibrational transitions of HD^+ and H_2^+ in their ground state: Maxwell rate coefficients.

meV the $\Delta N^+ = 4$ transition shows quite different resonance patterns and becomes almost one order of magnitude smaller than the other two transitions.

And finally, in order to obtain the thermal rate coefficients, we have convoluted our cross sections with the isotropic Maxwell distribution function for the kinetic energy of the incident electrons:

$$\alpha(T) = \frac{8\pi}{(2\pi kT)^{3/2}} \int_0^{+\infty} \sigma(\varepsilon) \varepsilon \exp(-\varepsilon/kT) d\varepsilon, \quad (10)$$

where σ is one of the cross sections calculated according the eqs. (6) and (9) and k is the Boltzmann constant.

The DR and RVT Maxwell rate coefficients for electron temperatures between 10 and 3000 K are given in Fig. 4 for HD^+ and H_2^+ targets initially in their ground ro-vibrational state $(N_i^+, v_i^+) = (0, 0)$. The resonant EC rates are overall constantly the highest. Among the othess proceses the DR ones predominates at very low temperatures, and is surpassed by the lowest rotational excitation above 50 K. The higher excitations become notable above 2000 K only. Figure 4 also illustrates the isotopic effects: it is important for $\Delta N^+ = 2$ and 4 rotational excitations and for DR below 100 K electron temperature.

4. CONCLUSIONS

The multichannel quantum defect theory results in the detailed modeling of the reactive collisions of electrons with H_2^+ and HD^+ . The account of the interfering mechanisms - direct and indirect - as well as of the major interactions - Rydberg/valence, ro-vibronic and rotational - result in accurate state-to-state theoretical cross sections and rate coefficients.

The results of the present paper are a first step in the extension of our previous studies on reactive collision of HD^+ and H_2^+ with electrons to a wider range of incident collision energy and to mixed - i.e. simultaneous rotational and vibrational - transitions. The results concerning higher ro-vibrational levels are the subject of an ongoing work. We do expect a strong dependence of the cross sections and Maxwell rate coefficients on the target state. The provided collisional data are available on demand to be used in the kinetics modeling in astrochemistry - early Universe, interstellar molecular space - and cold plasma physics.

Acknowledgements. The authors acknowledge support from Agence Nationale de la Recherche *via* the project MONA, Centre National de la Recherche Scientifique *via* the GdR TheMS, PCMI program of INSU (ColEM project, co-funded by CEA and CNES), PHC program Galilée between France and Italy, and DYMCOM project, Fédération de Recherche Fusion par Confinement Magnétique (CNRS, CEA and Eurofusion), La Région Normandie, FEDER and LabEx EMC³ *via* the projects Bioengine, EMoPlaF, CO₂-VIRIDIS and PTOLEMEE, COMUE Normandie Université, the Institute for Energy, Propulsion and Environment (FR-IEPE), the European Union *via* COST (European Cooperation in Science and Technology) actions TUMIEE (CA17126), MW-GAIA (CA18104) and MD-GAS (CA18212), and ERASMUS-plus conventions between Université Le Havre Normandie and Politehnica University Timisoara, West University Timisoara and University College London. NP is grateful for the support of the Romanian Ministry of Research and Innovation, project no. 10PFE/16.10.2018, PERFORM-TECH-UPT. JZsM thanks the financial support of the National Research, Development and Innovation Fund of Hungary, under the FK 19 funding scheme with project no. FK 132989. IFS and VL thank Carla Coppola and Daniele Galli for having suggested the present work, as well as for their constant interest and encouragement.

REFERENCES

- S. Lepp, P. C. Stancil, and A. Dalgarno, *J. Phys. B: At. Mol. Opt. Phys.* **35** (2002)
- C. M. Coppola, G. Mizzi, D. Bruno, F. Esposito, D. Galli, F. Palla, S. Longo, *MNRAS* **457**, 4, 3732–3742.
- Bates, D. R. and Massey, H. S. W.: 1947, *Proc. Roy. Soc.* **192**, 1.
- Chakrabarti, K., Backodissa-Kiminou, D. R., Pop, N., Mezei, J. Zs., Motapon, O., Lique, F., Dulieu, O., Wolf, A. and Schneider, I. F.: 2013, *Phys. Rev. A* **87**, 022702.
- Epée Epée, M. D., Mezei, J. Z., Motapon, O., Pop, N. and Schneider, I. F.: 2016, *MNRAS* **455**, 276.
- Florescu, A. I., Ngassam, V., Schneider, I. F. and Suzor-Weiner, A.: 2003, *J. Phys. B: At. Mol. Opt. Phys.* **36**, 1205.

- Giusti, A.: 1980, *J. Phys. B: At. Mol. Phys.* **13**, 3867.
- Kashinski, D. O., Talbi, D., Hickman, A. P., Di Nallo, O. E., Colboc, F., Chakrabarti, K., Schneider, I. F. and Mezei, J. Zs.: 2017, *H. Chem. Phys.* **146**, 204109.
- Mezei, J. Zs., Epée Epée, M. D., Motapon, O. and Schneider, I. F.: 2019, *Atoms* **7**, 82.
- Motapon, O., Fifiring, M., Florescu, A., Waffeu Tamo, F. O., Crumeyrolle, O., Varin-Bréant, G., Bultel, A., Vervisch, P., Tennyson, J. and Schneider, I. F.: 2006, *Plasma Sources Sci. Technol.* **15**, 23.
- Motapon, O., Pop, N., Argoubi, F., Mezei, J. Zs., Epée Epée, M. D., Faure, A., Telmini, M., Tennyson, J. and Schneider, I. F.: 2014, *Phys. Rev. A* **90**, 012706.
- Ngassam, V., Florescu, A., Pichl, L., Schneider, I. F., Motapon, O. and Suzor-Weiner, A.: 2003, *Eur. Phys. J. D* **26**, 165.
- Niyonzima, S., Ilie, S., Pop, N., Mezei, J. Zs., Chakrabarti, K., Morel, V., Pérès, B., Little, D. A., Hassouni, K., Larson, Å., Orel, A. E., Benredjem, D., Bultel, A., Tennyson, J., Reiter, D. and Schneider, I. F.: 2017, *Atomic Data and Nuclear Data Tables* **115-116**, 287.
- Niyonzima, S., Pop, N., Iacob, F., Larson, Å., Orel, A. E., Mezei, J. Zs., Chakrabarti, K., Laporta, V., Hassouni, K., Benredjem, D., Bultel, A., Tennyson, J., Reiter, D. and Schneider, I. F.: 2018, *Plasma Sources Sci. Technol.* **27**, 025015.
- Pop, N., Iacob, F., Mezei, J. Zs., Motapon, O., Niyonzima, S., Kashinski, D. O., Talbi, D., Hickman, A. P. and Schneider, I. F.: 2017, *AIP Conference Proceedings* **2071**, 020007.
- Schneider, I. F., Dulieu, O., Giusti-Suzor, A. and Roueff, E.: 1994, *Astrophys. J.* **424**, 983.
- Seaton, M. J.: 1983, *Rep. Prog. Phys.* **46**, 16.
- Waffeu Tamo, F. O., Buhr, H., Motapon, O., Altevogt, S., Andrianarijaona, V. M., Grieser, M., Lammich, L., Lestinsky, M., Motsch, M., Nevo, I., Novotny, S., Orlov, D. A., Pedersen, H. B., Schwalm, D., Sprenger, F., Urbain, X., Weigel, U., Wolf, A. and Schneider, I. F.: 2011, *Phys. Rev. A* **84**, 022710.
- Shafir D., Novotny S., Buhr H., Altevogt S., Faure A., Grieser M., Harvey A. G., Heber O., Hoffmann J., Kreckel H., Lammich L., Nevo I., Pedersen H. B., Rubinstein H., Schneider I. F., Schwalm D., Tennyson J., Wolf A. and Zajfman D.: 2009, *Phys. Rev. Lett.* **102**, 223202.
- Wakelam, W. et al.: 2012, <http://kida.astrophy.u-bordeaux.fr>.

Received on 28 April 2020

Bibliography

- [1] J. A. Bittencourt. *Fundamentals of Plasma Physics*. Springer New York, 2004.
- [2] D Hunting M A Huels L Sanche B. Boudaiffa, P Cloutier. Resonant formation of DNA strand breaks by low-energy (3-20eV) electrons. *Science*, 287(5458):1658–1660, March 2000.
- [3] Jonathan Tennyson. Electron-molecule collision calculations using the *R*-matrix method. *Phys. Rep.*, 491(2-3):29 – 76, 2010.
- [4] P. G. Burke. *R-Matrix Theory of Atomic Collisions: Application to Atomic, Molecular and Optical Processes*. Springer, 2011.
- [5] N. Pop, F. Iacob, S. Niyonzima, A. Abdoulanziz, V. Laporta, D. Reiter, I.F. Schneider, and J.Zs. Mezei. Reactive collisions between electrons and bet^+ : Complete set of thermal rate coefficients up to 5000 k. *Atomic Data and Nuclear Data Tables*, 139:101414, May 2021.
- [6] M. Born and R. Oppenheimer. Zur quantentheorie der molekeln. *Annalen der Physik*, 389(20):457–484, 1927.
- [7] Attila Szabo and Neil S. Ostlund. *Modern Quantum Chemistry: Introduction to Advanced Electronic Structure Theory*. Dover Publications, Inc., Mineola, first edition, 1996.
- [8] Céline Léonard. Introduction aux calculs de structure électronique. *Master 2 PCMA lesson*, 1(1):1–97, November 2016.
- [9] C. C. J. Roothaan. New developments in molecular orbital theory. *Reviews of Modern Physics*, 23(2):69–89, April 1951.

- [10] S.M Blinder and J.E House. *Mathematical Physics in Theoretical Chemistry*. Elsevier, 2019.
- [11] M. Lanza. *Collisions inélastiques et réactives pour les milieux astrophysiques et pour les plasmas froids : Théorie et modélisation*. PhD thesis, Université du Havre, October 2014.
- [12] S. Niyonzima. *Collisions réactives dans les gaz d'intérêt énergétique*. PhD thesis, Université du Havre, 2013.
- [13] Thom H. Dunning. Gaussian basis sets for use in correlated molecular calculations. i. the atoms boron through neon and hydrogen. *The Journal of Chemical Physics*, 90(2):1007–1023, January 1989.
- [14] I F. SCHNEIDER. *Processus élémentaire et calculs de cinétique dans les plasmas en regime de recombinaison*. PhD thesis, Université Paris XI Orsay, 1992.
- [15] Takatoshi Ichino, Jürgen Gauss, and John F. Stanton. Quasidiabatic states described by coupled-cluster theory. *The Journal of Chemical Physics*, 130(17):174105, May 2009.
- [16] K. Razi Naqvi and W. Byers Brown. The non-crossing rule in molecular quantum mechanics. *International Journal of Quantum Chemistry*, 6(2):271–279, March 1972.
- [17] Ahren W. Jasper, Michael D. Hack, Donald G. Truhlar, and Piotr Piecuch. Coupled quasidiabatic potential energy surfaces for LiFH. *The Journal of Chemical Physics*, 116(19):8353, 2002.
- [18] Arkajit Mandal, Sharma SRKC Yamijala, and Pengfei Huo. Quasi-diabatic representation for nonadiabatic dynamics propagation. *Journal of Chemical Theory and Computation*, 14(4):1828–1840, February 2018.
- [19] Xiaolei Zhu and David R. Yarkony. Quasi-diabatic representations of adiabatic potential energy surfaces coupled by conical intersections including bond breaking: A more general construction procedure and an analysis of the diabatic representation. *The Journal of Chemical Physics*, 137(22):22A511, December 2012.
- [20] Johanna Brinne Ross. *Reaction dynamics on highly excited states. Doctoral Thesis in Physics*. Stockholm University, 2009.

- [21] M. J. Seaton. The quantum defect method. *Monthly Notices of the Royal Astronomical Society*, 118(5):504–518, October 1958.
- [22] U. Fano. Quantum defect theory of l uncoupling in h_2 as an example of channel-interaction treatment. *Phys. Rev. A*, 2:353–365, Aug 1970.
- [23] Ch. Jungen and O. Atabek. Rovibronic interactions in the photoabsorption spectrum of molecular hydrogen and deuterium: An application of multi-channel quantum defect methods. *J. Chem. Phys*, 66(12):5584–5609, jun 1977.
- [24] Ch. Jungen and Dan Dill. Calculation of rotational–vibrational preionization in h_2 by multichannel quantum defect theory. *The Journal of Chemical Physics*, 73(7):3338–3345, October 1980.
- [25] Chris H. Greene and Ch. Jungen. Molecular applications of quantum defect theory. In *Advances in Atomic and Molecular Physics*, pages 51–121. Elsevier, 1985.
- [26] C. M. Lee. Multichannel photodetachment theory. *Physical Review A*, 11(5):1692–1699, May 1975.
- [27] C. M. Lee. Multichannel dissociative recombination theory. *Physical Review A*, 16(1):109–122, July 1977.
- [28] A Giusti. A multichannel quantum defect approach to dissociative recombination. *Journal of Physics B: Atomic and Molecular Physics*, 13(19):3867, 1980.
- [29] U. Fano. Unified treatment of perturbed series, continuous spectra and collisions. *Journal of the Optical Society of America*, 65(9):979, September 1975.
- [30] U. Fano. Connection between configuration-mixing and quantum-defect treatments. *Physical Review A*, 17(1):93–99, January 1978.
- [31] U. FANO and A.R.P. RAU. CHARGED-PARTICLE COLLISIONS IN THE BORN APPROXIMATION. In *Atomic Collisions and Spectra*, pages 42–57. Elsevier, 1986.
- [32] C. Greene, U. Fano, and G. Strinati. General form of the quantum-defect theory. *Physical Review A*, 19(4):1485–1509, April 1979.

- [33] O Motapon, D Backodissa, F O Waffeu Tamo, D Tudorache, K Chakrabarti, J Zs Mezei, F Lique, A Bultel, L Tchang-Brillet, O Dulieu, J Tennyson, A Wolf, X Urbain, and I F Schneider. Electron–molecular cation reactive collisions: from channel mixing to competitive processes. *Journal of Physics: Conference Series*, 300(1):012018, 2011.
- [34] M J Seaton. Quantum defect theory. *Reports on Progress in Physics*, 46(2):167, 1983.
- [35] Chris H. Greene and Ch. Jungen. Molecular applications of quantum defect theory. *Advances in Atomic and Molecular Physics*, 21:51 – 121, 1985.
- [36] C. Jungen. 'molecular applications of quantum defect theory?', iop publishing, bristol. *"Molecular Applications of Quantum Defect Theory"*, IoP Publishing, Bristol, 1996.
- [37] C. Jungen. 'elements of quantum defect theory?', in m. quack and f. merkt (editors), handbook of high resolution spectroscopy, wiley, chichester, new york. *"Elements of Quantum Defect Theory"*, in M. Quack and F. Merkt (editors), *Handbook of High Resolution Spectroscopy*, Wiley, Chichester, New York, 2010.
- [38] J N Bardsley. Configuration interaction in the continuum states of molecules. *Journal of Physics B: Atomic and Molecular Physics*, 1(3):349, 1968.
- [39] Duncan Adam Little. Electron- n_2^+ scattering and dynamics. 1(1):1–136, 2015.
- [40] K Chakrabarti, D R Backodissa-Kiminou, N Pop, J Zs Mezei, O Motapon, F Lique, O Dulieu, A Wolf, and I F Schneider. Dissociative recombination of electrons with diatomic molecular cations above dissociation threshold: Application to h_2^+ and hd^+ . *Phys. Rev. A*, 87:022702, 2013.
- [41] V Sidis and H Lefebvre-Brion. A 'quasi-diabatic' representation for inelastic collisions application to the scattering of he^+ by ne . *Journal of Physics B: Atomic and Molecular Physics*, 4(8):1040, 1971.
- [42] Ngassam, V., Florescu, A., Pichl, L., Schneider, I. F., Motapon, O., and Suzor-Weiner, A. The short-range reaction matrix in mqdt treatment of dissociative recombination and related processes. *Eur. Phys. J. D*, 26(2):165–171, 2003.

- [43] E. S. Chang and U. Fano. Theory of electron-molecule collisions by frame transformations. *Phys. Rev. A*, 6:173–185, Jul 1972.
- [44] Vălcu, B., Schneider, I. F., Raoult, M., Strömholm, C., Larsson, M., and Suzor-Weiner, A. Rotational effects in low energy dissociative recombination of diatomic ions. *Eur. Phys. J. D*, 1(1):71–78, 1998.
- [45] T Takagi. Dissociative recombination and excitation of $\text{h } 2^+ , \text{hd}^+ ,$ and $\text{d } 2^+ ,$ with electrons for various vibrational states. *Physica Scripta*, 2002(T96):52, 2002.
- [46] M. Stroe and M. Fifrig. Dissociation and vibrational excitation of cold HD^+ by electron impact. *The European Physical Journal D*, 61(1):63–70, December 2010.
- [47] L. Carata, A. E. Orel, M. Raoult, I. F. Schneider, and A. Suzor-Weiner. Core-excited resonances in the dissociative recombination of ch^+ and cd^+ . *Phys. Rev. A*, 62:052711, Oct 2000.
- [48] M. J. Barlow, B. M. Swinyard, P. J. Owen, J. Cernicharo, H. L. Gomez, R. J. Ivison, O. Krause, T. L. Lim, M. Matsuura, S. Miller, G. Olofsson, and E. T. Polehampton. Detection of a noble gas molecular ion, $^{36}\text{arh}^+$, in the crab nebula. *Science*, 342(6164):1343–1345, dec 2013.
- [49] P. Schilke, D. A. Neufeld, H. S. P. Müller, C. Comito, E. A. Bergin, D. C. Lis, M. Gerin, J. H. Black, M. Wolfire, N. Indriolo, J. C. Pearson, K. M. Menten, B. Winkel, Á. Sánchez-Monge, T. Möller, B. Godard, and E. Falgarone. Ubiquitous argonium (arh^+) in the diffuse interstellar medium: A molecular tracer of almost purely atomic gas. *Astronomy & Astrophysics*, 566:A29, jun 2014.
- [50] Holger S. P. Müller, Sébastien Muller, Peter Schilke, Edwin A. Bergin, John H. Black, Maryvonne Gerin, Dariusz C. Lis, David A. Neufeld, and Sümeyye Suri. Detection of extragalactic argonium, ArH^+ , toward PKS 1830-211. *Astronomy & Astrophysics*, 582:L4, oct 2015.
- [51] David A. Neufeld and Mark G. Wolfire. THE CHEMISTRY OF INTERSTELLAR ARGONIUM AND OTHER PROBES OF THE MOLECULAR FRACTION IN DIFFUSE CLOUDS. *The Astrophysical Journal*, 826(2):183, jul 2016.

- [52] J B A Mitchell, O Novotny, J L LeGarrec, A Florescu-Mitchell, C Rebrion-Rowe, A V Stolyarov, M S Child, A Svendsen, M A El Ghazaly, and L H Andersen. Dissociative recombination of rare gas hydride ions: li. arh +. *Journal of Physics B: Atomic, Molecular and Optical Physics*, 38(10):L175, 2005.
- [53] F. D. Priestley, M. J. Barlow, and S. Viti. Modelling the arh+ emission from the crab nebula. *Monthly Notices of the Royal Astronomical Society*, 472(4):4444–4455, 2017.
- [54] Aleksey B. Alekseyev, Heinz–Peter Liebermann, and Robert J. Buenker. Theoretical study of the ArH⁺ photodissociation. *Physical Chemistry Chemical Physics*, 9(37):5088, 2007.
- [55] E. Roueff, A. B. Alekseyev, and J. Le Bourlot. Photodissociation of interstellar arh+. *Astronomy & Astrophysics*, 566:A30, jun 2014.
- [56] James R. Hamilton, Alexandre Faure, and Jonathan Tennyson. Electron-impact excitation of diatomic hydride cations – i. heh+, ch+, arh+. *Monthly Notices of the Royal Astronomical Society*, 455(3):3281, 2016.
- [57] A Abdoulanziz, F Colboc, D A Little, Y Moulane, J Zs Mezei, E Roueff, J Tennyson, I F Schneider, and V Laporta. Theoretical study of arh+ dissociative recombination and electron-impact vibrational excitation. *Monthly Notices of the Royal Astronomical Society*, 479(2):2415–2420, 2018.
- [58] Andrey V. Stolyarov and Mark S. Child. Theoretical study of the arh+ electronic states. *Phys. Chem. Chem. Phys.*, 7:2259–2265, 2005.
- [59] Ch. Jungen, A. L. Roche, and M. Arif. The rydberg spectrum of arh and krh: calculation by r-matrix and generalized quantum defect theory. *Philosophical Transactions of the Royal Society of London A: Mathematical, Physical and Engineering Sciences*, 355(1729):1481–1506, 1997.
- [60] Adam Kirrander, Mark S. Child, and Andrey V. Stolyarov. Ab initio and quantum-defect calculations for the rydberg states of arh. *Phys. Chem. Chem. Phys.*, 8:247–255, 2006.
- [61] J. M. Carr, P. G. Galiatsatos, J. D. Gorfinkiel, A. G. Harvey, M. A. Lysaght, D. Madden, Z. Masin, M. Plummer, J. Tennyson, and H. N. Varambhia. Ukrmol: a low-energy electron- and positron-molecule scattering suite. *The European Physical Journal D*, 66(3):58, Mar 2012.

- [62] Duncan A Little and Jonathan Tennyson. An r-matrix study of singlet and triplet continuum states of n 2. *Journal of Physics B: Atomic, Molecular and Optical Physics*, 47(10):105204, 2014.
- [63] D A Little, K Chakrabarti, J Zs Mezei, I F Schneider, and J Tennyson. Dissociative recombination of n+2 : An ab initio study. *Phys. Rev. A*, 90:052705, 2014.
- [64] Alexandre Faure, Jimena D Gorfinkiel, Lesley A Morgan, and Jonathan Tennyson. Gtobas: fitting continuum functions with gaussian-type orbitals. *Computer Physics Communications*, 144(2):224 – 241, 2002.
- [65] Jonathan Tennyson. R -matrix calculation of rydberg states of co. *Journal of Physics B: Atomic, Molecular and Optical Physics*, 29(24):6185, 1996.
- [66] Jonathan Tennyson and Cliff J. Noble. RESON a program for the detection and fitting of breit-wigner resonances. *Computer Physics Communications*, 33(4):421 – 424, 1984.
- [67] H. Hotop, T. E. Roth, M.-W. Ruf, and A. J. Yench. Diatomic potential well depths from analyses of high-resolution electron energy spectra for autoionizing collision complexes. *Theoretical Chemistry Accounts*, 100(1):36–50, Nov 1998.
- [68] A. Kramida, Yu. Ralchenko, J. Reader, and and NIST ASD Team. Nist atomic spectra database (ver. 5.5.2). NIST Atomic Spectra Database (ver. 5.5.2), [Online]. Available: <https://physics.nist.gov/asd> [2018, January 30]. National Institute of Standards and Technology, Gaithersburg, MD., 2018.
- [69] S Lepp, P C Stancil, and A Dalgarno. Atomic and molecular processes in the early universe. *Journal of Physics B: Atomic, Molecular and Optical Physics*, 35(10):R57–R80, may 2002.
- [70] A Dalgarno. Molecular processes in the early universe. *Journal of Physics: Conference Series*, 4(1):10, 2005.
- [71] J.B.A. Mitchell. in *Atomic and Molecular Processes in Fusion Edge Plasmas*. Springer US, 1995.
- [72] R.K. Janev. Collision processes of atomic and molecular hydrogen in fusion plasmas: The cross-section data status. In *Springer Series in Chemical Physics*, pages 415–435. Springer Berlin Heidelberg, 2005.

- [73] Keiji Nakashima, Hidekazu Takagi, and Hiroki Nakamura. Dissociative recombination of h_2^+ , HD^+ , and d_2^+ by collisions with slow electrons. *The Journal of Chemical Physics*, 86(2):726–737, January 1987.
- [74] I F Schneider, C Stromholm, L Carata, X Urbain, M Larsson, and A Suzor-Weiner. Rotational effects in dissociative recombination: theoretical study of resonant mechanisms and comparison with ion storage ring experiments. *Journal of Physics B: Atomic, Molecular and Optical Physics*, 30(11):2687–2705, June 1997.
- [75] M G Golubkov, G V Golubkov, and G K Ivanov. Low-temperature dissociative recombination of electrons with and molecular ions. *Journal of Physics B: Atomic, Molecular and Optical Physics*, 30(23):5511–5534, December 1997.
- [76] A. E. Orel. Time-dependent wave-packet study of the direct low-energy dissociative recombination of HD^+ . *Physical Review A*, 62(2), June 2000.
- [77] Sabine Morisset, Lukáš Pichl, Ann E. Orel, and Ioan F. Schneider. Wave-packet approach to rydberg resonances in dissociative recombination. *Physical Review A*, 76(4), October 2007.
- [78] Laurentiu Carata, Ioan Schneider, and Annick Suzor-Weiner. The role of rydberg states in dissociative recombination, as revealed by ion storage ring experiments. *Philosophical Transactions of the Royal Society of London. Series A: Mathematical, Physical and Engineering Sciences*, 355(1729):1677–1691, August 1997.
- [79] H. Takagi, S. Hara, and H. Sato. Off-the-energy-shell effect in the dissociative recombination of HD^+ . *Physical Review A*, 79(1), January 2009.
- [80] T. Tanabe, I. Katayama, H. Kamegaya, K. Chida, Y. Arakaki, T. Watanabe, M. Yoshizawa, M. Saito, Y. Haruyama, K. Hosono, K. Hatanaka, T. Honma, K. Noda, S. Ohtani, and H. Takagi. Dissociative recombination of HD^+ with an ultracold electron beam in a cooler ring. *Physical Review Letters*, 75(6):1066–1069, August 1995.
- [81] A. Al-Khalili, S. Rosén, H. Danared, A. M. Derkach, A. Källberg, M. Larsson, A. Le Padellec, A. Neau, J. Semaniak, R. Thomas, M. af Ugglas, L. Viktor, W. Zong, W. J. van der Zande, X. Urbain, M. J. Jensen, R. C. Bilodeau, O. Heber, H. B. Pedersen, C. P. Safvan, L. H. Andersen, M. Lange,

- J. Levin, G. Gwinner, L. Knoll, M. Scheffel, D. Schwalm, R. Wester, D. Zajfman, and A. Wolf. Absolute high-resolution rate coefficients for dissociative recombination of electrons with HD^+ : comparison of results from three heavy-ion storage rings. *Physical Review A*, 68(4), October 2003.
- [82] V. A. Krasnopolsky. Chemical composition of titan’s atmosphere and ionosphere: Observations and the photochemical model. *Icarus*, 236:83–91, 2014.
- [83] J. L. Elliot, D. F. Strobel, X. Zhu, J. A. Stansberry, L. H. Wasserman, and O. G. Franz. The thermal structure of triton’s middle atmosphere. *Icarus*, 143:425–428, 2020.
- [84] V. A. Krasnopolsky. A photochemical model of pluto’s atmosphere and ionosphere. *Icarus*, 335:113374, 2020.
- [85] L. A. Young, F. Braga-Ribas, and R. E. Johnson. Volatile evolution and atmospheres of trans-neptunian objects. In D. Prialnik, M. A. Barucci, and L. A. Young, editors, *The Trans-Neptunian solar system*, chapter 6, pages 127–151. Elsevier, The Netherlands, 2020.
- [86] R. A. Armstrong, D. M. Suszcynsky, W. A. Lyons, and T. E. Nelson. Multi-color photometric measurements of ionization and energies in sprites. *Geophys. Res. Lett.*, 27(5):653–656, 2000.
- [87] M. R. Torr. Neutral and ioan chemistry and solar fluxes. *J. Geomag. Geoelectr.*, 35:131–153, 1983.
- [88] H Lammer, W Stumptner, G.J Molina-Cuberos, S.J Bauer, and T Owen. Nitrogen isotope fractionation and its consequence for titan’s atmospheric evolution. *Planetary and Space Science*, 48(6):529–543, May 2000.
- [89] Y. L. Yung and J. R. Lyons. Triton: Topside ionosphere and nitrogen escape. *Geophysical Research Letters*, 17(10):1717–1720, September 1990.
- [90] J. Annaloro and A. Bultel. Vibrational and electronic collisional-radiative model in air for earth entry problems. *Phys. Plasmas*, 21:123512, 2020.
- [91] Y. Plastinin, G. Karabadzhak, B. Khmelinin, B. Zemliansky, A. Gorshkov, and G. Zalogin. *Measurements of the UV Radiation Generated by the Soyuz Spacecraft Transport Capsule During Reentry*.

- [92] T. Sakakura, N. Murakami, Y. Takatsuji, M. Morimoto, and T. Haruyama. Contribution of discharge excited atomic n, n_2^* , and n_2^+ to a plasma/liquid interfacial reaction as suggested by quantitative analysis. *Chem. Phys. Chem.*, 20:1467–1474, 2019.
- [93] I. A. Morozov, A. S. Mamaev, I. V. Osorgina, L. M. Lemkina, V. P. Korobov, A. Y. Belyaev, S. E. Porozova, and M. G. Sherban. Structural-mechanical and antibacterial properties of a soft elastic polyurethane surface after plasma immersion n_2^+ implantation. *Material Sci. Eng. C*, 62:242–248, 2016.
- [94] M. K. Sharma and B. K. Saikia. Discharge conditions and emission spectroscopy of n_2 and n_2^+ active species in a variable power dc pulsed plasma used for steel nitriding. *Indian J. Pure and Appl. Phys.*, 46:463–470, 2008.
- [95] J. D. Holcomb and A. Schucker. Helium plasma skin regeneration: evaluation of skin tissue effects in a porcine model and comparison to nitrogen plasma skin regeneration. *Lasers in Surgery and Medicine*, 52(1):23–32, 2020.
- [96] Edward C. Zipf. The dissociative recombination of vibrationally excited n_2^+ ions. *Geophysical Research Letters*, 7(9):645–648, September 1980.
- [97] A J Cunningham and R M Hobson. Dissociative recombination at elevated temperatures. IV. n_2^+ dominated afterglows. *J. Phys. B: Atomic and Molecular Physics*, 5(12):2328–2331, December 1972.
- [98] S. K. Mitra. Active nitrogen. *Phys. Rev.*, 90:516–521, May 1953.
- [99] Joseph Kaplan. Active nitrogen. *Phys. Rev*, 73(5):494–496, March 1948.
- [100] Manfred A. Biondi and Sanborn C. Brown. Measurement of electron-ion recombination. *Phys. Rev*, 76(11):1697–1700, December 1949.
- [101] Craig Noren, Farook B. Yousif, and J. Brian A. Mitchell. Dissociative recombination and excitation of n_2^+ . *Journal of the Chemical Society, Faraday Transactions 2*, 85(10):1697, 1989.
- [102] J. R. Peterson, A. Le Padellec, H. Danared, G. H. Dunn, M. Larsson, A. Larsson, R. Peverall, C. Strömholm, S. Rosén, M. af Ugglas, and W. J. van der Zande. Dissociative recombination and excitation of n_2^+ : Cross sections and product branching ratios. *J. Chem. Phys.*, 108(5):1978–1988, February 1998.

- [103] Steven L. Guberman. Spectroscopy above the ionization threshold: Dissociative recombination of the ground vibrational level of $\text{n}2^+$. *J. Chem. Phys.*, 137(7):074309, August 2012.
- [104] Steven L. Guberman. The vibrational dependence of dissociative recombination: Cross sections for $\text{n}2^+$. *J. Chem. Phys.*, 139(12):124318, September 2013.
- [105] Steven L. Guberman. The vibrational dependence of dissociative recombination: Rate constants for n_2^+ . *The Journal of Chemical Physics*, 141(20):204307, November 2014.
- [106] A. Abdoulanziz, C. Argentin, V. Laporta, K. Chakrabarti, A. Bultel, J. Tennyson, I. F. Schneider, and J. Zs. Mezei. Low-energy electron impact dissociative recombination and vibrational transitions of n_2^+ . *Journal of Applied Physics*, 129(5):053303, February 2021.
- [107] Duncan A Little and Jonathan Tennyson. An r-matrix study of singlet and triplet continuum states of $\text{n } 2$. *J. Phys. B: At. Mol. Opt. Phys.*, 47(10):105204, 2014.
- [108] Duncan A Little and Jonathan Tennyson. An r-matrix study of singlet and triplet continuum states of $\text{n } 2$. *Journal of Physics B: Atomic, Molecular and Optical Physics*, 47(10):105204, 2014.
- [109] Hans-Joachim Werner, Peter J. Knowles, Gerald Knizia, Frederick R. Manby, and Martin Schütz. Molpro: a general-purpose quantum chemistry program package. *WIREs Comput Mol Sci*, 2(2):242–253, 2012.
- [110] Andrew P. Ingersoll and Conway B. Leovy. The atmospheres of mars and venus. *Annual Review of Astronomy and Astrophysics*, 9(1):147–182, September 1971.
- [111] Herzberg Gerhard 1904-1999. *Molecular spectra and molecular structure. Volume 3, Electronic spectra and electronic structure of polyatomic molecules*. R.E. Krieger Pub. Co, Malabar, Fla, 1991.
- [112] E. Wigner and E. E. Witmer. Über die struktur der zweiatomigen molekel-spektren nach der quantenmechanik. *Zeitschrift für Physik*, 51(11-12):859–886, November 1928.

- [113] E. Biémont. *Spectroscopie moléculaire: Structures moléculaires et analyse spectrale*. LMD Physique. De Boeck Supérieur, 2008.
- [114] H.-J. Werner, P. J. Knowles, G. Knizia, F. R. Manby, M. Schütz, P. Celani, W. Györffy, D. Kats, T. Korona, R. Lindh, A. Mitrushenkov, G. Rauhut, K. R. Shamasundar, T. B. Adler, R. D. Amos, S. J. Bennie, A. Bernhardtsson, A. Berning, D. L. Cooper, M. J. O. Deegan, A. J. Dobbyn, F. Eckert, E. Goll, C. Hampel, A. Hesselmann, G. Hetzer, T. Hrenar, G. Jansen, C. Köppl, S. J. R. Lee, Y. Liu, A. W. Lloyd, Q. Ma, R. A. Mata, A. J. May, S. J. McNicholas, W. Meyer, T. F. Miller III, M. E. Mura, A. Nicklass, D. P. O'Neill, P. Palmieri, D. Peng, K. Pflüger, R. Pitzer, M. Reiher, T. Shiozaki, H. Stoll, A. J. Stone, R. Tarroni, T. Thorsteinsson, M. Wang, and M. Welborn. Molpro, version 2019.2, a package of ab initio programs, 2019. see.
- [115] J H Callomon, E Hirota, K Kuchitsu, W J Lafferty, A G Maki, and C S Pote. *Structure data of free polyatomic molecules. Volume VII*.
- [116] M. C. Lin and S. H. Bauer. Bimolecular reaction of n_2o with CO and the recombination of o and CO as studied in a single-pulse shock tube. *The Journal of Chemical Physics*, 50(8):3377–3391, April 1969.
- [117] Mechanism of chemiluminescent combination reactions involving oxygen atoms. *Proceedings of the Royal Society of London. Series A. Mathematical and Physical Sciences*, 269(1338):404–418, September 1962.
- [118] G. J. van Rooij, D. C. M. van den Bekerom, N. den Harder, T. Minea, G. Berden, W. A. Bongers, R. Engeln, M. F. Graswinckel, E. Zoethout, and M. C. M. van de Sanden. Taming microwave plasma to beat thermodynamics in CO_2 dissociation. *Faraday Discussions*, 183:233–248, 2015.
- [119] Qiang Huang, Diyu Zhang, Dongping Wang, Kezhao Liu, and Aart W Kleyn. Carbon dioxide dissociation in non-thermal radiofrequency and microwave plasma. *Journal of Physics D: Applied Physics*, 50(29):294001, June 2017.
- [120] Yingying Ma, Liang Peng, Hao Zhang, and Jian-Guo Yu. The potential energy surfaces of the ground and excited states of carbon dioxide molecule. *Russian Journal of Physical Chemistry A*, 88(13):2339–2347, November 2014.
- [121] Makoto Abe, Yousuke Inagaki, Larry L. Springsteen, Yutaka Matsumi, Masahiro Kawasaki, and Hiroto Tachikawa. Collisional excitation of CO

- molecules by o(1d) atoms. *The Journal of Physical Chemistry*, 98(48):12641–12645, December 1994.
- [122] Der-Yan Hwang and Alexander M. Mebel. Ab initio study of spin-forbidden unimolecular decomposition of carbon dioxide. *Chemical Physics*, 256(2):169–176, June 2000.
- [123] Peter J. Knowles, Pavel Rosmus, and Hans-Joachim Werner. On the assignment of the electronically excited singlet states in linear CO₂. *Chemical Physics Letters*, 146(3-4):230–235, May 1988.
- [124] A. Spielfiedel, N. Feautrier, G. Chambaud, P. Rosmus, and H.-J. Werner. Interactions of rydberg and valence states in CO₂. *Chemical Physics Letters*, 183(1-2):16–20, August 1991.
- [125] A. Spielfiedel, N. Feautrier, C. Cossart-Magos, G. Chambaud, P. Rosmus, H.-J. Werner, and P. Botschwina. Bent valence excited states of CO₂. *The Journal of Chemical Physics*, 97(11):8382–8388, December 1992.
- [126] B deB Darwent. Bond dissociation energies in simple molecules. Technical report, 1970.
- [127] G. J. Schulz. Cross sections and electron affinity for O-ions From O₂, CO, and CO₂ by electron impact. *Physical Review*, 128(1):178–186, October 1962.
- [128] Donald Rapp and Donald D. Briglia. Total cross sections for ionization and attachment in gases by electron impact. ii. negative-ion formation. *J. Chem. Phys.*, 43(5):1480–1489, 1965.
- [129] P. J. Chantry. Dissociative attachment in carbon dioxide. *The Journal of Chemical Physics*, 57(8):3180–3186, October 1972.
- [130] R Abouaf, R Paineau, and F Fiquet-Fayard. *Journal of Physics B: Atomic and Molecular Physics*, 9(2):303–314, February 1976.
- [131] Michel Tronc, Laurence Malegat, and Roger Azria. Zero kinetic energy ions in dissociative attachment on triatomic molecules: S-/OCS, o-/CO₂. *Chemical Physics Letters*, 92(5):551–555, November 1982.
- [132] S. K. Srivastava and O. J. Orient. Double-beam technique for collision studies from excited states: Application to vibrationally excited CO₂. *Physical Review A*, 27(2):1209–1212, February 1983.

- [133] Rainer Dressler and Michael Allan. Energy partitioning in the o-/CO₂ dissociative attachment. *Chemical Physics*, 92(2-3):449–455, January 1985.
- [134] P. Cicman, G. Senn, G. Denifl, D. Muigg, J.D. Skalny, P. Lukac, A. Stamatovic, and T.D. Märk. *Czechoslovak Journal of Physics*, 48(10):1135–1145, 1998.
- [135] Hao Li, Xiao-Fei Gao, Xin Meng, and Shan Xi Tian. Dissociative electron attachment to vibrationally excited CO₂. *Physical Review A*, 99(3), March 2019.
- [136] M. J. W. Boness and G. J. Schulz. Vibrational excitation in CO₂ via the 3.8-eV resonance. *Physical Review A*, 9(5):1969–1979, May 1974.
- [137] M. Allan. Selectivity in the excitation of fermi-coupled vibrations in CO₂ by impact of slow electrons. *Physical Review Letters*, 87(3), June 2001.
- [138] T. N. Rescigno, W. A. Isaacs, A. E. Orel, H.-D. Meyer, and C. W. McCurdy. Theoretical study of resonant vibrational excitation of CO₂ by electron impact. *Physical Review A*, 65(3), February 2002.
- [139] David C Cartwright and Sandor Trajmar. Resonant electron-impact excitation of vibrational modes in polyatomic molecules. *Journal of Physics B: Atomic, Molecular and Optical Physics*, 29(8):1549–1562, April 1996.
- [140] D S Slaughter, H Adaniya, T N Rescigno, D J Haxton, A E Orel, C W McCurdy, and A Belkacem. Dissociative electron attachment to carbon dioxide via the 8.2 eV feshbach resonance. *Journal of Physics B: Atomic, Molecular and Optical Physics*, 44(20):205203, September 2011.
- [141] A. Moradmand, D. S. Slaughter, D. J. Haxton, T. N. Rescigno, C. W. McCurdy, Th. Weber, S. Matsika, A. L. Landers, A. Belkacem, and M. Fogle. Dissociative electron attachment to carbon dioxide via the $2^2\pi_u$ shape resonance. *Physical Review A*, 88(3), September 2013.
- [142] Claude Bloch. Une formulation unifiée de la théorie des réactions nucléaires. *Nuclear Physics*, 4:503–528, August 1957.
- [143] Andrew C. Brown, Gregory S.J. Armstrong, Jakub Benda, Daniel D.A. Clarke, Jack Wragg, Kathryn R. Hamilton, Zdeněk Mašín, Jimena D.

- Gorfinkiel, and Hugo W. van der Hart. RMT: R-matrix with time-dependence. solving the semi-relativistic, time-dependent schrödinger equation for general, multielectron atoms and molecules in intense, ultrashort, arbitrarily polarized laser pulses. *Computer Physics Communications*, 250:107062, May 2020.
- [144] Michael A. Morrison, Neal F. Lane, and Lee A. Collins. Low-energy electron-molecule scattering: Application of coupled-channel theory to CO₂ collisions. *Physical Review A*, 15(6):2186–2201, June 1977.
- [145] C. W. McCurdy, W. A. Isaacs, H.-D. Meyer, and T. N. Rescigno. Resonant vibrational excitation of CO₂ by electron impact: Nuclear dynamics on the coupled components of the 2^2_u resonance. *Physical Review A*, 67(4), April 2003.
- [146] A. Dutrey, S. Guilloteau, and M. Guelin. Chemistry of protosolar-like nebulae: The molecular content of the DM Tau and GG Tau disks. *Astronomy & Astrophysics*, 317:L55–L58, January 1997.
- [147] E. F. van Dishoeck, W.-F. Thi, and G.-J. van Zadelhoff. Detection of dco⁺ in a circumstellar disk. *Astronomy & Astrophysics*, 400(1):L1–L4, February 2003.
- [148] Chunhua Qi, Jacqueline E. Kessler, David W. Koerner, Anneila I. Sargent, and Geoffrey A. Blake. Continuum and CO/hco⁺ emission from the disk around the t tauri star LkCa 15. *The Astrophysical Journal*, 597(2):986–997, November 2003.
- [149] Wayne M. Schlingman, Yancy L. Shirley, David E. Schenk, Erik Rosolowsky, John Bally, Cara Battersby, Miranda K. Dunham, Timothy P. Ellsworth-Bowers, Neal J. Evans, Adam Ginsburg, and Guy Stringfellow. THE BOLOCAM GALACTIC PLANE SURVEY. v. hco⁺ and n₂h⁺ spectroscopy of 1.1 mm dust continuum sources. *The Astrophysical Journal Supplement Series*, 195(2):14, July 2011.
- [150] D. BUHL and L. E. SNYDER. Unidentified interstellar microwave line. *Nature*, 228(5268):267–269, October 1970.
- [151] Nayana A. J., Naslim N., T. Onishi, F. Kemper, K. Tokuda, S. C. Madden, O. Morata, S. Nasri, and M. Galametz. Alma observations of hco⁺ and hcn emission in the massive star-forming region n55 of the large magellanic cloud. *The Astrophysical Journal*, 902(2):140, October 2020.

- [152] Vladimir A. Krasnopolsky. Mars' upper atmosphere and ionosphere at low, medium, and high solar activities: Implications for evolution of water. *Journal of Geophysical Research: Planets*, 107(E12):11–1–11–11, December 2002.
- [153] W D Geppert, R D Thomas, A Ehlerding, F Hellberg, F Österdahl, M Hamberg, J Semaniak, V Zhaunerchyk, M Kaminska, A Källberg, A Paal, and M Larsson. Dissociative recombination branching ratios and their influence on interstellar clouds. *Journal of Physics: Conference Series*, 4:26–31, January 2005.
- [154] T. Amano. The dissociative recombination rate coefficients of h_3^+ , hn_2^+ , and hco^+ . *The Journal of Chemical Physics*, 92(11):6492–6501, June 1990.
- [155] N. G. Adams, D. Smith, and Erich Alge. Measurements of dissociative recombination coefficients of h_3^+ , hco^+ , n_2h^+ , and ch^+ at 95 and 300 k using the falp apparatus. *The Journal of Chemical Physics*, 81(4):1778–1784, August 1984.
- [156] A Le Padellec, C Sheehan, D Talbi, and J B A Mitchell. A merged-beam study of the dissociative recombination of. *Journal of Physics B: Atomic, Molecular and Optical Physics*, 30(2):319–327, January 1997.
- [157] Åsa Larson, Stefano Tonzani, Robin Santra, and Chris H Greene. Dissociative recombination of hco^+ . *Journal of Physics: Conference Series*, 4:148–154, January 2005.
- [158] Ivan A. Mikhailov, Viatcheslav Kokoouline, Åsa Larson, Stefano Tonzani, and Chris H. Greene. Renner-teller effects in hco^+ dissociative recombination. *Physical Review A*, 74(3), September 2006.
- [159] Ch. Jungen and S. T. Pratt. Renner-teller interactions in the dissociative recombination of hco^+ . *The Journal of Chemical Physics*, 129(16):164311, October 2008.
- [160] Nicolas Douguet, Viatcheslav Kokoouline, and Chris H. Greene. Theoretical rate of dissociative recombination of hco^+ and dco^+ ions. *Physical Review A*, 77(6), June 2008.
- [161] Nicolas Douguet, Viatcheslav Kokoouline, and Chris H. Greene. Theory of dissociative recombination of a linear triatomic ion with permanent electric dipole moment: Study hco^+ . *Physical Review A*, 80(6), December 2009.

- [162] Å. Larson, M. Stenrup, and A. E. Orel. Role of the direct mechanism in dissociative recombination of hco^+ and hoc^+ . *Physical Review A*, 85(4), April 2012.
- [163] S. Fonseca dos Santos, N. Douguet, V. Kokoouline, and A. E. Orel. Scattering matrix approach to the dissociative recombination of hco^+ and n_2h^+ . *The Journal of Chemical Physics*, 140(16):164308, April 2014.
- [164] Viatcheslav Kokoouline, Mehdi Ayouz, János Zsolt Mezei, Khalid Hassouni, and Ioan F Schneider. Theoretical study of dissociative recombination and vibrational excitation of the bf_2^+ ion by an electron impact. *Plasma Sources Science and Technology*, 27(11):115007, November 2018.
- [165] C. William McCurdy and Thomas N. Rescigno. Collisions of electrons with polyatomic molecules: Electron-methane scattering by the complex kohn variational method. *Physical Review A*, 39(9):4487–4493, May 1989.
- [166] A. E. Orel, T. N. Rescigno, and B. H. Lengsfeld. Dissociative excitation of HeH^+ by electron impact. *Physical Review A*, 44(7):4328–4335, October 1991.
- [167] Brianna J. Mount, Matthew Redshaw, and Edmund G. Myers. Dipole moments of hco^+ and nh^+ from cyclotron frequency polarizability shifts. *Physical Review A*, 85(1), January 2012.
- [168] J. M. L. Martin, Peter R. Taylor, and Timothy J. Lee. Accurate ab initio quartic force fields for the ions hco^+ and hoc^+ . *The Journal of Chemical Physics*, 99(1):286–292, July 1993.
- [169] Yukio Yamaguchi, Claude A. Richards, and Henry F. Schaefer. High level ab initio study on the ground state potential energy hypersurface of the hco^+ - coh^+ system. *The Journal of Chemical Physics*, 101(10):8945–8954, November 1994.
- [170] Eric E. Mayer, Hartmut G. Hedderich, and Edward R. Grant. Double-resonance spectroscopy of the high rydberg states of HCO. III. multiple pathways in the vibrational autoionization of the bending overtone. *The Journal of Chemical Physics*, 108(20):8429–8435, May 1998.
- [171] Jonathan Tennyson, Daniel B Brown, James J Munro, Iryna Rozum, Hemal N Varambhia, and Natalia Vinci. Quantemol-n: an expert system

- for performing electron molecule collision calculations using the r-matrix method. *Journal of Physics: Conference Series*, 86:012001, October 2007.
- [172] Bridgette Cooper, Maria Tudorovskaya, Sebastian Mohr, Aran O'Hare, Martin Hanicinec, Anna Dzarasova, Jimena Gorfinkiel, Jakub Benda, Zdeněk Mašín, Ahmed Al-Refaie, Peter Knowles, and Jonathan Tennyson. Quantemol electron collisions (QEC): An enhanced expert system for performing electron molecule collision calculations using the r-matrix method. *Atoms*, 7(4):97, October 2019.
- [173] M A Ayouz, C H Yuen, N Balucani, C Ceccarelli, I F Schneider, and V Kokoouline. Dissociative electron recombination of NH_2choh^+ and implications for interstellar formamide abundance. *Monthly Notices of the Royal Astronomical Society*, 490(1):1325–1331, September 2019.
- [174] C H Yuen, M A Ayouz, N Balucani, C Ceccarelli, I F Schneider, and V Kokoouline. Dissociative recombination of CH_2nh_2^+ : a crucial link with interstellar methanimine and titan ammonia. *Monthly Notices of the Royal Astronomical Society*, 484(1):659–664, January 2019.
- [175] P Dirac. The quantum theory of the emission and absorption of radiation. *Proc Roy Soc London Ser A*, 114(767):243–265, 1927.